ADVANCED FIBRE GRATINGS AND THEIR APPLICATIONS

Yu LIU

Doctor of Philosophy

ASTON UNIVERSITY

April 2001

ABSTRACT

ADVANCED FIBRE GRATINGS AND THEIR APPLICATIONS

Yu LIU
Doctor of Philosophy
April 2001
ASTON UNIVERSITY

This thesis describes a detailed study of advanced fibre grating devices using Bragg (FBG) and long-period (LPG) structures and their applications in optical communications and sensing. The major contributions presented in this thesis are summarised below.

One of the most important contributions from the research work presented in this thesis is a systematic theoretical study of many distinguishing structures of fibre gratings. Starting from the Maxwell equations, the coupled-mode equations for both FBG and LPG were derived and the mode-overlap factor was analytically discussed. Computing simulation programmes utilising matrix transform method based on the models built upon the coupled-mode equations were developed, enabling simulations of spectral response in terms of reflectivity, bandwidth, sidelobes and dispersion of gratings of different structures including uniform and chirped, phase-shifted, Moiré, sampled Bragg gratings, phase-shifted and cascaded long-period gratings. Although the majority of these structures were modelled numerically, analytical expressions for some complex structures were developed with a clear physical picture. Several apodisation functions were proposed to improve sidelobe suppression, which guided effective production of practical devices for demanding applications.

Fibre grating fabrication is the other major part involved in the Ph.D. programme. Both the holographic and scan-phase-mask methods were employed to fabricate Bragg and long-period gratings of standard and novel structures. Significant improvements were particularly made in the scan-phase-mask method to enable the arbitrarily tailoring of the spectral response of grating devices. Two specific techniques - slow-shifting and fast-dithering the phase-mask implemented by a computer controlled piezo – were developed to write high quality phase-shifted, sampled and apodised gratings. A large number of LabVIEW programmes were constructed to implement standard and novel fabrication techniques. In addition, some fundamental studies of grating growth in relating to the UV-exposure and hydrogenation induced index were carried out. In particular, Type IIa gratings in non-hydrogenated B/Ge co-doped fibres and a re-generated grating in hydrogenated B/Ge fibre were investigated, showing a significant observation of thermal coefficient reduction.

Optical sensing applications utilising fibre grating devices form the third major part of the research work presented in this thesis. Several experiments of novel sensing and sensing-demodulating were implemented. For the first time, an intensity and wavelength dual-coding interrogation technique was demonstrated showing significantly enhanced capacity of grating sensor multiplexing. Based on the mode-splitting measurement, instead of using conventional wavelength-shifting detection technique, successful demonstrations were also made for optical load and bend sensing of ultra-high sensitivity employing LPG structures. In addition, edge-filters and low-loss high-rejection bandpass filters of 50nm stop-band were fabricated for application in optical sensing and high-speed telecommunication systems.

Key words: fibre Bragg grating, long-period grating, optical sensing.

ACKNOWLEDGEMENTS

I would like to take this opportunity to express my gratitude to my supervisor, Prof. Ian Bennion, who offered me a great opportunity and guidance to research in the field of fibre grating technology. His enthusiasm for science and tireless attention to the research work has set me an icon and motivated me through out my years at Aston University. He always gives me high credits for any minor achievement I could ever made, which makes me feel deeply encouraged. Because of his recommendation, I was awarded a LEOS'99 fellowship, which is one of only two awards made in Europe.

I would like to thank Dr. Lin Zhang, who gave me most of the direct guidance on fibre grating fabrication. She showed me the first experiment and the first computer control programme. She encouraged me to learn Matlab and LabVIEW programmes, which offered me great help in theoretically simulating and experimentally designing and fabricating a range of new fibre grating devices. Based on her works, ideas and discussions, I developed several novel fibre grating sensing devices and systems, which form an important part of this thesis.

I would like to thank Dr. J A R Williams. Through discussions with him, I gained better understandings in waveguide theories and fibre grating fabrication techniques. Because of his recommendation, I successfully applied for LEOS'99 fellowship. I would like to thank Mr. Bert Biggs for not just offering me countless help in designing and preparing experiments, but also kindly making direct contribution to this thesis by checking and correcting English. I also would like to thank Dr. Kate Sugden, Mr. B. A. L. Gwandu and Mr. Yicheng Lai for their contributions to this thesis. My thanks also go to Dr. Wei Zhang, Dr. Lorna Everall, and Dr. Karen Chisholm for their useful discussions and helps throughout my Ph.D. programme.

I would like to take this chance to thank Prof. Hai Ming and Prof. Jianping Xie of the University of Science and Technology of China (USTC), who were the first people led me to the fibre optics world. I would like to thank Dr. Sang Bae Lee and Dr. Sang Sam Choi of Korea Institute of Science and Technology (KIST), who provided me a visiting fellowship in KIST for two years before I came to UK, which led me into the field of fibre grating technology. I also would like to thank Dr. Kam Tai Chan, the professor of Chinese University of Hong Kong, who recommended me as a Ph.D. candidate to Aston University. My thanks also goes to Dr. Xi Jia Gu, who is the manager of Photonics Research Ontario in Toronto University, for his kind offer of some amplitude masks which were particularly helpful for long-period grating studies towards this thesis.

Finally, I would like to express my deepest gratitude to my parents who are living in the countryside of China. They made me the first ever university student among the six thousand people village who lived in there for many generations. They devotedly supported my four-year undergraduate education through their hard laboring work, sometimes even under poor health. Their spirits always encourage me to be honest and to be diligent. I also would like to thank my wife Qiuli and daughter Mimi. Without their patient understandings and support, I could not finish my studies smoothly and effectively.

LIST OF CONTENTS

LIST OF FIGURES

LIST OF TABLES

CHAPTER 1

Introduction

1.1 Perspective

Although dielectric guides have been studied since the early years of last century (Hondros and Debye, 1910), the interest in optical applications only came about seventy years later. During the last twenty years, single mode fibres have been developed to offer the ultimate bandwidth for optical communications, less to mention their small size, low loss and reduced susceptibility to electromagnetic interference and reliability in many fields. In the passed ten years, fibre gratings as optical fibre devices have been developed and commercialised in optical communications, signal processing, smart structure sensing, fibre lasers and the dispersion compensation in long distance high-bit-rate fibre transmission systems. The research on new kinds of gratings and their novel applications such as long length and complex structure gratings for high-order dispersion compensation, WDM systems and sensing applications is currently carried out worldwide and is the main research emphasis covered in this thesis.

1.2 Thesis Overview

This thesis is mainly covers fibre grating simulations, fabrication techniques and their novel applications. The major results are summarized as

- Four types of new devices: fibre Bragg grating edge filters, intensity and wavelength division multiplexing systems, long-period fibre grating load sensing and bend sensing;
- Systematic theory for modelling of fibre Bragg gratings and long-period fibre gratings;

- Simulation and fabrication programmes in LabVIEW for numerous grating structures. They include apodised, chirped, wavelength-shifted, self-apodised, Moiré, sampled, phase-shifted, cascaded and long length fibre Bragg gratings, and phase-shifted and cascaded long-period fibre gratings.

The thesis overview and a review of relevant research are presented in the first two chapters to provide background information on the subject of fibre gratings and introduce the fundamental concepts. The main contents of the thesis can be grouped into three parts as illustrated in the following table.

Table 1.1 List of contents

	Chapter	Title
	1	Thesis overview
	2	Review
Part I	3	Coupled-mode theory
Part II	4	Bragg Grating Fabrication Techniques
	5	Modelling of Fibre Bragg Gratings
	6	Modelling of Long-Period Fibre Gratings
Part III	7	Applications of Fibre Gratings
	8	Conclusions
	9	References
	Appendix	Publications, List of programmes

Part I details the coupled-mode theory. Using the Maxwell equations, the coupled-mode equations for both long- and short-period fibre gratings are derived. The mode overlaps between the fundamental core mode and the possible coupled-modes are discussed analytically and calculated for up to 60-order cladding modes. The results directly reflect mode coupling corresponding to the spatial distribution of mode fields. By solving the coupled-mode equations for Bragg gratings, the peak reflectance is obtained by taking an integration of the grating coupling coefficient with respect to the grating length. For a weak grating, the reflectance is given by a Fourier transform of the coupling coefficient,

which suggests a *sinc* profile coupling coefficient results in a square reflection shape. For uniform gratings, the power distribution of the transmitted and reflected light along the grating length, the characteristics of spectra and photon-induced refractive index are investigated. For non-uniform gratings, the simulation technique utilising matrix transforms is detailed. Furthermore, the analysis is also applied to long-period fibre grating structures.

Part II consists of chapter 4, 5 and 6, containing grating fabrication and modelling. Chapter 4 discusses a number of techniques for fabricating fibre Bragg gratings. Two typical techniques, the two-beam holographic and the scanning phase mask techniques were adopted experimentally. In the two-beam holographic technique, expressions for the accurate computation of the central wavelength and chirp-rate are developed analytically, which offer great convenience and guidance during grating fabrication. A main contribution to the experimental system of this thesis is the fabrication of apodised gratings as a kind of complex grating structures, where, two approaches - slow shifting and fast dithering phase mask implemented by a computer controlled PZT stage are employed experimentally. In the slow shifting phase mask technique, the relationship between the phase mask shift and the grating coupling coefficient is an inverse *cosine* transform, while this relationship is an inverse *sinc* transform in the fast dithering phase mask technique. The shift regions of the phase mask in these two techniques are a quarter and a grating period, respectively. This technique has been extended to the fabrication of wavelength-shifted Bragg gratings, self-apodised chirped, phase-shifted, Moiré, sampled and long-length fibre Bragg gratings. The respective fabrication programmes in LabVIEW are implemented effectively with user-friendly interface controls for wider use in the Photonics Research Group.

Chapter 5 details the modelling of fibre Bragg gratings, including apodised, chirped, Moiré, sampled, phase-shifted and Type IIa gratings. In grating apodisation, simulation results show that the small truncation in the gaussian profile limits its sidelobe suppression. In order to overcome this limitation, an improved gaussian profile is proposed, in which the gaussian profile is forced to zero at the ends of the grating. This

apodisation profile produces a 15dB improvement in the sidelobe suppression compared with the gaussian profile. Simulation results also show this improved gaussian profile apodisation provides more sidelobe suppression and smoother reflection profile compared with the well-known Blackman profile apodisation. Fabrication programmes in LabVIEW are constructed and 20dB-reflectivity gratings with more than 30dB sidelobe suppression are successfully fabricated experimentally. Meanwhile, gratings with square reflection profile are also covered, where a *sinc* apodisation profile is used. This grating is a desirable filter for WDM systems. For chirped Bragg gratings, simulation results show a strong background reflection that can be suppressed by apodisation techniques. This section also discusses how to design the reflection profiles of chirped Bragg gratings with specific reflection shape for the application of the EDFA gain flattening. Simulation shows a high-order gaussian profile apodisation results in a quasi-square reflection profile. Chirped Moiré gratings are explored theoretically and experimentally as a kind of comb filters. The number of transmission peaks depends on the difference of the central wavelength of the two chirped gratings in modulus of the FSR of the grating Fabry-Perot cavity, which is equivalent to the nodes of the Moiré period. Another kind of comb filters is proposed based on sampled fibre Bragg grating structures. When a composite cosine sampling profile is applied to sample a uniform Bragg grating, a comb filter with equivalent reflectivity and wavelength spacing is obtained. For a rectangular sampling profile introduced by a shutter blocking the UV beam, sampled gratings were fabricated experimentally exhibiting dual-characteristics of Bragg and long-period gratings. Another useful grating structure is the phase-shifted fibre Bragg grating. An analytical expression with clear physical picture described by complex Fabry-Perot cavity is proposed, which extends to the cases of two and three phase shifts. By pumping a high concentration Er^{+3}/Yb^{+3}-doped fibre containing a π phase-shifted grating, a 1 kHz line-width single mode and single polarisation distributed feedback fibre laser (DFB) was realised experimentally.

Additionally, Type IIa gratings were observed by the UV holographically overexposure of non-hydrogenated B/Ge-doped fibres. However, in hydrogenated B/Ge-doped fibres, up to 18nm red shift and 16dB-reflectivity re-generated grating was obtained

experimentally. Further investigation showed that these re-generated gratings have a reduced temperature coefficient compared with the Type I gratings in the same fibres.

Chapter 6 contains the modelling of long-period fibre gratings. The spectral evolution of a long-period grating against the UV exposure was examined experimentally and theoretically, showing up to 100nm red shift and a periodical power coupling between the fibre core and cladding. The processes of hydrogen out- and in-diffusion from a fibre core and cladding were investigated by measuring the shift of a long-period fibre grating resonance. Up to 150nm wavelength shift was observed experimentally when hydrogen out-diffused from long-period fibre gratings. As complex grating structures, phase-shifted and cascaded long-period fibre gratings are detailed in this chapter. An expression with physical meaning of Mach-Zehnder interferometer is proposed. The transmission spectra with flattened, raised and sunken loss shape, or multi-peak transmission are obtained theoretically and experimentally.

Part III mainly consists of Chapter 7, with six sections to present novel applications using grating structures. They include:

1. **Grating edge filters:** details the first reported grating filter based on tilted chirped fibre Bragg gratings. These grating edge filters are stable to the ambient temperature and their slope, spectral range, loss depth, and central wavelength can be controlled effectively during grating fabrication;
2. **Wide stop-band narrow transmission filters:** presents a kind of high rejection, wide stop-band and narrow transmission filters by cascading four chirped Bragg gratings;
3. **IWDM system:** discusses the improvement to the capability of the Bragg grating sensors, involving an intensity and wavelength division multiplexing (IWDM) system first demonstrated experimentally;
4. **Long-period fibre grating index sensing:** describes theoretical and experimental results of the cladding modes of a long-period fibre grating shifting to short wavelengths with increasing the ambient refractive index.
5. **Long-period fibre grating transverse pressure sensing:** details the first

reported long-period grating resonance splitting into two sets of orthogonal polarisation states by as much as 20.5nm when a 0.08kg/mm transverse pressure of weight load is applied. The sensitivity is several hundred times higher than the results reported using fibre Bragg gratings;

6. **Long-period fibre grating bend sensing:** details the mode splitting of long-period fibre gratings by bending, where up to 85nm mode splitting was observed experimentally and exhibiting a near linear relationship between the mode splitting and the applied bend curvature, which is remarkable result in this field.

Lastly, overall conclusions of the thesis are drawn and suggestions for future work are presented in Chapter 8. A listing of 25 publications, tens of simulation and fabrication programmes in LabVIEW are contained in Appendix.

CHAPTER 2

Review

By exposing the core of germanium-doped silica optical fibre with a UV laser interference pattern, the refractive index of the fibre core is changed periodically according to the power distribution of the UV beam along the fibre axis, thereby producing a fibre Bragg grating. The grating period is of the order of the UV wavelength and the grating shows strong resonant reflection at a certain wavelength, called the Bragg wavelength, which is determined by a phase matching condition in which the ambient temperature and strain are encoded. This device is widely used in strain and temperature sensing. It is also used in optical communications for dispersion compensation and channel adding/dropping in WDM systems [1].

2.1 Background

The first fibre Bragg grating was made and used as a narrow-band reflector in 1978 by Hill and co-workers [2]. However, it did not receive great attention as the grating was formed by the standing-wave interference pattern, set up by counter-propagating beams of light at 488nm or 514.5nm from an argon-ion laser. The grating resonance is at the wavelength of the writing laser, which greatly limited its application. Subsequent investigations revealed that the photoinduced index depended on the square of the writing power, which suggested a two-photon process at the blue/green writing wavelength [3]. The grating became a popular device starting from the work of Meltz *et al.* in 1989 [4], dramatically improving the writing efficiency by demonstrating the possibility for producing gratings with an arbitrarily selected Bragg wavelength, simply by adjusting the angle between the exposure beams. Since then, interest and activity in the field has increased rapidly to the point where fabrication methods have been significantly refined;

many different fibre types have been used for grating fabrication, including several non-germanosilicate compositions. Many applications have been identified and demonstrated, and ranges of gratings are now available commercially from several suppliers.

Analysis techniques are based on expressing the grating coupling coefficient and phase as a function of the propagation direction z in the coupled-mode equations, which can be solved numerically [5, 6, 7, 8, 9, 10, 11, 12, 13]. One popular method replaces the non-uniform grating by a series of short uniform structures, each of which can be characterized by a transfer matrix. The response of the overall structure is obtained by numerical matrix multiplication [14, 15].

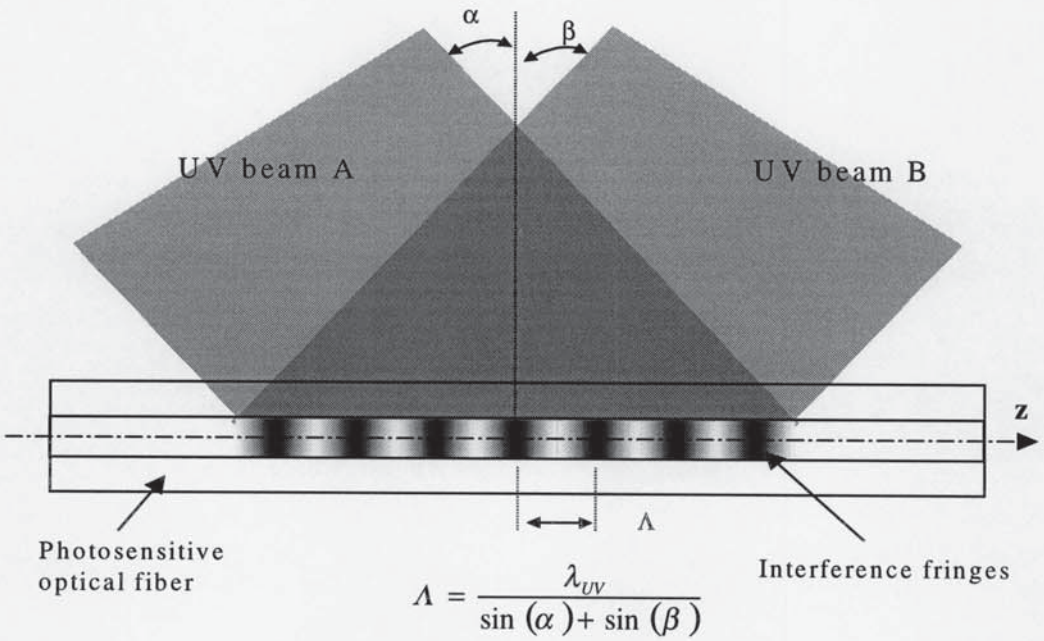

Figure 2.1 Inscription of a periodic grating in the core of a photosensitive optical fibre by two interfering UV beams of wavelength λ_{UV}

The inscription of a periodic grating into the core of an optical fibre by transverse two-beam interference is shown in Figure 2.1. The grating is photoinduced as a spatial modulation of the core refractive index with a period $\Lambda = \lambda_{UV} / (\sin\alpha + \sin\beta)$, determined by the angle α and β between the UV writing beams. The index distribution along the fibre axis given by $n(z) = n_0 + \Delta n_0 [1 + \cos(2\pi z / \Lambda)]$, with n_0 being the

unexposed core refractive index and Δn_0 the amplitude of the photoinduced index. The Bragg resonance is therefore $\lambda_B = 2n_{eff}\Lambda$, where n_{eff} is the index of LP_{01}^{co} core mode commonly called the effective index. For a 10mm long uniform grating, the full width half maximum (FWHM) is about 0.20nm theoretically. When one beam is slightly diverged or converged by inserting a cylindrical lens in just one arm, then the corresponding beam angle (α) exhibits a variable z-dependence and, thus, variation of the grating pitch is obtained as $\Lambda(z) = \lambda_{UV} / [\sin\alpha(z) + \sin\beta]$. Near-linear pitch variation results in wide-band chirped gratings.

2.2 Mechanism of Fibre Photosensitivity

Although the mechanism of photosensitivity still remains unclear and the details of the processes are not yet full resolved, the origin of the photosensitivity of Ge-doped silica fibre is understood to be linked with the UV absorption band resulting from oxygen deficiencies in the chemical structure of the fibre [16]. A strong absorption band was measured at the central wavelength 240.3nm, with FWHM of 25nm in a germanium-doped fibre [17]. The oxygen-vacancy bond is easily broken by absorbing one UV photon at about 240nm, or by two-photon absorption at 480nm, and creates a GeE' centre, characterized by a singly charged oxygen-vacancy. The formation of the GeE' centre was monitored by electron spin resonance techniques and was reported to have a strong correlation with the photosensitive grating inscription phenomenon [16, 18, 19]. The electrons released by the bleaching procedure are believed to form new absorption centres [20, 21, 22, 23]. The resultant colour centres are responsible for changes in the UV absorption spectrum of the glass, and the refractive index change follows from the Kramers-Kronig relationship [24].

$$\Delta n(\lambda) = \frac{1}{2\pi^2} P \int_0^{\infty} \frac{\Delta\alpha(\lambda')}{1 - (\lambda'/\lambda)^2} d\lambda' \tag{2.1}$$

where P is the principal part of the integral, and $\Delta\alpha$ is the net absorption change of the fibre core, confirmed with Ge-doped fibres in the IR region [25] and in the visible ranges

[23].

The support for the GeE' centre model for the photosensitivity derives from many experiments [16, 20, 21, 22, 26, 27], and it has now become clear that the mechanism responsible for the original Hill gratings [2] was two-photon absorption in the 480nm band. However, there is also evidence which suggests that the colour-centre model does not provide the complete explanation for all experimentally supported observations [28, 29, 30], and an alternative model based on glass densification induced by photoionization of the GeO defects has been suggested [31] which also has experimental support [32]. It is likely that more than one mechanism is in fact involved and that the relative influence of each is dependent on the parameters of individual fibre types, as well as the writing power and wavelength.

Measurements of the spectral changes accompanying the UV irradiation and grating inscription have shown bleaching of the 240nm band and the growth of the absorption feature at shorter wavelengths [20, 21, 22]. The new absorption bands created by the UV irradiation were reported at centres around 280nm and 215nm, both in fibres [22, 23, 33] and also in preforms [33, 34]. In particular, the measurements reported by Atkins *et al.* [20] have revealed the presence of an absorption peak at ~195nm and Kramers-Kronig analysis of their data yields values for the refractive index changes in very close agreement with those inferred from measurements on photoinduced gratings, providing support for the colour-centre model. It is also consistent with the same model that the bleaching of the 240nm band can be reversed subsequently by heating to 900°C [20]. Malo *et al.* have shown [35], however, that annealing standard germanosilicate telecommunications fibre in air at 1200°C can remove its photosensitivity irrecoverably.

To enhance the photosensitivity of a Ge-doped fibre Williams *et al.* [36] introduced Boron as a codopant and achieved an index change up to 10^{-3}. With hydrogen loaded optical fibres, 10^{-2} refractive index variation was observed [37, 38]. Both enhancements of the UV-induced refractive index changes are believed to be different from the bleaching phenomenon related to the germanium-oxygen deficiency-centre. Wong *et al.*

[21] proposed a stress relief model, where the index change arises from relaxation of the thermoelastic stress in the core of the fibre. They postulated that the wrong bonds, broken during the UV irradiation, allowed the tensioned glass network to relax and hence to increase the refractive index via the elastic-optic effect [39, 40].

Lemaire *et al.* first described a very effective photosensitisation method based on high-pressure hydrogen loading that is now widely used with GeO_2-containing fibres. In this method, the fibres are soaked in hydrogen at a pressure in the range 20-750 atmospheres (~ 150atm is typical) in the temperature range 20-75°C (room temperature is commonly used) for a period of several days. Fibres treated in this way exhibit very large values of photoinduced Δn, typically two orders of magnitude greater than in the same, non-hydrogen-loaded fibre and easily exceeding 10^{-3} [41]. The dissolved hydrogen does not produce any marked increase in the fibre absorption at 240nm, and it appears that the mechanism underlying the increase in photosensitivity stems from UV-initiated reactions of the hydrogen with the doped glass matrix forming Si-OH groups and oxygen-deficient Ge defects, both of which contribute to the observed Δn. These reactions can occur at every Ge site, and are not dependent on the presence of defects. Deuterium has been substituted for the hydrogen in some experiments to avoid the loss associated with the OH overtone at 1.39μm [42].

Archambault *et al.* [43] succeeded in inducing index changes of as much as 6×10^{-3} from single-pulse exposure and the resulting grating spectrum behavior is similar to that obtained with surface-relief gratings [44]. Microscopic examination of this kind of grating revealed the presence of a periodic damage track at the core-cladding interface [43]. Observation of periodic surface damage on the outer cladding surface has also been reported [45]. Archambault *et al.* also revealed the existence of a threshold pulse energy below which the normally encountered photorefractive response prevailed, and above which the new damage-like behavior was observed: these two regimes of grating formation are designed Type I and Type II, respectively [43]. Type II gratings were found to exhibit superior thermal stability compared with Type I, showing no degradation after prolonged periods at 800°C. Later research revealed the existence of another kind of

grating different from Type I and Type II with a negative photoinduced index [46, 47, 48]. This type of grating has a good thermal stability, similar to Type II and has been named Type IIa. It is believed that the photosensitivity is related to the UV photo-bleaching of a germanium oxygen defect centre absorption band near 5eV, although the exact mechanism has not been fully clarified and the microscopic origins of Type IIa grating spectrum formation are not well understood [49].

2.3 Fabrication Techniques

Gratings may be conveniently classified as short-period gratings (Bragg gratings) and long-period gratings, depending on whether the grating period is the order, or much larger than the propagating wavelength, respectively. The pitch of long-period gratings is normally in the range of tens to hundreds of μm, while it is typically 0.5μm for Bragg gratings. Thus, long-period gratings may be fabricated using a relatively inexpensive amplitude mask or by point-by-point side writing.

The usual experimental arrangement for writing uniform fibre Bragg gratings into optical fibres by transverse UV two-beam interferometric exposure is shown in Figure 2.1, either holographic or phase mask methods are adopted experimentally. In order to enhance the UV intensity, the beams are focused on to the fibre core in one dimension only by means of cylindrical lenses. An aperture is used to select the central portion of the gaussian beam profile to produce a near-uniform intensity profile, which precludes undesired self-chirping, resulting from the spatially non-uniform UV exposure. Although free-space holographic exposure has shown it is capable of producing gratings of the highest performance, with the Bragg wavelength arbitrarily selectable by the angle between the interfering beams, an alternative method based on near-contact exposure through a phase mask has significant advantages and has rapidly become the method of choice for reproducible grating fabrication. The phase mask is produced as a one-dimensional periodic surface relief pattern with period Λ_{PM}. The exposing UV beam is incident normal to the phase mask and diffracted by the periodic relief pattern. Generally, most of

the light is contained in the 0, +1 and -1 diffracted orders. The phase mask corrugations are designed so that the zero-order diffraction is suppressed, typically less that 5%, with approximately 40% of the total light intensity in each of the +1 and -1 orders. The grating is written with half the period of the phase mask ($\Lambda = \Lambda_{PM}/2$) by interference between the ±1-order diffraction, independent of the wavelength of the UV writing beam, shown in Figure 2.2.

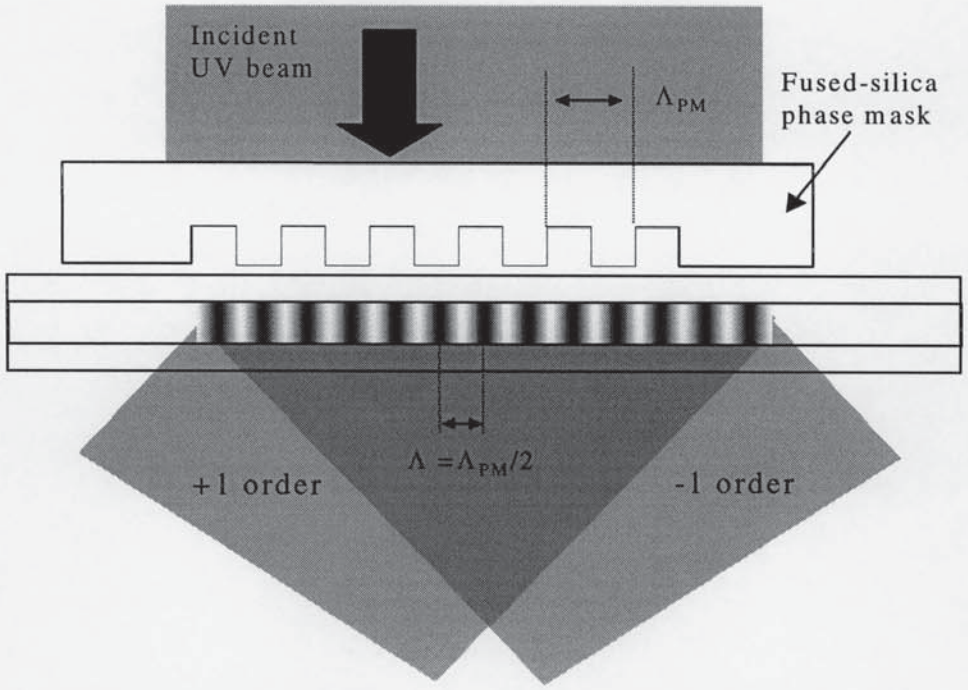

Figure 2.2 Fibre grating inscription by the UV exposure through a phase mask

A disadvantage of the phase mask method stems from the need to have a different phase mask pattern for each Bragg wavelength required. It has been demonstrated, however, that a magnifying lens placed before the mask permits variation of λ_B by almost 2nm from the unmagnified value [50]. Furthermore, it has been shown that stretching the fibre during the writing process provides a means of changing the Bragg wavelength when the fibre is relaxed following exposure [51, 52]. Further advantageous properties of phase mask writing have been demonstrated by Martin *et al.* [53] and Rourke *et al.* [54], and 15mm and 50mm long gratings have been written by the UV beam scanning across a phase mask. This writing technique has been greatly extended and 1m and longer gratings have now been fabricated [55].

Real-time monitoring of grating growth is carried out during the writing process by illuminating the grating with a broadband light source covering the grating reflection spectrum and displaying the reflected signal on an optical spectrum analyser. Limited by most optical spectrum analyser resolution (~0.1nm), an accurate grating line-width is normally obtained from higher resolution characterization, such as with a tunable laser with 0.001nm resolution.

There are many applications for which the reflection bandwidth of a uniform grating, typically <0.5nm, is too narrow. Strong uniform gratings can provide wider bandwidth but are then inevitably accompanied by substantial, unavoidable losses on the short-wavelength side of Bragg wavelength and a significant overall UV-induced loss. An alternative approach to realizing wider reflection bandwidths is to produce a grating in which the Bragg condition varies continuously or quasi-continuously along its length, with the Bragg condition given by $\lambda_B(z) = 2n_{eff}(z)\Lambda(z)$, which amounts to making either $n_{eff}(z)$ or $\Lambda(z)$ (or both) vary with position z along the grating length. Clearly, different wavelengths reflected from different positions have correspondingly different time delays, as shown in Figure 2.3; this property is widely used to compensate for standard fibre dispersion in high-bit-rate optical communication systems and in laser cavities.

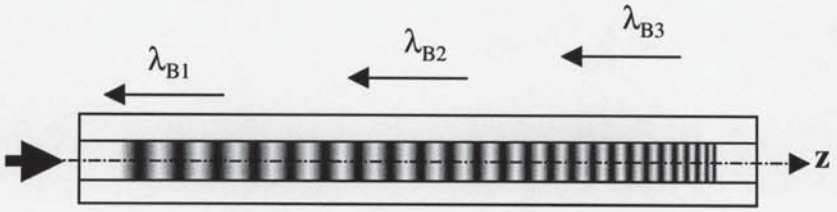

Figure 2.3 Schematic diagram of a chirped fibre Bragg grating showing longer wavelengths travel further in the grating than shorter ones

By writing a uniform grating in a tapered length of photosensitive fibres, chirped gratings were achieved with an approximately linear variation of the fibre $n_{eff}(z)$ [56]. By post UV exposure of a uniform grating to the UV beam of constant intensity but with variable velocity scanning, known as the dual scanning method, gratings of up to 2nm bandwidth

have been obtained in experiments. By bending a uniform-period grating, resulting in an effective fringe separation that varies continuously along the exposure length, a chirped grating capable of >99% reflectivity over a 7.5nm reflection bandwidth was obtained in hydrogenated, high-germanium fibre without incurring short-wavelength loss [57]. A UV beam scanning a phase-mask with continuous stretching of the fibre, allowed gratings of up to 10nm bandwidth to be achieved [58]. A chirped phase-mask has also been used in making chirped fibre gratings with the chirp in the range 1nm to 60nm [59]. A much more flexible and controllable approach to chirped grating fabrication using the two-beam interference is based on the use of dissimilar curvatures in the interfering wavefronts [60]. This technique has been used to produce chirped gratings across a wider parameter range than any other methods. Gratings with ~100% reflectivity have been produced with reflection bandwidth throughout the range from less than 1nm to greater than 100nm.

2.4 Grating Applications

Fibre gratings have been widely used in fibre optics. Amongst numerous applications are: sensing for axial strain, transverse pressure, bending, temperature, and chemical concentration and refractive index; filtering in signal processing, tunable microwave signal filtering; channel adding/dropping in WDM systems; tunable single frequency fibre lasers, multi-wavelength fibre lasers, mode-locked lasers and soliton lasers; dispersion compensation for high-bit-rate long-distance communications, higher-order dispersion compensation; fibre amplifier gain flattening; wavelength stabilization of semiconductor lasers; optical switching based on grating nonlinear effects; and so on. A few of the more important applications are introduced below.

2.4.1 Fibre grating sensors

Fibre Bragg gratings have been pursued as sensor elements for measurements of parameters including strain, vibration, temperature, pressure, and composite material cure

and response [61, 62]. A principal advantage derives from the absolute nature of the information-encoding in measurable wavelength which, in contrast to an alternative intensity-based detection approach, renders the sensor effectively independent of fluctuating light levels, source power, or connector losses. Arrays of sensor elements may be formatted in several architectures [63] and addressed by wavelength- or time-division multiplexing, or a combination of both. Wavelength-multiplexed grating sensors with up to 60 grating elements have been achieved in experiments [64]. With an applied strain ε and the ambient temperature T, the shift of the Bragg wavelength is given by

$$\frac{d\lambda}{\lambda_B} = (1-\rho_e)\varepsilon + (\xi+\alpha)dT \tag{2.2}$$

where $\rho_e = -\frac{1}{n}\frac{\partial n}{\partial \varepsilon}$ is the photo-elastic constant; $\rho_e = 0.22$ for pure silica glass, and doping the glass with germanium or other irons results in an increase of ρ_e of up to 0.26. $\alpha = \frac{1}{\Lambda}\frac{\partial \Lambda}{\partial T} \sim 0.5\times10^{-6}$ is the coefficient of linear expansion, $\xi = \frac{1}{n}\frac{\partial n}{\partial T} \sim 7\times10^{-6}$ is the thermo-optic coefficient, and dT is the temperature change [65, 66]. For a grating at 1550nm wavelength, the wavelength shifts are typically of order ~1 $pm/\mu\varepsilon$ for strain, and 10 $pm/^{\circ}C$ for temperature.

2.4.2 Fibre grating filters

Bandpass filters using phase-shifted, Moiré or cascaded chirped grating configurations [67, 68], are capable of great wavelength selectivity and can produce a narrow passband within either a relatively narrow, or a very wide stop-band, outside of which the filter returns to essentially total transmission. Further variations have been achieved using Milchelson and Mach-Zehnder interferometric approaches, which are employed in wavelength adding/dropping multiplexing systems [69, 70]. Comb filters based on Fabry-Perot resonance and sampled grating structures have been produced with very high values of finesse and have been used in a series of fibre laser demonstrations [71, 72, 73].

2.4.3 Fibre grating lasers

Use of in-fibre gratings as reflectors in fibre lasers is a natural and powerful application with not only robustness and low-cost advantages associated with integration, but also several performance-enhancing features. Gratings have been applied to silica fibres with a range of active dopants including erbium [24, 74, 75, 76, 77], neodymium [78, 79], praseodymium [80], ytterbium [81], erbium-ytterbium [82, 83, 84], and thulium [85].

Single mode Er-doped fibre lasers have been developed to the point where stable operation has been demonstrated in a 5Gbit/s system with 10^{-15} BER [86]. Sampled fibre gratings have been used to generate 101 wavelengths over a 44nm range with simultaneous output frequencies from a single laser [87]. Continuous wavelength tuning of a single-mode out of a 20mm long fibre laser has been demonstrated over a 32nm range without mode-hopping by mounting the cavity in a motor-driven precision ferrule arrangement which permitted the application of compressive stress [77]. In actively mode-locked fibre lasers, a 4mm-long chirped grating with ~100% reflectivity and 3.5nm bandwidth centred on wavelength 1556nm, giving a dispersion of ± 11ps/nm, was used to give stable mode-locked operation with 25ps output pulses [88]. In passively mode-locked fibre lasers, an output power of 170mW from near bandwidth-limited 4ps pulses with up to 10nJ pulse energy has been obtained directly from a fibre oscillator [89]. 60GHz trains of 2.2ps soliton pulses have been produced by amplifying the beat signal output of dual-frequency fibre grating lasers [90].

2.4.4 Dispersion compensation

Of the many applications envisaged for in-fibre gratings, their use as dispersion compensating elements has attracted particularly widespread interest, notably in amplified high-bit-rate fibre transmission systems where cancellation of the ~17ps/nm/km dispersion of standard telecommunication fibre is increasingly important as data rates progress to 10Gb/s and beyond.

When light propagates along a fibre, the group velocity is dependent on the light wavelength and this variation is described by the dispersion. The propagation constant β may be expressed as

$$\beta(\omega)=\beta(\omega_0)+\beta'(\omega_0)(\omega-\omega_0)+\frac{1}{2!}\beta''(\omega_0)(\omega-\omega_0)^2+\frac{1}{3!}\beta^{(3)}(\omega_0)(\omega-\omega_0)^3+\cdots \tag{2.3}$$

where $\beta=\frac{2\pi n_{eff}(\lambda)}{\lambda}$ is the propagation constant, $\omega=\frac{2\pi c}{\lambda}$ is the angle frequency while ω_0 is the reference angle frequency, c is the light velocity in vacuum and $\beta^{(n)}(\omega_0)=\left.\frac{\partial^n\beta}{\partial\omega^n}\right|_{\omega=\omega_0}$ is the *n*-order derivative at wavelength λ_0. The phase and group velocity of the light in the fibre are given by

$$\begin{cases} v_{phase}=\omega/\beta \\ v_{group}=d\omega/d\beta \end{cases} \tag{2.4}$$

where v_{phase} is the phase velocity while v_{group} is the group velocity. The dispersion coefficient is defined as the time delay (ps) for a unit wavelength spacing (nm) propagating in a unit distance (km): $D=dt/(Ld\lambda)$, where L is the fibre length. Using eqn. (2.4), the dispersion is then expressed in terms of the propagation constant when only the lowest dispersion, i.e. linear dispersion is considered [91]

$$D=\frac{d}{d\lambda}\left(\frac{1}{v_{group}}\right)=-\frac{2\pi c}{\lambda_0^{\,2}}\left.\frac{\partial^2\beta}{\partial\omega^2}\right|_{\omega=\omega_0} \tag{2.5}$$

where the time delay $t=L/v_{group}$ has been used. $\beta''<0$, $D>0$ indicates negative dispersion (shorter wavelengths travel faster than the longer wavelengths) while $\beta''>0$ indicates positive dispersion. For a silica fibre, the zero-dispersion wavelength is located at 1.27μm, the dispersion of 1550nm wavelength is about +17ps/nm/km, which leads the pulse to be stretched and expanded spatially as the shorter-wavelengths have a relatively faster propagation velocity. For a chirped grating with length L_g and bandwidth $\Delta\lambda$, the time delay between wavelengths reflected from the respective ends of the grating is

$\Delta t = \frac{2n_{eff}L_g}{c}$, and the total dispersion is thus [1]

$$\sigma = \frac{2n_{eff}L_g}{c\Delta\lambda} \tag{2.6}$$

where n_{eff} is the effective refractive index (LP_{01}^{co} mode index); $\Delta\lambda$ is the difference in wavelengths reflected from the two ends of the grating. Here the intrinsic fibre dispersion is neglected for very shorter grating length, L_g. It is apparent that by inverting the orientation of the chirped grating, dispersion of the opposite sign is realised simply.

In principle, through introducing a dispersive element that has an opposite sign and the same magnitude, dispersion-induced pulse broadening can be eliminated completely. For a pulse with bandwidth $\Delta\lambda_{pulse}$, propagating in a linear dispersion fibre, the time delay for the same wavelength spacing is the same, and can be compensated completely by a linearly chirped grating. The optimum fibre length for which the dispersion is compensated

$$L = \frac{\sigma}{D} = \frac{1}{D} \cdot \frac{2n_{eff}L_g}{c\Delta\lambda_g} \tag{2.7}$$

where D (ps/nm/km) is the fibre dispersion coefficient and $\Delta\lambda_{pulse} \approx \Delta\lambda_g$, L_g and $\Delta\lambda_g$ are the linearly chirped grating length and bandwidth, respectively [92, 93].

First practical demonstrations of dispersion compensation used 2ps pulses at 908nm wavelength in 200m long of fibre with -100ps/nm/km dispersion and a 5mm long linearly chirped grating [94], and 400fs pulses at 1560nm in 320m long of fibre with ~17-18ps/nm/km dispersion and an 8mm-long grating [95]. The experimental arrangement described by Williams *et al.* [94] is typical of those used in experiments. Subsequent dispersion-compensated system measurements have been reported at 20Gbit/s [96, 97] and the highest bit-rate-distance product reported is 2.7Tbitkm/s using a 12cm-long grating [97].

In very long-distance, high-bit-rate transmission systems and femtosecond-pulse lasers, in order to obtain a perfect dispersion compensation, higher-levels of nonlinear dispersion, the cubic dispersion term becomes significant, which is expressed as

$$D_2 = -\frac{2\pi c}{\lambda_0^2}\left[\left.\frac{\partial^2\beta}{\partial\omega^2}\right|_{\omega_0} + \left.\frac{\partial^3\beta}{\partial\omega^3}\right|_{\omega_0}(\omega-\omega_0)\right] \tag{2.8}$$

Clearly, in this case, the dispersion depends on the absolute wavelength rather than the relative wavelength as in linear dispersion case. By using complex grating structures or combinations of gratings, higher levels of compensation may be achieved [98, 99].

2.5 Long-period Fibre Gratings

Long-period gratings, as a counterpart of fibre Bragg gratings, have become increasingly popular as fibre-optic devices for applications in fibre optic communication and sensing. Long-period gratings have been demonstrated as band-rejection and gain-flattening filters for improving Er-doped fibre amplifier systems [100, 101], and also used as temperature/strain sensors [102, 103] as well as sensing demodulators [104, 105]. One of their most useful properties - the sensitivity to the ambient refractive index of the cladding modes - has led to a unique application of long-period grating sensing to measuring different concentrations of chemical solutions [106, 107, 108]. Furthermore, long-period gratings fabricated in high-birefringence fibres have exhibited high polarisation extinction ratio and low loss, showing considerable potential as fibre polarisers for optical signal processing [109, 110].

Long-period gratings are easy and inexpensive to fabricate as the grating period is typically a few hundred micrometers, compared to 0.5μm in fibre Bragg gratings. The large period enables the UV writing of long-period gratings using amplitude masks, which are significantly less expensive and less critical than the phase masks generally used in fabricating fibre Bragg gratings. The large period also permits long-period gratings to be produced using point-by-point writing technique, which removes the need

for amplitude masks, and offers the added advantage of arbitrary periods and profiles [111, 112]. Recently, several non-UV-writing techniques have been reported, showing that long-period gratings can even be produced using only a CO_2 laser or a fusion splicer [113, 114].

2.6 Chapter Summary

To summarise, this chapter has presented briefly an overview of the most fundamental concepts, which concern with fibre gratings: the history, the mechanism of photosensitivity, the fabrication techniques, the reported grating structures, and the achieved applications.

CHAPTER 3

Coupled-Mode Theory

This chapter presents the derivation of the coupled-mode equations for both long- and short-period fibre gratings from the Maxwell equations. The overlap factors between the fundamental core mode and the possible coupled-modes are analysed and calculated. By solving the coupled-mode equations for fibre Bragg gratings, the peak reflection, the weak grating approximation and the simulation technique utilising transform matrix for non-uniform gratings are investigated. For uniform Bragg gratings, the analytical solutions, calculated spectra, sidelobes, line-width, dispersion and the photoinduced refractive index are discussed. For the purpose of comparison, the analysis of long-period fibre gratings is involved in the last section.

3.1 Coupled-Mode Theory

Coupled-mode theory is one approach to obtaining an approximate solution for the propagation of electromagnetic wave in a periodic layered medium. As such, it is a useful tool for modelling how grating refractive index fringes affect a light propagation in an optical fibre. The Maxwell equation for electric field is given by [115,116]

$$\nabla \times \nabla \times \vec{E}(\vec{r},t) = -\mu_0 \frac{\partial^2 \vec{D}(\vec{r},t)}{\partial t^2} \tag{3.1}$$

where $\vec{E}(\vec{r},t)$ and $\vec{D}(\vec{r},t)$ are the electric field and its flux densities, respectively, μ_0 is the vacuum permeability. Using the identity

$$\nabla \times \nabla \times \vec{E}(\vec{r},t) \equiv \nabla\left(\nabla \cdot \vec{E}(\vec{r},t)\right) - \nabla^2 \vec{E}(\vec{r},t) \tag{3.2}$$

and the relationship between electric flux densities and electric field

$$\vec{D}(\vec{r},t)=\varepsilon_0\varepsilon_r(\vec{r})\vec{E}(\vec{r},t) \tag{3.3}$$

Eqn. (3.1) becomes

$$\nabla^2\vec{E}(\vec{r},t)=\frac{n^2(\vec{r})}{c^2}\frac{\partial^2\vec{E}(\vec{r},t)}{\partial t^2} \tag{3.4}$$

where ε_0 is the vacuum permittivity, $c=1/\sqrt{\mu_0\varepsilon_0}$ is the velocity of light in vacuum, $\varepsilon_r(\vec{r})=n^2(\vec{r})$, $n(\vec{r})$ is the fibre index, $\varepsilon_r(\vec{r})$ is the relative dielective constant. The loss and the chromatic dispersion are ignored since the grating length is only tens of millimeters. $\nabla\varepsilon(\vec{r})$ is taken to be orthogonal to $\vec{D}(\vec{r},t)$ as the perturbation is very weak ($\Delta n/n\sim10^{-4}$). Additionally, since the longitudinal part of the electric field in a fibre is much weaker than the transverse part, the transverse part of the field is selected to represent the full field as an approximation. Then, eqn. (3.4) reduces to a scalar form

$$\nabla^2E_t(\vec{r},t)-\frac{n_0{}^2}{c^2}\frac{\partial^2E_t(\vec{r},t)}{\partial t^2}=\frac{1}{c^2}\left[n^2(\vec{r})-n_0{}^2\right]\frac{\partial^2E_t(\vec{r},t)}{\partial t^2} \tag{3.5}$$

where $E_t(\vec{r},t)$ is the transverse part of the electric field, n_0 is the fibre core index prior to the perturbation of the UV beam exposure. The RHS of eqn. (3.5) describes the perturbation. In a single mode fibre, the electric field with perturbations can be expressed as the superposition of the modes of the ideal fibre, a series of cladding and core eigen-modes [117]. Hence, the total electric field is the sum of the input fundamental core mode LP_{01}^{co} and all possible coupled-modes LP_{lp}^{i} given by

$$E_t(\vec{r},t)=A_{01}^{co}(z)E_{t,01}^{co}(\vec{r},t)+\sum_{i=co,cl}\sum_{lp}B_{lp}^{i}(z)E_{t,lp}^{i} \tag{3.6}$$

where

$$E_{t,lp}^{i}=U_{lp}^{i}(\vec{r})\exp\left[-j(\omega t-\beta_{lp}^{i}z)\right] \tag{3.7}$$

where *i=co, cl* indicates the core and cladding modes, respectively. *l* and *p* are integers and extend to all discrete set confined cladding modes and core modes except the

launched core mode LP_{01}^{co}. $E_{t,01}^{co}(\bar{r},t)$ and A_{01}^{co} are the field of the launched core mode and its amplitude, respectively. $E_{t,lp}^{i}(\bar{r},t)$ and $B_{lp}^{i}(z)$ are the coupled-mode LP_{lp}^{i} fields and their amplitudes. $U_{lp}^{i}(\bar{r})\exp\left[-j(\omega t-\beta_{lp}^{i}z)\right]$ and $U_{lp}^{i}(\bar{r})$ are the fields of the eigen-modes and their amplitudes. For a fibre grating, the distribution of the fibre core refractive index along the grating length is given normally in the form of

$$n(\bar{r})=n_0+\Delta n(z)\cos\left[\frac{2\pi}{\Lambda(z)}z\right]F(\bar{r}) \tag{3.8}$$

where $\Delta n(z)<<n_0$, $\Delta n(z)$ and $\Lambda(z)$ are the amplitude of the grating index fringes and its spatial period, respectively. $F(\bar{r})$ describes the distribution of the photoinduced refractive index in the fibre cross-section.

Substituting eqn. (3.6), eqn. (3.7), and eqn. (3.8) into eqn. (3.5) yields

$$\begin{aligned}&2j\beta_{01}^{co}\frac{dA_{01}^{co}}{dz}E_{t,01}^{co}+\sum_{i=co,cl}\sum_{lp}2j\beta_{lp}^{i}\frac{dB_{lp}^{i}}{dz}E_{t,lp}^{i}\\&=2\mu_0\varepsilon_0 n_0\Delta n\cos\left(\frac{2\pi}{\Lambda}z\right)_0\left(-\omega^2\right)\left[A_{01}^{co}(z)E_{t,01}^{co}+\sum_{i=co,cl}\sum_{lp}B_{lp}^{i}(z)E_{t,lp}^{i}\right]\end{aligned} \tag{3.9}$$

where "slow" variation approximation is used so that $\frac{d^2B_{lp}^{i}}{dz^2}<<\beta_{lp}^{i}\frac{dB_{lp}^{i}}{dz}$, and the $E_{t,lp}^{i}$ obeys the unperturbed wave equation used. Multiplying both sides of eqn. (3.9) by $\left(E_{t,lp}^{i}\right)^{*}$, followed by integrating and making use of the normalized orthogonality relationship [6, 11]

$$\int_{+\infty}^{+\infty}\int E_{t,lp}^{i}E_{t,qm}^{i}dxdy=\delta_{lq}\delta_{pm} \tag{3.10}$$

Eqn. (3.9) becomes

$$\frac{dB_{lp}^{i}}{dz} = \pm j\frac{\pi\Delta n}{\lambda}\left\{C_{lp}^{i}A_{01}^{co}\left[e^{j\left(\beta_{01}^{co}-\beta_{lp}^{i}-\frac{2\pi}{\Lambda}\right)z}+e^{j\left(\beta_{01}^{co}-\beta_{lp}^{i}+\frac{2\pi}{\Lambda}\right)z}\right]+B_{lp}^{i}\left(e^{j\frac{2\pi}{\Lambda}z}+e^{-j\frac{2\pi}{\Lambda}z}\right)\right\} \tag{3.11}$$
$$-\frac{dA_{01}^{co}}{dz}\cdot\frac{\beta_{01}^{co}}{\beta_{lp}^{i}}e^{j\left(\beta_{01}^{co}-\beta_{lp}^{i}\right)z}\int\int_{-\infty}^{\infty}U_{01}^{co}(\bar{r})U_{lp}^{i}(\bar{r})dxdy$$

where $\beta_{lp}^{i} = \pm n_{lp}^{i}\omega/c$ has been used. β_{lp}^{i} is LP_{lp}^{i} mode propagation constant given by

$$\beta_{lp}^{i} = \pm\frac{2\pi n_{lp}^{i}}{\lambda} \tag{3.12}$$

where i=*co, cl.* + and - represent the forward and the backward directions, corresponding to the codirectional and contradirectional coupling, respectively. n_{lp}^{i} is LP_{lp}^{i} mode index. C_{lp}^{i} is the mode overlap factor given by

$$C_{lp}^{i} = \int\int_{-\infty}^{\infty}F(\bar{r})U_{01}^{co}(\bar{r})U_{lp}^{i}(\bar{r})dxdy \tag{3.13}$$

where C_{lp}^{i} describes the overlap between the core mode LP_{01}^{co} and the coupled-mode LP_{lp}^{i}, determined by the distribution of the mode fields.

Although, in practise, an infinite number of modes are involved, strong coupling will occur dominantly at the wavelength such that $\beta_{01}^{co}-\beta_{lp}^{i}-2\pi/\Lambda \approx 0$, which is known as the phase matching condition or resonance. Thus, only this synchronous term needs to be considered and eqn. (3.11) reduces to eqn. (3.14) (b), describing the coupling from input LP_{01}^{co} core mode to LP_{lp}^{i} coupled-modes. The coupling is for both sides as the LP_{lp}^{i} coupled-modes re-couple to LP_{01}^{co} mode at the same time. In order to examine those coupling, multiplying $\left(E_{t,01}^{co}\right)^{*}$ to both sides of eqn. (3.11), integrating and keeping the synchronous terms with $\beta_{01}^{co}-\beta_{lp}^{i}-2\pi/\Lambda \approx 0$, eqn. (3.14) (a) is then obtained. Finally, the coupled-mode equations are given by [118, 119, 120]

$$\begin{cases} \dfrac{dA_{01}^{co}(z)}{dz} = j\dfrac{\pi\Delta n}{\lambda} C_{lp}^{i} e^{-j2\delta_{lp}^{i}z} B_{lp}^{i}(z) \\ \dfrac{dB_{lp}^{i}(z)}{dz} = \pm j\dfrac{\pi\Delta n}{\lambda} C_{lp}^{i} e^{j2\delta_{lp}^{i}z} A_{01}^{co}(z) \end{cases} \tag{3.14}$$

where

$$\delta_{lp}^{i} = \frac{1}{2}\left(\beta_{01}^{co} - \beta_{lp}^{i} - \frac{2\pi}{\Lambda}\right) \tag{3.15}$$

where i=*co, cl* indicates core and cladding modes, respectively, l=0, 1, 2, …, p=1, 2, 3,… indicates the order of the coupled-modes LP_{lp}^{i}, δ_{lp}^{i} is the detuning from the Bragg resonance. The upper and lower signs of eqns. (3.14) correspond, respectively, to forward coupling and backward coupling. At resonance condition, $\delta_{lp}^{i} = 0$ gives

$$\Lambda = \frac{\lambda}{n_{01}^{co} \mp n_{lp}^{i}} \tag{3.16}$$

n_{01}^{co} and n_{lp}^{i} are the mode indexes of LP_{01}^{co} core mode and LP_{lp}^{i} coupled-modes, respectively. Clearly, the grating with contradirectional coupling requires $\Lambda \sim \dfrac{\lambda}{n_{01}^{co} + n_{lp}^{i}} < \lambda$ which is termed as short-period gratings or fibre Bragg gratings (FBGs) while the codirectional coupling requires $\Lambda = \dfrac{\lambda}{n_{01}^{co} - n_{lp}^{cl}} >> \lambda$ which is named as long-period gratings (LPGs).

Rearranging eqn. (3.16), the resonance conditions for long-period fibre gratings and Bragg gratings are given by

$$\lambda_{lp} = \left(n_{01}^{co} \mp n_{lp}^{i}\right)\Lambda = \begin{cases} \left(n_{01}^{co} - n_{lp}^{cl}\right)\Lambda & \left(LPG\right. \\ 2n_{01}^{co}\Lambda & \left(Bragg\ \ reflection\ \ in\ \ FBG\right. \\ \left(n_{01}^{co} + n_{lp}^{cl}\right)\Lambda & \left(Cladding\ \ mode\ \ in\ \ FBG\right. \end{cases} \tag{3.17}$$

Note that the dominant coupling in long-period grating is between LP_{01}^{co} core mode and LP_{0p}^{cl} cladding modes. Simplifying eqn. (3.14) yields the following identities

$$\frac{d}{dz}\left[\left|A_{01}^{co}(z)\right|^2 \pm \left|B_{lp}^{i}(z)\right|^2\right] \equiv 0 \tag{3.18}$$

Very clearly, Eqns. (3.18) expresses the conservation of energy along the grating length in both long-period fibre gratings and fibre Bragg gratings.

To summarise, the coupled-mode theory treats the period variation of the fibre core index as a perturbation that couples the unperturbed normal modes of the structure. This type of analysis usually assumes that the fibre is weakly-guiding; the difference between the refractive index of the fibre core and cladding is very small. Also the absorption, radiation mode coupling, dispersion of the fibre, nonlinear effect are neglected. Then the coupled-mode equations are obtained by solving the Maxwell equations. One useful factor of mode overlaps, describing possible mode coupling determined by spatial distributions of the mode fields have been introduced, which will be further discussed in the next section.

3.2 Mode Overlap and Mode Index

As stated in eqn. (3.13), the coupling from one mode to others results from the interaction of the mode-fields, determined by the distributions of the spatial mode-fields and described by mode overlap factors. For a weakly-guiding fibre, the eigenvalue equation for a core mode and low-order cladding modes is given by [115]

$$\frac{J_l(u^i)}{u^i J_{l+1}(u^i)} - \frac{K_l(w^i)}{w^i K_{l+1}(w^i)} = 0 \tag{3.19}$$

where i=*co, cl* indicates the core and cladding modes respectively, l=0, 1, 2, ... indicates the order of modes, u^i and w^i are propagation parameters for the core and cladding modes, respectively, $(u^i)^2 + (w^i)^2 = (V^i)^2$, $J_l(u^i)$, $K_l(w^i)$ are l-order Bessel function and l-order modified Hankel function. V^i is normalized propagation frequency, defined as

$$\begin{cases} V^{co} = \dfrac{2\pi \cdot r_{co}}{\lambda} \sqrt{n_{co}^{\,2} - n_{cl}^{\,2}} \\ V^{cl} = \dfrac{2\pi \cdot r_{cl}}{\lambda} \sqrt{n_{cl}^{\,2} - n_{amb}^{\,2}} \end{cases} \tag{3.20}$$

where n_{co}, n_{cl} and n_{amb} are the indexes of the fibre core, cladding and ambient, respectively. r_{co} and r_{cl} are the radiuses of the fibre core and cladding, respectively. For an l-order mode, eqn. (3.19) has P roots u_{lp}^i (p=1, 2, 3, ..., P), each root corresponds to the mode named by LP_{lp}^i. The normalized frequency for each mode is given by

$$(u_{lp}^i)^2 + (w_{lp}^i)^2 = (V^i)^2 \tag{3.21}$$

For a single mode fibre, eqn. (3.19) has only one root u_{01}^{co} corresponding to the fundamental core mode LP_{01}^{co}. In general, for a multiple mode fibre, the fields of LP_{lp}^i modes are given by [115, 116]

$$U_{lp}^{i}=\begin{cases}-2\tilde{A}\beta\cdot r_i\dfrac{J_l\left(u_{lp}^{i}r/r_i\right)}{J_l\left(u_{lp}^{i}\right)}\cos(l\theta) & (r\le r_i)\\ -2\tilde{A}\beta\cdot r_i\dfrac{K_l\left(w_{lp}^{i}r/r_i\right)}{K_l\left(w_{lp}^{i}\right)}\cos(l\theta) & (r>r_i)\end{cases} \tag{3.22}$$

where i=*co, cl* indicates the core and cladding modes, l=0, 1, 2,..., p=1, 2, 3,..., l and p indicate the order of LP_{lp}^{i} modes. Eqn. (3.22) describes the field distributions in a fibre core and cladding, respectively. It should be noted that the fibre cladding is no longer a weakly-guiding, the low-order modes of the hundreds modes it supports still follow this approximation [115, 116].

In general case, the mode fields are not normalized, the overlap factors between LP_{lp}^{co} core and LP_{qm}^{i} coupled-modes are thus expressed as

$$C_{lp\_qm}^{i}=\int_{-\infty}^{\infty}\int F(\bar{r})\frac{U_{lp}^{co}(\bar{r})}{\sqrt{\int_{+\infty}^{+\infty}\int U_{lp}^{co}(\bar{r})U_{lp}^{co}(\bar{r})dxdy}}\frac{U_{qm}^{i}(\bar{r})}{\sqrt{\int_{+\infty}^{+\infty}\int U_{qm}^{i}(\bar{r})U_{qm}^{i}(\bar{r})dxdy}}rdrd\theta \tag{3.23}$$

where $F(\bar{r})=\begin{cases}1 & r\le r_{co}\\ 0 & r>r_{co}\end{cases}$, taking the grating fringes to be confined to the fibre core and uniformly distributed in its cross-section. Substituting eqn. (3.22) into eqn. (3.23), the overlap factors are thus obtained. One useful observation is the following relationship

$$\int_0^{2\pi}\cos(l\theta)\cos(q\theta)d\theta=\begin{cases}2\pi & (l=q=0)\\ \pi & (l=q\neq 0)\\ 0 & (l\neq q)\end{cases} \tag{3.24}$$

It is clear that the dominant coupling is limited to identical azimuthal modes ($l=q$), where the mode fields have the same axis symmetry. However, for practical gratings due to some asymmetrical effects, there are always some weak couplings between the modes with $l\neq q$. In order to develop analytical expressions, eqn. (3.23) is discussed for two special cases, the coupling between LP_{01}^{co} core modes and LP_{01}^{co} core mode and LP_{0p}^{cl}

cladding modes, respectively.

3.2.1 Overlap factor between LP_{01}^{co} core modes

For a single mode fibre, there is only one core mode LP_{01}^{co}, hence, $l=0$, $p=1$, then, eqn. (3.23) reduces to

$$C_{01}^{co} = \frac{\int_0^{r_{co}} U_{01}^{co}(\bar{r}) U_{01}^{co}(\bar{r}) r dr}{\int_0^{\infty} U_{01}^{co}(\bar{r}) U_{01}^{co}(\bar{r}) r dr} \tag{3.25}$$

where C_{01}^{co} represents $C_{01\_01}^{co}$ in eqn. (3.23). Clearly, eqn. (3.25) describes the ratio of the power distributed in a fibre core to the total mode power as

$$C_{01}^{co} = \frac{P_{01}^{co}}{P_{01}^{co} + P_{01}^{cl}} \tag{3.26}$$

where P_{01}^{co} and P_{01}^{cl} are the power distributed in a fibre core and cladding, respectively. It is well known that around 80% total power is limited in the core of a single mode fibre, which is the maximum overlap factor between the core mode and all possible coupled-modes. In order to obtain a clear analytical expression, substituting eqn. (3.22) into eqn.(3.25) yields

$$C_{01}^{co} = \frac{\int_0^{r_{co}} \frac{J_0^{\,2}\left(u_{01}^{co} r / r_{co}\right)}{J_0^{\,2}\left(u_{01}^{co}\right)} r dr}{\int_0^{r_{co}} \frac{J_0^{\,2}\left(u_{01}^{co} r / r_{co}\right)}{J_0^{\,2}\left(u_{01}^{co}\right)} r dr + \int_{r_{co}}^{\infty} \frac{K_0^{\,2}\left(w_{01}^{co} r / r_{co}\right)}{K_0^{\,2}\left(w_{01}^{co}\right)} r dr} \tag{3.27}$$

where u_{01}^{co} is the root of eqn. (3.19). Using identities

$$\int_0^{r_{co}} J_v^{\,2}\left(u_{01}^{co} r / r_{co}\right) \cdot r dr \equiv \frac{r_{co}^{\,2}}{2}\left[J_v^{\,2}\left(u_{01}^{co}\right) - J_{v+1}\left(u_{01}^{co}\right) J_{v-1}\left(u_{01}^{co}\right)\right] \tag{3.28}$$

and

$$\int_{r_{co}}^{\infty} K_v^{\,2}\left(w_{01}^{co} r / r_{co}\right) \cdot r dr \equiv \frac{r_{co}^{\,2}}{2}\left[K_{v+1}\left(w_{01}^{co}\right) K_{v-1}\left(w_{01}^{co}\right) - K_v^{\,2}\left(w_{01}^{co}\right)\right] \tag{3.29}$$

to obtain

$$\int_{0}^{r_{co}} \frac{J_0^{\,2}\left(u_{01}^{co} r / r_{co}\right)}{J_0^{\,2}\left(u_{01}^{co}\right)} r dr = \frac{r_{co}^{\,2}}{2}\left[1 + \frac{J_1^{\,2}\left(u_{01}^{co}\right)}{J_0^{\,2}\left(u_{01}^{co}\right)}\right] \tag{3.30}$$

and

$$\int_{r_{co}}^{\infty} \frac{K_0^{\,2}\left(w_{01}^{co} r / r_{co}\right)}{K_0^{\,2}\left(w_{01}^{co}\right)} r dr = \frac{r_{co}^{\,2}}{2}\left[\frac{K_1^{\,2}\left(w_{01}^{co}\right)}{K_0^{\,2}\left(w_{01}^{co}\right)} - 1\right] \tag{3.31}$$

where the relationship $J_1\left(u_{01}^{co}\right) = -J_{-1}\left(u_{01}^{co}\right)$ and $K_1\left(w_{01}^{co}\right) = K_{-1}\left(w_{01}^{co}\right)$ have been used. Substituting eqn. (3.29), eqn. (3.30) and eqn. (3.31) into eqn. (3.27) and using eqn. (3.19), finally, the overlap factor for core modes becomes

$$C_{01}^{co} = \frac{\left(w_{01}^{co}\right)^2}{\left(u_{01}^{co}\right)^2 + \left(w_{01}^{co}\right)^2}\left[1 + \frac{J_0^{\,2}\left(u_{01}^{co}\right)}{J_1^{\,2}\left(u_{01}^{co}\right)}\right] \tag{3.32}$$

It is very clear that the calculation of the overlap factor reduces to solving the root u_{01}^{co} from eqn. (3.19).

Alternatively, a geometric-optics approximation can be applied to a weakly-guiding step-index fibre, an eigenvalue equation corresponding to eqn. (3.19) is given by [115]

$$2\sqrt{\left(u_{lp}^{i}\right)^2 - l^2} - 2l \arccos\left(\frac{l}{u_{lp}^{i}}\right) - \left(p - \frac{3}{4}\right)2\pi = 2\arccos\left[\frac{\sqrt{\left(u_{lp}^{i}\right)^2 - l^2}}{V^i}\right] \tag{3.33}$$

where i=*co*, *cl* indicates the core and cladding modes. It should be noted that eqn. (3.33) has a physical picture: the LHS gives the phase of the transverse component in modulus of 2π for a light propagating along the fibre core or cladding, and the RHS represents the phase delays due to the total internal reflection (TIR) at the interface between fibre core

and cladding, or fibre cladding and the environment. For LP_{01}^{co} core mode (l=0, p=1), eqn. (3.33) reduces to

$$u_{01}^{co} = \arccos\left(\frac{u_{01}^{co}}{V^{co}}\right) + \left(\frac{1}{4}\right)\pi \tag{3.34}$$

Obviously, for a given V^{co}, two overlap factors are obtained by solving the roots (u_{01}^{co}) from the two eigenvalue equations, eqn. (3.34) and eqn. (3.19), respectively. The overlap factors against the normalized propagation frequency V^{co} are contained in Table 3.1. Comparing the two sets of overlap factors, the values calculated from the approximation of geometric optics are slightly larger than that from mode theory. It can be understood that the power of the core mode is relatively more confined within the fibre core in the geometric profile, rather than gradually extending to the fibre cladding in the mode theory. A good approximation is given by [1, 116]

$$C_{01}^{co} \approx 1 - \frac{1}{\left(V^{co}\right)^2} \tag{3.35}$$

where, V^{co} is normalized propagation frequency. For a single mode fibre, $V^{co} \sim 2$ (V must be less than 2.404), the mode overlap is thus around 0.8.

Table 3.1 *Calculated overlap factors between forward and backward* LP_{01}^{co} *modes against the normalized propagation frequency at wavelength 1500nm for a fibre with NA=0.12,* r_{co} *=4μm and* r_{cl} *=62.5μm*

V^{co}	C_{01}^{co} (Geometric optics)	C_{01}^{co} (Mode theory)	$1-\left(V^{co}\right)^{-2}$
1.702541	0.691536	0.638216	0.6550
1.945761	0.779261	0.72506	0.7359
2.188981	0.840084	0.787021	0.7913
2.404829	0.878996	0.827581	0.8271

3.2.2 Overlap factors between LP_{01}^{co} core and LP_{0p}^{cl} cladding modes

For the coupling between LP_{01}^{co} core mode and LP_{0p}^{cl} cladding modes, the overlap factors expressed in eqn. (3.23) becomes

$$C_{0p}^{cl} = \frac{\int_0^{r_{co}} U_{01}^{co}(\bar{r}) U_{0p}^{cl}(\bar{r}) r dr}{\sqrt{\int_0^{\infty} U_{01}^{co}(\bar{r}) U_{01}^{co}(\bar{r}) r dr} \sqrt{\int_0^{\infty} U_{0p}^{cl}(\bar{r}) U_{0p}^{cl}(\bar{r}) r dr}} \tag{3.36}$$

where C_{0p}^{cl} represents $C_{01\_0p}^{cl}$ in eqn. (3.23). Using identities of eqn. (3.28) and (3.29) to obtain

$$\int_0^{r_{co}} \frac{J_0^{\,2}\left(u_{01}^{co} r / r_{co}\right)}{J_0^{\,2}\left(u_{01}^{co}\right)} r dr + \int_{r_{co}}^{\infty} \frac{K_0^{\,2}\left(w_{01}^{co} r / r_{co}\right)}{K_0^{\,2}\left(w_{01}^{co}\right)} r dr = \frac{r_{co}^{\,2}}{2} \frac{\left(V^{co}\right)^2}{\left(w_{01}^{co}\right)^2} \frac{J_1^{\,2}\left(u_{01}^{co}\right)}{J_0^{\,2}\left(u_{01}^{co}\right)} \tag{3.37}$$

and

$$\int_0^{r_{cl}} \frac{J_0^{\,2}\left(u_{0p}^{cl} r / r_{cl}\right)}{J_0^{\,2}\left(u_{0p}^{cl}\right)} r dr + \int_{r_{cl}}^{\infty} \frac{K_0^{\,2}\left(w_{0p}^{cl} r / r_{cl}\right)}{K_0^{\,2}\left(w_{0p}^{cl}\right)} r dr = \frac{r_{cl}^{\,2}}{2} \frac{\left(V^{cl}\right)^2}{\left(w_{0p}^{cl}\right)^2} \frac{J_1^{\,2}\left(u_{0p}^{cl}\right)}{J_0^{\,2}\left(u_{0p}^{cl}\right)} \tag{3.38}$$

where $V^{co} = \sqrt{\left(u_{01}^{co}\right)^2 + \left(w_{01}^{co}\right)^2}$, $V^{cl} = \sqrt{\left(u_{0p}^{cl}\right)^2 + \left(w_{0p}^{cl}\right)^2}$ and eigenvalue equations for the fibre core and cladding modes given by eqn. (3.19) as $\frac{K_1\left(w_{01}^{co}\right)}{K_0\left(w_{01}^{co}\right)} = \frac{u_{01}^{co}}{w_{01}^{co}} \frac{J_1\left(u_{01}^{co}\right)}{J_0\left(u_{01}^{co}\right)}$ and $\frac{K_1\left(w_{0p}^{cl}\right)}{K_0\left(w_{0p}^{cl}\right)} = \frac{u_{0p}^{cl}}{w_{0p}^{cl}} \frac{J_1\left(u_{0p}^{cl}\right)}{J_0\left(u_{0p}^{cl}\right)}$ have been used. Substituting eqn. (3.37) and eqn. (3.38) into eqn. (3.36), the overlap factors are obtained as

$$C_{0p}^{cl} = \frac{\int_0^{r_{co}} J_0\left(u_{01}^{co} r / r_{co}\right) J_0\left(u_{0p}^{cl} r / r_{cl}\right) r dr}{\frac{r_{co} r_{cl}}{2} \frac{V^{co} V^{cl}}{w_{01}^{co} w_{0p}^{cl}} J_1\left(u_{01}^{co}\right) J_1\left(u_{0p}^{cl}\right)} \tag{3.39}$$

Obviously, the calculation of the overlap factors also reduces to solving the roots u_{01}^{co} and u_{0p}^{cl} from the eigenvalue equation eqn. (3.19). For a fibre with NA=0.12, r_{co}=4μm and r_{cl}=62.5μm at wavelength 1500nm, the overlap factors against the order of the cladding modes is shown in Figure 3.1 and the first 10 overlaps are contained in Table 3.2. Note that $C_{05}^{cl} = 0.2358$ is referred in Chapter 6 and matched experimental results.

Table 3.2 *Overlap factors between LP_{01}^{co} core mode and LP_{0p}^{cl} cladding modes at wavelength 1500nm for a fibre with NA=0.12, r_{co}=4μm and r_{cl}=62.5μm*

Order	1	2	3	4	**5**	6	7	8	9	10
Overlap	0.1036	0.1563	0.1921	0.2178	**0.2358**	0.2472	0.2526	0.2525	0.2475	0.2380

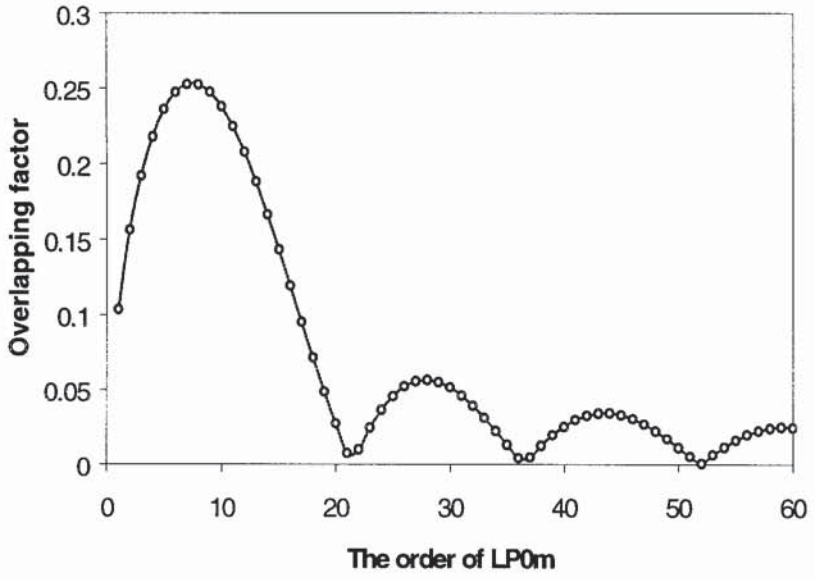

Figure 3.1 Calculated overlap factors between LP_{01}^{co} core mode and LP_{0p}^{cl} cladding modes at wavelength 1500nm showing a slow varying profile with multiple minimums for a fibre with NA=0.12, r_{co}=4μm and r_{cl}=62.5μm

It can be observed from Figure 3.1 that for the mode order lower than 7, a higher-order cladding mode has a relatively larger overlap factor compared with the lower one. The overall overlap factors are a slow varying profile with multiple minimums against the mode order, which are consistent with experimental observation discussed in section 4.1.

Note that the overlap factor between LP_{01}^{co} core and LP_{lp}^{cl} ($l \neq 0$) cladding modes may only be calculated from eqn. (3.23) numerically.

3.2.3 Fibre material index and mode index

For a pure silica glass, when the light wavelength is far from the material resonance, the refractive index $n(\omega)$ is well approximated by the Sellmerier equation as [115, 116]

$$n_{cl}(\omega) = \sqrt{1 + \sum_{j=1}^{M} \frac{B_j \omega_j^{\,2}}{\omega_j^{\,2} - \omega^2}} \tag{3.40}$$

where ω_j is the resonance frequency and B_j is the oscillator strength: $B_1 = 0.6961663$, $B_2 = 0.4079426$, $B_3 = 0.8974794$, $\lambda_1 = 0.0684043\mu m$, $\lambda_2 = 0.1162414\mu m$, $\lambda_3 = 9.896161\mu m$. The composition of a fibre cladding is almost a pure glass, but the fibre core normally dopes with B/Ge for raising the refractive index to produce a waveguide. The index of the fibre core is also given by eqn. (3.40) with slightly different coefficients and resonance [115, 116]. For simplicity, the index of a fibre core is given by

$$n_{co}(\omega) = n_{cl}(\omega) \frac{\sqrt{[n_{cl}(w_0)]^2 + [NA(w_0)]^2}}{n_{cl}(w_0)} \tag{3.41}$$

where $NA(w_0) = \sqrt{[n_{co}(w_0)]^2 - [n_{cl}(w_0)]^2}$, $NA(w_0)$ is the numerical aperture of a fibre at w_0 wavelength, normally 0.6328μm He-Ne laser wavelength.

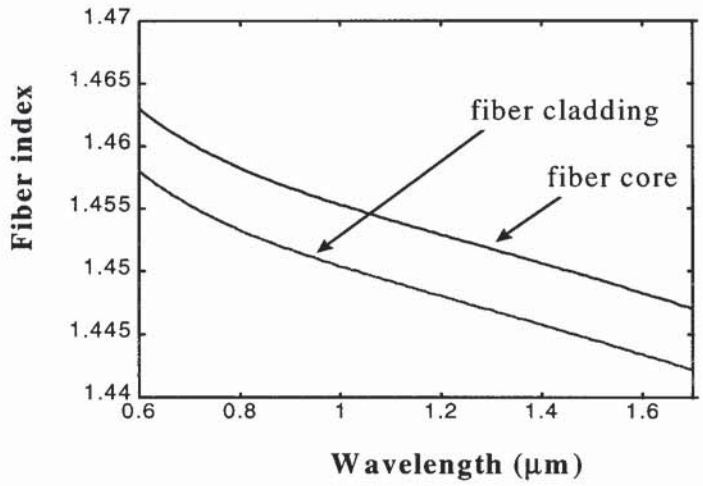

Figure 3.2 Refractive indexes of a fibre core and cladding against the operating wavelength, where NA=0.12 at wavelength 0.6328μm

For LP_{lp}^{i} mode, when the eigenvalues u_{lp}^{i} (i=co, cl) are derived from the mode eigenvalue eqn. (3.19) or the geometric optics approximation eqn. (3.33), the mode index is then given by

$$n_{lp}^{i}(\omega) = \sqrt{n_i^{\,2} - \left(\frac{u_{lp}^{i}}{2\pi r_i / \lambda}\right)^2} \tag{3.42}$$

where $i = co, cl$ indicates the core and cladding modes, respectively, l=0, 1, 2,..., p=1, 2, 3,..., l and p indicate the order of LP_{lp}^{i} modes.

To summarise, the overlap factors between core modes as well as between core and cladding modes have been investigated analytically and up to 60 overlap factors have been calculated. For the Bragg coupling, the overlap factor indicates the ratio of the power confined within the fibre core to the total power. For the coupling between the core and cladding modes, the calculation shows a slow varying profile with multiple minimums against the order of cladding modes. In addition, the index of a fibre material and mode indexes have been discussed.

3.3 Coupled-Mode Solution for Bragg gratings

This section is designed to solve the coupled-mode equations for the case of contradirectional coupling in Bragg gratings. Since the coupled-mode equations can be expressed in the form of Schrödinger equation, a series of approximation methods which was developed for solving Schrödinger equation may be used to solve the coupled-mode equations. For uniform Bragg gratings, the analytical expressions, calculated spectra, sidelobes, line-width, dispersion are discussed. In addition, the modelling technique utilising matrix transforms is detailed for non-uniform Bragg gratings.

3.3.1 Coupled-mode equations

As discussed in section 3.1, for Bragg gratings the coupled-mode equations are given by eqn. (3.14) as

$$\begin{cases} \dfrac{dA_{01}^{co}(z)}{dz} = j\kappa_{lp}^{i}(z)e^{-j2\delta_{lp}^{i}(z)z}B_{lp}^{i}(z) \\ \dfrac{dB_{lp}^{i}(z)}{dz} = -j\kappa_{lp}^{i}(z)e^{j2\delta_{lp}^{i}(z)z}A_{01}^{co}(z) \end{cases} \tag{3.43}$$

where $A_{01}^{co}(z)$ and $B_{lp}^{i}(z)$ are the amplitudes of the forward and backward core modes with absolute phases. $i = co, cl$, l=0, 1, 2, ..., p=1, 2, 3, ... indicate the order of LP_{lp}^{i} coupled modes, $\kappa_{lp}^{i}(z)$ is the coupling coefficient given by

$$\kappa_{lp}^{i}(z) = \frac{\pi\Delta n(z)}{\lambda} C_{lp}^{i} \tag{3.44}$$

where C_{lp}^{i} is mode overlap factor discussed in section 3.2. For core mode coupling, the Bragg coupling $C_{01}^{co} \approx 0.8$ is given in Table 3.1. $\delta_{lp}^{i}(z)$ is the local detuning from the Bragg resonance given by

$$\delta_{lp}^{i}(z)=\frac{1}{2}\left[\beta_{01}^{co}-\beta_{lp}^{i}-\frac{2\pi}{\Lambda(z)}\right]=\frac{\pi\left(n_{01}^{co}+n_{lp}^{i}\right)}{\lambda(z)}-\frac{\pi}{\Lambda(z)} \tag{3.45}$$

where β_{01}^{co} is LP_{01}^{co} mode propagation constant. The local Bragg resonance $\lambda_{lp}(z)$ is given by

$$\lambda_{lp}^{i}(z)=\left[n_{01}^{co}+n_{lp}^{i}(z)\right]\Lambda(z) \tag{3.46}$$

The dominant coupling in Bragg gratings is between the forward and backward core modes, $i=co$, $l=0$, $p=1$. In order to simplify eqns. (3.43), the following discussions focus on only the Bragg coupling, but the results are suitable for the coupling of backward cladding modes when corresponding coupling coefficient and resonance are used. For Bragg coupling, the electric field of the propagating light is expressed in the form of

$$E(z)=\left[A^{+}(z)e^{-j\delta_{01}(z)z}\right]e^{j\beta_{01}^{co}z}+\left[A^{-}(z)e^{j\delta_{01}(z)z}\right]e^{-j\beta_{01}^{co}z} \tag{3.47}$$

where δ_{01} is used to represent δ_{01}^{co}, $A^{+}(z)$ and $A^{-}(z)$ are the amplitudes of the forward and backward core modes with relative phases. Then the following relationships are obtained as

$$\begin{cases}A_{01}^{co}(z)=A^{+}(z)e^{-j\delta_{01}(z)z}\\ B_{01}^{co}(z)=A^{-}(z)e^{j\delta_{01}(z)z}\end{cases} \tag{3.48}$$

Substituting eqns. (3.48) into eqns. (3.43) yields

$$\begin{cases}\dfrac{dA^{+}(z)}{dz}=j\left[\delta_{01}(z)\cdot A^{+}(z)+\kappa_{01}(z)\cdot A^{-}(z)\right]\\ \dfrac{dA^{-}(z)}{dz}=-j\left[\delta_{01}(z)\cdot A^{-}(z)+\kappa_{01}(z)\cdot A^{+}(z)\right]\end{cases} \tag{3.49}$$

where κ_{01} is used to represent κ_{01}^{co}. Substituting eqns. (3.49) into each other yields

$$\begin{cases} \dfrac{d^2A^+(z)}{dz^2} = -\left[\delta_{01}{}^2(z) - \kappa_{01}{}^2(z)\right]A^+(z) \\ \dfrac{d^2A^-(z)}{dz^2} = -\left[\delta_{01}{}^2(z) - \kappa_{01}{}^2(z)\right]A^-(z) \end{cases} \tag{3.50}$$

where the approximation of slow varying quantities about the local detuning $\delta_{01}(z)$ and the local coupling coefficient $\kappa_{01}(z)$ have been used [118].

In general, the calculated spectrum of Bragg gratings is achieved by solving eqns. (3.50) numerically. An interesting observation is that the eqns. (3.50) is a typical form of Schrödinger equation in quantum theory and thus many approximation methods such as WKB method may be used to solve eqn. (3.50) for Bragg gratings [119].

3.3.2 Riccati differential equation

Although the two second-order differential equations expressed in eqns. (3.50) are of the same forms, they have different boundary conditions. In order to find a relatively simple differential equation, the index distribution along the fibre axis is given by [121]

$$n(z) = n_0\left\{1 + \sigma(z) + h(z)\cos\left[\frac{2\pi}{\Lambda_0}z + \phi(z)\right]\right\} \tag{3.51}$$

Comparing with eqn. (3.8) yields

$$\frac{2\pi}{\Lambda(z)}z = \frac{2\pi}{\Lambda_0}z + \phi(z) \tag{3.52}$$

and the detuning is given by

$$\delta_{01}(z) = \beta_{01}^{co} - \frac{\pi}{\Lambda(z)} = \delta_0 - \frac{\phi(z)}{2z} \tag{3.53}$$

where δ_0 is the average detuning defined as

$$\delta_0 = \beta_{01}^{co} - \frac{\pi}{\Lambda_0} \approx -\frac{2\pi n_{01}^{co}}{\lambda_0^{\,2}} \Delta\lambda \tag{3.54}$$

When the amplitude of the electric field is given by the following form, slightly different from eqns. (3.48), as

$$\begin{cases} A_{01}^{co}(z) = T(z)e^{-j\delta_0 z} \\ B_{01}^{co}(z) = R(z)e^{j\delta_0 z} \end{cases} \tag{3.55}$$

where $T(z)$ and $R(z)$ represent the amplitudes of the forward and backward propagating electric fields, respectively. Substituting eqns. (3.55) into eqns. (3.43) and using eqn. (3.53), the coupled-mode equations become

$$\begin{cases} \dfrac{dT(z)}{dz} = j\left[\delta_0 T(z) + \kappa_{01}(z)e^{j\phi} R(z)\right] \\ \dfrac{dR(z)}{dz} = -j\left[\delta_0 R(z) + \kappa_{01}(z)e^{-j\phi} T(z)\right] \end{cases} \tag{3.56}$$

where $-\dfrac{L}{2} \le z \le \dfrac{L}{2}$ indicates the locations of the grating; L is the grating length. The boundary conditions are normally given by

$$\begin{cases} T(-L/2) = 1 \\ R(L/2) = 0 \end{cases} \tag{3.57}$$

Define the coefficient of the local reflection $\rho(z)$ as

$$\rho(z) = \frac{R(z)}{T(z)} e^{j\phi} \tag{3.58}$$

By taking logarithms and differentiating eqn. (3.58) yields

$$\frac{\rho'(z)}{\rho(z)} = \frac{R'(z)}{R(z)} - \frac{T'(z)}{T(z)} + j\phi' \tag{3.59}$$

Substituting eqns. (3.56) into eqn. (3.59), the Riccati differential equation is given by [13]

$$\rho' = -j(2\delta_0 - \phi')\rho - j\kappa_{01}(z)(1+\rho^2) \tag{3.60}$$

The boundary condition now becomes $\rho(L/2) = 0$. Clearly, by solving eqn. (3.60) numerically, the amplitude reflectance of the entire grating structure $\rho(-L/2)$ is obtained. It should be noted that eqn. (3.60) is equivalent to eqns. (3.50) in modelling.

For a special case, the grating with $\phi'(z) = 0$ at the Bragg resonance ($\delta_0 = 0$), eqn. (3.60) reduces to

$$\frac{d\rho}{1+\rho^2} = -j\kappa_{01}(z)dz \tag{3.61}$$

Integrating eqn. (3.61) yields

$$\rho(-L/2) = j\tanh\left[\int_{-L/2}^{L/2}\kappa_{01}(z)dz\right] \tag{3.62}$$

where the boundary condition $\rho(L/2) = 0$ has been used. Obviously, eqn. (3.62) is a useful expression for calculating the peak reflection of non-uniform gratings. For uniform Bragg gratings, $\kappa_{01}(z) = \kappa_0$, eqn. (3.62) reduces to

$$\left|\rho(-L/2)\right|^2 = \tanh^2(\kappa_0 L) \tag{3.63}$$

Eqn. (3.62) and eqn. (3.63) are the well-known relationships for fibre Bragg gratings.

3.3.3 Weak grating approximation

In order to find possible analytical solutions from eqn. (3.60) with some approximations, define the reflectance with a new variable σ for a weak grating as

$$\rho = \sigma \cdot e^{-j(2\delta_0 z - \phi')} \tag{3.64}$$

where $\sigma << 1$. Substituting eqn. (3.64) into eqn. (3.60) yields

$$\sigma' = -j\kappa_{01}(z)\left[e^{j(2\delta_0 z-\phi')} + \sigma^2 e^{-j(2\delta_0 z-\phi')}\right] \tag{3.65}$$

Clearly, the term σ^2 can be neglected as $\sigma << 1$ for a weak grating. Integrating eqn. (3.65) and substituting into eqn. (3.64) yields

$$\rho(-L/2) = je^{j[\delta_0 L+\phi'(-L/2)]}\int_{-L/2}^{L/2}\kappa_{01}(z)e^{j(2\delta_0 z-\phi')}dz \tag{3.66}$$

Eqn. (3.66) describes the amplitude reflectance of a weak grating. Further, for a grating with $\phi' = 0$, eqn. (3.66) reduces to

$$\left|\rho(-L/2)\right|^2 = \left|\int_{-L/2}^{L/2}\kappa_{01}(z)e^{j2\delta_0 z}dz\right|^2 \tag{3.67}$$

Eqn. (3.67) exhibits a Fourier transform of the coupling coefficient with respect to the detuning. Thus, a *sinc* profiled $\kappa_{01}(z)$ results in a square reflection spectrum since the inverse Fourier transform of a rectangle function is the *sinc* profile.

3.3.4 Characteristics of uniform fibre Bragg gratings

In general, no analytical solution can be derived from the coupled-mode equations for Bragg gratings except the case of a simple structure like a uniform Bragg grating. For a uniform Bragg grating, the period (Λ), phase (ϕ), and the coupling coefficient (κ_0) are z-independent. Hence, $\phi' = 0$, $\delta_{01}(z) = \delta_0$, eqn. (3.60) reduces to

$$\frac{d\rho}{dz} = -j\kappa_0\left(\rho^2 + \frac{2\delta_0}{\kappa_0}\rho + 1\right) \tag{3.68}$$

Rearranging and taking integration operation to eqn. (3.68) yields

$$\int_{-L/2}^{L/2} \frac{d\left[\frac{\kappa_0}{S}\left(\rho+\frac{\delta_0}{\kappa_0}\right)\right]}{\left[\frac{\kappa_0}{S}\left(\rho+\frac{\delta_0}{\kappa_0}\right)\right]^2+1} = \int_{-L/2}^{L/2} -jSdz \tag{3.69}$$

where S is the effective detuning defined as

$$S = \sqrt{\kappa_0{}^2 - \delta_0{}^2} \tag{3.70}$$

$\delta_0 = -\frac{2\pi n_{01}^{co}\Delta\lambda}{\lambda_0{}^2}$ is the detuning, $\Delta\lambda = \lambda - \lambda_0$ is the wavelength detuning, and $\lambda_0 = 2n_{01}^{co}\Lambda$ is the Bragg resonance. Integrating eqn. (3.69) yields

$$\arctan\left[\frac{\kappa_0}{S}\left(\rho(L/2)+\frac{\delta_0}{\kappa_0}\right)\right] - \arctan\left[\frac{\kappa_0}{S}\left(\rho(-L/2)+\frac{\delta_0}{\kappa_0}\right)\right] = -jSL \tag{3.71}$$

Rearranging eqn. (3.71) yields

$$\rho(-L/2) = \frac{S}{\kappa_0}\tan\left[\arctan\left(\frac{\delta_0}{S}\right) + jSL\right] - \frac{\delta_0}{\kappa_0} \tag{3.72}$$

where, the boundary condition $\rho(L/2) = 0$ has been used. Using the identity $\tan(jSL) = j\tanh(SL)$ and simplifying eqn. (3.72), the amplitude reflectance is given by [1, 5]

$$r(\lambda) = \frac{j\kappa_0 \tanh(SL)}{S - j\delta_0 \tanh(SL)} \tag{3.73}$$

where $r(\lambda) = \rho(-L/2)$ describes the amplitude reflectance of the entire grating structure.

For the wavelength at the Bragg resonance, $\delta_0 = 0$ yields $S = \kappa_0 = C_{01}^{co}\pi\Delta n / \lambda_0$, then eqn. (3.73) reduces to eqn. (3.62), the power reflectance at the resonance is thus,

$$R = \tanh^2\left(C_{01}^{co}\pi\Delta nL/\lambda_0\right) \tag{3.74}$$

where $R = |r(\lambda_0)|^2$ represents the power reflection, C_{01}^{co} is core mode overlap factor. Δn is the amplitude of the grating index fringes. Note that, eqn. (3.74) is equivalent to eqn. (3.63).

In order to describe the coupling process along the grating length, the amplitudes for both forward and backward directions require to be detailed rather than the response of the entire structure only. For this purpose, eqns. (3.50) are solved directly and give

$$\begin{cases} A^+(z) = \dfrac{S\cosh[S(z-L/2)] + \mathbf{j}\delta_0 \sinh[S(z-L/2)]}{S\cosh(SL) - \mathbf{j}\Delta\beta\sinh(SL)} e^{-\mathbf{j}\delta_0(z+L/2)} \\ A^-(z) = \dfrac{-\mathbf{j}\kappa_0 \sinh[S(z-L/2)]}{S\cosh(SL) - \mathbf{j}\delta_0\sinh(SL)} e^{j\delta_0(z+L/2)} \end{cases} \tag{3.75}$$

where the boundary conditions $A^+(-L/2) = 1$ and $A^-(L/2) = 0$ have been used. In this case the amplitude reflectance and transmittance are given by $r(\lambda) = A^-(-L/2)$, $t(\lambda) = A^+(L/2)$ as

$$\begin{cases} t(\lambda) = \dfrac{S}{S\cosh(SL) - \mathbf{j}\delta_0\sinh(SL)} \\ r(\lambda) = \dfrac{\mathbf{j}\kappa_0\sinh(SL)}{S\cosh(SL) - \mathbf{j}\delta_0\sinh(SL)} \end{cases} \tag{3.76}$$

Eqns. (3.76) are important expressions for fibre Bragg gratings [122,123, 124].

Figure 3.3 shows the incident power drops off exponentially along the grating region; the relationship of $\dfrac{d(T-R)}{dz} \equiv 0$ exhibits the conservation of energy. For a 99% reflectivity grating, more than 90% power is reflected before the grating centre as illustrated in Figure 3.3 (a). The average reflection depth rapidly decreases with increasing grating reflectivity. This will be discussed in section 5.5.

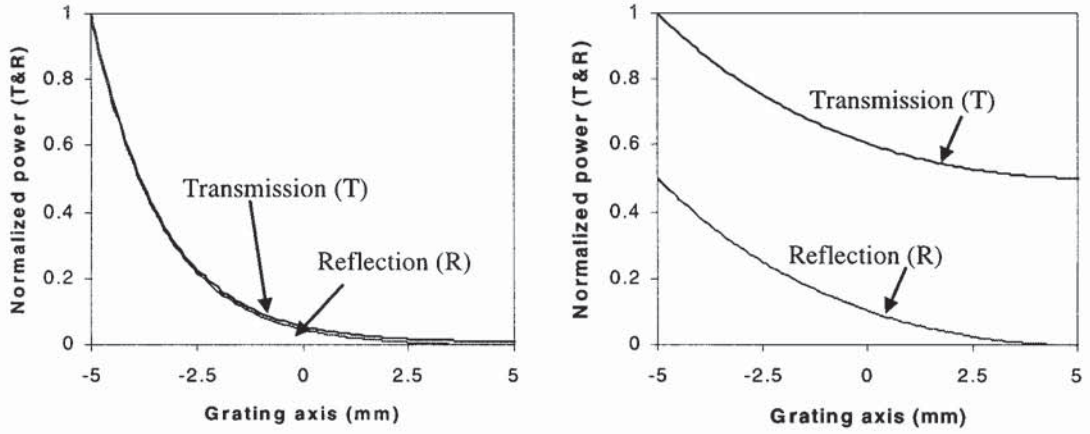

Figure 3.3 The distribution of transmitted and reflected power against the grating length in a 10mm Bragg grating, indicating a shorter reflection depth in a stronger grating compared with that in a weaker grating: (a) 99% reflectivity; (b) 50 % reflectivity

3.3.4.1 Spectral sidelobes

As expressed in eqn. (3.70), with increasing the wavelength detuning $|\Delta\lambda|$, $\kappa_0^2 - \delta_0^2$ decreases rapidly to zero and then $\kappa_0^2 - \delta_0^2 < 0$, so that the effective detuning S goes into its imaginary regime. In this case a new effective detuning W is defined as

$$S = \mathbf{j}\sqrt{\delta_0^2 - \kappa_0^2} = \mathbf{j}W \tag{3.77}$$

Using identities $\sinh(jWL) = j\sin(WL)$, $\cosh(jWL) = \cos(WL)$, the power reflectivity is obtained

$$|r_i(\lambda)|^2 = \begin{cases} \dfrac{\kappa_0^2 \sinh^2(SL)}{S^2\cosh^2(SL) + \delta_0^2 \sinh^2(SL)} & \left(\kappa_0^2 - \delta_0^2 \geq 0\right) \\ \dfrac{\kappa_0^2 \sin^2(WL)}{W^2\cos^2(WL) + \delta_0^2 \sin^2(WL)} & \left(\kappa_0^2 - \delta_0^2 < 0\right) \end{cases} \tag{3.78}$$

Clearly when

$$WL = N\pi \tag{3.79}$$

where N=1, 2, 3, ... indicates the order of the zero reflections, exhibiting many sidelobes since between two zero reflections there is a sub-peak reflection. In order to describe the locations of the sidelobes, substituting eqn. (3.79) into eqn. (3.77), the wavelengths of zero-reflections are given by

$$\lambda_N = \lambda_0 \pm \frac{\lambda_0^{\,2}}{2n_{01}^{co}L}\sqrt{\left(\frac{\kappa_0 L}{\pi}\right)^2 + N^2} \tag{3.80}$$

where $|r(\lambda_N)|^2 = 0$. The wavelength spacing between two symmetric zero reflections is thus given by

$$\Delta\lambda_{N,-N} = \frac{\lambda_0^{\,2}}{n_{eff}L}\sqrt{\left(\frac{\kappa_0 L}{\pi}\right)^2 + N^2} \tag{3.81}$$

where n_{eff} is used instead of n_{01}^{co} for convenience, and referred to as the effective index. By plotting eqn. (3.78), the reflection spectrum of a uniform Bragg grating is illustrated in Figure 3.4, showing many sidelobes.

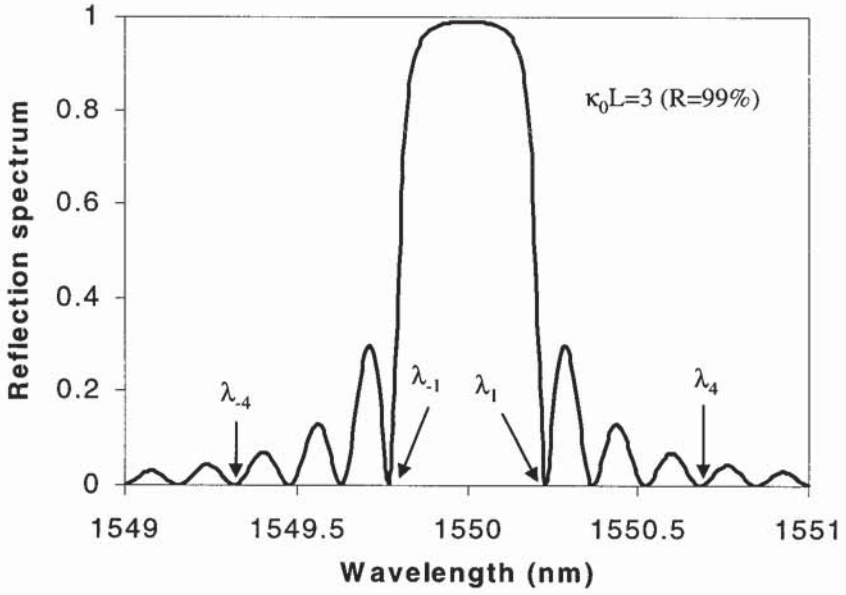

Figure 3.4 Calculated reflection spectrum of a typical fibre Bragg grating of 5mm long and 20dB-reflectivity, indicating many sidelobes

For a 10mm long uniform Bragg grating with 20dB-reflectivity at 1.55μm, eqn. (3.81) yields $\Delta\lambda_{1,-1} = 0.23\,\text{nm}$, $\Delta\lambda_{2,-2} = 0.37\,\text{nm}$, $\Delta\lambda_{3,-3} = 0.52\,\text{nm}$. Increasing the values of coupling strength ($\kappa_0 L$), the reflectivity of the grating increases and the line-width broadens, as shown in Figure 3.5. It is clear that for a strong grating the raised and down edges of the reflection spectrum are very sharp and *FWHM* is thus almost $\Delta\lambda_{1,-1}$. For a weak grating the spectral behavior between the Bragg resonance and the first zero-reflection is a near linear relationship and thus $FWHM \approx \Delta\lambda_{1,-1}/2$. In general, the *FWHM* of a uniform grating is given by [1]

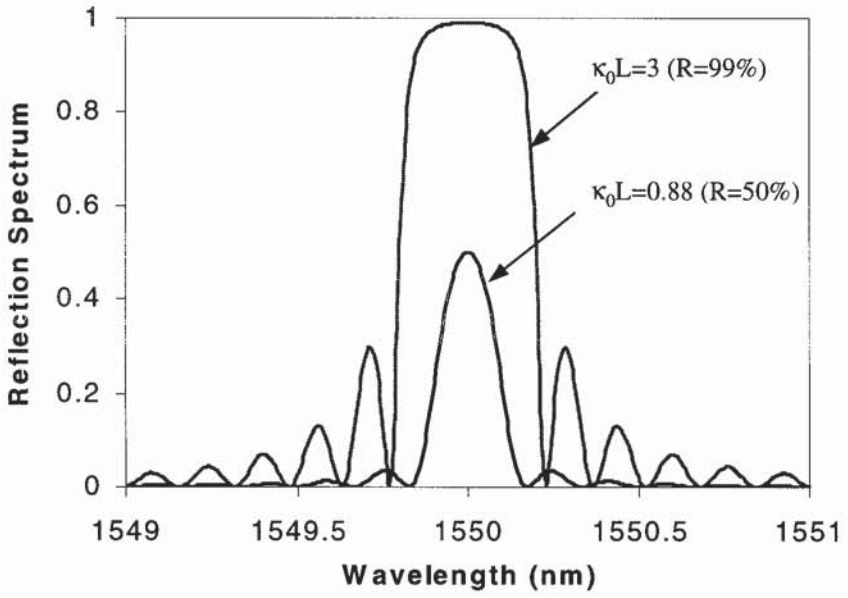

Figure 3.5 Calculated reflection spectra of 5mm long Bragg gratings with different values of reflectivities: 99% and 50%

$$FWHM = \mu \cdot \frac{\lambda_0^{\,2}}{n_{eff} L} \cdot \sqrt{\left(\frac{\kappa_0 L}{\pi}\right)^2 + 1} \tag{3.82}$$

where $0.5 < \mu < 1$ reflects the coupling strength: $\mu \approx 0.5$ for a weak grating and $\mu \approx 1$ for a strong grating. For a very weak grating $\kappa_0 L \to 0$, eqn. (3.82) reduces to the free

spectrum range (FSR) of the grating length Fabry-Perot cavity as

$$FWHM \rightarrow \frac{\lambda_0^{\,2}}{2n_{eff}L} \tag{3.83}$$

Eqn. (3.82) also shows a long length grating results in a narrower line-width when the coupling strength remains unchanged. The grating line-width (*FWHM*) against the grating length for several values of the coupling strength is shown in Figure 3.6. For a 10mm long uniform Bragg grating of 20dB peak reflectivity (99%), calculation shows *FWHM*≈0.19nm, corresponding to μ=0.826 in eqn. (3.82), where $n_{eff} = 1.446$ is used.

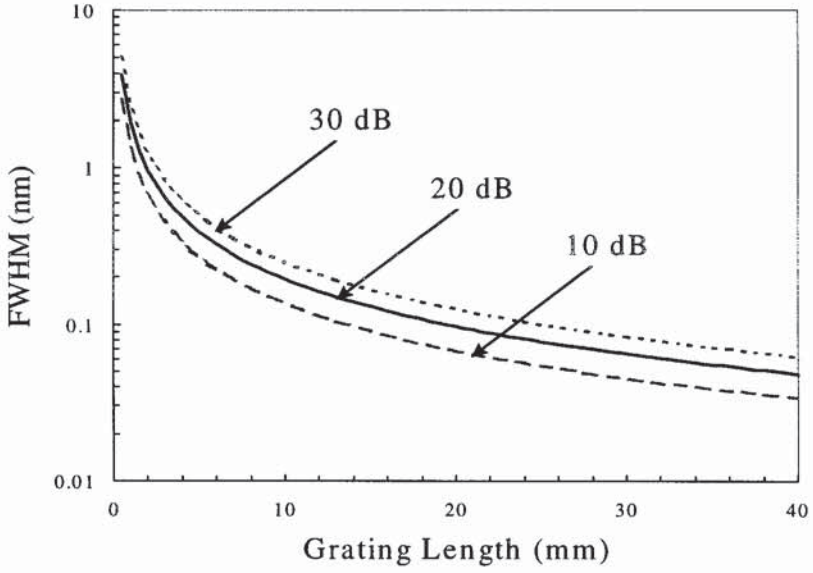

Figure 3.6 Calculated line-width of Bragg gratings against the grating length for different values of reflectivities: 30dB, 20dB and 10dB

One very useful observation from eqn. (3.81) and Figure 3.5 is that the magnitudes and locations of the sidelobes are coupling coefficient related. This suggests that sidelobes can be suppressed by tapering the grating coefficient to a specific profile, which is known as grating apodisation.

3.3.4.2 Dispersion

Using eqn. (2.5), the dispersion of Bragg gratings may be written as [91, 124]

$$D = -\frac{2\pi c}{L\lambda_0^2}\frac{\partial^2 \Psi}{\partial \omega^2} \tag{3.84}$$

where $\beta = \Psi / L$ has been used, L is the grating length, c is the speed of the light in vacuum, λ_0 is the Bragg wavelength, ω is the light circle frequency. Ψ is the phase of the reflected light, which can be derived from eqn. (3.76) as

$$\Psi = \arctan\left[\frac{\delta_0 \tanh(SL)}{S}\right] + \frac{\pi}{2} \tag{3.85}$$

Substituting eqn. (3.85) into eqn. (3.84), the dispersion is obtained as illustrated by Figure 3.7 (a) and (b). Very strong positive and negative dispersions are located at the edges of the spectrum while a much weak dispersion is found around the Bragg resonance. The maximum time delay is the light reflected from respective ends of the grating as $\Delta t = \frac{2n_{eff}L_g}{c}$, where L_g is the grating length, $n_{eff} \approx 1.446$ is LP_{01}^{co} mode index, c is the light velocity in vacuum. As shown in Figure 3.7 (b), for a 5mm long grating, this maximum time delay is about 48ps.

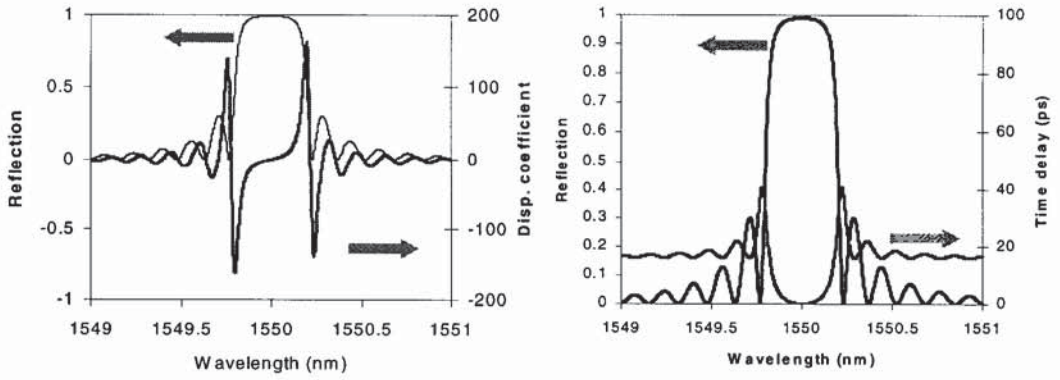

(a) (b)

Figure 3.7 Modelled dispersion and reflection spectrum of a 5mm long 20dB-reflectivity uniform Bragg grating: (a) reflection and dispersion coefficient; (b) reflection and time delay.

3.3.4.3 *Photoinduced refractive index*

The distribution of the refractive index is given by eqn. (3.51), which may be simplified for a uniform structure as

$$n(z) = n_0\left\{1 + \Delta n_0\left[1 + \gamma \cdot \cos\left(\frac{2\pi}{\Lambda_0} z\right)\right]\right\} \tag{3.86}$$

where, $0 \le \gamma \le 1$ indicates the visibility of the grating index fringes. In this case, the amplitude of the index fringes and the average photoinduced index are $\gamma \cdot \Delta n_0$ and Δn_0, respectively. Since the Bragg wavelength and the peak reflection are measurable using an optical spectrum analyser (OSA), the coupling strength of the grating is thus derivable using eqn. (3.74) as

$$\kappa_0 L = \tanh^{-1}\left(\sqrt{R}\right) \tag{3.87}$$

Using eqn. (3.44), the total photoinduced index is given by

$$\Delta n_0 = \frac{\kappa_0 L \cdot \lambda}{\pi \cdot \gamma \cdot L \cdot C_{01}^{co}} \tag{3.88}$$

Clearly, Δn_0 and $\gamma \cdot \Delta n_0$ correspond to the shift of the Bragg wavelength and the reflectivity, respectively.

3.3.5 Modelling technique utilising matrix transforms

In general, for non-uniform gratings, the coupling coefficient $\kappa(z)$ and the Bragg resonance $\lambda_B(z)$ are slow varying along the grating length. One calculation technique used replaces the grating by a series of short length sections, each of which can be characterized by a uniform structure. In order to obtain the overall spectral response, eqns. (3.50) has to be re-solved for arbitrary boundary conditions and yields

$$\begin{bmatrix} A^{+}(z_i) \\ A^{-}(z_i) \end{bmatrix} = M_i \begin{bmatrix} A^{+}(z_{i-1}) \\ A^{-}(z_{i-1}) \end{bmatrix} \tag{3.89}$$

where, $z_{i-1} \le z < z_i$, z indicates the locations of the sub-grating G_i, which is treated as approximately a short length uniform structure; i=1, 2, 3, ..., N, N is the total number of the sub-gratings. M_i is the matrix describing the uniform sub-grating G_i given by

$$M_i = \begin{bmatrix} 1/t_i^{*} & -(r_i/t_i)^{*} \\ -r_i/t_i & 1/t_i \end{bmatrix} \tag{3.90}$$

with

$$\begin{cases} t_i(\lambda) = \dfrac{S_i}{S_i \cosh(S_i L_i) - \mathbf{j}\delta_i \sinh(S_i L_i)} \\ r_i(\lambda) = \dfrac{\mathbf{j}\kappa_i \sinh(SL_i)}{S_i \cosh(S_i L_i) - \mathbf{j}\delta_i \sinh(S_i L_i)} \end{cases} \tag{3.91}$$

where $L_i = L/N$ is the length of the sub-grating G_i. Note that solving eqns. (3.50) is very tedious, but it is necessary as the matrix expression given in eqn. (3.90) in terms of the sub-grating amplitude reflectance and transmittance is obtained. This results in an analytical solution with clear physical picture for the structure of phase-shifted fibre Bragg gratings.

Consider that the sub-grating G_i is short enough to be treated as a uniform structure, the values of the coupling coefficient and the local Bragg wavelength at its central position $\bar{z}_i$, $\kappa(\bar{z}_i)$ and $\lambda_B(\bar{z}_i)$ are used to represent this sub-grating. The central position of G_i is given by

$$\bar{z}_i = -\frac{L}{2} + \frac{L}{N}\left(i - \frac{1}{2}\right) \tag{3.92}$$

where, $i = 1,2,3,...,N$, $\bar{z}_i$ indicates the central position of the sub-grating G_i. The detuning and the effective detuning are given by

$$\begin{cases} \delta_i(\bar{z}_i) = 2\pi n_{eff}\left[\dfrac{1}{\lambda} - \dfrac{1}{\lambda_B(\bar{z}_i)}\right] \\ S_i(\bar{z}_i) = \sqrt{\kappa^2(\bar{z}_i) - \delta_i^{\,2}(\bar{z}_i)} \end{cases} \tag{3.93}$$

The matrix M_i for each sub-grating is given by substituting eqn. (3.91) into eqn. (3.90) using eqn. (3.92) and eqn. (3.93), supposing the profiles of the grating coupling coefficient $\kappa(z)$ and the Bragg wavelength $\lambda_B(z)$ are given, respectively.

For a typical linearly chirped grating structure, the local Bragg wavelength of the sub-grating G_i is given by

$$\lambda(\bar{z}_i) = \lambda_0 + \frac{\bar{z}_i}{L}\Delta\lambda \tag{3.94}$$

where λ_0 and $\Delta\lambda$ are the central wavelength and chirp of the linearly chirped grating, respectively, $\bar{z}_i$ is the central position of sub-grating G_i, given by eqn. (3.92).

For i=1, 2, 3, …, N, using eqn. (3.89) yields

$$\begin{bmatrix} A^+(L) \\ A^-(L) \end{bmatrix} = M \cdot \begin{bmatrix} A^+(0) \\ A^-(0) \end{bmatrix} \tag{3.95}$$

where

$$M = \begin{bmatrix} M11 & M12 \\ M21 & M22 \end{bmatrix} = M_N M_{N-1} M_{N-1} \cdots M_1 \tag{3.96}$$

Consider the usual boundary conditions $A^+(-L_0/2) = 1$, $A^-(L_0/2) = 0$, the amplitude reflectance (r) and transmittance (t) of the entire grating structure are thus

$$\begin{cases} t = 1/M22 \\ r = -M21/M22 \end{cases} \tag{3.97}$$

In this way, the simulation of Bragg gratings reduces to the calculation of the transform-

matrix for the entire grating structure, which is the main simulation model used in this thesis.

It should be noted that the accuracy depends on the number of the sub-gratings (N). One useful observation is that the minimum N can be given by the FSR $\frac{\lambda_0^{\,2}}{2n_{eff}L/N}$, of the sub-grating length (L/N) Fabry-Perot cavity, since it must be wider than the total observed spectral region. Hence

$$N > \frac{span}{\lambda_0^{\,2}/(2n_{eff}L)} \tag{3.98}$$

where the $span$ is the total observed spectral region. For a 10mm long Bragg grating at wavelength of 1550nm and the total observed spectral region $span$=10nm, eqn. (3.98) yields N>120. In this case, N=200 is enough for modelling the spectrum.

For a special case, where there are no grating fringes, i.e. $\kappa_0 = 0$, eqn. (3.70) reduces to $S = j\delta_0$ and thus eqns. (3.91) reduces to $r = 0$ and $t = \exp(j\delta_0 L_i)$, eqn. (3.90) becomes

$$M_i = \begin{bmatrix} e^{j\delta_0 L_i} & 0 \\ 0 & e^{-j\delta_0 L_i} \end{bmatrix} \tag{3.99}$$

Clearly, matrix eqn. (3.99) describes the propagation of the light in a fibre with no grating fringes, where $2\delta_0 L_i$ is relative propagation phase. Comparing with eqn. (3.99), the matrix for a pure phase shift (ϕ) is thus given by

$$M = \begin{bmatrix} e^{j\phi/2} & 0 \\ 0 & e^{-j\phi/2} \end{bmatrix} \tag{3.100}$$

It should be noted that eqn. (3.99) and eqn. (3.100) are not only restricted to the backward coupling in Bragg gratings, but also applies to the forward coupling in long-period fibre gratings.

To summarise, the coupled-mode equations for Bragg gratings in the form of Schrödinger equation and Riccati differentiating equation have been discussed. The peak reflectivity depends on the integration of the coupling coefficient with respect to the grating length expressed in eqn. (3.62). For a weak Bragg grating, the reflected spectrum is a Fourier transform of the coupling coefficient with respect to the detuning δ_0 given by eqn. (3.67), hence suggesting that a *sinc* profiled coupling coefficient will yield a square reflection spectrum. For a uniform Bragg grating, the analytical solution, the peak reflectivity, line-width, sidelobes, dispersion, and the photoinduced index have been investigated. The modelling technique utilising matrix transforms for non-uniform Bragg gratings has been discussed. In addition, the free spectrum range (FSR) of a Fabry-Perot cavity is found a very basic element in spectrum of Bragg gratings.

3.4 Coupled-Mode Solution for Long-period Fibre Gratings

This section discusses the codirectional coupling in long-period fibre gratings. The modelling technique utilising transform matrix, the spectral response of uniform long-period fibre gratings and the photoinduced refractive index are discussed.

3.4.1 Coupled-mode equations

The coupled-mode equations for codirectional coupling in long-period fibre gratings are derived from eqn. (3.14) and follow

$$\begin{cases} \dfrac{dA_{01}^{co}(z)}{dz} = j\kappa_{lp}^{cl} e^{-j2\delta_{lp}^{cl} z} B_{lp}^{cl}(z) \\ \dfrac{dB_{lp}^{cl}(z)}{dz} = j\kappa_{lp}^{cl} e^{j2\delta_{lp}^{cl} z} A_{01}^{co}(z) \end{cases} \tag{3.101}$$

where $-L/2 \le z \le L/2$, z indicates the locations of the grating, L is grating length, $A_{01}^{co}(z)$ and $B_{lp}^{cl}(z)$ are the amplitudes of the forward core mode and coupled cladding modes with absolute phases. κ_{lp}^{cl} is the coupling coefficient given by

$$\kappa_{lp}^{cl} = \frac{\pi \Delta n_0 C_{lp}^{cl}}{\lambda_{lp}} \frac{2}{\pi} \tag{3.102}$$

where C_{lp}^{cl} is the overlap factors between LP_{01}^{co} core and LP_{lp}^{cl} cladding modes, $\dfrac{2}{\pi}$ accounts for the rectangular shape transformation into cosine shape of the refractive index profile induced by the UV exposure on white/black amplitude mask. $\kappa_{lp}^{cl} L$ is the coupling strength, δ_{lp}^{cl} is the detuning from the resonance of a long-period fibre grating and given by

$$\delta_{lp}^{cl} = \frac{1}{2}\left[\beta_{01}^{co} - \beta_{lp}^{cl} - \frac{2\pi}{\Lambda}\right] = \left(n_{01}^{co} - n_{lp}^{cl}\right)\left(\frac{1}{\lambda_0} - \frac{1}{\lambda(z)}\right) \tag{3.103}$$

where β_{01}^{co} and β_{lp}^{cl} are propagation constants of the light in a fibre core and cladding,

respectively. Λ is the grating period, n_{01}^{co} and n_{lp}^{cl} are the indexes of the core mode LP_{01}^{co} and cladding modes LP_{lp}^{cl}, respectively, as discussed in section 3.2. λ_{lp} is the resonance wavelength given by $\delta_{lp}^{cl} = 0$ as [101]

$$\lambda_{lp} = \left(n_{01}^{co} - n_{lp}^{cl}\right)\Lambda \tag{3.104}$$

where l=0, 1, 2, ... and m=1, 2, 3, ... indicate the order of the LP_{lp}^{cl} cladding modes. Similar to eqn. (3.47), the electric field may be written in the form [6]

$$E(z) = \left[A(z)e^{-j\delta_{lp}^{cl}z}\right]e^{j\beta_{01}^{co}z} + \left[B_{lp}(z)e^{j\delta_{lp}^{cl}z}\right]e^{j\beta_{lp}^{cl}z} \tag{3.105}$$

where $A(z)$ and $B_{lp}(z)$ are the amplitudes of the input core mode LP_{01}^{co} and the coupled cladding modes LP_{lp}^{cl} with relative phases, respectively. The coupled-mode equations of long-period fibre gratings are then given by

$$\begin{cases} \dfrac{dA(z)}{dz} = j\left[\delta_{lp}^{cl} \cdot A(z) + \kappa_{lp}^{cl} \cdot B_{lp}(z)\right] \\ \dfrac{dB_{lp}(z)}{dz} = j\left[-\delta_{lp}^{cl} \cdot B_{lp}(z) + \kappa_{lp}^{cl} \cdot A(z)\right] \end{cases} \tag{3.106}$$

Substituting eqns. (3.106) into each other yields

$$\begin{cases} \dfrac{d^2A(z)}{dz^2} = -\left[\left(\delta_{lp}^{cl}\right)^2 + \left(\kappa_{lp}^{cl}\right)^2\right]A(z) \\ \dfrac{d^2B_{lp}(z)}{dz^2} = -\left[\left(\delta_{lp}^{cl}\right)^2 + \left(\kappa_{lp}^{cl}\right)^2\right]B_{lp}(z) \end{cases} \tag{3.107}$$

where the approximation of slow varying quantities about the detuning $\delta_{lp}^{cl}(z)$ and the coupling strength $\kappa_{lp}^{cl}(z)$ have been used. Eqn. (3.107) is the basic equation for modelling of long-period fibre gratings.

3.4.2 Modelling technique utilising matrix transforms

As discussed in section 3.3.5, a non-uniform grating can be replaced by a series of short

length uniform structures; each of them can be characterized analytically. For this purpose, solving eqn. (3.107) for a uniform sub-grating LPG_i with arbitrary boundary conditions yields

$$\begin{bmatrix} A(z_i) \\ B_{lp}(z_i) \end{bmatrix} = M_i \begin{bmatrix} A(z_{i-1}) \\ B_{lp}(z_{i-1}) \end{bmatrix} \tag{3.108}$$

where i=1, 2, 3 ..., N, $z_{i-1} \le z < z_i$, z indicates the locations of the sub-grating LPG_i; $L_i = L/N$ is its length, N is the number of the total sub-gratings, M_i is the matrix describing the uniform sub-grating LPG_i and given by

$$M_i = \begin{bmatrix} t_i & r_i \\ r_i & t_i^* \end{bmatrix} \tag{3.109}$$

with

$$\begin{cases} t_i = \cos\left(S_{lp}^{cl} L_i\right) + j\dfrac{\delta_{lp}^{cl}}{S_{lp}^{cl}} \sin\left(S_{lp}^{cl} L_i\right) \\ r_i = j\dfrac{\kappa_{lp}^{cl}}{S_{lp}^{cl}} \sin\left(S_{lp}^{cl} L_i\right) \end{cases} \tag{3.110}$$

where

$$S_{lp}^{cl} = \sqrt{\left(\kappa_{lp}^{cl}\right)^2 + \left(\delta_{lp}^{cl}\right)^2} \tag{3.111}$$

where S_{lp}^{cl} is the effective detuning. The matrix for the entire grating structure is obtained in the same forms of eqn. (3.96) as

$$M = \begin{bmatrix} M11 & M12 \\ M21 & M22 \end{bmatrix} = M_N M_{N-1} M_{N-1} \cdots M_1 \tag{3.112}$$

The amplitude transmittance (t) and coupling ratio (r) are given by

$$\begin{cases} t = M11 \\ r = M21 \end{cases} \tag{3.113}$$

where the usual boundary conditions $A(z_0)=1$ and $B_{lp}(z_0)=0$ have been used. In this way, similar to Bragg gratings, the modelling of long-period gratings also reduces to the calculation of the transform matrix. As a simple case like a uniform long-period grating, the amplitude transmission and cladding mode coupling-ratio are given by eqn. (3.110), instead of the L_i by L.

As stated previously, for a fibre with no grating fringes, i.e. $\kappa_{lp}^{cl}=0$, eqn. (3.110) yields $r_i=0$ and $t_i=\exp\left(i\delta_{lp}^{cl}L_i\right)$. Eqn. (3.109) then reduces to eqn. (3.99) and hence the matrix of a pure phase shift for a long-period fibre grating is also given by eqn. (3.100).

3.4.3 Characteristics of uniform long-period fibre gratings

In general, no analytical solution can be derived from the coupled-mode equations for a long-period fibre grating except the simplest case of a uniform structure. For a uniform long-period grating, the dominant coupling is between LP_{01}^{co} core and LP_{0p}^{cl} cladding modes. The amplitude transmittance is given by eqn. (3.110) (replacing the length L_i by L) and the power transmission is thus

$$T_{0p}(\lambda)=1-\frac{\sin^2\left[\kappa_{0p}^{cl}L\sqrt{1+\left(\delta_{0p}^{cl}/\kappa_{0p}^{cl}\right)^2}\right]}{1+\left(\delta_{0p}^{cl}/\kappa_{0p}^{cl}\right)^2} \tag{3.114}$$

Clearly, the spectral response of long-period gratings and Bragg gratings is different intrinsically. For the wavelength at the resonance, $\delta_{0p}^{cl}=0$, the power transmission becomes

$$T_{0p}(\lambda_{0p})=1-\sin^2\left(\kappa_{0p}^{cl}L\right) \tag{3.115}$$

Eqn. (3.115) shows that the power coupling between the LP_{01}^{co} core mode and LP_{0p}^{cl} cladding modes against the coupling strength changes periodically.

3.4.4 Photoinduced refractive index

Similar to the case of Bragg gratings, the peak loss of a long-period fibre grating is measurable. The coupling coefficient is thus derivable using eqn. (3.115) and given by

$$\kappa_{0p} L = m \cdot \pi \pm \sin^{-1} \sqrt{1 - T_{0p}(\lambda_{0p})} \tag{3.116}$$

where m=0, 1, 2, ... indicates the region of the coupling coefficient. The amplitude of the grating index fringes is obtained using eqn. (3.102). The increase of the average index is thus

$$\Delta n_0 = duty \cdot \frac{\kappa_{0p}^{cl} L \cdot \lambda_{0p}}{2 C_{0p}^{cl} L} \tag{3.117}$$

where $0 < duty < 1$, $duty$ indicates the duty cycle of the rectangular profile index fringes. Clearly, this Δn_0 is the increase of the average fibre core index, resulting in the shifting of the resonance wavelength. Up to 100nm shift was observed experimentally.

To summarise, this section discussed the analysis of a long-period fibre grating. A modelling technique utilising matrix transforms for a non-uniform long-period fibre grating has been proposed. For a uniform long-period fibre grating, the analytical solution, the photoinduced refractive index have been discussed.

3.5 Chapter Summary

This chapter has given details on the theory for both fibre Bragg gratings and long-period fibre gratings. Starting from the Maxwell equations, the coupled-mode equations for the two kinds of gratings have been discussed. The mode overlap factor for describing possible mode coupling has been introduced and discussed analytically. The strongest coupling between the launched core mode and the possible coupled-modes is the Bragg coupling; the overlap factor indicates the ratio of the power confined within the fibre core to the total power. Up to 60 overlap factors between the core mode and cladding modes have been calculated. Results show a slow varying profile with multiple minimums against the order of the cladding modes, which are consistent with experimental results.

The coupled-mode equations for fibre Bragg gratings can be expressed in the form of Schrödinger equation and approximation methods which were developed for solving Schrödinger equation can be used to solve the coupled equations for fibre Bragg gratings. The coupled-mode equations can also be reduced to a single second-order Riccati differential equation, from which the peak reflectance as an integration of the coupling coefficient with respect to the grating length and a weak grating approximation in a form of Fourier transform have been obtained. For uniform Bragg gratings, the analytical expressions, calculated spectra, sidelobes, line-width, dispersion and photoinduced refractive index have been investigated. In addition, a modelling technique utilising matrix transforms has been discussed for non-uniform gratings.

For a codirectional coupling in long-period fibre gratings, as in the case of Bragg gratings, the modelling technique utilising matrix transforms has been proposed. The characteristics of a uniform long-period grating have been discussed, showing a periodic power coupling between the core and cladding modes against the coupling strength, which is in good agreement with experimental results.

CHAPTER 4

Bragg Grating Fabrication Techniques

This chapter discusses the fabrication of fibre Bragg gratings. Two typical fabrication techniques - holographic and scanning phase mask methods - are adopted experimentally. For the fabrication using the two-beam holographic method, analytical expressions for predicting the central wavelengths and chirps have been developed. This chapter further discusses the theory behind the fabrication of complex structure gratings using the method of scanning the UV beam across a phase mask, where a computer controlled piezoelectric transducer (PZT) stage is used to dither the phase mask to introduce a varying coupling coefficient along the grating length. Based on this fabrication technique, grating structures like apodised, wavelength-shifted, self-apodised chirped, phase-shifted, Moiré and sampled gratings can be fabricated experimentally. This fabrication technique also extends to the fabrication of long length gratings. In addition, the dependence of the UV beam parameters, such as the beam width and its polarisation are also discussed.

4.1 Two-Beam Holographic Fabrication Technique

This section details the theory behind the two-beam holographic technique for fabricating fibre Bragg gratings. The analytical expressions for predicting the Bragg wavelengths and chirps are proposed, which are very useful in guiding the grating fabrication.

4.1.1 Introduction

There are many techniques used to fabricate fibre Bragg gratings and a widely used one is the two-beam holographic method. Gratings fabricated in this manner were found to be much more efficient and were not limited in designing the Bragg wavelength and chirp.

A disadvantage of this technique is that the total length of each grating fabricated is limited by the size of the two interfering beams. Also, inherent with this system is the 'self-chirping' of the gratings which occurs due to the beam profile producing a non-uniform exposure over the length of the grating, exhibiting some oscillations located at the short wavelength side of the Bragg resonance.

The experimental arrangement is shown in Figure 4.1. The UV beam is split into two with equivalent power (50%) at mirror C ($\theta_0 = \pi / 4$). The two beams are then reflected by highly reflective mirrors *A* and *B* to meet on the photosensitive fibre to produce the interfering fringes. In order to introduce chirp into the gratings, dissimilar wavefront implemented by inserting two cylindrical lenses *D* and *E* into the one arm of the holographic system is adopted [60]. Through setting the off-focus $df = DE - (f_D + f_E)$, a convergent or divergent beam is thus obtained. The cylindrical lens *F* is used to focus the two UV beams on the photosensitive fibre to enhance the power intensity.

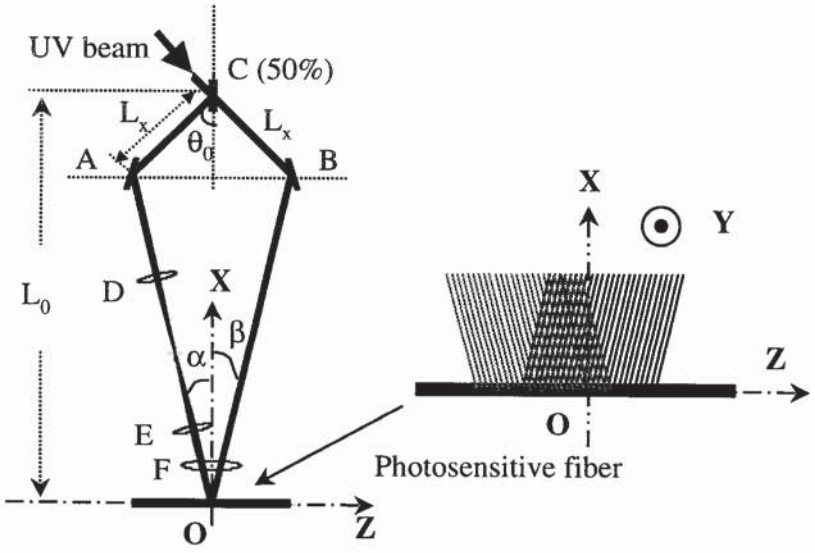

Figure 4.1 Schematic diagram of the two-beam holographic interferometric fabrication technique

4.1.2 Uniform-period Bragg gratings

When $df = 0$, ($DE = f_D + f_E$) or without the lenses D and E, each of the two interfering UV beams are parallel lights and produce a uniform-period grating. As illustrated in Figure 4.1, defining the two meeting angles of the two UV beams (AO and BO) with respect to the **x**-axis in the XZ Cartesian coordinate system as α and β, respectively, the vector propagation constants $\vec{\beta}_1$ and $\vec{\beta}_2$ are then given by

$$\begin{cases} \vec{\beta}_1 = \dfrac{2\pi}{\lambda_{UV}}\left(\sin\alpha \cdot \vec{z}^{\,0} - \cos\alpha \cdot \vec{x}^{\,0}\right) \\ \vec{\beta}_2 = \dfrac{2\pi}{\lambda_{UV}}\left(-\sin\beta \cdot \vec{z}^{\,0} - \cos\beta \cdot \vec{x}^{\,0}\right) \end{cases} \tag{4.1}$$

where $\vec{x}^{\,0}$ and $\vec{z}^{\,0}$ indicate the unit vectors of the **x**-axis and **z**-axis, respectively. $\lambda_{UV} = 244\,\text{nm}$ is the wavelength of the UV writing beam. When the UV beam is s-polarised or y-orientated, the composed amplitude of the two UV beams at the meeting point $\vec{r} = x \cdot \vec{x}^{\,0} + z \cdot \vec{z}^{\,0}$ is obtained as

$$\begin{aligned} A(x,z) &= e^{j\vec{\beta}_1 \cdot \vec{r}} + e^{j\vec{\beta}_2 \cdot \vec{r}} \\ &= \exp\left[j\frac{2\pi}{\lambda_{UV}}(z \cdot \sin\alpha - x \cdot \cos\alpha)\right] + \exp\left[j\frac{2\pi}{\lambda_{UV}}(-z \cdot \sin\beta - x \cdot \cos\beta)\right] \end{aligned} \tag{4.2}$$

where $A(x,z)$ is the composed amplitude. The intensity distribution along the photosensitive fibre is thus

$$I(z) = |A(0,z)|^2 = 2 + 2\cos\left[\frac{2\pi z}{\Lambda}\right] \tag{4.3}$$

with

$$\Lambda = \frac{\lambda_{uv}}{\sin\alpha + \sin\beta} \tag{4.4}$$

where Λ is the fibre Bragg grating period. The Bragg wavelength is thus given by

$$\lambda_B = 2n_{eff}\frac{\lambda_{UV}}{\sin\alpha + \sin\beta} \tag{4.5}$$

where n_{eff} is the LP_{01}^{co} mode index. For a non-slanted grating, the axis of the photosensitive fibre is perpendicular to the bisector of the two UV writing beams, hence, $\alpha = \beta$ with

$$\begin{aligned}\alpha &= \arctan\left[\frac{L_x \sin(\theta_0)}{L_0 - L_x\cos(\theta_0)}\right] \\ &= \arcsin\left(\frac{n_{eff}\lambda_{UV}}{\lambda_B}\right)\end{aligned} \tag{4.6}$$

For a grating at 1.55μm wavelength, eqn. (4.6) and eqn. (4.4) yield $\alpha = \beta = 13.16^\circ$ and $\Lambda = 0.540\,\mu\text{m}$, respectively. In order to express the Bragg wavelength in terms of the interferometer arm-lengths L_x, using eqn. (4.6), eqn. (4.5) becomes

$$\lambda_B = \frac{n_{eff}\lambda_{UV}}{\sin\left[\arctan\left(\dfrac{L_x \sin\theta_0}{L_0 - L_x\cos\theta_0}\right)\right]} \tag{4.7}$$

where non-slanted condition $\alpha = \beta$ has been used. By plotting eqn. (4.7), the Bragg wavelength against the arm-length (L_x) is shown in Figure 4.2.

The accuracy of eqn. (4.7) depends on the measurement of L_x since L_0 is fixed. For a measurement error ΔL_x, differentiating eqn. (4.7) the wavelength error is given by

$$\frac{\Delta\lambda_B}{\lambda_B} = -\frac{\Delta L_x}{L_x}\cdot\frac{\sqrt{2}L_0 - L_x}{\sqrt{2}L_0 - 2L_x} \tag{4.8}$$

where $\theta_0 = \pi/4$ has been used. The problem lies in measuring the arm-length L_x between the two reflection points on the mirrors A, B and C with error <1%. For L_0=522mm and L_x=142mm, this 1% error yields $\Delta\lambda_B \approx$20nm given by eqn. (4.8). Obviously, this is far from predicting grating wavelengths.

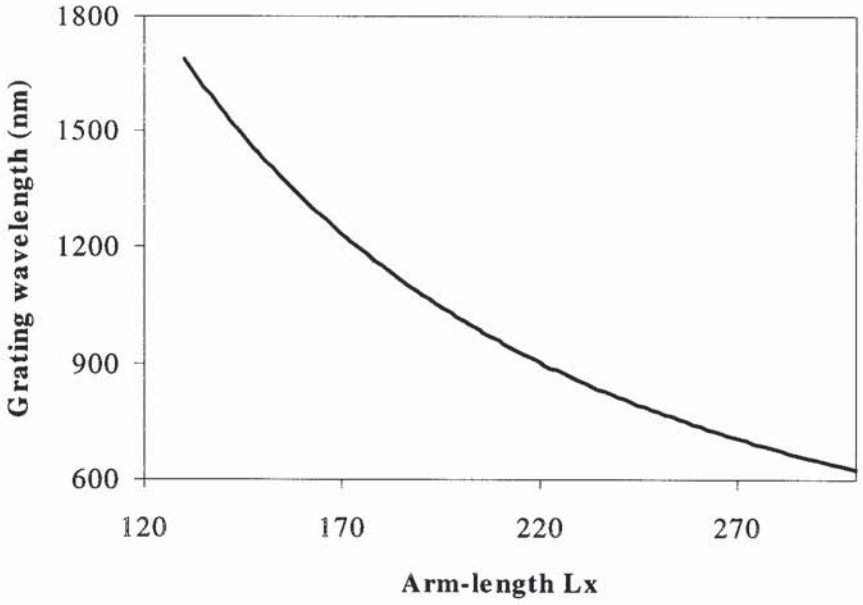

Figure 4.2 Calculated Bragg wavelength against the arm-length L_x for L_0=522mm, n_{eff}=1.446, θ_0=45° and λ_{UV}=244nm

Since L_0 is fixed, the grating wavelength changes according to the arm-length L_x. This suggests a way to predict the grating wavelength by using a reference grating. The arm-length L_{ref} may be roughly measured with relative errors of 1% or more; a reference grating is made with measured wavelength λ_{ref}. Rearranging eqn. (4.7) yields

$$L_0 = \frac{L_{ref}}{\sqrt{2}} + \frac{L_{ref}}{\sqrt{2}\tan\left[\arcsin\left(\frac{n_{efff}\lambda_{UV}}{\lambda_{reff}}\right)\right]} \tag{4.9}$$

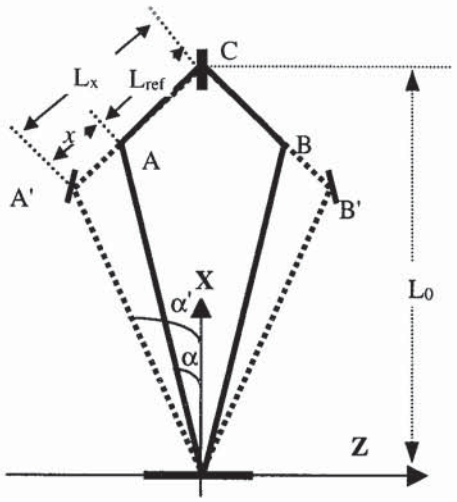

Figure 4.3 Schematic diagram of optical set-up for changing the Bragg wavelength in the holographic method

As shown in Figure 4.3, when moving the mirrors A and B to new positions A' and B' with the new arm-lengths $L_x = L_{ref} + x$, where x is the displacement measured with accuracy of 0.01mm by using a micrometer-driver. The new grating wavelength is then given by

$$\lambda_B = \frac{n_{eff}\lambda_{UV}}{\sin\left\{\arctan\left[\frac{L_{reff}+x}{\sqrt{2}L_0-(L_{reff}+x)}\right]\right\}} \tag{4.10}$$

where L_0 is given by eqn. (4.9). Rewriting eqn. (4.8) with respect to the reference grating yields

$$\frac{\Delta\lambda_B}{\lambda_B} = -\frac{\Delta x}{L_{reff}+x}\cdot\frac{\left|\sqrt{2}L_0-(L_{reff}+x)\right|}{\sqrt{2}L_0-2(L_{reff}+x)} \tag{4.11}$$

For Δx=0.01mm, L_0=522mm and L_x=142mm, eqn. (4.11) yields $\Delta\lambda_B = 0.2$nm. Obviously, it is enough for predicting grating wavelengths in guiding grating fabrication.

As stated, the two-beam holographic method is flexible in designing the grating wavelength. Limited by the range of the optical spectrum analyser and the light source in

the experiment, the gratings fabricated are normally in the range of 800nm and 1700nm. The transmission spectra of the gratings are shown in Figure 4.4 (a) and (b). Note that eqn. (4.10) offers great convenience in predicting the new grating wavelength during fabrication.

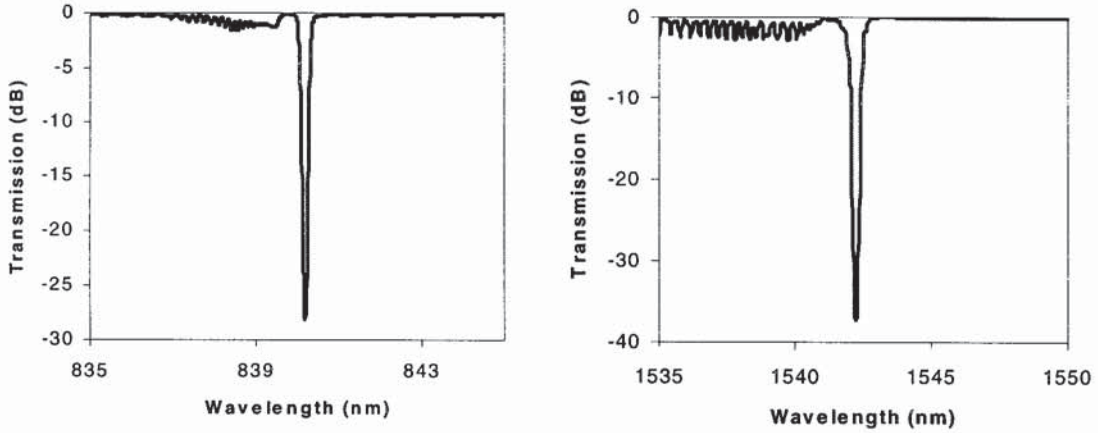

Figure 4.4 Typical transmission spectra of Bragg gratings fabricated using the two-beam holographic method at wavelengths of: (a) 800nm band; (b) 1550nm band

For a strong grating, shown in Figure 4.5 (a) and (b), the coupling of the cladding modes and radiation mode will become significant, exhibiting a loss and oscillations superimposed at the short wavelength side of the Bragg resonance. One useful observation is that the relative coupling strength of the cladding modes against the mode order is a slow varying profile with multiple minimums, consistent with the calculation of the overlap factors discussed in section 3.2. The other result is that the coupling between LP_{01}^{co} core and LP_{1m}^{cl} cladding modes is no longer forbidden when the grating fringes are tilted. Weak peaks appear between two neighbourly cladding modes as shown in Figure 4.5 (b).

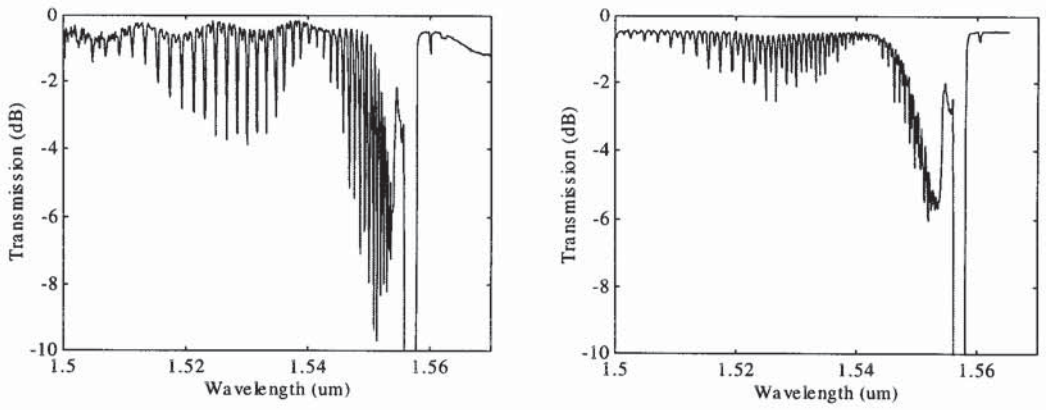

Figure 4.5 Typical transmission spectra of 5mm long strong Bragg gratings fabricated using the two-beam holographic method, showing radiation mode loss and cladding mode coupling: (a) a non-tilted strong grating; (b) a tilted strong grating

4.1.3 Chirped Bragg gratings

In the case of chirped fibre Bragg gratings, the length DE will not be equal to $f_D + f_E$. As illustrated by Figure 4.1, one of the two interfering UV beams is no longer parallel instead of converging when $DE > f_D + f_E$ or diverging when $DE < f_D + f_E$. Using matrix optics, the expression for describing the parallel beam through the two lenses D and E is given by

$$\begin{bmatrix} u_x \\ d_x \end{bmatrix} = \begin{bmatrix} 1 & \frac{1}{f_E} \\ 0 & 1 \end{bmatrix} \begin{bmatrix} 1 & 0 \\ -DE & 1 \end{bmatrix} \begin{bmatrix} 1 & \frac{1}{f_D} \\ 0 & 1 \end{bmatrix} \begin{bmatrix} 0 \\ x \end{bmatrix} \tag{4.12}$$

where the last matrix on the RHS of eqn. (4.12) describes the light incident on lens D with deviation to the light axis by height x ($-d/2 \le x \le d/2$) and angle 0; d is the width of the UV beam. The other three matrixes describe the transform of the lenses D and E and the free space propagation between the lenses D and E, respectively. u_x and d_x on the LHS of eqn. (4.12) indicates the height and the angle of the light at lens E, respectively. Simplifying eqn. (4.12) yields

$$\begin{cases} u_x = \left(\frac{1}{f_D} + \frac{1}{f_E} - \frac{DE}{f_D f_E} \right) x \\ d_x = \left(1 - \frac{DE}{f_D} \right) x \end{cases} \tag{4.13}$$

As illustrated by Figure 4.6, the light with height x and angle 0 is incident on lens D, the height and the angle of this light at lens E is given by eqn. (4.13) as d_x and angle u_x. This light crosses the photosensitive fibre on the **z**-axis and yields

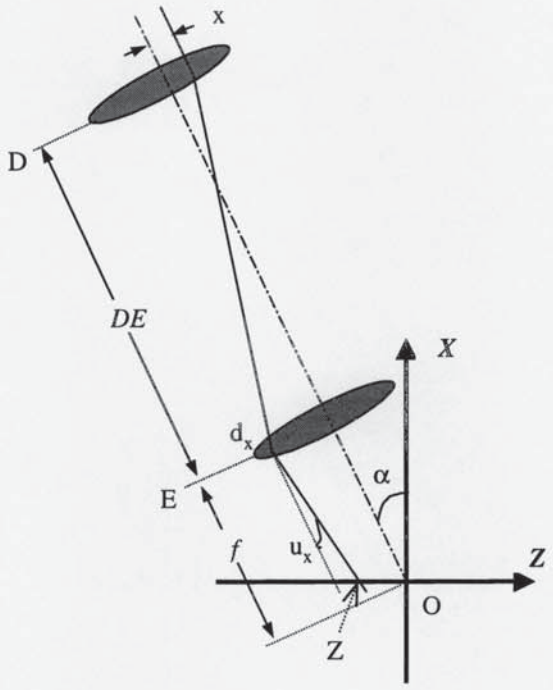

Figure 4.6 A graph showing the incident light $\begin{bmatrix} 0 \\ x \end{bmatrix}$ *crossing the photosensitive fibre at Z*

$$z = -\frac{x}{\cos\alpha} \tag{4.14}$$

where $-d/2 \le x \le d/2$, z indicates the locations of the light $\begin{bmatrix} 0 \\ x \end{bmatrix}$ crossing the photosensitive fibre, d is the UV beam width, α is given by eqn. (4.6). The angle of this light with respect to the **x**-axis is thus $\alpha - u_x$. Substituting eqn. (4.13) and eqn. (4.14)

into eqn. (4.5), the Bragg wavelength is obtained as

$$\lambda = \frac{2n_{eff}\lambda_{UV}}{\sin\left[\arctan\left(\frac{L_x}{\sqrt{2}L_0 - L_x}\right) + \left(\frac{2}{f} - \frac{DE}{f^2}\right)\cos\alpha \cdot z\right] + \sin\left[\arctan\left(\frac{L_x}{\sqrt{2}L_0 - L_x}\right)\right]} \tag{4.15}$$

where $f = f_D = f_E$ has been used as normally two identical cylindrical lenses are used. Obviously, eqn. (4.15) shows that the grating wavelength is varying along **z**-axis, i.e. a chirped Bragg grating. In order to see the structure of the chirp, simplifying eqn. (4.15) yields

$$\lambda = \lambda_0\left(1 + \frac{1}{2}\frac{DE - 2f}{f^2}\frac{z}{\sin\alpha}\right) \tag{4.16}$$

with

$$\begin{cases} \lambda_0 = \dfrac{n_{eff}\lambda_{UV}}{\sin\alpha} \\ \alpha = \arctan\left(\dfrac{L_x}{\sqrt{2}L_0 - L_x}\right) \end{cases} \tag{4.17}$$

where, linear approximations, $\sin(u_x) \approx u_x$, $\cos(u_x) \approx 1$ and $\frac{1}{1+u_x} \approx 1 - u_x$ have been used, λ_0 and α are the grating central wavelength and one beam angle with respect to the **x**-axis, respectively. Clearly, eqn. (4.16) exhibits a linearly chirped grating structure and the chirp is given by

$$chirp = \frac{1}{2}\frac{|df|}{f^2}\frac{d}{\sin\alpha}\lambda_0 \tag{4.18}$$

where $df = DE - 2f$. For L_0=522mm, L_x=142mm, n_{eff}=1.446, λ_{UV}=244nm, f=100mm and d= 6mm, eqn. (4.18) reduces to

$$chirp = 2.04 \cdot |df| \tag{4.19}$$

where *df* and *chirp* are in the units of millimetre and nanometre, respectively. For

$df = 5\,\text{mm}$, eqn. (4.19) yields $chirp \approx 10\,\text{nm}$.

By plotting eqn. (4.15), the Bragg wavelengths along the grating length is shown in Figure 4.7 (a). By changing the spacing of the two lenses DE around $2f$, the grating chirps against df is shown in Figure 4.7 (b), where the negative chirp means that the grating wavelength decreases along the grating length. Experimental transmission and reflection spectra are shown in Figure 4.8, where the short wavelength loss results from the coupling of the radiation mode.

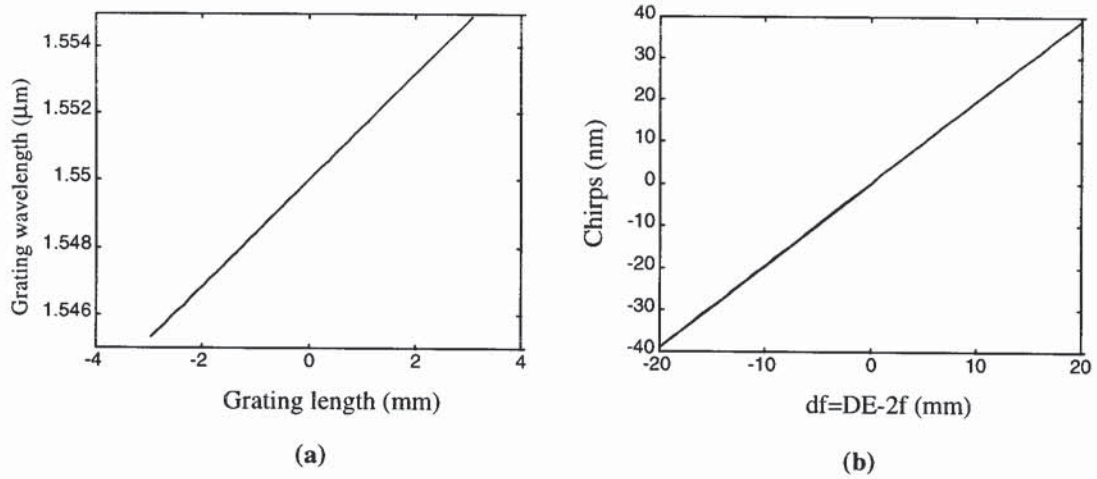

Figure 4.7 Graphs showing: (a) local Bragg wavelengths along the grating length; (b) chirps of the grating against df for $L_0 = 523mm$, $L_x = 142mm$, $n_{eff} = 1.446$, $\lambda_{UV} = 244nm$, $f_D = f_E = 100mm$ *and* $d = 6mm$

When slightly shifting the lens D in the direction perpendicular to the axis of the UV beam, the grating central wavelength shifts to long or short wavelengths by several nanometres, in addition, the grating length decreases due to reduced overlap part of the two UV beams. This is a useful technique to control the central wavelength accurately during grating fabrication.

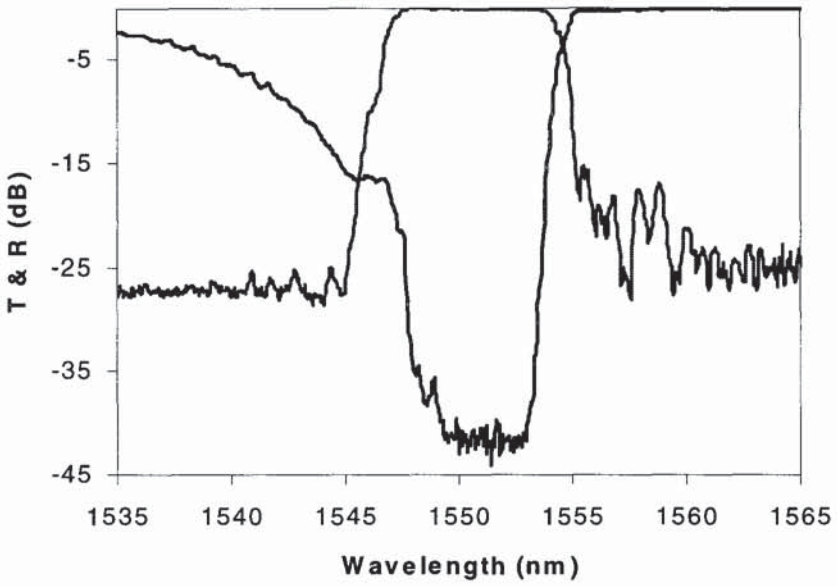

Figure 4.8 Typical transmitted and reflected spectra of a chirped Bragg grating fabricated using the two-beam holographic method

To summarise, this section discussed the computation used in predicting the Bragg wavelength and chirp using the holographic fabrication technique. Analytical expressions have been proposed, exhibiting a good linear profile for a chirped grating.

4.2 Phase Mask Fabrication Technique

This section discusses the technique using translated UV beam across a phase mask for the fabrication of complex gratings, such as apodised, wavelength-shifted, self-apodised chirped, phase-shifted, chirped Moiré and sampled gratings. This technique can be extended to the fabrication of long length gratings.

Based on the investigation contained within this section, the fabrication programmes in computer language LabVIEW have been developed for applications to the gratings described in this thesis and for wider use in the Photonics Research Group.

4.2.1 Introduction

Although the holographic fabrication technique is particularly flexible, an alternative technique based on the exposure of the fibre through a phase mask, placed in near-contact to the fibre has been widely used. As detailed in Chapter 2, this technique has now proved itself to be the preferred method of grating fabrication due to the simplicity and reproducibility. Meanwhile, the phase mask technique offers a number of advantages over the holographic technique. The fabrication process allows the spatial and temporal coherence of the UV-source to be less crucial. This technique has been extended by the use of a number of 'step-chirped' phase masks to increase the overall length and thus the bandwidth of the grating [125]. The main advantage of this fabrication technique is capable of making high quality complex grating structures, including grating array, chirped, apodised, phase-shifted, Moiré, sampled and long length gratings.

4.2.2 The fabrication of apodised Bragg gratings

It is well known that in addition to the central reflection peak, standard fibre Bragg gratings exhibit a series of sidelobes on either side of the main peak as discussed in section 3.3.4. These sidelobes are inherent in Bragg gratings and are highly undesirable for most grating applications. In wavelength division multiplexing (WDM) systems these sidelobes induce cross talk between adjacent channels and in dispersion compensating

systems they induce ripples in the dispersion characteristic of a chirped Bragg grating, degrading the system performance [126]. The suppression of grating sidelobes, apodised gratings are thus particularly important.

Although one can achieve apodisation simply by varying the intensity of the UV beam along the grating length, the accompanying variation in the average refractive index induces an undesired chirp, which produces a lot of oscillations resulting from the distributed Fabry-Perot effect. In this technique another exposure to an amplitude mask must be applied for the UV intensity compensation [127, 128] which makes the grating fabrication inconvenient and of a low repeatability. Alternatively, a complex phase mask with variable diffraction efficiency has been used to produce pure apodisation [129], but the need to have a different phase mask pattern for each Bragg wavelength required makes it uneconomical.

This section presents a technique for grating apodisation by dithering phase mask during the UV writing [130]. Two approaches, slow shifting and fast dithering phase mask methods are adopted experimentally [99, 130]. The experimental arrangement is shown in Figure 4.9, the phase mask is mounted on a computer-controlled piezoelectric transducer (PZT) stage, it can be moved relative to the photosensitive fibre, permitting phase shifts to be incorporated into the fibre grating during the UV writing. Thus it is capable of introducing a profiled coupling coefficient into a grating for the fabrication of complex grating structures.

During the UV writing, the phase mask is dithering relative to the photosensitive fibre, introducing a phase shift $\phi(z,t)$ into the grating. The coupling coefficient of the grating is thus profiled while the average index remains a constant along the grating length because of the uniform intensity UV exposure. In this case, the index distribution along the grating length given by eqn. (3.51) becomes

$$n(z,t) = n_0 + \Delta n_0 \cos\left[\frac{2\pi}{\Lambda} z + \phi(z,t)\right] \tag{4.20}$$

where $\phi(z,t)$ indicates the introduced phase shift, slow varying along the grating axis compared with the propagation phase $\beta_{01}^{co}z$, Λ is the grating period.

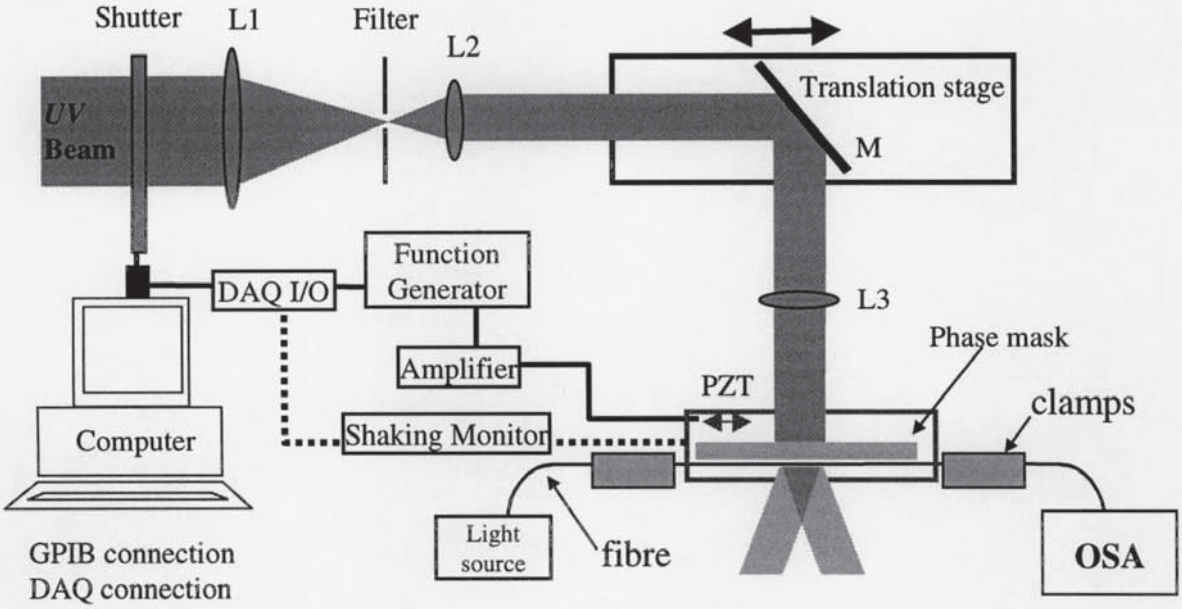

Figure 4.9 Experimental arrangement for fabricating complex structure gratings using the UV beam scanning across a phase mask and a PZT dithering phase mask

Consider that the phase shift $\phi(z,t)$ is varying between $-\pi/2$ and $\pi/2$, substituting eqn. (4.20) into the coupled-mode equation eqns. (3.9), the coupling coefficient is obtained as

$$\kappa(z,t)=\kappa_0\cos\left[2\pi\frac{a(z,t)}{\Lambda}\right] \tag{4.21}$$

where $\kappa_0=\pi\Delta n_0 C_{01}^{co}/\lambda_0$ is the maximum coupling coefficient, $\phi(z,t)=2\pi\dfrac{a(z,t)}{\Lambda}$ is the phase shift, $a(z,t)$ is the shift of the phase mask relative to the photosensitive fibre. Clearly, it is capable of introducing a specific profile into the grating coefficient $\kappa(z)$.

Depending on whether the phase shift is time dependent or independent, the apodisation profile can be realised by two different approaches, slow shifting or fast dithering phase mask techniques [131].

4.2.2.1 Slow shifting phase mask technique

One technique used for producing an apodisation profile into a grating is by introducing a time independent phase shift through the slow shifting the phase mask during the UV writing. When the shift of the phase mask is defined as

$$a(z)=\frac{\Lambda}{2\pi}\cos^{-1}[Fun(z)] \tag{4.22}$$

where $0 \le Fun(z) \le 1$ is a normalized apodisation profile. The coupling coefficient is given by substituting eqn. (4.22) into eqn. (4.21) as

$$\kappa(z)=\kappa_0 Fun(z) \tag{4.23}$$

Obviously, a profiled coupling coefficient, grating apodisation is realised. The shift of the phase mask is thus in the range of

$$0 \le a(z) \le \Lambda/4 \tag{4.24}$$

As an example, for a *cosine* profile apodisation given by

$$Fun(z)=\cos\left(\frac{\pi z}{L}\right) \tag{4.25}$$

Substituting into eqn. (4.22) a triangle profile is obtained as

$$a(z)=\frac{\Lambda}{2}\frac{|z|}{L} \tag{4.26}$$

where $-L/2 \le z \le L/2$ indicates the locations of the grating.

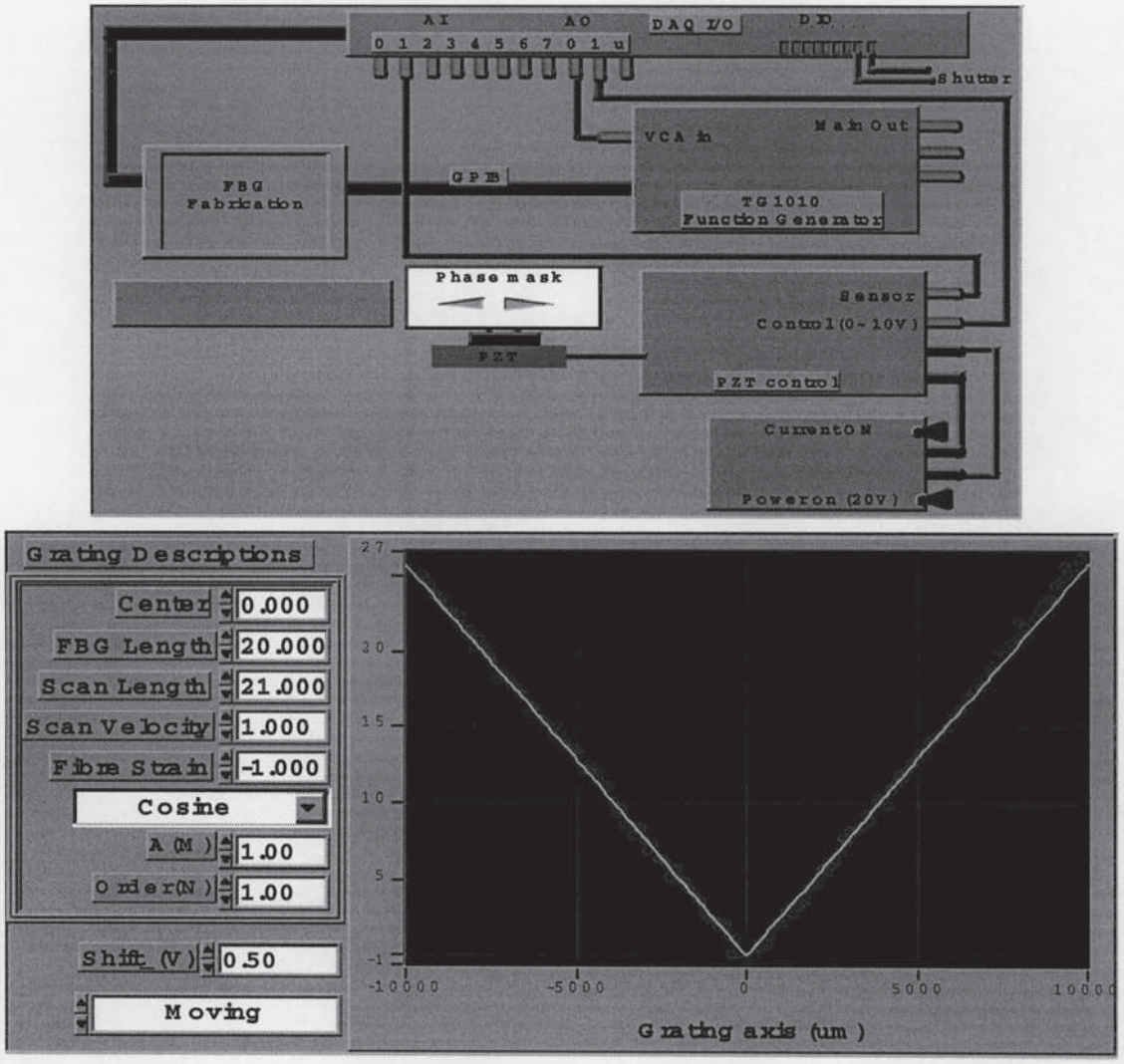

Figure 4.10 Schematic diagram for fabricating apodised fibre gratings: (up) connections of the fabrication system; (down) the control panel of LabVIEW programme, solid line indicates the shift of the phase mask; the circles indicate the measured shift of the phase mask in mV showing a good agreement

The control panel in LabVIEW for this kind of grating fabrication is shown in Figure 4.10. The DAQ card I/O terminators are used to write a triangle profiled voltage to and read the sensing signal of the phase mask shift from the PZT stage, respectively. As shown in Figure 4.10 (down), the PZT sensing signal (dots) is close to the triangle profile (straight line). In this technique, a feedback may be needed to eliminate the DC shifting of the PZT stage.

4.2.2.2 *Fast dithering phase mask technique*

The other technique used to produce an apodisation profile is by introducing a time dependent phase shift during the UV writing, using a periodical triangle wave to dither the phase mask to erase the grating fringes partly or completely. In this case, the shift of the phase mask is given by

$$a(z,t) = a_0(z) \cdot triangle(f \cdot t) \tag{4.27}$$

where $0 \le triangle(f \cdot t) \le 1$ is a normalized periodical triangle wave; f is its frequency, $a_0(z)$ is the amplitude: slow varying along the z-axis.

Since the fast dithering phase mask results in the fast dithering grating index fringes, the real coupling coefficient is thus the integration of the coupling coefficient with respect to the time. Using eqn. (4.27) and taking integration operation to eqn. (4.21), the coupling coefficient is expressed as

$$\kappa(z) = \frac{1}{T_0}\int_{-T_0/2}^{T_0/2} \kappa(z,t)dt = \kappa_0 \frac{1}{T/2}\int_{-T/4}^{T/4} \cos\left[\frac{2\pi a_0(z)}{\Lambda}\frac{t}{T/2}\right]dt \tag{4.28}$$

where $T = \frac{1}{f}$ is the time period of the triangle function, $T_0 = d / v_{scan}$, T_0 is total average time, d is the UV beam width and v_{scan} is the scanning velocity. Simplifying eqn. (4.28) yields,

$$\kappa(z) = \kappa_0 \frac{\sin[\pi a_0(z)/\Lambda]}{\pi a_0(z)/\Lambda} = \kappa_0 \,\mathrm{sinc}\left[\frac{a_0(z)}{\Lambda}\right] \tag{4.29}$$

Clearly, if an apodisation profile $Fun(z)$ is required, the profile of the phase mask shift is thus given by

$$a_0(z) = \Lambda \cdot \mathrm{sinc}^{-1}[Fun(z)] \tag{4.30}$$

where $Fun(z)$ is a normalized apodisation profile. In this case, the relationship between

the amplitude profile and the apodisation profile is an inverse *sinc* transform, rather than an inverse *cosine* transform given by eqn. (4.22). The maximum shift of the phase mask is thus in the region of

$$0 \le a_0(z) \le \Lambda \tag{4.31}$$

Comparing eqn. (4.31) with eqn. (4.24), it is clear that the region of the shift in the technique of fast dithering phase mask is four times of that slow shifting phase mask case. The resolution for controlling the PZT stage is thus improved four times. In addition, the DC shifting of the PZT stage in this case of fast dithering phase mask is no longer a problem.

As an example, if a apodisation profile is a gaussian function given by

$$Fun(z) = \exp\left[-4\left(\frac{z}{L/2}\right)^2\right] \tag{4.32}$$

Taking *inversinc* operation to eqn. (4.30), the profile of the dithering amplitude of the phase mask is shown in Figure 4.11. This dithering amplitude decreases from the grating ends to centre gradually until there is no dithering at the grating centre. Using this technique, apodised gratings with more than 30dB extinction and 20dB-reflectivity have been obtained experimentally.

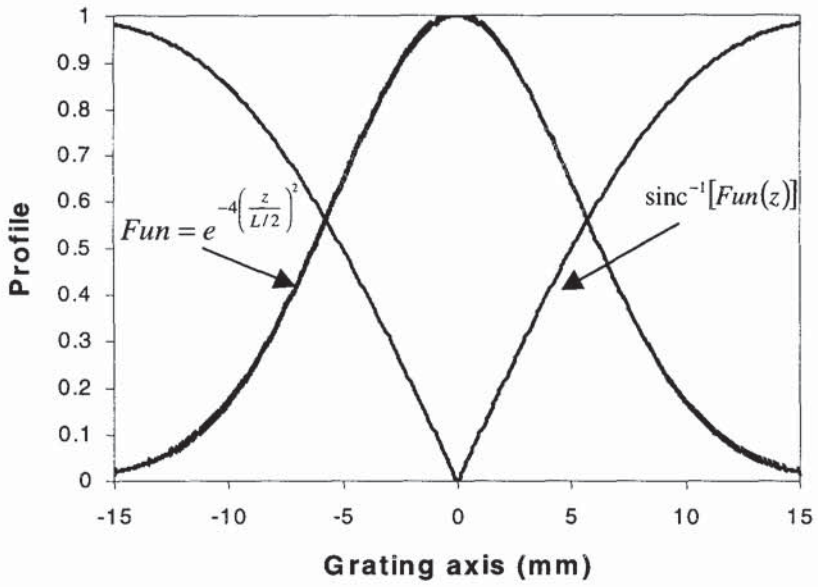

Figure 4.11 A graph showing a normalized gaussian profile and inverse sinc transform along the grating length

As illustrated by Figure 4.9, through the GPIB and DAQ connections, 25Hz triangle wave with maximum peak-peak voltage around 0.9V was used to drive the PZT stage. The DAQ card output a normalized apodisation profile to modulate the function generator (FG) during the UV writing and read the signals from the function generator and the dithering sensor of the PZT stage to computer. The normalized apodisation function, the amplitude profile, the modulated function generator output, and the shift of the phase mask are shown in Figure 4.12 (a), (b), (c), and (d). Clearly, in the middle of the grating, the dithering amplitude is zero $a_0(0)=0$ and the coupling coefficient thus reaches its maximum. When the load of the PZT is not very heavy, up to 100Hz dithering frequency may be used to drive the PZT stage experimentally. It should be noted that it is required to confirm non-dithering in the grating centre as $a_0(0)=0$ by DAQ I/O waveform or an oscilloscope during experiment.

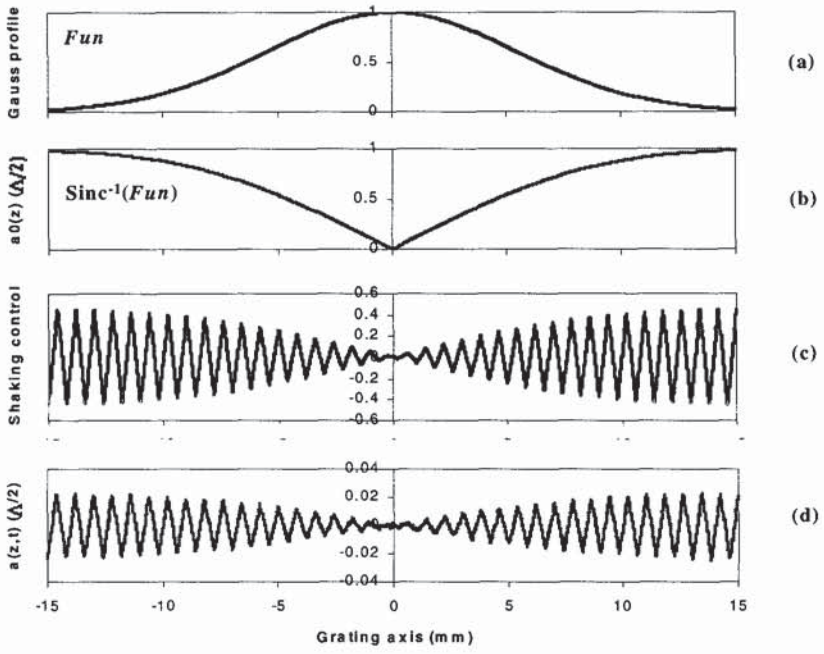

Figure 4.12 Graphs for illustrating the fabrication of apodised gratings using DAQ I/O: (a) the apodisation profile $Fun(z)=\exp\left[-4\left(\frac{z}{L/2}\right)^2\right]$*; (b) the profile of dithering amplitude of the phase mask* $sinc^{-1}(Fun)$*; (c) 25Hz triangle wave used to drive the PZT; (d) the shift of the phase mask in mV*

For a *cosine* apodised profile, the LabVIEW control panel is shown in Figure 4.13. The evolution of the triangle function (broken line) is $\text{sinc}^{-1}[\cos(z)]$, which is slightly deviating from the straight line illustrated in Figure 4.10, the case of slow shifting phase mask technique.

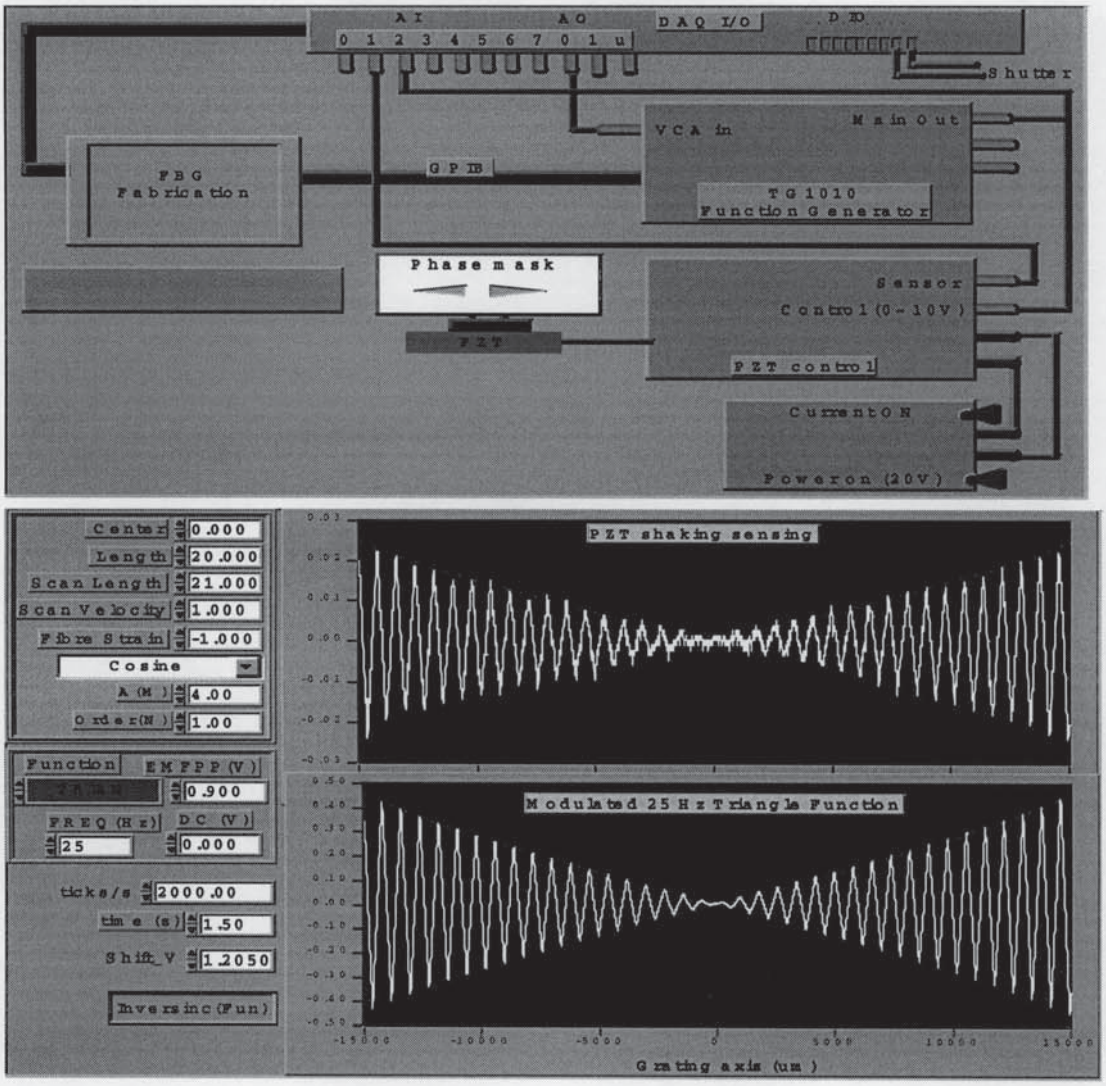

Figure 4.13 Schematic diagram for fabricating apodised gratings: (up) the connections of the fabrication system; (down) the control panel of LabVIEW programme indicates the 25Hz triangle-wave PZT driving signal and the dithering of the phase mask, showing a good agreement, the envelope is inverse sinc transform of the cosine profile

4.2.3 Wavelength-shifted Bragg gratings

As mentioned in Chapter 2, a disadvantage of the fabrication method using a phase mask stems from the need to have a different phase mask pattern for each Bragg wavelength required. The technique of stretching the fibre during the writing process provides a means of changing the Bragg wavelength when the fibre is relaxed following the UV exposure. Here an alternative technique is presented to change the Bragg wavelength by means of moving the phase mask slowly during the UV writing.

When the phase mask is moving with a uniform velocity v_{mask} relative to the photosensitive fibre during the UV writing, a gradual phase shift is thus to be added to the grating. In this case eqn. (4.20) becomes

$$n(z) = n_0 + \Delta n_0 \cos\left[\frac{2\pi}{\Lambda_0} z \pm \frac{2\pi}{\Lambda_0} \cdot \frac{v_{mask} \cdot z}{v_{scan}}\right] \tag{4.33}$$

where, the upper and lower signs indicate, respectively, the codirectional and contradirectional moving of the phase mask with respect to the UV beam scanning direction, $v_{mask} << v_{scan}$, v_{mask} and v_{scan} are the velocity of the phase mask and the UV beam scanning, respectively, Λ_0 is the grating period when the phase mask is not moved. Rearranging eqn. (4.33) yields

$$n(z) = n_0 + \Delta n_0 \cos\left[\frac{2\pi z}{\Lambda_0 (1 \mp v_{mask} / v_{scan})}\right] \tag{4.34}$$

where approximation $1 + x \approx \frac{1}{1 - x}$ has been used for $x << 1$. It is clear that the grating period is changed and thus the Bragg wavelength is shifted by $\Delta\lambda$ as [132]

$$\Delta\lambda = \mp \frac{v_{mask}}{v_{scan}} \lambda_0 \tag{4.35}$$

Obviously, it is a valuable technique to adjust the Bragg wavelength. For $|v_{mask}| / v_{scan} \sim 0.1\%$, eqn. (4.35) exhibits ±1.5nm tunable range at 1550nm band. In this

case, the coupling coefficient given by eqn. (4.21) becomes

$$\kappa(z)=\kappa_0\cos\left[2\pi\frac{v_{mask}}{\Lambda}\cdot\frac{z}{v_{scan}}\right] \tag{4.36}$$

The average coefficient is thus given by taking integration operation to eqn. (4.36) as

$$\overline{\kappa}=\frac{1}{T_0}\int_{-T_0/2}^{T_0/2}\kappa(z)dt=\kappa_0\int_{-d/2}^{d/2}\cos\left(\frac{2\pi v_{mask}}{\Lambda}\cdot\frac{z}{v_{scan}}\right)\frac{dz}{d} \tag{4.37}$$

where d is the width of the UV beam, $T_0=d/v_{scan}$, T_0 indicates the average time. Rearranging eqn. (4.37) yields

$$\kappa=\kappa_0\cdot\frac{\sin\left(2\pi n_{eff}d\Delta\lambda/\lambda_0{}^2\right)}{\left(2\pi n_{eff}d\Delta\lambda/\lambda_0{}^2\right)} \tag{4.38}$$

where eqn. (4.35) and the Bragg resonance $\lambda_0=2n_{eff}\Lambda$ have been used. Clearly, when $\Delta\lambda=0$, the coupling coefficient has its maximum $\kappa(z)=\kappa_0$, which is the normal UV beam scanning standing phase mask case. When the shift of the Bragg wavelength is equivalent to the FSR of the UV beam width Fabry-Perot cavity given by

$$\Delta\lambda=\frac{\lambda_0{}^2}{2n_{eff}d} \tag{4.39}$$

where d is the UV beam width. Substituting eqn. (4.39) into eqn. (4.38), the coupling coefficient becomes $\kappa(z)=0$. This means the grating fringes vanish. Obviously, the shift of the Bragg wavelength is at the price of decreasing the grating coupling strength. The maximum shift is thus given by

$$|\Delta\lambda|=\frac{|v_{mask}|}{v_{scan}}\lambda_0<\frac{\lambda_0{}^2}{2n_{eff}d} \tag{4.40}$$

It is clear that the maximum shift strongly depends on the UV writing beam width; a small beam width results in a large range in the shift of the Bragg wavelength. For a given UV beam width d, the moving velocity of the phase mask must be in the region of

$$\frac{|v_{mask}|}{v_{scan}} < \frac{\lambda_0^{\,2}}{2n_{eff}d} / \lambda_0 \tag{4.41}$$

For a 0.5mm width UV writing beam, eqn. (4.41) yields $|v_{mask}|/v_{scan} < 0.1\%$ and ±1.5nm shift range. By reducing the size of the UV beam to around 0.1~0.2mm, a 5nm wavelength shift has been obtained experimentally [132].

4.2.4 Chirped Bragg gratings

As discussed above, moving the phase mask slowly relative to the photosensitive fibre results in a Bragg wavelength shift, thus this can be utilised to fabricate chirped gratings. Supposing the phase mask is moving with a linearly varying velocity, form 0 to v_{mask}, the acceleration of the phase mask is simply given by

$$acc = \frac{v_{mask} \cdot v_{scan}}{L} \tag{4.42}$$

where acc indicates the acceleration of the phase mask. Since acc is very small and the width of the UV beam is narrow ($d < 0.5\,\text{mm}$), the velocity of the phase mask is considered a uniform during a short time period, $T_0 = d / v_{scan}$. Then a square phase shift with respect to the fibre axis is introduced and eqn. (4.20) becomes

$$n(z) = n_0 + \Delta n_0 \cos\left[\frac{2\pi}{\Lambda_0} z + \frac{2\pi}{\Lambda_0} \cdot acc \cdot \left(\frac{z}{v_{scan}}\right)^2\right] \tag{4.43}$$

Substituting eqn. (4.42) into eqn. (4.43) yields

$$n(z) = n_0 + \Delta n_0 \cos\left[\frac{2\pi z}{\Lambda_0\left(1 - \frac{v_{mask}}{v_{scan}}\frac{z}{L}\right)}\right] \tag{4.44}$$

where $-L/2 \le z \le L/2$ indicates the locations of the grating. It is clear that the grating period is varying linearly along the grating axis: a linearly chirped grating with chirp of

$\Delta\lambda = \frac{v_{mask}}{v_{scan}}\lambda_0$ is achieved. When the velocity of the phase mask is linearly varying between $\pm\frac{\lambda_0 v_{scan}}{2n_{eff}d}$ during the UV beam scanning through the entire phase mask, a grating with total chirp $\frac{\lambda_0^{\,2}}{n_{eff}d}$ is thus obtained. In this case, the local Bragg wavelength is given by

$$\lambda(z) = \lambda_0 + \frac{\lambda_0^{\,2}}{2n_{eff}d}\frac{z}{L/2} \tag{4.45}$$

where $-L/2 \le z \le L/2$. Using eqn. (4.45), the coupling coefficient given by eqn. (4.38) reduces to

$$\kappa(z) = \kappa_0 \frac{\sin(2\pi z/L)}{2\pi z/L} \tag{4.46}$$

Obviously, it is a *sinc* apodisation profile, which gives self-apodised gratings.

4.2.5 Phase-shifted Bragg gratings

As discussed in section 4.2.2.1, this technique can easily extend to the fabrication of phase-shifted Bragg gratings. When the introduced phase shift along the grating length is given by

$$\phi(z) = \begin{cases} 0 & -L/2 \le z < 0 \\ \pi & 0 \le z \le L/2 \end{cases} \tag{4.47}$$

a phase-shifted Bragg grating is fabricated with a narrow transmission peak located in the Bragg stop-band. It should be noted that when introducing a profile into the coupling coefficient of a chirped or uniform grating with multiple zeros and π phase shifts, corresponding to a long-period modulation, this technique is then extended to the fabrication of chirped Moiré and sampled gratings, respectively.

The experimental arrangement for fabricating phase-shifted gratings is also shown in

Figure 4.9. About 0.5V DC voltage was output from a DAQ AO terminator to shift the phase mask by half a grating period through a PZT stage when the UV beam reaches the centre of the mask. As illustrated in Figure 4.14, the phase mask is shifted by a half grating period, corresponding to 26mV sensor voltage.

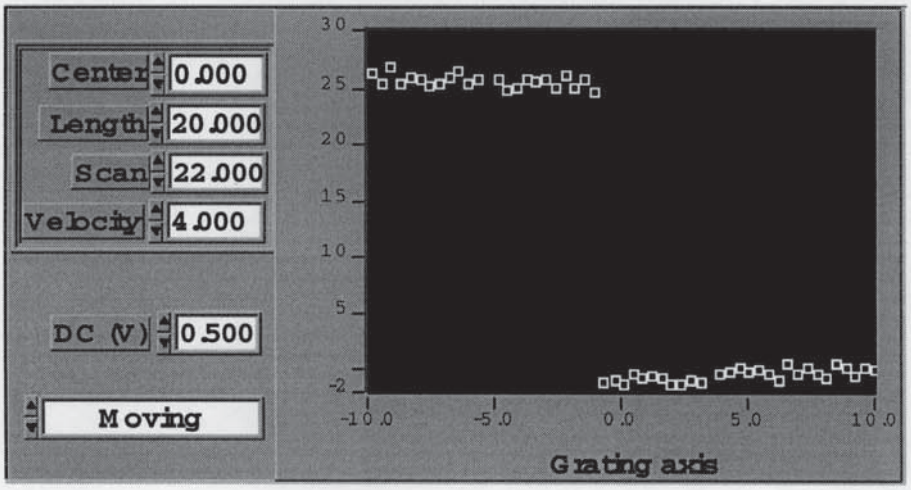

Figure 4.14 Schematic diagram of LabVIEW control panel for fabricating phase-shifted gratings, showing the phase mask moves half a grating period when the UV beam reaches the centre of the phase mask, corresponding to the change of 26mV sensing voltage

In general, three methods are employed in the fabrication of phase-shifted Bragg gratings: using a phase-shifted phase mask [133], post-exposure a uniform grating [134, 135, 136, 137], and shifting the phase mask during the UV writing. The phase-shifted phase mask is expensive and the wavelength is fixed. The post-exposure method has a poor repeatability as the phase is determined by Δn introduced by the extra UV exposure in the grating, which has uncontrolled changes during annealing. Thus, the third fabrication method presented in this section compares favourably with high repeatability. Further theoretical and experimental investigation is contained in section 5.5.

4.2.6 Long length fibre Bragg gratings

In the fabrication technique of scanning the UV beam across a phase mask, the length of

the phase mask limits the grating length. An improved approach is translating a phase mask and the modulated UV beam across a photosensitive fibre and 1m length Bragg gratings have been fabricated experimentally [55].

The experimental arrangement is shown in Figure 4.15, one difference from the set-up illustrated in Figure 4.9 is that the lens L_3 and the phase mask are mounted on the motion stage, translating the phase mask across a photosensitive fibre. In this case, the refractive index distribution along the fibre length given by eqn. (4.20) becomes

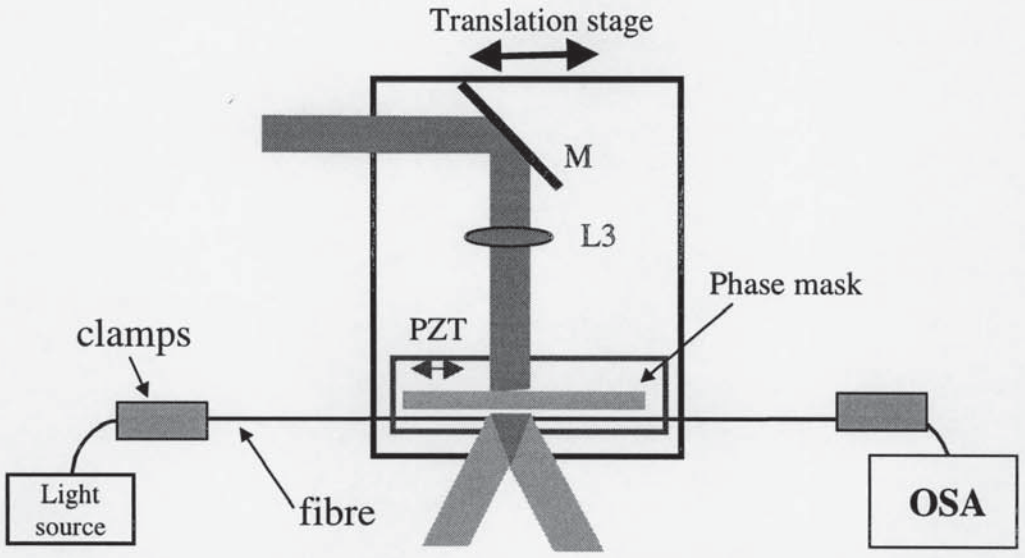

Figure 4.15 Experimental arrangement of a phase mask scanning across a photosensitive fibre for fabricating long length gratings

$$n(z) = n_0 + \Delta n_0 \cos\left[\frac{2\pi}{\Lambda_0} z + \phi_1(z) + \phi_2(z)\right] \tag{4.48}$$

where $\phi_1(z) = \frac{2\pi v_{scan} \cdot t}{\Lambda_0}$ is the phase shift resulting from the moving of the phase mask relative to the fibre, $\phi_2(z) = \frac{2\pi a(z)}{\Lambda_0}$ is the phase shift introduced by the extra moving of the phase mask through a PZT stage. The total phase shift $\phi(z) = \phi_1(z) + \phi_2(z)$ must be a constant or varying slowly between $-\pi/2$ and $\pi/2$ along the grating length and the coupling coefficient is given by eqn. (4.21).

Clearly, it can be realised by applying a periodical ramp function to the PZT stage. The physical picture is that the PZT stage drives the phase mask moving in the opposite direction while the motion stage moves. Then the phase mask and grating fringes remain stationary temporarily when the two opposite velocities v_{scan} and v_{mask} are equivalent. When the motion stage travels one grating periodicity (~0.5μm) in the time period of the ramp wave, all grating fringes will remain quasi stationary. Thus, the relationship between the velocity of the motion stage and the frequency of the ramp wave is obtained as

$$v_{scan} = \Lambda \cdot f \tag{4.49}$$

where, $f = \frac{1}{T}$, f is the frequency of the ramp wave and T is its time period. $\Lambda \sim 0.5\,\mu m$ is the grating period. The total scanning time is thus given by

$$Time = \frac{L}{\Lambda \cdot f} \tag{4.50}$$

where L is the grating length. The limitation of this technique is the low response of the PZT stage. For a relatively high frequency $f = 100\,Hz$, eqn. (4.50) yields approximately 5.5 hours to fabricate a 1m long grating, which is not practical. Increasing the frequency of the PZT stage to 500Hz it would still take 1 hour for a 1m long scan.

A practical approach is using the Acoustic Optical Modulator (AOM) to modulate the UV beam periodically with time period of T. Consider that the time of the motion stage travelling one grating period is equivalent to a period of the AOM, the relationship between the scanning velocity and the modulation frequency is also given by eqn. (4.49). For a rectangular modulation profile, define the duty cycle as

$$q = \frac{T_{on}}{T_{on} + T_{off}} \tag{4.51}$$

where $0 < q < 1$, q indicates the duty cycle of the modulation, T_{on} is the time of the UV bream transmitted while T_{off} is the time blocked ($T = T_{on} + T_{off}$). Clearly, in one

modulation period of the AOM, the grating fringes move

$$a_0 = q \cdot \Lambda \tag{4.52}$$

As discussed in section 4.2.2.2, the technique of the dithering phase mask for grating apodisation, the grating coupling coefficient is given by eqn. (4.29). Substituting eqn. (4.52) into eqn. (4.29), the coupling coefficient is obtained as

$$\kappa = \kappa_0 \frac{\sin(\pi q)}{\pi q} \tag{4.53}$$

Clearly, when $q = 0.5$, an optimum coupling coefficient as $\kappa \approx 0.637\kappa_0$ is obtained. The grating coupling coefficient decreases due to the moving of the grating fringes compared with the stationary case. In this case, there is no limitation for the grating writing rate since the response of the AOM is fast. Using eqn. (4.50), it can estimated that when the modulation frequency is about 2000Hz it will take only 17 minutes to write a 1m long grating.

To summarise, the realisation of apodised gratings has been detailed and two techniques have been adopted experimentally. In the slow shifting phase mask technique, the profile of the phase mask shift is an inverse *cosine* transform of the apodisation profile and the maximum shift of the phase mask is a quarter of a grating period. In the fast dithering phase mask technique, the shift profile of the phase mask is an inverse *sinc* transform of the apodisation profile and the maximum shift is a grating period. The fabrication of wavelength-shifted, self-apodised chirped and phase-shifted gratings using a uniform phase mask has been discussed. This technique is capable of fabricating chirped Moiré and sampled gratings when the appropriate profiles are introduced into the grating coupling coefficient. In addition, this section also discussed how this technique extends to a long length grating fabrication using a phase mask scanning across a long photosensitive fibre.

4.3 Dependence of the UV Beam Parameters

This section discusses how the UV beam polarisation and beam-width affect the formation of the grating fringes. In phase mask fabrication technique, the effective grating length is less than the UV exposure region by an amount that depends on the spacing between the phase mask and fibre axis. The polarisation of the UV writing beam affects the visibility of the grating fringes.

4.3.1 The influence of the UV beam width

As discussed in the fabrication of complex gratings, a narrow UV writing beam is normally required for introducing a precise apodisation profile into a grating. In the fabrication of the wavelength-shifted and self-apodised chirped gratings, a narrow UV beam is particularly important as detailed in section 4.2.3 and section 4.2.4. However, the writing efficiency decreases significantly as a result.

The optical setup is shown in Figure 4.9. The spacing between the phase mask and the fibre axis is the sum of the radius of the fibre cladding and the gap between the fibre cladding and the phase mask, which is more than 62.5μm. This spacing decreases the overlap length of the two UV beam. As shown in Figure 4.16 (a), the overlap and non-overlap lengths of the UV beam are indicated by L_G and L_I as and given by

$$\begin{cases} L_G = d - 2(s + r_{clad}) \tan\alpha \\ L_{total} = d + 2(s + r_{clad}) \tan\alpha \end{cases} \tag{4.54}$$

where, s indicates the spacing between the surfaces of the phase mask and the fibre cladding, r_{clad} is the radius of the fibre cladding, normally 62.5μm, d is the width of the UV beam. Note that the far-filed approximation has been used to describe the interfering along the fibre core. α is the diffraction angle of the phase mask and given by

$$\alpha = \arcsin\left(\frac{\lambda_{UV} n_{eff}}{\lambda_0}\right) \tag{4.55}$$

For the Bragg wavelength at λ_0=1550nm, eqn. (4.55) yields the diffraction angle of the phase mask as $\alpha \sim 13.2^{\circ}$. Since the non-overlap UV beam exposure decreases the fibre photosensitive or erases the grating fringes, the writing efficiency is defined as

$$Efficiency = L_G / L_{total} \tag{4.56}$$

Clearly, $0 \leq Efficiency < 1$.

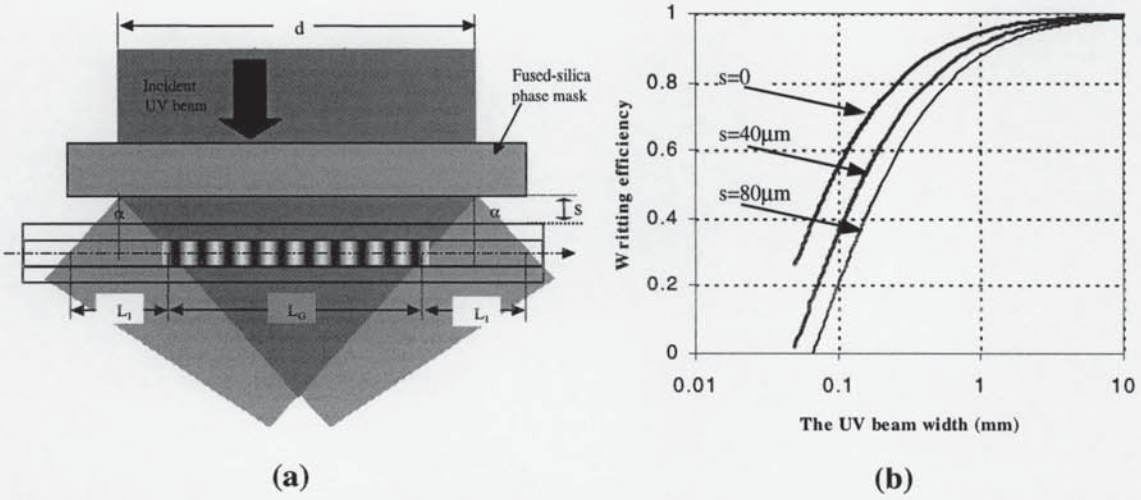

(a) **(b)**

Figure 4.16 (a) Schematic diagram showing the overlap of the ±1-order diffraction through a phase mask; (b) the writing efficiency versus the width of the UV beam for different values of spacing of the fibre cladding and the phase mask: 0, 40μm and 80μm

For $h \to 0$ or $d>>h$, eqn, (4.56) yields $Efficiency \approx 1$. As an effectively writing, the *Efficiency* is required to be large. The *Efficiency* against the width of the UV beam for different values of spacing (s) is illustrated in Figure 4.16 (b), showing a significant decrease for reducing the width of the UV beam. For s=80μm and d=0.1mm, *Efficiency* is only 0.2. When the fibre is placed close to the phase mask, this efficiency can be improved but it will risk damaging the phase mask.

4.3.2 Dependence of UV beam polarisation

Since the two UV beams are interfering to produce the grating fringes, the polarisation orientation of the UV beam affects the visibility of the grating fringes. The visibility is

defined as

$$visibility = \frac{I_{\max} - I_{\min}}{I_{\max} + I_{\min}} \tag{4.57}$$

As illustrated in Figure 4.17 (a), when the UV beam with s-polarisation or y-orientation is incident on the phase mask, it is diffracted into two beams of ±1-order maintaining the s-polarisation. This is the case discussed in the section 4.1.2, the visibility of the interfering fringes is given by substituting eqn. (4.3) into eqn. (4.57) as

$$visibility\big|_{s-polarised} = 100\% \tag{4.58}$$

However, when the UV beam with p-polarisation or z-orientation is incident on the phase mask, the two diffracted beams of ±1-orders are no longer with the same orientations in the XZ-coordinate system as shown in Figure 4.17 (b). In this case, the resultant amplitude at the meeting point is given by

$$\begin{aligned} \vec{A}(x,z) &= A_z(x,z)\cdot\vec{z}^{\,0} + A_x(x,z)\cdot\vec{x}^{\,0} \\ &= \left(e^{j\vec{\beta}_1\cdot\vec{r}} + e^{j\vec{\beta}_2\cdot\vec{r}}\right)\cos\alpha\cdot\vec{z}^{\,0} + \left(e^{j\vec{\beta}_2\cdot\vec{r}} - e^{j\vec{\beta}_1\cdot\vec{r}}\right)\sin\alpha\cdot\vec{x}^{\,0} \end{aligned} \tag{4.59}$$

where α is the phase mask diffraction angle, given by eqn. (4.55). The vector propagation constant $\vec{\beta}_1$ and $\vec{\beta}_2$ are given by eqn. (4.1). Rearranging eqn. (4.59), the distribution of the UV intensity along the **z**-axis is obtained as

$$\begin{aligned} I(z) &= \left|A_z(0,z)\right|^2 + \left|A_x(0,z)\right|^2 \\ &= 2 + 2\cos\left(\frac{2\pi z}{\Lambda}\right)\cos(2\alpha) \end{aligned} \tag{4.60}$$

where $\Lambda = \dfrac{\lambda_{UV}}{2\sin\alpha}$ is the grating period given by eqn. (4.4) ($\alpha = \beta$). The *visibility* in this case is obtained as

$$visibility\big|_{p-polarised} = \cos\left[2\sin^{-1}\left(n_{eff}\frac{\lambda_{UV}}{\lambda_B}\right)\right] \tag{4.61}$$

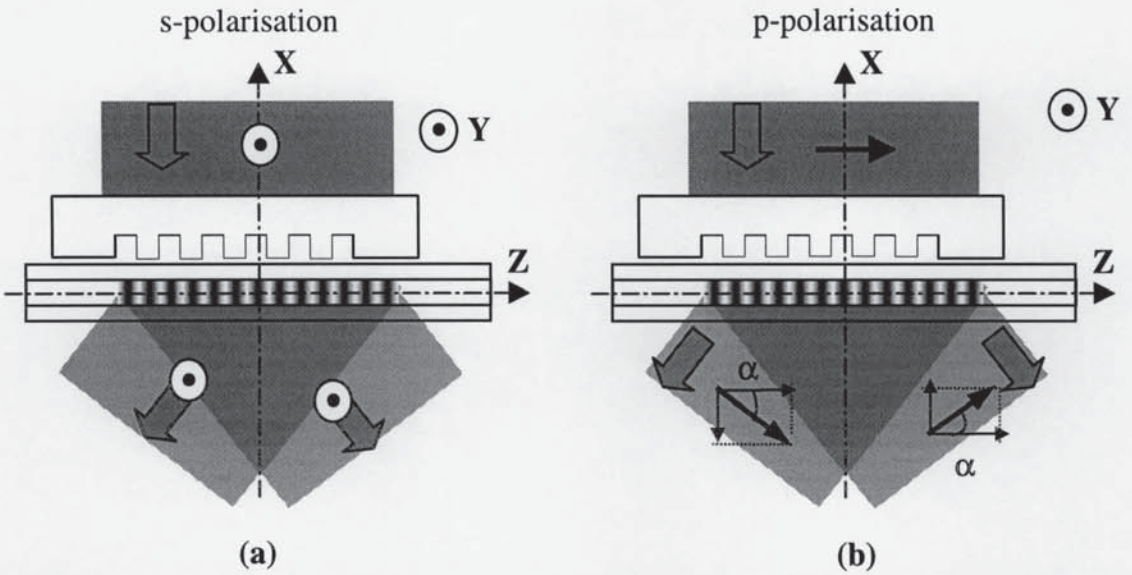

Figure 4.17 Schematic diagrams showing the polarisation orientations of the UV beam before and after a phase mask diffraction: (a) s-polarisation; (b) p-polarisation

where, the Bragg condition $\lambda_B = 2n_{eff}\Lambda$ has been used. For a grating with the Bragg resonance at 1550nm, eqn. (4.61) yields $visibility\big|_{p-polarised} \approx 0.90$. This is seems not serious as only 10% less than the ideal case. However, for the Bragg wavelength at 980nm or 800nm, this visibility rapidly decreases to 0.74 and 0.61, respectively, as shown in Figure 4.18. This significantly affects the formation of a strong grating at those wavelengths and suggests that the UV beam with s-polarisation should be used. It should be noted that the polarisation state of the writing UV beam affects the birefringence of Bragg gratings.

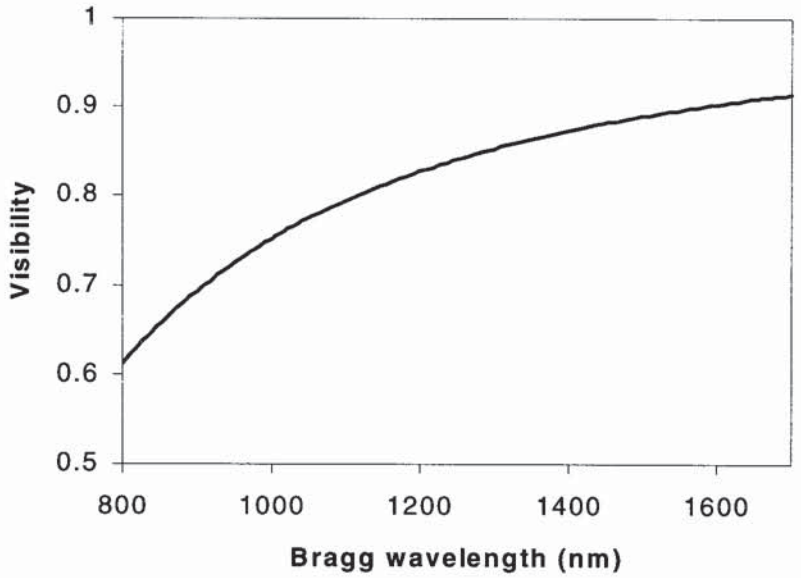

Figure 4.18 A graph showing the visibility of the grating fringes against the Bragg wavelength using p-polarised UV beam for fabricating Bragg gratings

To summarise, the influence of the UV beam width and its polarisation for writing fibre Bragg gratings has been discussed theoretically. Calculation shows that reducing the UV beam size or increasing the spacing of the fibre and phase mask decreases the writing efficiency in the phase mask fabrication technique. The polarisation of the UV beam affects the visibility of the interfering fringes. Comparing with s-polarised UV writing beam, calculation results show that the p-polarised UV writing beam results in the decrease of the visibility about 10% and 40% at 1550nm and 800nm Bragg wavelengths, respectively. This suggests s-polarised UV beam should be used in the fabrication of fibre Bragg gratings.

4.4 Chapter Summary

In this chapter, the theories behind the two common techniques for the fabrication of fibre Bragg gratings - holographic and phase mask techniques – have been investigated in detail. In holographic fabrication technique, analytical expressions for predicting Bragg wavelengths and chirps have been developed. This fabrication technique is flexible in designing grating wavelengths and chirps. Gratings in wavelength band of 800mm and 1500nm were fabricated experimentally.

The main contents within this chapter discuss the technique of scanning phase mask technique for the fabrication of complex grating structures. Two techniques, slow shifting and fast dithering phase mask through a PZT stage during the UV writing were adopted experimentally. In the case of the slow shifting technique, the profile of the phase mask shift is an inverse *cosine* transform of the apodisation profile and the maximum shift is a quarter of a grating period. While in the case of the fast dithering technique, the profile of the phase mask shift is an inverse *sinc* transform of the apodisation profile and the maximum shift is a grating period. This section also discussed how this technique extends to the fabrication of wavelength-shifted, self-apodised chirped, phase-shifted, Moiré and sampled and long length fibre Bragg gratings.

Based on the investigation contained within this chapter, the fabrication programmes in LabVIEW have been developed for wider use in the Photonics Research Group.

CHAPTER 5

Modelling of Fibre Bragg Gratings

This chapter details the modelling of a number of complex grating structures, including apodised, chirped, Moiré, sampled, phase-shifted gratings. In addition, the normal and abnormal spectral evolutions and the formation of Type IIa gratings are also discussed.

The modelling theory has been discussed in section 3.3.5 for given profiles of the coupling coefficient $\kappa(z)$ and the Bragg wavelength $\lambda(z)$. Based on the investigation contained within this chapter, the simulation programmes in LabVIEW were constructed for wider use in Photonics Research Group.

5.1 Apodised Fibre Bragg Gratings

As discussed in section 3.3.4, standard fibre Bragg gratings exhibit a series of sidelobes on either side of the main peak. Their wavelength locations and magnitudes depend on the grating coupling coefficient $\kappa(z)$, hence suggesting a method to suppress them by tapering the coupling coefficient to a specific profile that continuously varies between 0 and κ_0 from the grating ends to the centre symmetrically. The experimental realisation has been discussed in section 4.2.2. This section focuses on the modelling of apodised grating in order to find some useful apodisation profiles with high sidelobe suppression. For convenience, the grating coupling coefficient is defined as

$$\kappa(z) = \kappa_0 \cdot Fun(z) \tag{5.1}$$

where, $0 \le Fun(z) \le 1$, $Fun(z)$ is a normalized apodisation profile, κ_0 indicates the maximum coupling coefficient and the corresponding coupling strength is then $\kappa_0 L$.

5.1.1 Uniform Bragg gratings

For a 10mm long uniform grating ($Fun(z)=1$) with $\kappa_0 L=3$ at the wavelength 1.55μm, the amplitude of index fringes is about $2\Delta n=3.70\times10^{-4}$ as shown in Figure 5.1 (a), where the grating period is magnified by a factor of 500 times and $C_{01}^{co}=0.80$ has been used. The reflection spectrum with 99% peak reflectivity is shown in Figure 5.1 (b), exhibiting many sidelobes distributed at both sides of the Bragg wavelength [129, 138, 139]. The extinction between the Bragg resonance and the first sidelobe is only 5.2dB theoretically, which heavily limits its applications.

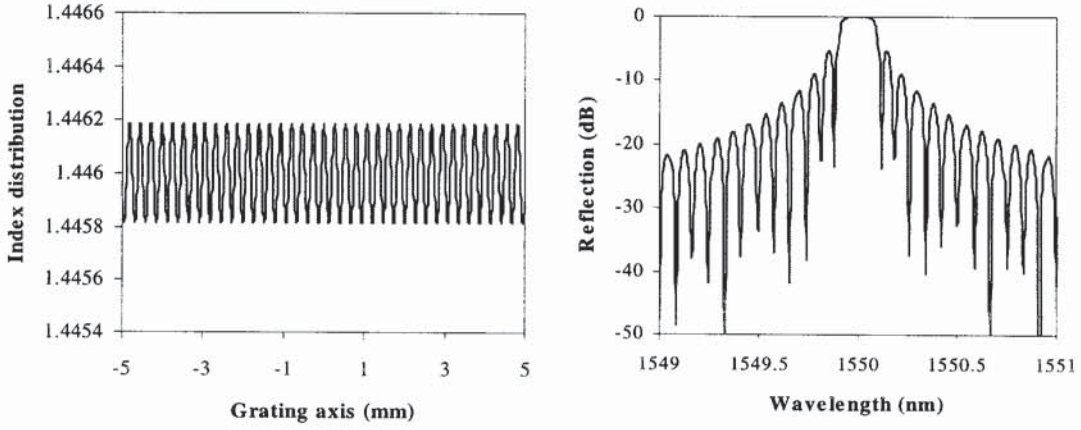

Figure 5.1 Calculated index distribution and reflection spectrum of a 10mm long uniform fibre grating of 20dB-reflectivity: (a) index distribution along the grating length; (b) reflection spectrum exhibiting many sidelobes around the Bragg resonance ($\kappa_0 L=3$)

A comparison between theoretical and experimental results of a 30mm long uniform Bragg grating shows a good agreement as illustrated in Figure 5.2.

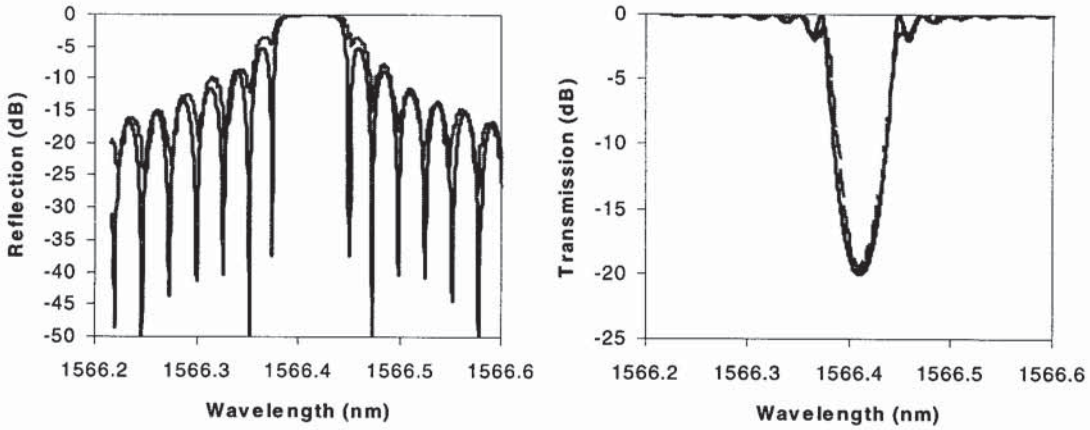

Figure 5.2 A comparison between theoretical and experimental spectra of a 30mm long 20dB-reflectivity uniform Bragg grating showing good agreement: (a) reflection spectrum; (b) transmission spectrum

5.1.2 Gaussian profile apodisation

When a Bragg grating is apodised with a gaussian profile given by

$$Gauss(z,m) = e^{-m\left(\frac{z}{L/2}\right)^2} \tag{5.2}$$

where $-L/2 \le z \le L/2$ indicates the locations of the grating; L is grating length, $m > 0$ indicates the order of the gaussian function, $Gauss(z,m)$ is the normalized apodisation profile. For a 10mm long grating of 20dB-reflectivity apodised with $Gauss(z,6)$, the index distribution is shown in Figure 5.3 (a) and the reflection spectrum is shown in Figure 5.3 (b), exhibiting sidelobe suppression up to 62.84dB, where $\kappa_0 L = 8.36$.

Simulation results also show that regardless the apodisation profile and the resulting sidelobe suppression, the peak reflectance of gratings only depends on the integration of the coupling coefficient with respect to the grating length $\overline{\kappa}L = \int_{-L/2}^{L/2} \kappa(z)dz$, which is in agreement with eqn. (3.62).

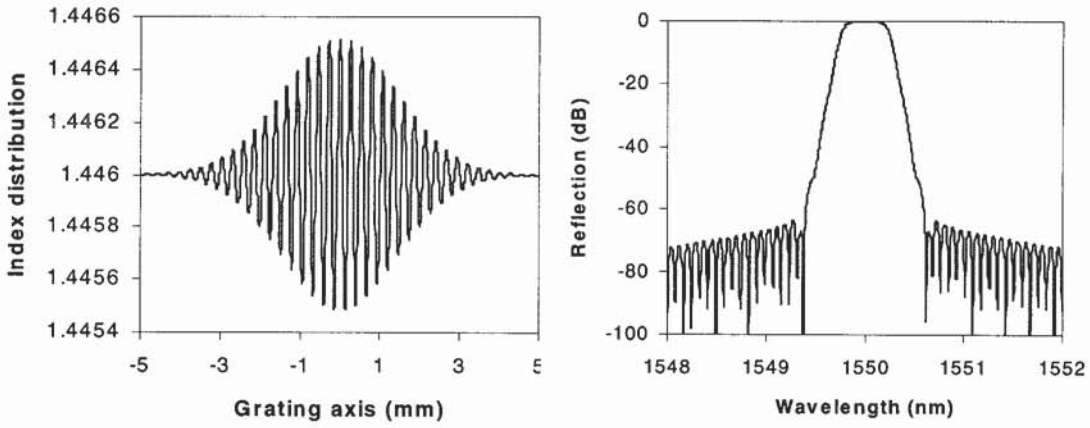

Figure 5.3 Calculated index distribution and reflection spectrum of a 10mm long grating of 20dB-reflectivity apodised with gaussian profile: (a) Gauss(z,6) profiled index distribution along the grating length; (b) reflection spectrum exhibiting 62.84dB sidelobe suppression and 0.454nm line-width, ($\kappa_0 L = 8.28$)

A comparison between theoretical and experimental spectra for a 30mm long grating apodised with *Gauss*(*z*,6) exhibits a good agreement as illustrated in Figure 5.4; results show 30dB sidelobe suppression for a grating of 20dB-reflectivity.

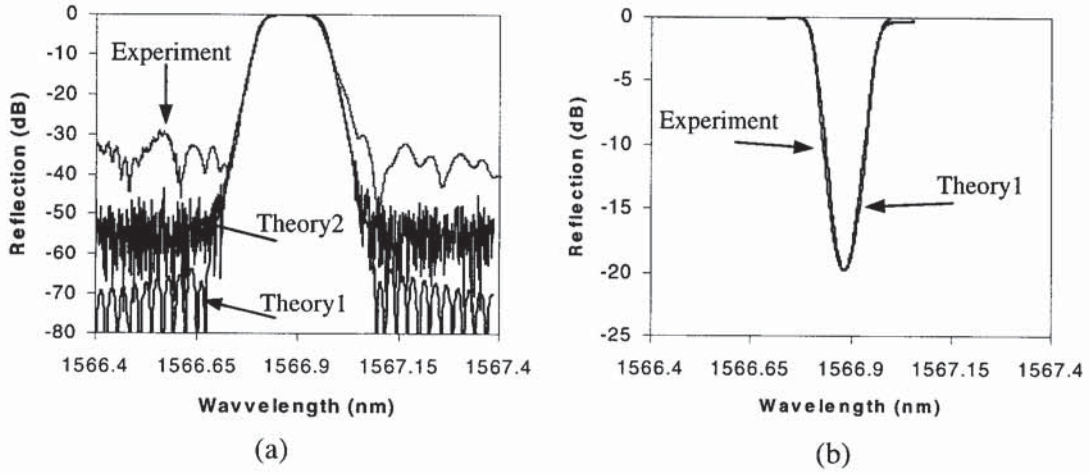

Figure 5.4 A comparison between theoretical and experimental spectrum of 30mm long gratings of 20dB-reflectivity apodised with Gauss(z,6), showing 30dB extinction in experiment, theory1 and theory2 indicate the simulations of the ideal case and the case with 2.5% fluctuation of the scanning velocity: (a) reflection spectrum; (b) transmission spectrum

Note that due to various errors like stitch errors in the phase mask and optical misalignment, it is not possible to obtain sidelobe suppression as high as the simulation results.

5.1.3 Improved gaussian profile apodisation

It should be noted that the best normalized apodisation profile varies gradually from 0 to 1. However, the gaussian function is always truncated: non-zero at both ends of the grating, which limits the sidelobe suppression. In order to overcome this problem, an improved gaussian function is proposed given by

$$ImGauss(z,m) = e^{-m\left(\frac{z}{L/2}\right)^2} \cdot \left[1-\left(\frac{z}{L/2}\right)^4\right] \tag{5.3}$$

where $-L/2 \le z \le L/2$, $ImGauss(z,m)$ is the normalized apodisation profile, $m>0$ indicates the order of the improved gaussian function. Clearly, the gaussian function is forced to zero at both ends of the grating $\kappa(\pm L/2)=0$. For the same line-width and reflectivity compared with the grating illustrated in Figure 5.3 (b), the improved gaussian profile $ImGauss(z,5.739)$ produces 78.19dB sidelobe suppression. This is a 15.36dB improvement in sidelobe suppression compared with the gaussian profile apodisation as shown in Table 5.1 and Figure 5.5.

Table 5.1 A comparison of 10mm long 20dB-reflectivity gratings, showing 15.36dB improvement in sidelobe suppression for apodisation profile $ImGauss(z,5.739)$ compared with $Gauss(z,6)$, ($\kappa_0 L = 8.2775$)

Apodisation profiles	*FWHM* (nm)	Sidelobe suppression (dB)
$Gauss(z,6.000)$	0.454	62.837
$ImGauss(z,5.739)$	0.455	78.192
Comparison	0.001	15.36

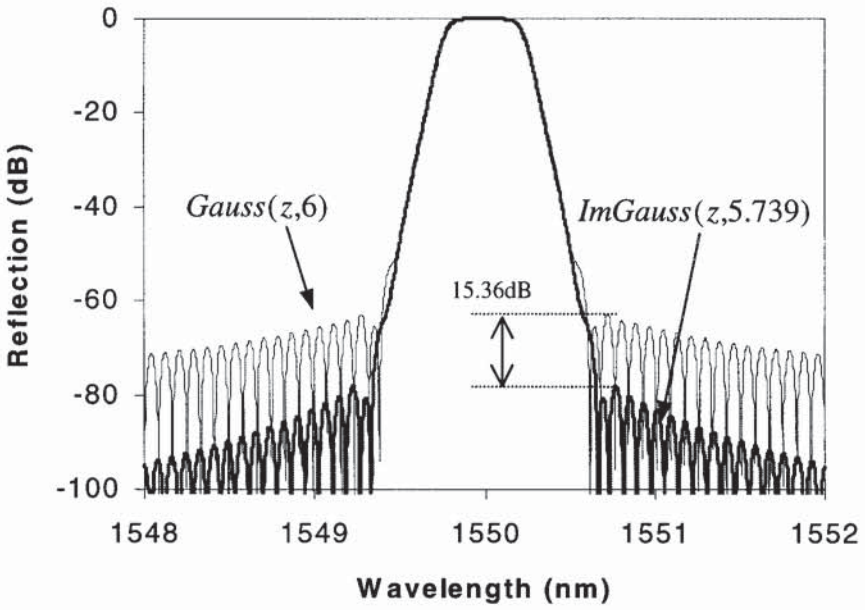

Figure 5.5 A comparison of reflection spectra of 10mm long 20dB-reflectivity gratings apodised with two types of profiles showing 15.36dB improvement in sidelobe suppression for apodisation profile Gauss(z,6) compared with ImGauss(z,5.739), ($\kappa_0 L = 8.28$)

5.1.4 Blackman profile apodisation

The Blackman apodisation profile has been reported to produce the best sidelobe suppression given by [130]

$$Blackman(z) = \left[1.19\cos\left(\frac{\pi z}{L/2}\right) + 0.19\cos\left(\frac{2\pi z}{L/2}\right)\right] / 2.38 \tag{5.4}$$

where $-L/2 \le z \le L/2$, $Blackman(z)$ is the normalized apodisation profile. For a 10mm long 20dB-reflectivity grating, a 58.2dB sidelobe suppression is obtained. This is 1.87dB less compared with $ImGauss(z,4.077)$ apodisation profile as shown in Table 5.2 and Figure 5.6.

Table 5.2 A comparison of 10mm long 20dB-reflectivity gratings, showing 1.87dB improvement in sidelobe suppression and smoother reflection profile for apodisation profile ImGauss(z,4.077) compared with the Blackman(z), ($\kappa_0 L = 7.1239$)

Apodisation profiles	FWHM (nm)	Sidelobe suppression (dB)
Blackman(z)	0.393	58.915
ImGauss(z,4.077)	0.393	60.786
Comparison		1.87

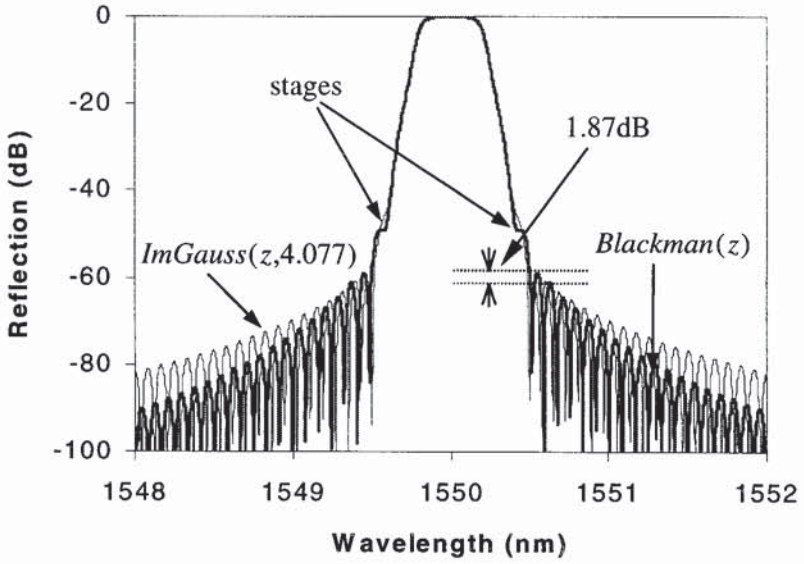

Figure 5.6 A comparison of reflection spectra of 10mm long 20dB-reflectivity gratings apodised with two types of profiles, showing 1.87dB improvement in sidelobe suppression and smoother reflection profile for apodisation profile ImGauss(z,4.077) compared with the Blackman(z), ($\kappa_0 L = 7.124$)

It can be seen that although *ImGauss(z,4.077)* profile produces a 1.87dB improvement in sidelobe suppression compared with the *Blackman(z)* profile, the grating reflection spectrum is smoother as there are two small stages in the *Blackman(z)* profiled grating as shown in Figure 5.6. For 20dB-reflectivity 10mm long gratings, *ImGauss(z,5)* and *ImGauss(z,6)* apodisation profiles result in 66dB and 80dB sidelobe suppression, respectively. It should be noted that increasing the sidelobe suppression widens the grating line-width due to the shortened effective grating length.

5.1.5 *Cosine* profile apodisation

A cosine apodisation profile is given by

$$Fun(z) = \cos(\pi z / L) \tag{5.5}$$

where $-L/2 \le z \le L/2$. As shown in Figure 5.7, only 20dB extinction is obtained theoretically for 10mm long 20dB-reflectivity gratings, but the grating line-width is much narrower compared with the case of the gaussian profile apodisation due to the longer effective grating length. This kind of apodisation profile is normally not adopted experimentally. However, when superimposing two linear gratings with wavelength spacing of a FSR of the grating Fabry-Perot cavity, a cosine profile apodisation is then obtained.

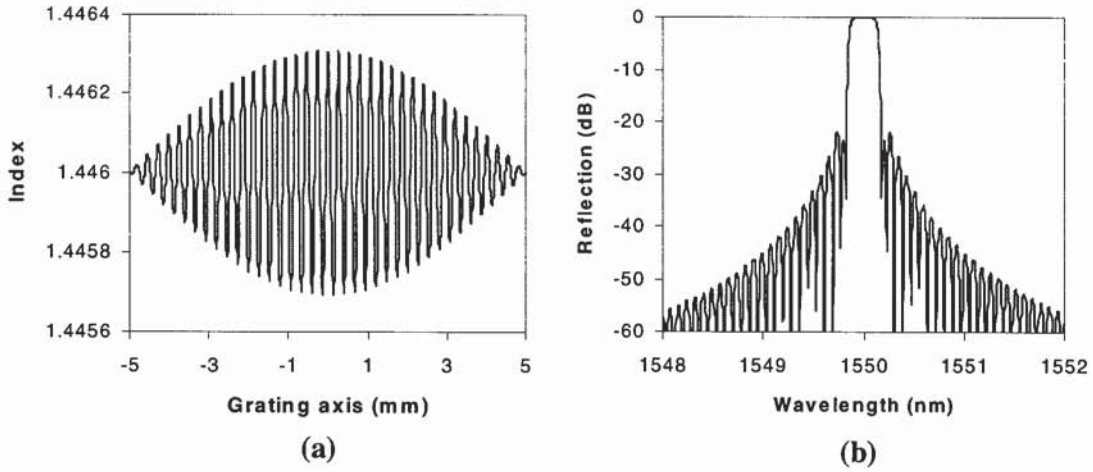

Figure 5.7 Calculated index distribution and reflection spectrum of a 10mm long 21dB-reflectivity grating apodised with cosine profile: (a) cosine profiled index distribution; (b) reflection spectrum, ($\kappa_0 L = 5$)

5.1.6 *Sinc* profile apodisation

As discussed in section 3.3.3, the amplitude reflectance of a weak grating is a Fourier transform of the coupling coefficient, given by eqn. (3.67). This suggests that a *sinc* profiled coupling coefficient will result in a square reflection spectrum. For a *sinc* apodisation profile given by

$$sinc(z,N)=\frac{\sin(2N\pi z/L)}{2N\pi z/L} \tag{5.6}$$

where $-L/2 \le z \le L/2$ indicates the locations of the grating; L is the grating length, $sinc(z,N)$ in the normalized *sinc* profile. For a 50mm long grating apodised with a $sinc(z,10)$ profile, the normalized apodisation profile is shown in Figure 5.8 (a). It should be noted that when eqn. (5.6) gives negative values, the grating fringes have a π phase shift compared with that of positive values. The grating reflection spectrum is illustrated in Figure 5.8 (b), showing a square reflection profile.

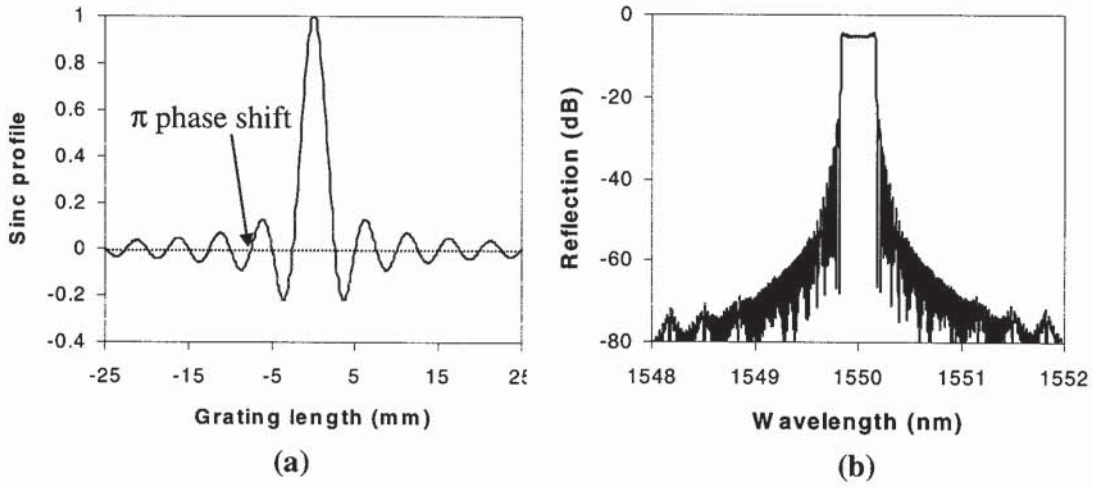

Figure 5.8 Calculated index distribution and reflection spectrum of a 50mm long grating apodised with sinc profile: (a) sinc profiled index distribution $Fun = \mathrm{sinc}(20z/L_0)$*; (b) square shape reflection spectrum*

To summarise, the modelling of grating apodisation with different profiles has been investigated in this section. The gaussian profile is normally used to apodise a grating for more than 60dB extinction in reflection. By forcing the gaussian function to zero at the ends of the grating, an improved gaussian apodisation profile is formed to offer 15.36dB improvement in sidelobe suppression compared with the gaussian apodisation. Simulation results also show that this improved gaussian apodisation produces a smoother reflection profile and improved sidelobe suppression compared with the well-known Balckman profile. In addition, the investigation of a square reflection spectrum is discussed by a *sinc* profile apodisation.

5.2 Linearly Chirped Fibre Bragg Gratings

As mentioned in Chapter 2 and illustrated in Figure 2.3, a chirped Bragg grating with such orientation that the long wavelengths are reflected first, at near end of the grating, while the short wavelengths are reflected at the far end of the grating. Since the short wavelengths travel further within the grating, they encounter a long delay relative to the long wavelengths. These results can be used for dispersion compensation in high-bit-rate transmission in standard fibre systems. This section discusses the modelling of linearly chirped fibre Bragg gratings.

5.2.1 Uniform strength gratings

For a 10mm long linearly chirped grating with $\Delta\lambda$=7.8nm and κL=20, the local Bragg wavelength is given by eqn. (3.94). In the simplest case of a uniform strength linearly chirped grating, the simulation and experimental results are as shown in Figure 5.9, where the chirped Bragg grating was fabricated using the two-beam holographic method.

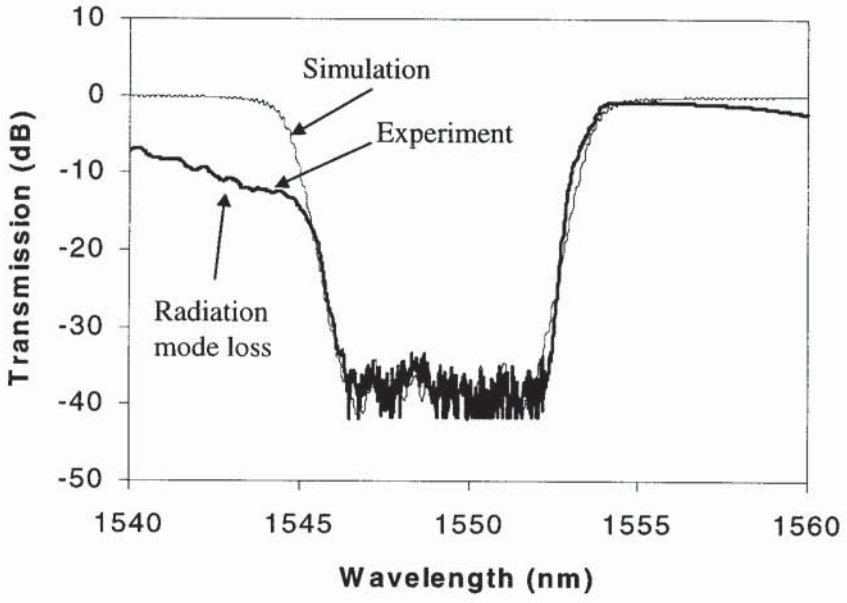

Figure 5.9 A comparison of theoretical and experimental transmission spectra of a 5mm long 7.8nm bandwidth chirped fibre grating centred at wavelength 1549.2nm, (κL=20)

The radiation mode loss at short wavelengths becomes significant for a strong grating, and this effect is not included in the coupled-mode equations in this thesis. The loss band is shifted to an even shorter wavelength with a square transmission spectrum when depressed cladding fibre is used [140].

5.2.2 *Sinc* profile apodisation

As discussed in section 3.3.5, a non-uniform grating can be regarded as a composition of a series of short length uniform sub-gratings. The superimposed sidelobes of all sub-gratings thus produce a continuous reflection background. Apodisation is used to suppress the sidelobes of a uniform grating, and hence is capable of suppressing the background reflection of a chirped grating to achieve a high extinction. In addition, apodisation will also smooth or remove the ripple effect on dispersion.

Figure 5.10 (a) shows the grating profile for a uniform and *sinc*-type apodisation, respectively. The corresponding reflection spectra are shown in Figure 5.10 (b), where $sinc(z,1)$ function is given by eqn. (5.6). Obviously, the background reflection is suppressed and more than 60dB extinction is obtained theoretically.

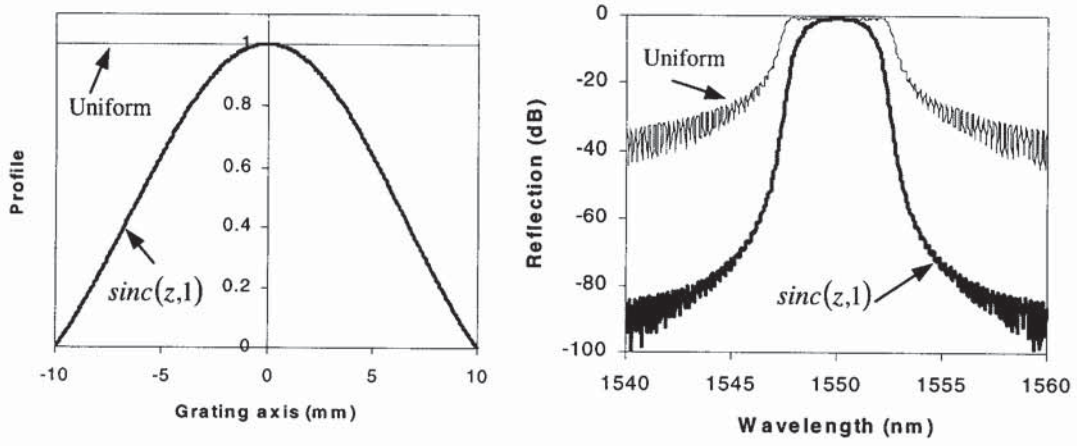

(a) (b)

Figure 5.10 Normalized apodisation profiles and reflection spectra of 20mm long chirped fibre gratings with 5nm bandwidth 20dB-reflectivity: (a) uniform and sinc-type apodisation; (b) reflection spectra showing suppressed background reflection for apodisation

5.2.3 High-order gaussian profile apodisation

The reflection shape of a chirped grating depends on the apodisation profile. For a high-order gaussian apodisation profile given by

$$\kappa(z) = \kappa_0 \exp\left[-6\left(\frac{z}{L/2}\right)^8\right] \tag{5.7}$$

A quasi-square reflection spectrum compared with the $sinc(z,1)$ apodisation profile is obtained theoretically. Figure 5.11 (a) shows two profiles, $sinc(z,1)$ and high-order gaussian profile given by eqn. (5.6) and eqn. (5.7), respectively. The corresponding reflection spectra are illustrated in Figure 5.11 (b).

In order to achieve a square reflection shape or to design a specific reflection profile, it is necessary to find a mathematical method to derive the apodisation profile from the reflection spectrum. An effective method based on inverse-scatting has been described by Feced et al [141], but utilisation lies outside the scope of this thesis.

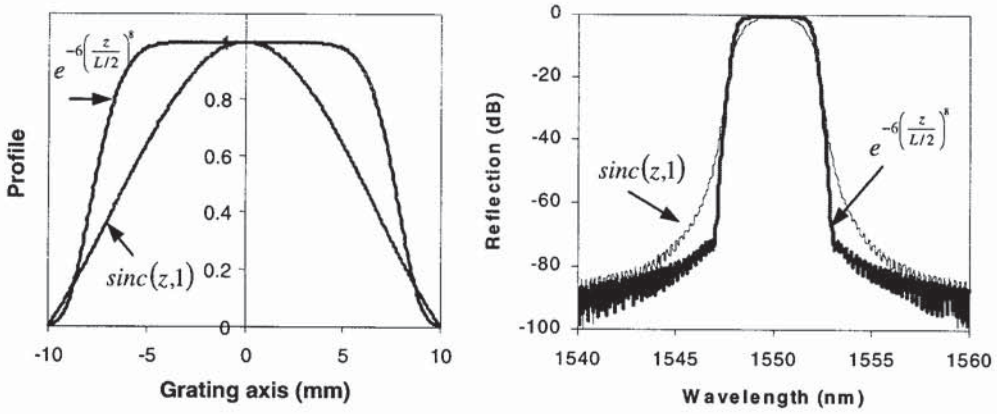

(a) (b)

Figure 5.11 Normalized apodisation profiles and reflection spectra of 10mm long chirped Bragg gratings with 5nm bandwidth 20dB-reflectivity: (a) apodisation profiles; (b) reflection spectra

To summarise, the modelling of a linearly chirped fibre Bragg grating has been discussed. An apodisation profile can be used to suppress the background reflection and a high-order apodisation profile results in a quasi-square shape reflection spectrum.

5.3 Chirped Moiré Bragg Gratings

This section presents the modelling of chirped Moiré Bragg gratings. This kind of grating structure provides grating filters with wide stop-bands, narrow passbands and high-rejection levels.

5.3.1 Introduction

Currently, there is a high level of interest in the fabrication of filters for providing wavelength selectivity and noise filtering in WDM systems [142, 143], quasi-distributed point sensing systems [144], and multiple wavelengths fibre lasers [87]. In-fibre filters, using properly designed Bragg gratings have the potential to provide wide stop-bands, narrow passbands and high-rejection levels and have the further advantages of fibre-compatibility and potentially low-cost.

A grating resonator consists of two closely spaced gratings separated by a phase shift, resulting in the formation of one or more narrow passband in the grating spectrum. The Moiré technique is one of many techniques used to fabricate Bragg grating resonators. The fabrication of narrowband transmission filters using this technique was originally described by Reid *et al* [145], where a modified holographic technique was used to form two surface relief gratings, each having a slightly different period, in the fibre core. This 'double exposure' formed an interference pattern in the fibre, introducing phase shifts at various points along the length of the fibre. The first report of the extension of the technique to accommodate chirped grating were used to fabricate high finesse transmission filters and these filters were then concatenated to other standard broadband reflection gratings to obtain a narrow passband within a very wide stop-band.

5.3.2 Moiré Theory

As described above, chirped Moiré gratings are fabricated by superimposing two linearly chirped gratings. The two linearly chirped gratings have the same chirps and lengths but a slightly different central wavelength. The index distribution along the grating axis is thus

expressed as

$$n = n_0 + \frac{\Delta n_0}{2}\cos\left[\frac{2\pi}{\Lambda_1(z)}z\right] + \frac{\Delta n_0}{2}\cos\left[\frac{2\pi}{\Lambda_2(z)}z + \varphi\right] \tag{5.8}$$

where φ is the phase of the second grating with respect to the first. $\Lambda_1(z)$ and $\Lambda_2(z)$ are the periods of two gratings, respectively, $\frac{\Lambda_1(z)-\Lambda_2(z)}{[\Lambda_1(z)+\Lambda_2(z)]/2} << 1$, $-L/2 \le z \le L/2$, and L is the grating length. The Bragg resonance for the two linearly chirped gratings are given by

$$\begin{cases} \lambda_1(z) = 2n_{eff}\Lambda_1(z) = \lambda_{01} + \dfrac{\Delta\lambda}{L}z \\ \lambda_2(z) = 2n_{eff}\Lambda_2(z) = \lambda_{02} + \dfrac{\Delta\lambda}{L}z \end{cases} \tag{5.9}$$

where $\Delta\lambda$ is the bandwidth of the two chirped gratings. Using eqn. (3.45), the detunings for the two chirped gratings are given by

$$\begin{cases} \delta_1(z) = \beta_{01}^{co} - \pi/\Lambda_1(z) \\ \delta_2(z) = \beta_{01}^{co} - \pi/\Lambda_2(z) \end{cases} \tag{5.10}$$

where δ_1 and δ_2 are the detuning of the two gratings. Rearranging eqn. (5.8) gives

$$n = n_0 + \Delta n(z)\cos\left[\frac{2\pi}{\overline{\Lambda}(z)}z + \varphi/2\right] \tag{5.11}$$

where $\overline{\Lambda}(z)$ and $\Delta n(z)$ are the average grating period and index amplitude, respectively, given by

$$\overline{\Lambda}(z) = \frac{2\Lambda_2(z)\Lambda_1(z)}{\Lambda_2(z)+\Lambda_1(z)} \tag{5.12}$$

and

$$\Delta n(z) = \Delta n_0 \cos\left[\frac{2\pi}{\Lambda_{beat}(z)} z - \varphi/2\right] \tag{5.13}$$

where the period of the beat frequency $\Lambda_{beat}(z)$, or the Moiré period is given by

$$\Lambda_{beat}(z) = \frac{2\Lambda_2(z)\Lambda_1(z)}{|\Lambda_2(z) - \Lambda_1(z)|} \approx \frac{1}{n_{eff}} \frac{\lambda_0^2}{\delta\lambda} \tag{5.14}$$

where the Bragg condition has been used and $\lambda_0 = (\lambda_{01} + \lambda_{02})/2$ is the average central wavelength of the two chirped gratings while $\delta\lambda = |\lambda_{01} - \lambda_{02}|$ is their spacing.

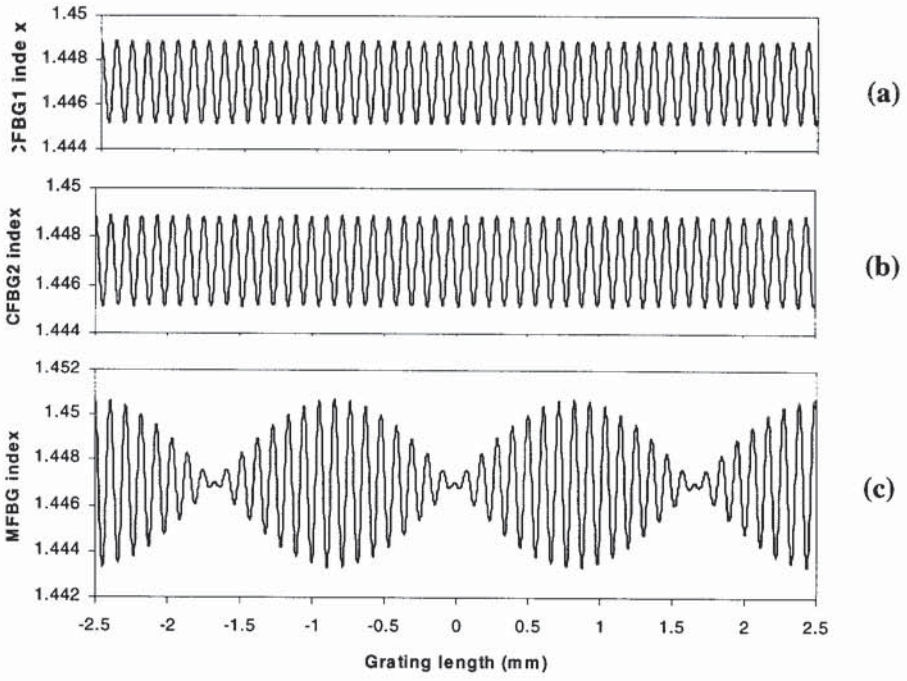

Figure 5.12 The index distribution illustrating a 5mm long chirped Moiré grating: (a) and (b) two chirped gratings centred at wavelengths 1550nm and 1550.5nm with 5nm bandwidth; (c) the index distribution by superimposing the two chirped gratings showing Moiré fringes, ($\kappa_1 L = \kappa_2 L = 7.5$)

The respective fringe patterns of two chirped gratings each with 5nm chirp, 5mm long, and coupling strength $\kappa_1 L = \kappa_2 L = 7.5$, centred at $\lambda_{01} = 1550\,\text{nm}$ and $\lambda_{01} = 1550.5\,\text{nm}$, respectively, are shown in Figure 5.12 (a) and (b). The 5nm chirps in the grating fringes

are indistinguishable to eye. However, superimposing the two chirped gratings produces the Moiré fringes as shown in Figure 5.12 (c). Note that the grating period (~0.5μm) is magnified here by a factor of 200.

Substituting eqn. (5.13) into eqn. (3.44) and using eqn. (5.9), the slow varying coupling coefficient is obtained as

$$\kappa(z) = \kappa_0 \cos\left[\frac{2\pi n_{ef} \cdot \delta\lambda}{(\lambda_0 + \Delta\lambda z / L)^2} z - \frac{\varphi}{2}\right] \tag{5.15}$$

where $\kappa_0 = \frac{\pi \Delta n_0 C_{01}^{co}}{\lambda_0}$, $\lambda_0 = (\lambda_{01} + \lambda_{02})/2$, $\delta\lambda = |\lambda_{01} - \lambda_{02}|$.

5.3.3 Simulation spectra

For a 5mm long linearly chirped Moiré grating with $\Delta\lambda$=5nm, λ_{01}=1550nm, λ_{02}=1550.5nm and $\kappa_1 L = \kappa_2 L$=7.5, the calculated spectrum showing three transmissions in the stop-band is shown in Figure 5.13.

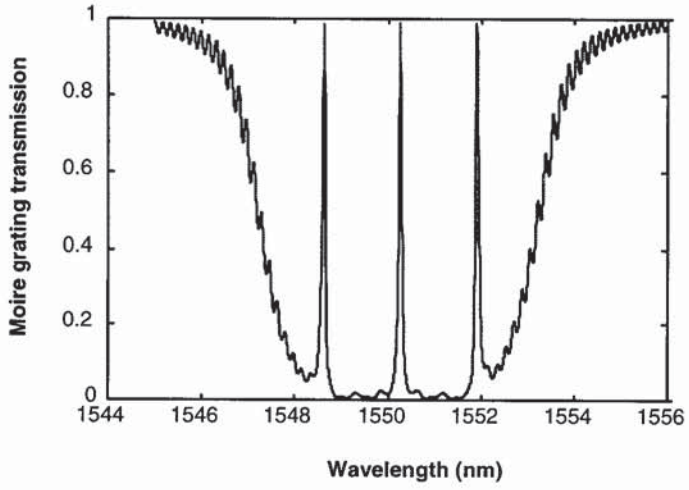

Figure 5.13 Calculated transmission spectrum of a 10mm long 5nm bandwidth chirped Moiré grating centred at wavelength 1550.25nm showing three transmission peaks for $\delta\lambda$ =0.5nm, ($\kappa_1 L = \kappa_2 L$=7.5)

Simulation result shows that the number of the transmission peaks depends on the spacing ($\delta\lambda$) of the central wavelengths of the two chirped gratings. An experiment was carried out by overwriting two identical chirped gratings with one slightly shifted (δd mm) along the grating axis with respect to the other. The schematic diagram of the structure is shown in Figure 5.14 (a). Sub-grating G2 consists of the Moiré structure and the spacing of the two central wavelengths is thus given by

$$\delta\lambda = \frac{\Delta\lambda \cdot \delta d}{L} \tag{5.16}$$

Changing $\delta\lambda$ by adjusting the shift δd , the desirable number of transmission peaks is realised within the chirped grating stop-band.

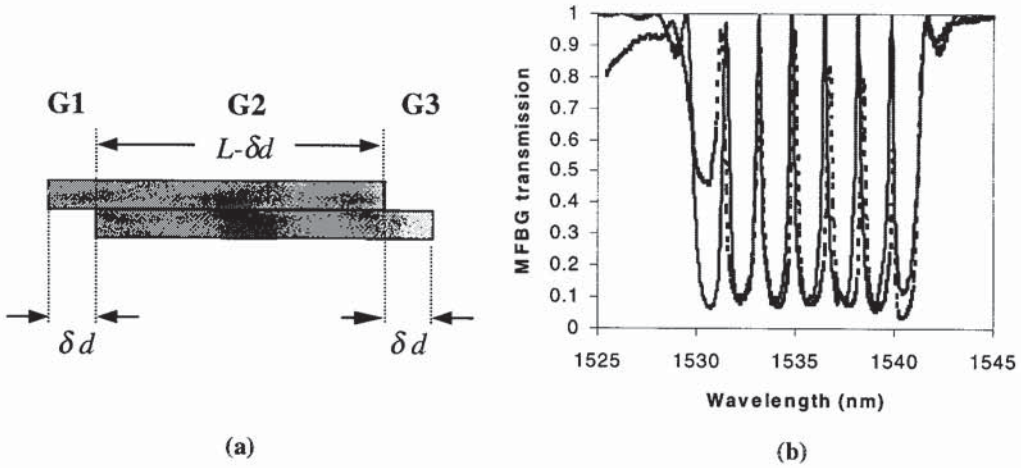

Figure 5.14 (a) Schematic diagram of a 5mm long 11nm bandwidth chirped Moiré fibre grating centred at 1535.5nm fabricated by superimposing two chirped gratings; (b) A comparison of theoretical and experimental transmission spectra showing 6 transmission peaks, dot line: experimental spectrum; solid line: calculated result (δd =500μm)

As discussed in section 4.1, the two-beam holographic fabrication technique, chirped Moiré gratings were fabricated by superimposing two 5mm long identical chirped gratings with $\Delta\lambda$=11nm but one having 500μm shift with respect to the other. The experimental spectrum (dot line) and calculated result (solid line) are shown in Figure 5.14 (b). Note that the two δd long non-overlapped sub-gratings G1 and G3 as shown in Figure 5.14 (a), are considered in simulation, corresponding to the small ripples at the both edges of the grating stop-band as shown in Figure 5.14 (b).

5.3.4 Other characteristics

It is clear that when $\delta\lambda = 0$, eqn. (5.15) reduces to $\kappa(z) = \kappa_0$, as for a uniform strength chirped grating. However, when $\Delta\lambda = 0$, $\varphi = 0$, and the wavelength spacing is the FSR of the grating Fabry-Perot cavity given by

$$\delta\lambda = \frac{\lambda_0^{\,2}}{2n_{eff}L} \tag{5.17}$$

where L is the grating length. Substituting eqn. (5.17) into eqn. (5.15) yields eqn. (5.5) as $\kappa(z) = \kappa_0 \cos(\pi z / L)$. This is a *cosine* profile apodised grating as discussed in section 5.1.5.

One useful result obtained from the simulation is that the number of transmission peaks depends on the wavelength spacing ($\delta\lambda$) in modulus of the FSR of the grating Fabry-Perot cavity given by

$$N = \frac{\delta\lambda}{\lambda_0^{\,2}/(2n_{eff}L)} \approx \frac{2L}{\Lambda_{beat}} \tag{5.18}$$

where Λ_{beat} is the Moiré period given by eqn. (5.14). Clearly, the number of transmission peaks is twice the Moiré periodicity or the number of nodes. For two 5mm long chirped gratings with the central wavelengths separated by 0.5nm and 1.1nm as illustrated by Figure 5.13 and Figure 5.14, respectively, eqn (5.18) yields N=3 and N=6, respectively. This is in good agreement with the theoretical and experimental results, where $n_{eff} = 1.446$ is used.

To summarise, the fabrication and modelling of chirped Moiré fibre Bragg gratings as multiple transmission filters has been investigated. The simulation spectrum and the experimental result are in good agreement. The number of the transmission peaks is given by the separation of the two chirped grating central wavelengths in modulus of the FSR of the grating Fabry-Perot cavity, which is equivalent to the number of the Moiré nodes.

5.4 Sampled Fibre Bragg Gratings

This section presents the modelling of sampled fibre Bragg gratings as multiple reflection filters. The calculated spectrum and the wavelength spacing are discussed for rectangular and composite *cosine* sampling profiles. The cladding mode coupling due to the long period sampling profile was observed experimentally.

5.4.1 Rectangular sampling profile

When a uniform Bragg grating is modulated or sampled with a longer periodical profile compared with the Bragg period, a sampled Bragg grating results. The main Bragg coupling in this case will be coupled to a series of side-peaks located at the both sides of the Bragg resonance. The principle is similar to the amplitude modulation of radio wave, where a series of harmonics frequencies around carrier frequency is produced.

For a rectangular sampling profile introduced experimentally by using a shutter to block the UV beam periodically, the configuration of the grating structure is illustrated in Figure 5.15 (a), (b) and (c), showing a long-period periodic modulation or sampling profile superimposed in the Bragg gratings. In general, the sampling profile is expressed in the form [72]

$$profile(z) = \sum_{-\infty}^{\infty} a_m e^{jm\frac{2\pi}{\Lambda}z} \tag{5.19}$$

For a rectangular sampling profile, eqn. (5.19) becomes

$$profile_{rect}(z) = \sum_{m=-\infty}^{\infty} \frac{1}{j2m\pi}\left(1 - e^{-jm\frac{2\pi}{1+q}}\right)e^{j\frac{2m\pi}{L/M}z} \tag{5.20}$$

where M=1, 2, 3, ..., refers to the number of modulation periods along the grating length (L) while q is the ratio of the exposed to unexposed lengths in one such period, i.e. the duty cycle. Thus, q=1 indicates 50% duty cycle. The index distribution of the grating is given by

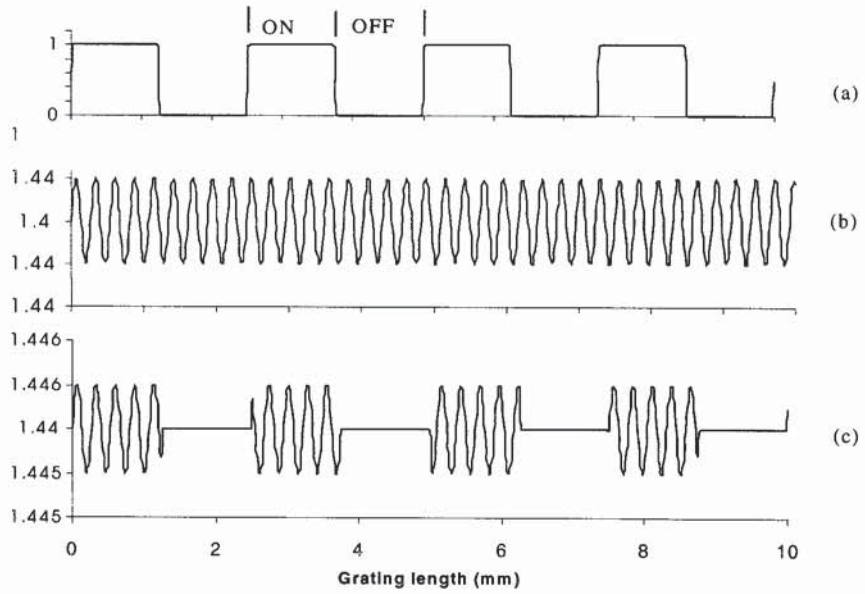

Figure 5.15 The index distribution for illustrating the configuration of a 10mm long sampled fibre grating: (a) rectangular sampling profile; (b) index distribution of a uniform Bragg grating; (c) index distribution of the sampled grating

$$n(z) = n_0 + \Delta n_0 \left\{ \frac{1}{2} + \sum_{m=0}^{\infty} \frac{2}{(2m+1)\pi} \sin\left[\frac{2\pi(2m+1)}{L/M} z \right] \right\} \cos\left(\frac{2\pi}{\Lambda_0} z \right) \tag{5.21}$$

where Λ_0 is the period of the uniform grating. The normalized rectangular sampling profile is shown in Figure 5.15 (a). With this modulation, the uniform grating as shown in Figure 5.15 (b) becomes the sampled grating structure as illustrated by Figure 5.15(c). L/M is the sample length or the sub-grating length.

Substituting eqn. (5.21) into eqn.(3.9) and using the phase matching condition, it is clear that each term on the RHS of eqn. (5.21) corresponds to one sub-coupled-mode equation and has one resonance condition. Then, a series of grating periods is given by

$$\begin{cases} \dfrac{1}{\Lambda} = \dfrac{1}{\Lambda_0} \\ \dfrac{1}{\Lambda} = \dfrac{1}{\Lambda_0} \pm \dfrac{2m+1}{L/M} \end{cases} \tag{5.22}$$

where m=0, 1, 2, 3,... is the order of the resonance. Using eqn. (5.22) and the Bragg

resonance $\lambda_0 = 2n_{eff}\Lambda$ yields

$$\begin{cases} \lambda = \lambda_0 \\ \lambda \approx \lambda_0 \mp (2m+1)\Delta\lambda \end{cases} \tag{5.23}$$

with

$$\Delta\lambda = \frac{{\lambda_0}^2}{2n_{eff}L/M} \tag{5.24}$$

where the approximation $\frac{1}{1 \pm (2m+1)M\Lambda/L} \approx 1 \mp (2m+1)M\Lambda/L$ has been used as $(2m+1)M\Lambda/L << 1$. $\Delta\lambda$ is the FSR of one sample length (L/M) Fabry-Perot cavity. For a 10mm long grating at 1550nm wavelength sampled with M=10 periods (50% duty cycle), eqn. (5.24) yields $\Delta\lambda = 0.83\,\text{nm}$. The wavelengths for the coupling of different orders are thus λ_0, $\lambda_{\pm 1} = \lambda_0 \pm \Delta\lambda\,\text{nm}$, $\lambda_{\pm 2} = \lambda_0 \pm 3\Delta\lambda$ ....

If the coupling between different orders is neglected, the coefficient of each term on the RHS of eqn. (5.21) corresponds the coupling strength of the respective orders as

$$\begin{cases} (\kappa L)_0 = \frac{1}{2}\frac{C_{01}^{co}\pi\Delta nL}{\lambda} \\ (\kappa L)_{\pm m} = \frac{1}{(2m+1)\pi}\frac{C_{01}^{co}\pi\Delta nL}{\lambda} \end{cases} \tag{5.25}$$

where m=0, 1,2, ..., and the overlap factor $C_{01}^{co} \approx 0.8$.

Taking the sampling profile as an apodisation profile, the simulation programme for grating apodisation is suitable for the modelling of sampled Bragg gratings and the calculated spectrum is shown in Figure 5.16.

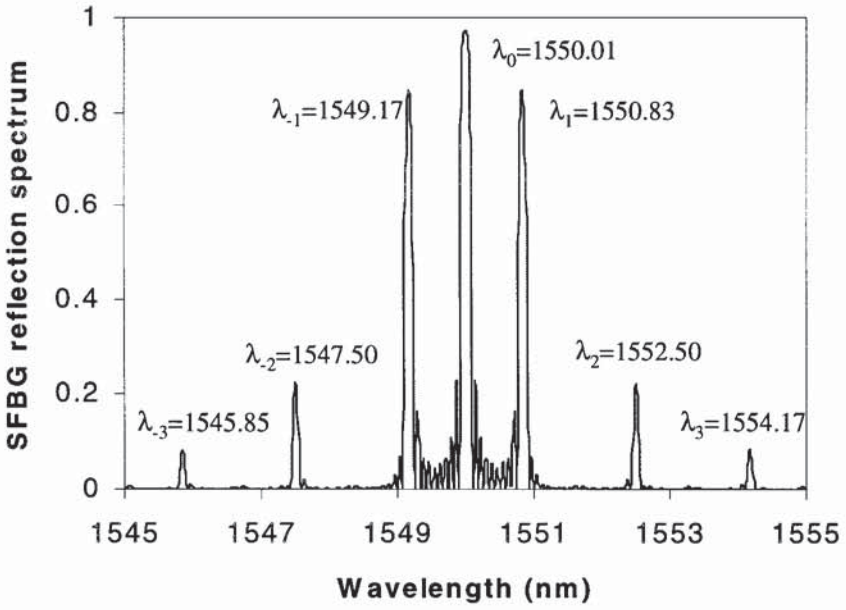

Figure 5.16 Calculated reflection spectrum of a 10mm long sampled Bragg grating with 10 samples, ($\kappa L = 5$, 50% duty cycle)

5.4.2 Composite cosine sampling profile

As shown in Figure 5.16, a higher-order coupling has a relatively weaker reflectivity compared with a lower-order. In order to obtain the same reflectivity and wavelength spacing for all predictable reflection peaks, the normalized sampling profile is designed as

$$Fun(z,M,N) = \frac{1}{N+0.5}\left[\frac{1}{2} + \sum_{m=1}^{N} \cos\left(\frac{2m\pi}{L/M} z\right)\right] \tag{5.26}$$

where $0 \le Fun(z,M,N) \le 1$, $Fun(z,M,N)$ indicates the normalized sampling profile, Λ and L are the grating period and length, respectively. Simulation shows that there are $2N+1$ reflection peaks with equivalent reflectivities and a constant wavelength spacing, $\Delta\lambda = \frac{\lambda_0^{\,2}}{2n_{eff}L/M}$, the FSR of L/M length Fabry-Perot cavity. For a 10mm long grating profiled with $Fun(z,2,2)$, the normalized sampling profile, the index fringes of the uniform and sampled gratings are as shown in Figure 5.17 (a), (b), and (c).

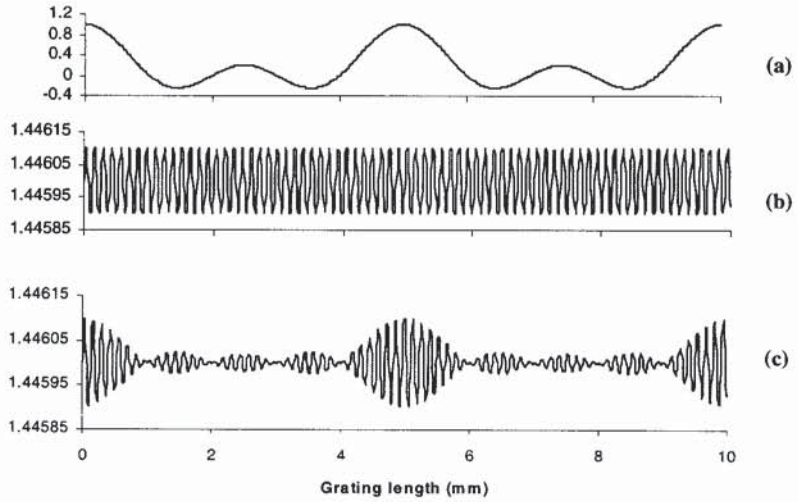

Figure 5.17 The index distribution for illustrating a composite cosine profile sampled fibre grating: (a) composite cosine sampling profile Fun(z,2,2); (b) index fringes of a uniform grating; (c) the index distribution of the sampled grating

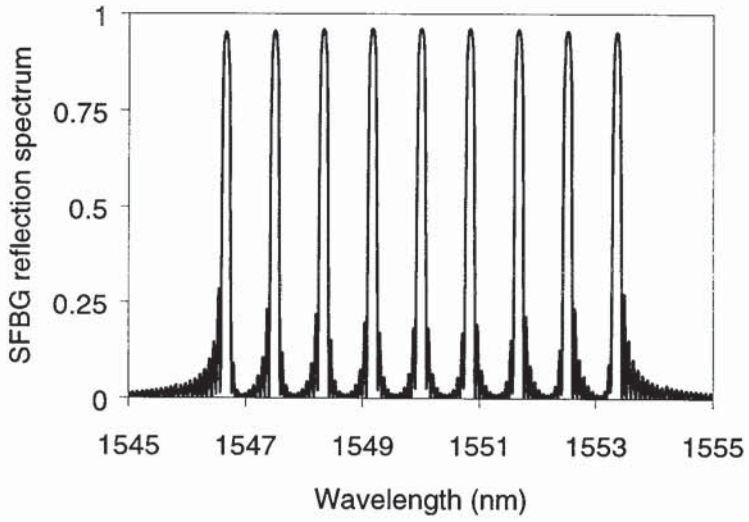

Figure 5.18 Calculated reflection spectrum of a 10mm long sampled fibre grating with a composite cosine sampling profile Fun(z,10,4), showing a equivalent reflectivity (95.7%) and a constant wavelength spacing (0.84nm), ($\kappa L = 20$)

For a 10mm long grating with $\kappa L = 20$ profiled with *Fun*(*z*,10,4), the calculated reflection spectrum is shown in Figure 5.18, showing nine reflection peaks with equivalent reflectivity (95.7%) and a constant wavelength spacing ($\Delta\lambda = 0.84$ nm).

5.4.3 Cladding mode coupling

One interesting observation in sampled gratings is the coupling of cladding modes as shown in Figure 5.19. This is due to the period of the sampling profile is around hundreds micrometer. Actually, it is a typical point-by-point writing method in fabricating a long-period fibre grating using a shutter blocking the UV beam. The fabrication and modelling of long-period fibre gratings will be discussed in next chapter.

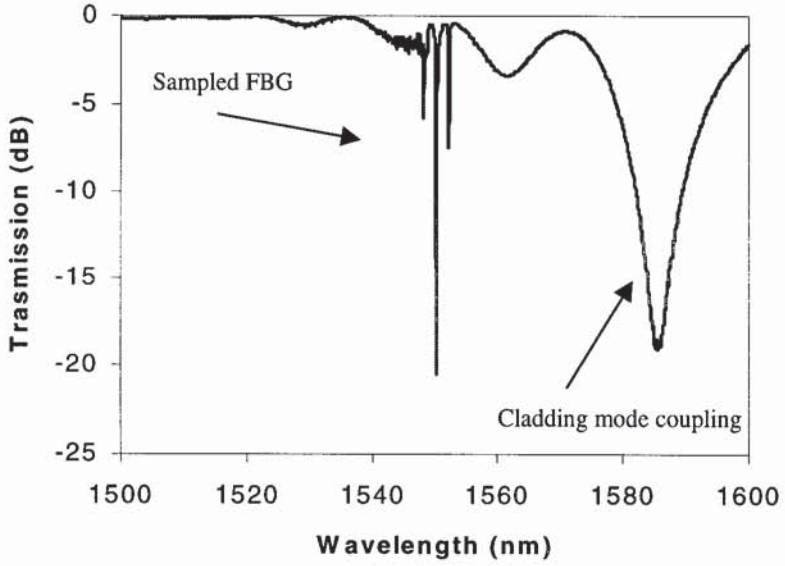

Figure 5.19 Experimental transmission spectrum of a 50mm long sampled fibre Bragg grating with rectangular sampling profile and 100 samples, exhibiting the coupling of cladding modes

To summarise, multiple reflection filters based on the structure of sampled fibre Bragg gratings have been discussed in this section. The calculated reflection spectrum shows multiple reflection peaks and the wavelength spacing depends on the FSR of one sample length Fabry-Perot cavity. When a composite *cosine* sampling profile is applied to a uniform Bragg grating, multiple peak reflection filters with equivalent reflectivities and constant wavelength spacing have been obtained theoretically. In addition, the dual-characteristics of the Bragg and long-period gratings have been observed experimentally in the sampled fibre Bragg gratings.

5.5 Phase-Shifted Fibre Bragg Gratings

The fabrication technique of phase-shifted fibre Bragg gratings has been discussed in section 4.2.5. This section is designed to present a theoretical and experimental investigation of a phase-shifted fibre Bragg grating and its application as DFB fibre lasers.

5.5.1 Introduction

In addition to the Moiré technique and sampled gratings, there are a number of other methods for fabricating multi-passband devices. These include the introduction of a phase shift into the grating structure. Alferness *et al* [146] originally demonstrated that the introduction of a quarter-wave shift at the centre of a waveguide opens up a transmission peak within its stop-band. There have been many reports on different techniques to introduce phase shifts into a grating, which has been discussed previously. For the requirement of broader transmission, it can be realised by introducing multiple phase shifts into a grating [147,148]. Due to the very narrow line-width and easy tunability by applied strain or temperature, phase-shifted fibre gratings have many applications in optical communications and fibre sensors [68, 149, 150].

As presented in section 3.3.5, the grating matrix expressed in the form of eqn. (3.90) results in an analytical solution with a clear physical picture named as complex Fabry-Perot cavity. This expression extends to the case of the gratings with two or three phase shifts, composed by possible Fabry-Perot sub-cavities. The conventional modelling technique utilising matrix transforms is a numerical calculation without any analytical expression [151].

5.5.2 Theory

Consider that a phase shift (ϕ) is located at $z = L_1$ along the grating length, the grating is thus divided into two uniform sub-gratings (G_1 and G_2) with length L_1 and L_2. The

matrix of the entire grating structure given by eqn. (3.96) reduces to [148]

$$M = \begin{bmatrix} 1/t_2^* & -(r_2/t_2)^* \\ -r_2/t_2 & 1/t_2 \end{bmatrix} \begin{bmatrix} e^{j\phi/2} & 0 \\ 0 & e^{-j\phi/2} \end{bmatrix} \begin{bmatrix} 1/t_1^* & -(r_1/t_1)^* \\ -r_1/t_1 & 1/t_1 \end{bmatrix} \tag{5.27}$$

where t_i and r_i (i=1, 2) are the amplitude transmittance and reflectance of the two sub-gratings (G_1 and G_2) given by eqn. (3.91), the three matrixes on the RHS of eqn. (5.27) indicate the matrixes of two sub-gratings and the phase shift between of them, respectively. The phase shift ϕ is given with respect to the grating period: π phase shift means missing a half of the grating period. Simplifying eqn. (5.27) and using eqn. (3.97), the transmittance and reflectance of a phase-shifted Bragg grating are obtained as (see Appendix A.3)

$$\begin{cases} t = \dfrac{e^{j\phi/2} t_1 t_2}{1 - e^{j\phi} r_1 r_2} \\ r = \dfrac{r_1 + e^{j\phi} r_2 (t_1/t_1^*)}{1 - e^{j\phi} r_1 r_2} e^{-j\phi/2} \end{cases} \tag{5.28}$$

where $|r_i|^2 + |t_i|^2 = 1$ (i=1, 2) and the relationship $(r_i/t_i)^* = -r_i/t_i$ for uniform gratings has been used. Eqn. (5.28) is similar to the expression for a Fabry-Perot resonator that consists of two mirrors with complex reflectance (r_1 and r_2) and complex transmittance (t_1 and t_2). Rewriting the transmittance in eqn. (5.28) yields

$$t = \frac{e^{j\left[\phi/2 + \arctan\left(\frac{\delta_0}{S}\tanh(\kappa_0 L_1) + \frac{\delta_0}{S}\tanh(\kappa_0 L_2)\right)\right]} |t_1||t_2|}{1 + e^{j\left[\phi + \arctan\left(\frac{\delta_0}{S}\tanh(\kappa_0 L_1) + \frac{\delta_0}{S}\tanh(\kappa_0 L_2)\right)\right]} |r_1||r_2|} \tag{5.29}$$

where κ_0 is the grating coupling coefficient. In the vicinity of Bragg resonance ($\delta_0 \approx 0$), eqn. (5.29) reduces to

$$|t|^2 = \left| \frac{\frac{1}{\cosh(\kappa_0 L_1)} \frac{1}{\cosh(\kappa_0 L_1)}}{1 + e^{j\left(\phi - \frac{4\pi n_{eff} d}{\lambda_0^2}\Delta\lambda\right)} \tanh(\kappa_0 L_1)\tanh(\kappa_0 L_2)} \right|^2 \tag{5.30}$$

with

$$d = \frac{\tanh(\kappa_0 L_1)}{\kappa_0 L_1}\frac{L_1}{2} + \frac{\tanh(\kappa_0 L_2)}{\kappa_0 L_2}\frac{L_2}{2} \tag{5.31}$$

where the approximation $\arctan(x) \approx x$ has been used for small values of the variable x, and d is the average cavity length. Eqn. (5.30) is equivalent to a conventional Fabry-Perot with cavity length d and two mirrors with amplitude reflectance $\tanh(\kappa_0 L_1)$ and $\tanh(\kappa_0 L_2)$, respectively. Clearly, it suggests that the grating with coupling strength $\kappa_0 L$ may be treated as a mirror with the power reflectivity R_0 and the average reflection depth D_0 in the vicinity of the Bragg resonance and given by

$$\begin{cases} R_0 = \tanh^2(\kappa_0 L) \\ D_0 = \dfrac{\tanh(\kappa_0 L)}{\kappa_0 L}\dfrac{L}{2} \end{cases} \tag{5.32}$$

where L is grating length. Eqn. (5.32) is useful for estimating the average reflection depth in a Bragg grating.

For two special cases, very weak ($\kappa_0 L \to 0$) and very strong gratings ($\kappa_0 L >> 1$), eqn. (5.32) yields

$$D_0\big|_{\kappa_0 L \to 0} = \frac{L}{2} \tag{5.33}$$

and

$$D_0\big|_{\kappa_0 L >> 1} = \frac{L}{2} \cdot \frac{1}{\kappa_0 L} \tag{5.34}$$

Clearly that for strong gratings, this average reflection depth decreases rapidly, which has been discussed in section 3.3.4 and graphically illustrated in Figure 3.3.

In order to describe the locations of the phase shift, define q as

$$q = z / L \tag{5.35}$$

where $-L/2 \le z \le L/2$, q indicates the location of the phase shift. For a phase with a gap d_{gap} in a grating, one more matrix given by eqn. (3.99) needs to be included in eqn. (5.27) and the result is simply replace "ϕ" wherever it appears in eqn. (5.28) by "$\phi + 4\pi n_{eff} d_{gap}\left(\frac{1}{\lambda} - \frac{1}{\lambda_0}\right)$".

For a multiple phase-shifted grating, the matrix for entire grating structure is given in the form of eqn. (5.27) but with more terms for phase shifts and sub-gratings. For $N-1$ phase shifts, the grating is divided into N sub-gratings. The transmittance of the grating with two and three phase shifts are given by a composite Fabry-Perot resonators as (see Appendix A.3)

$$t\big|_{\phi_1,\phi_2} = \frac{e^{j(\phi_1+\phi_2)/2} t_1 t_2 t_3}{1 - e^{j\phi_1} r_1 r_2 - e^{j\phi_2} r_2 r_3 - e^{j[\phi_1+\phi_2+2*\arg(t2)]} r_1 r_3} \tag{5.36}$$

and

$$t\big|_{\phi_1,\phi_2,\phi_3} = \frac{e^{j(\phi_1+\phi_2+\phi_3)/2} t_1 t_2 t_3 t_4}{\left[\begin{array}{c} 1 - r_1 r_2 e^{j\phi_1} - r_2 r_3 e^{j\phi_2} - r_3 r_4 e^{j\phi_3} - r_1 r_3 e^{j[\phi_2+\phi_1+2\arg(t2)]} - r_2 r_4 e^{j[\phi_2+\phi_3+2\arg(t3)]} \\ - r_1 r_4 e^{j[\phi_1+\phi_2+\phi_3+2\arg(t2)+2\arg(t3)]} + \left(-e^{j\phi_1} r_1 r_2\right)\left(-e^{j\phi_3} r_3 r_4\right) \end{array}\right]} \tag{5.37}$$

where r_i and t_i (i=1, 2, 3,4) describe L_i length sub-gratings G_i. Each term except the first in the denominators of eqn (5.36) and eqn. (5.37) represents a round trip resonance in each Fabry-Perot sub-resonator, consisting of the two sub-gratings at both sides of one phase shift. The last term in the denominator of eqn. (5.37) is the resonance between two

Fabry-Perot sub-cavities. The term $2\arg(t_i)$ is the phase shift of a round trip of light through the sub-grating G_i.

5.5.3 Simulation spectra

For 10mm long gratings with κL=3 and π phase shift in the centre of the grating length, the simulation shows that the line-width of the transmission and stop bandwidth are 0.017nm and 0.28nm, respectively. The theoretical transmission spectra for different coupling strengths are shown in Figure 5.20 (a), showing a centrally located transmission peak.

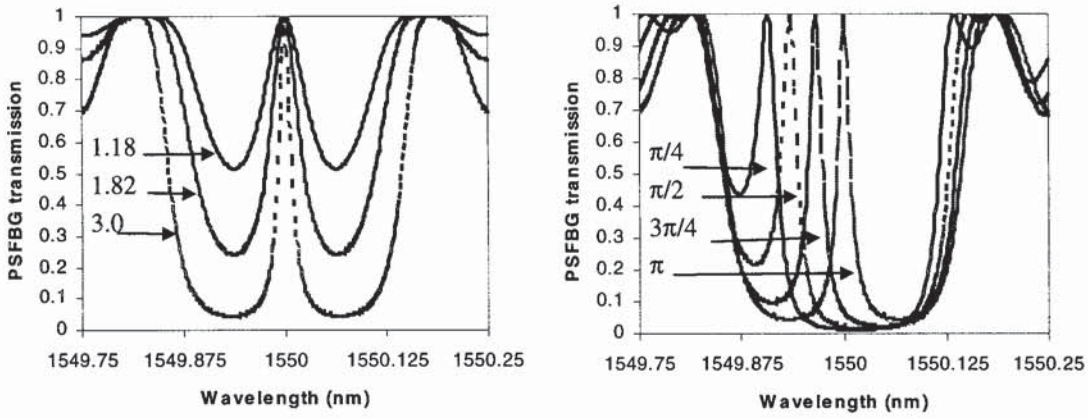

Figure 5.20 Calculated transmission spectrum of a 10mm long phase-shifted Bragg grating at wavelength 1.55μm (q=0): (a) with π phase shift but different values of coupling strength: 1.18, 1.82 and 3.0; (b) with the same coupling strength (κL=3) but different values of phase-shift: π/4, π/2, 3π/4, π

With increasing phase shift, the simulation shows that the transmission peak moves to the long wavelength side in the Bragg stop-band and the line-width remains unchanged, which is in agreement with experimental results. The transmission spectra for the phase shifts of $\pi/4$, $\pi/2$, $3\pi/4$, and π are shown in Figure 5.20 (b). However, when the π phase shift deviates from the centre of the grating length, located at one side of the grating, specified by $q \neq 0$, a transmission peak with loss appears at the stop-band of the Bragg

resonance, shown in Figure 5.21 (a).

Figure 5.21 (b) shows the reflection depth against the coupling strength, a strong grating has a short average reflective depth. For a 10mm long grating with $\kappa L = 3$, eqn. (5.32) yields average reflection depth as 1.66mm. For a 10mm long grating with $\kappa L = 3$ and a π phase shift at the grating centre, the average cavity length is thus 3.02mm.

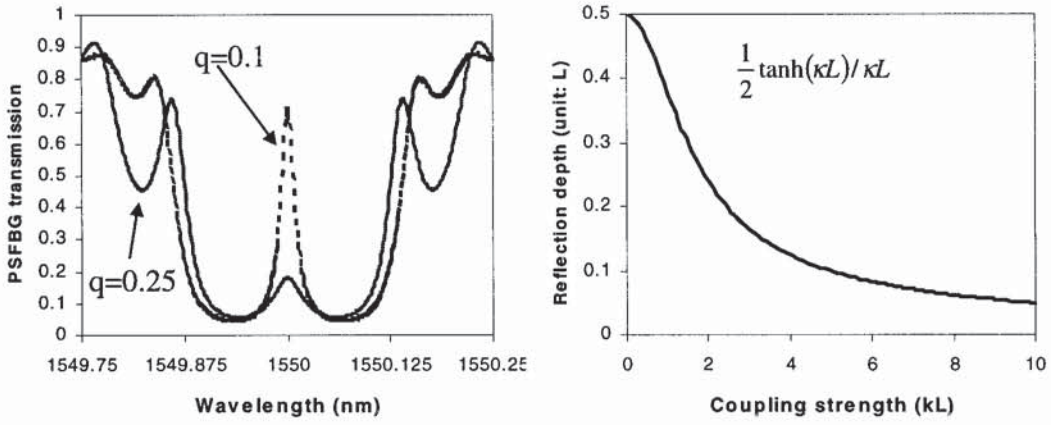

Figure 5.21 (a) Calculated transmission spectra of 10mm long π phase-shifted Bragg gratings with different phase locations indicated by q=0.1 and 0.25 at wavelength 1.55μm (κL=3); (b) calculated average reflection depth of a Bragg grating in the unit of the grating length versus the coupling strength

For 10mm long gratings with κL=3, the calculated transmission spectra of the gratings with two π-phase shifts ($L_1 : L_2 : L_3 = 1 : 2 : 1$) and the three π-phase shifts ($L_1 : L_2 : L_3 : L_4 = 1 : 2 : 2 : 1$) are shown in Figure 5.22 (a) and (b), respectively.

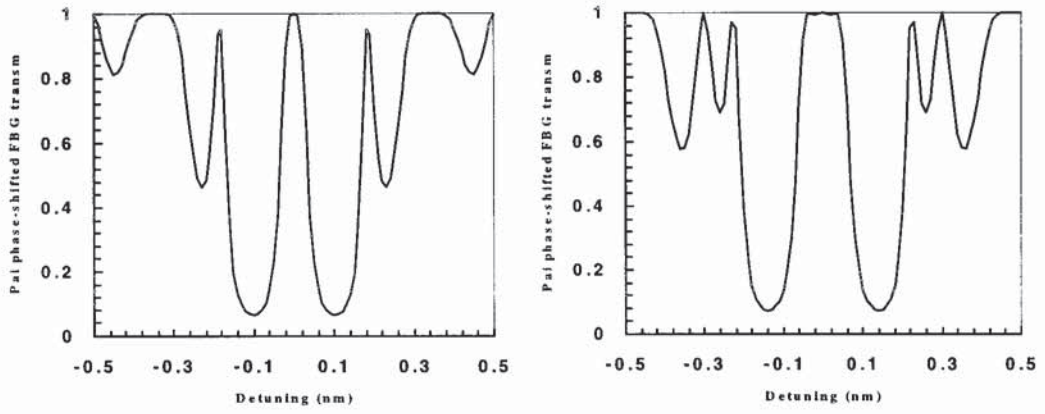

Figure 5.22 Calculated transmission spectra of 10mm long multiple π phase-shifted Bragg gratings at wavelength 1.55μm (κL=3), showing a square transmission profiles: (a) two π phase shifts with the locations of $L_1 : L_2 : L_3$=1:2:1; (b) three π phase shifts with the locations of $L_1 : L_2 : L_3 : L_4$=1:2:2:1

5.5.4 Experimental results

The experimental arrangement is illustrated in Figure 4.9 and discussed in section 4.2.5. When the UV beam scans to the centre of the phase mask, the computer outputs a voltage (~0.5V) through a Data Acquisition Card (DAQ I/O) to the PZT stage. The phase mask is shifted half a grating period as a result as shown in Figure 4.14. Clearly, in this technique it needs to know exactly how much the PZT control voltage results in the phase mask shift of half a grating period. The voltage of V=0.3, 0.4, 0.5, and 0.6V was applied to drive the PZT stage to shift the phase mask and 43mm long gratings were fabricated. The transmission spectra of phase-shifted gratings are shown in Figure 5.23 (a) and (b).

When the control voltage is 0.5V, the phase shift is around π as the transmission peak is almost located at the centre of the grating stop-band. Note that the positive voltage makes the phase mask shift back relative to the scan direction and the phase shift is thus counted in a negative as -ϕ in experiment. Then, a larger shift of the phase mask leads to a smaller phase shift and the transmission peak is thus located at the short wavelength side while a small shift of the phase mask makes the transmission peak at the long wavelength side.

This is in good agreement with the simulation as shown in Figure 5.20 (b).

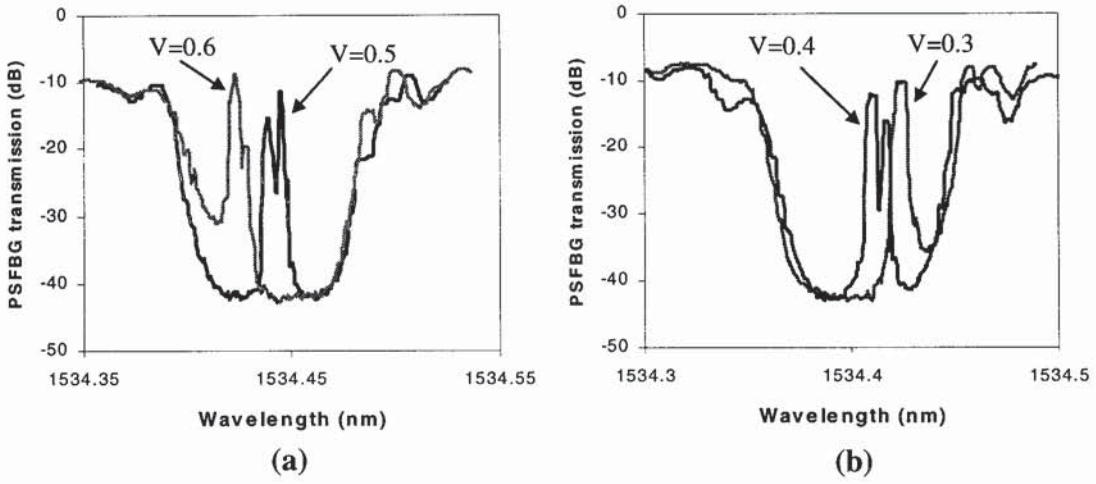

Figure 5.23 Experimental spectra of 43mm long phase-shifted Bragg gratings fabricated using the UV beam scanning across a phase mask technique under different values of PZT control voltages: (a) V=0.6 and 0.5V, (b); V=0.4 and 0.3V

It is clear that the two sub-peaks consist of the transmission peak, separated by between 0.88 and 1.2GHz as shown in Figure 5.23 (a) and (b), which have been confirmed resulting from the birefringence of the grating, relating to the polarisation states of the writing UV beam.

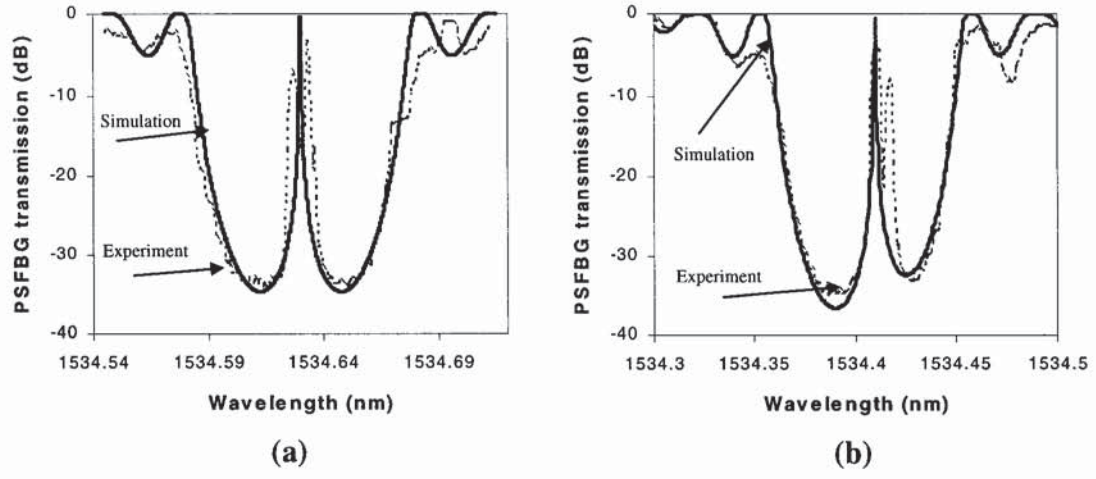

Figure 5.24 Comparison of theoretical and experimental transmission spectra of 43mm long phase-shifted Bragg gratings ($\kappa L = 5.9$) with different PZT control voltages - dot line indicates the experimental obtained while the solid line indicates the calculated results: (a) 0. 5V; (b) 0.4V, corresponding to –180° and -165° phase shifts, respectively

For a 43mm long grating with $\kappa L = 5.9$, when the applied voltage are 0.3, 0.4, 0.5 and 0.6V, corresponding to the phase of -115, -165, -180, and -235 degree, respectively, the simulated transmission spectra are in good agreement with the experimental results, as shown in Figure 5.24 (a) and (b). Note that the birefringence is not included in simulation.

5.5.5 Application - DFB lasers

As an application, a phase-shifted fibre Bragg grating was fabricated in a highly Er/Yb codoped fibre to form a DFB fibre laser. The absorption of this fibre at wavelengths 980nm and 1535nm are about 2500dB/m and 28dB/m, respectively. In order to avoid the unnecessary absorption, two sections of standard fibre were spliced to the ends of a 50mm long Er/Yb codoped fibre. The fibre was placed in a 150atm hydrogen tube for one week to enhance its photosensitivity and 43mm long phase-shifted gratings were fabricated. The typical transmission spectrum is shown in Figure 5.25 (a).

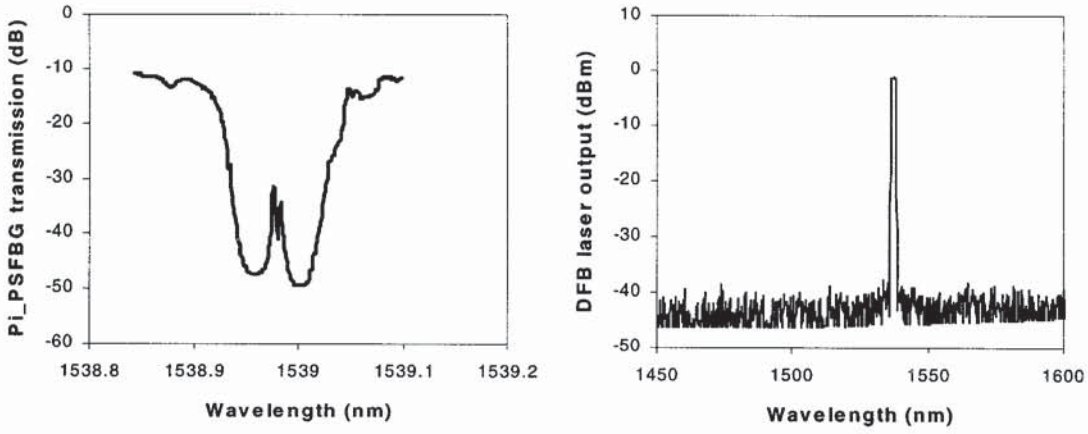

Figure 5.25 (a) Experimental transmission spectrum of a 43mm long π phase-shifted Bragg grating fabricated in Er/Yb co-doped fibre; (b) DFB laser spectrum pumped by 60mW 980nm LD

The two sub-peaks in Figure 5.25 (a) originate from the grating birefringence. The transmission peak has very large loss in this case due to the Fabry-Perot resonant absorption at this wavelength. In contrast, for the B/Ge-doped photosensitive fibre, there

is low loss at the transmission peak, as shown in Figure 5.23 (a) and (b). Using a 60mW 980nm LD laser to pump the Er/Yb codoped fibre containing a phase-shifted Bragg grating, a 1mW output single mode laser was obtained experimentally with the outputs in two orthogonal polarisations. The DFB laser has outputs from both sides of the phase-shifted grating: one polarisation was selected and feedback into the DFB to enhance that polarisation and suppress the other. Thus single mode (~1 kHz line-width) and single polarised output from the DFB laser was achieved experimentally. The laser spectrum is shown in Figure 5.25 (b).

To summarise, a useful analytical expression for phase-shifted fibre Bragg gratings with clear physical meaning describing the complex Fabry-Perot cavity has been presented. This expression extends to the multiple phase-shifted gratings, exhibiting a square transmission profile. By pumping the Er/Yb codoped fibre containing a phase-shifted grating, a single mode and single polarisation DFB laser has been realised experimentally.

5.6 Normal Spectral Evolution of Fibre Bragg Gratings

This section discusses the normal spectral evolution of fibre Bragg gratings fabricated using holographic method. With increasing UV exposure, the grating growth in reflectivity is accompanied by a Bragg wavelength shift due to the increase in the UV-induced average refractive index. The distributed Fabry-Perot effect results from the non-uniform power distribution of the UV beam is also discussed.

5.6.1 Fabry-Perot oscillations

As detailed previously, the two-beam holographic technique is widely used to fabricate fibre Bragg gratings. The grating profile depends on the power distribution of the UV beam and thus the grating has some degree of apodisation. The disadvantage of this fabrication technique is the 'self-chirping' resulting from the varying average index corresponding to the power distribution of the UV beam. Since the Bragg wavelength is proportional to the effective index of the grating, the non-uniform UV exposure induces a variation in the Bragg wavelength along the grating length, which is longer in the centre than at the edges of the grating. Consequently, the gratings act as a distributed Fabry-Perot resonator, producing resonances on the short wavelength side of the Bragg resonance.

For a 8mm long grating with $\overline{\kappa}L$=4.28 (30dB peak reflectivity), the profile of the coupling coefficient and the photoinduced average index resulting from a non-uniform UV exposure is given by

$$profile = \exp\left(-2\left|\frac{z}{L/2}\right|^{8}\right) \tag{5.38}$$

where, $-L/2 \le z \le L/2$, indicates the grating locations, L is the grating length. Clearly, this profile for the coupling coefficient of the grating produces some degree of apodisation.

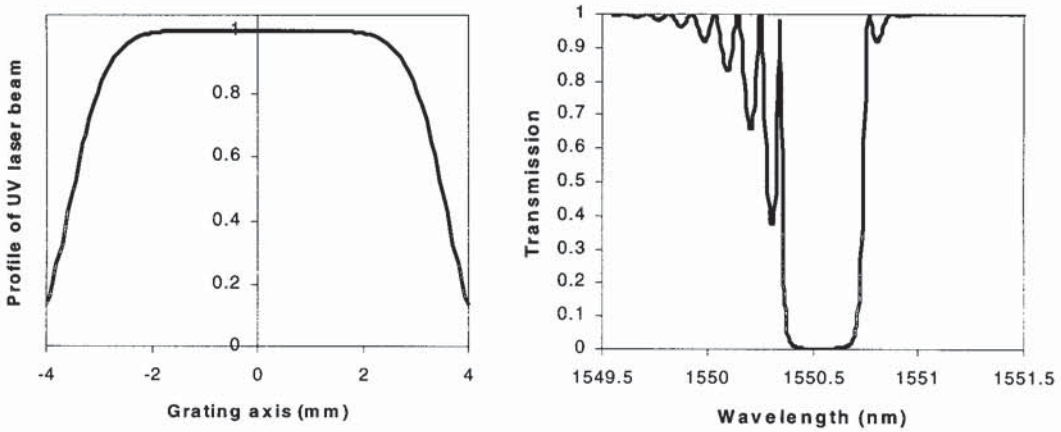

(a) **(b)**

Figure 5.26 (a) Normalized profile of a 8mm long grating of 30dB-reflectivity; (b) calculated transmission spectrum showing oscillations

However, the profiled average index makes a chirping structure: the short wavelength is located at the ends of the grating. This produces a distributed Fabry-Perot cavity. The simulated transmission spectrum is shown in Figure 5.26 (b), exhibiting oscillations superimposed in the grating spectrum located at the shorter wavelength side of the Bragg resonance.

5.6.2 Normal spectral evolution

In order to investigate the spectral evolution, the grating transmission is captured from an Optical Spectrum Analyser (OSA) every three seconds during the UV beam exposure as shown in Figure 5.27 (a). It can be seen that with the growth of the grating reflectivity, the Bragg wavelength shifts to long wavelengths.

As discussed in section 3.3.4.3, the UV exposure increases the average index of the fibre core ($\Delta\overline{n}_0$), the shift of the Bragg wavelength is thus given by

$$\Delta\lambda_{shift} = \frac{\Delta\overline{n}_0}{n_{eff}}\lambda_0 \tag{5.39}$$

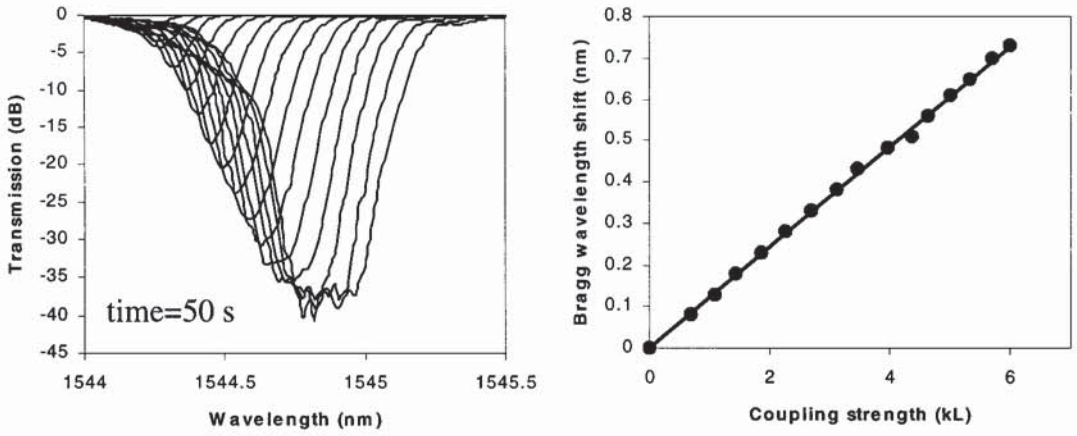

Figure 5.27 (a) A selection of transmission spectra for one 8mm long grating fabricated using holographic method, illustrating a normal evolution of the transmission profile with increasing UV exposure; (b) A comparison of the Bragg wavelength shifts of experimental results and calculated values using eqn. (5.39) against the coupling strength

where $\Delta\overline{n}_0 = \dfrac{\kappa_0 L \cdot \lambda}{\pi \cdot \gamma \cdot L \cdot C_{01}^{co}}$ is the average photoinduced index given by eqn. (3.88), the approximation $\Delta\overline{n}_0 \approx \Delta\overline{n}_{eff}$ has been used; $C_{01}^{co} = 0.8$ and $\gamma = 0.75$ indicate the mode overlap and the visibility of the interfering fringes, respectively, L=8mm is the grating length. A comparison of the shifts of the Bragg wavelength against the average coupling strength $\overline{\kappa}_0 L$ exhibits good agreement as shown in Figure 5.27 (b), where $\overline{\kappa}_0 L$ is given by eqn. (3.87), dots indicate the experimental results while the solid line indicates the calculation using eqn. (5.39).

As illustrated in Figure 5.28 (a), (b), (c) and (d), the comparison between the calculated transmission spectra (thin line) and the experimental results (thick line) show excellent agreement both in the transmission profiles and the red shifts ($\Delta\lambda_{shift}$). The slopes at short wavelengths in the experimental transmission spectra correspond to the evolution of the oscillations of the distributed Fabry-Perot effect. But this is not directly observed due to the limitation of the 0.1nm resolution of the optical spectrum analyser.

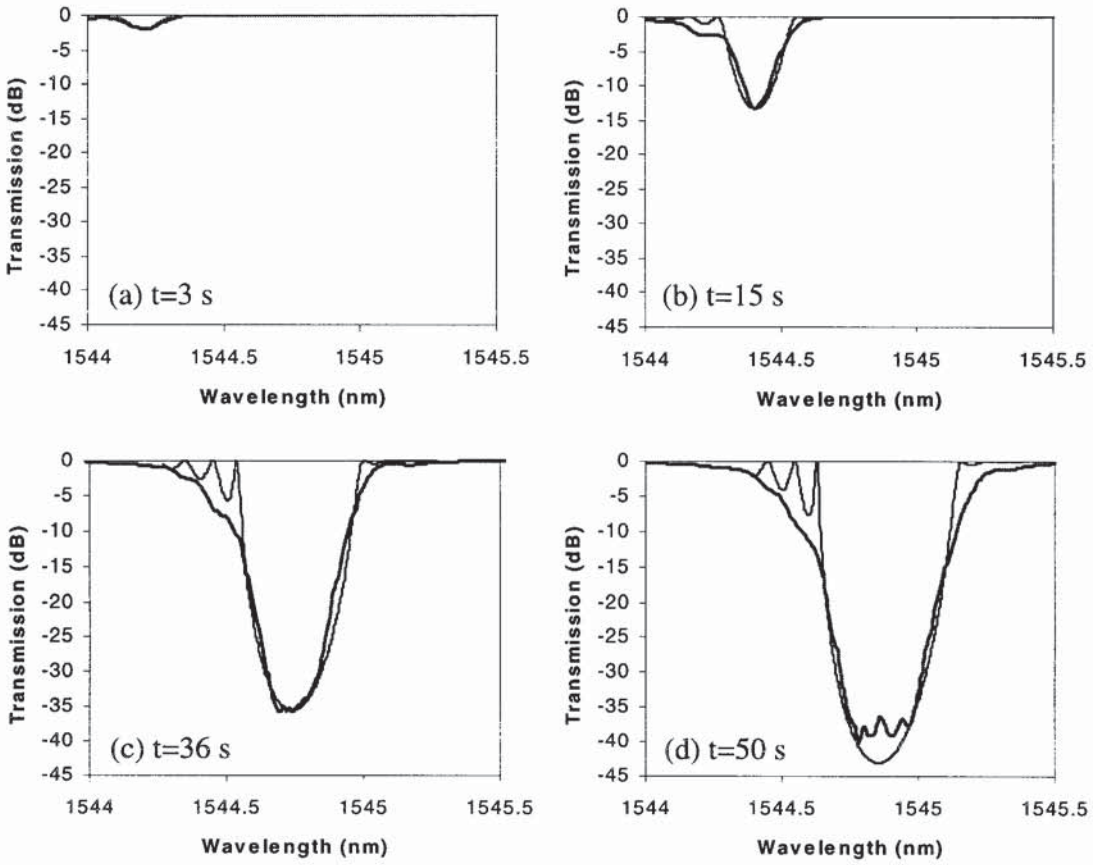

Figure 5.28 The comparison of theoretical and experimental transmission spectra of Bragg gratings with different values of the coupling strengths: (a) $\kappa L=0.81$; (b) $\kappa L=2.63$; (c) $\kappa L=5.85$; (d) $\kappa L=6.98$, showing good agreement both in the transmission profiles and the red-shifts

To summarise, the normal spectral evolution of Bragg gratings fabricated using the two-beam holographic method has been discussed. With increasing UV exposure, the Bragg wavelength shifts to long wavelengths, and offers a way to measure the photoinduced refractive index by measuring the peak reflectivity and the red shift. In addition, the distributed Fabry-Perot effect resulting from the non-uniform UV exposure producing oscillations superimposed in the short wavelength side of the Bragg resonance has been discussed theoretically and experimentally. For the UV overexposure gratings, abnormal spectral evolution of Bragg gratings will be discussed in the following section.

5.7 Type IIa Gratings and Abnormal Spectral Evolution

As mentioned in Chapter 2, positive index fringes exist in Type I and Type II gratings while negative index fringes exist in Type IIa gratings. This section discusses the grating formation with the UV overexposure in the B/Ge-doped fibre with and without hydrogen loading, respectively.

5.7.1 Type IIa gratings

As discussed in section 5.6.2, during the grating fabrication, it was observed that the central wavelength of the grating increases with the UV exposure, indicating that a positive refractive index change was being induced. These gratings are known as 'Type I' gratings. Such gratings are the most commonly fabricated, using both the holographic and the phase mask techniques, but are the least stable at high temperature.

With increasing UV exposure, the grating grows in reflectivity with a positive index change corresponding to a red shift of the Bragg wavelength before reaching its saturation. After the saturation of the Type I gratings then the growth of a 'Type IIa' grating commences, basically formed by the overexposure of a conventional grating. The initial grating decreases in reflectivity to almost zero before growing in reflectivity again. During the final stage of the growth process, the central wavelength of the grating decreases, indicating a negative induced refractive index change. The growth eventually saturates, producing what is known as a 'Type IIa' grating.

Type IIa gratings are normally inscribed by 193nm UV beam [152], reported by Xie *et al.* 1993 [28] and Douay *et al.* 1997 [153]; up to 27dB-reflectivity Type IIa gratings were achieved by Canning *et al.* [47]. Dong *et al.* 1996 [48] explained the higher temperature stability of the Type IIa compared with Type I gratings by three-energy-level system [47]. Though the exact mechanism is still not very clear, it is believed to be linked with stress and (or) defect concentrations with evidence of the formation of Type IIa in Ge-doped fibre but not in the same material preform [49].

The gratings were fabricated using the holographic method and the 244nm CW UV beam with 60mW power and 8mm beam-width. The computer captured the spectrum from an optical spectrum analyser. The formation of a 2.2dB-reflectivity Type I grating after about 2 minutes the UV exposure in non-hydrogenated B/Ge-doped fibre was obtained as shown in Figure 5.29 (a). After the maximum reflectivity reached (2.2dB), the grating reflectivity decreases with further UV exposure. The Type I grating is erased completely after 7 minutes of exposure with a maximum red shift of about 2nm. Maintaining the UV exposure, the Type IIa grating grows in reflectivity accompanied by a blue shift of the Bragg wavelength, indicating a negative refractive formation. Limited by the UV beam wavelength (244nm) and its power (~60mW), only a 8.7dB-reflectivity Type IIa grating and 0.66nm blue shift was observed after 37 minutes the UV exposure. After 12 hours 70°C annealing, a 0.55nm blue shift resulting from the relaxation of the positive photon-induced refractive index was observed. The grating reflectivity is remained unchanged exhibiting thermal stability, as shown in Figure 5.29 (b).

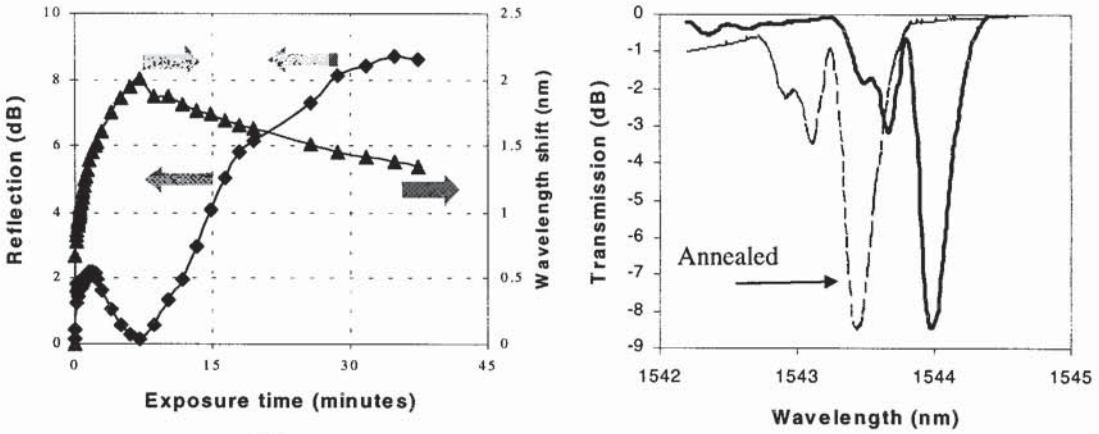

(a) (b)

Figure 5.29 (a) The formation of a Type IIa grating of 8mm long in non-hydrogenated B/Ge-doped fibre fabricated using holographic method: (a) the grating reflectivities and wavelength shifts against the exposure time; (b) transmission spectra before and after annealing

5.7.2 Abnormal spectral evolution

For the UV overexposure gratings fabricated in hydrogenated B/Ge-doped fibres, the Type I grating formation and complete erasure were observed. However, under further

UV exposure an abnormal grating spectrum is formed with a red shift as shown in Figure 5.30, Figure 5.31 (a) and (b). Four gratings (G1 to G4) have very similar behaviors against the UV exposure: after about 15 minutes, Type I gratings are erased completely; after about 60 minutes, the formation of the new spectra, the re-generated gratings reach their maximum with about 16dB-reflectivities and 18nm red shifts.

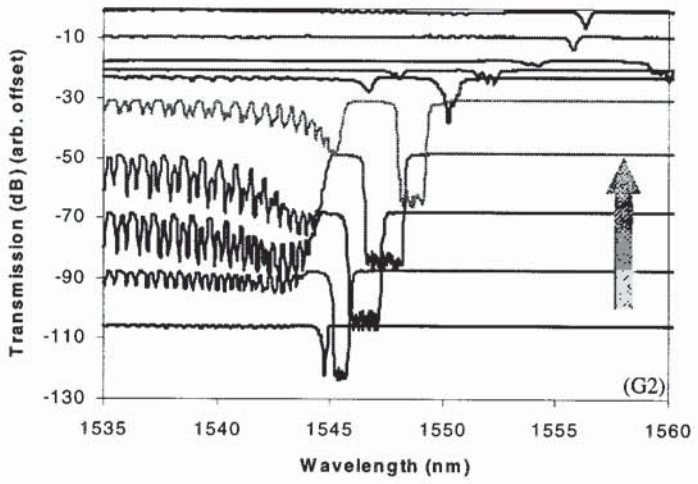

Figure 5.30 A selection of transmission spectra for one 8mm long grating fabricated using holographic method in hydrogenated B/Ge-doped fibre, illustrating an abnormal spectral evolution of transmission profiles with increasing UV exposure - the arrow direction

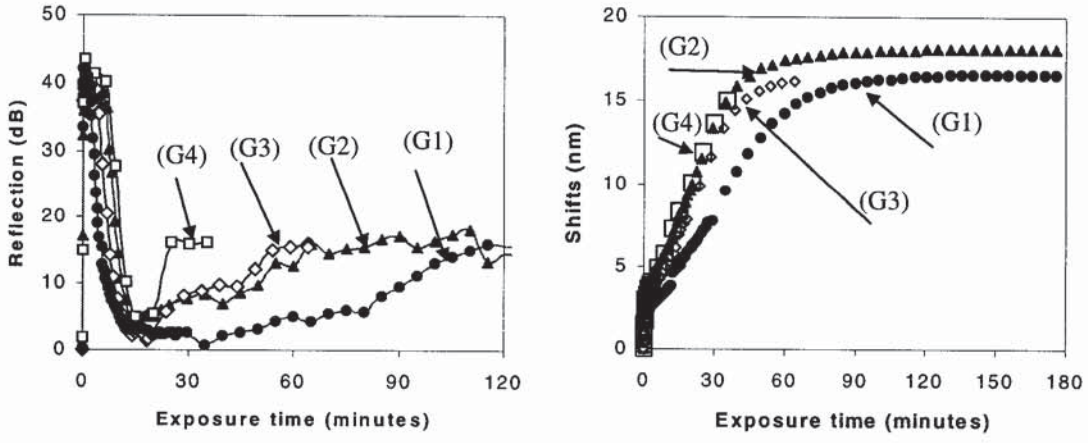

(a) (b)

Figure 5.31 The formation of four 8mm long gratings (G1-G4) fabricated using holographic method in hydrogenated B/Ge-doped fibre: (a) reflectivities in dB against the exposure time; (b) the Bragg wavelength shifts against the exposure time

There are no significant changes in the grating reflectivity and the shift for longer than an hour UV exposure, where four hours and six hours and a half were used experimentally. Using eqn. (5.39), 18nm observed red shift corresponds to the photoinduced refractive index as $\Delta n = 1.68 \times 10^{-2}$. Note that such a large photoinduced refractive index was produced only by around 60mW power 8mm beam-width 244nm wavelength UV beam.

It is noticeable that the numerical aperture of the grating fibre increases about 2.6 times because of the increase of the fibre core index resulting from the photoinduced refractive index. As shown in Figure 5.32, the ghost mode with 5.9nm wavelength spacing and 6dB strength relative to the 16dB-reflectivity Bragg resonance was obtained. After 70 °C 12 hours annealing, the Bragg wavelengths of these re-generated gratings shift to shorter wavelengths about 2 to 3nm and the grating coupling strengths are decreased significantly as shown in Figure 5.32 as 'annealed'.

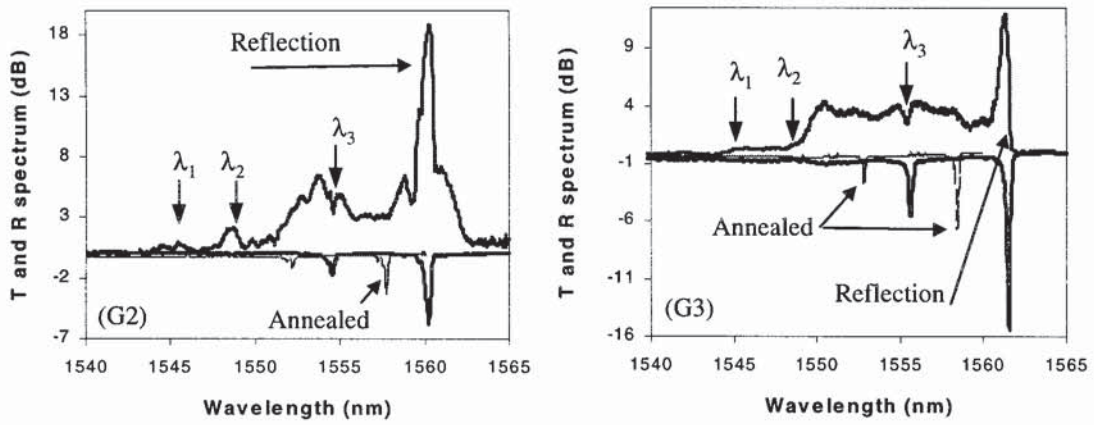

Figure 5.32 Reflection and transmission spectra of 8mm long gratings fabricated using holographic method in hydrogenated B/Ge-doped fibre for an hour UV exposure: (a) re-re-generated grating G2; (a) re-generated grating G3;

As shown in Figure 5.32 (a) and (b), the background reflection of these re-generated gratings have two raised stages, the first covering Type I grating region starting at λ_1 (~1544nm) and the second covering the new spectrum formation starting from λ_2 (~1550nm). Meanwhile, the ghost mode resulting from the cladding mode coupling is clearly indicated in background reflection at λ_3.

In hydrogenated standard fibre, the formation of Type I grating and its erasure after 33 minutes the UV exposure and followed by the formation of an abnormal spectral evolution have been also observed experimentally. After 95 minutes the UV exposure as shown in Figure 5.33, a grating with 25.1dB-reflectivity and 23.2dB ghost mode coupling separated to the Bragg wavelength by 2.77nm was obtained. The total shift of the Bragg wavelength is up to 8.07nm.

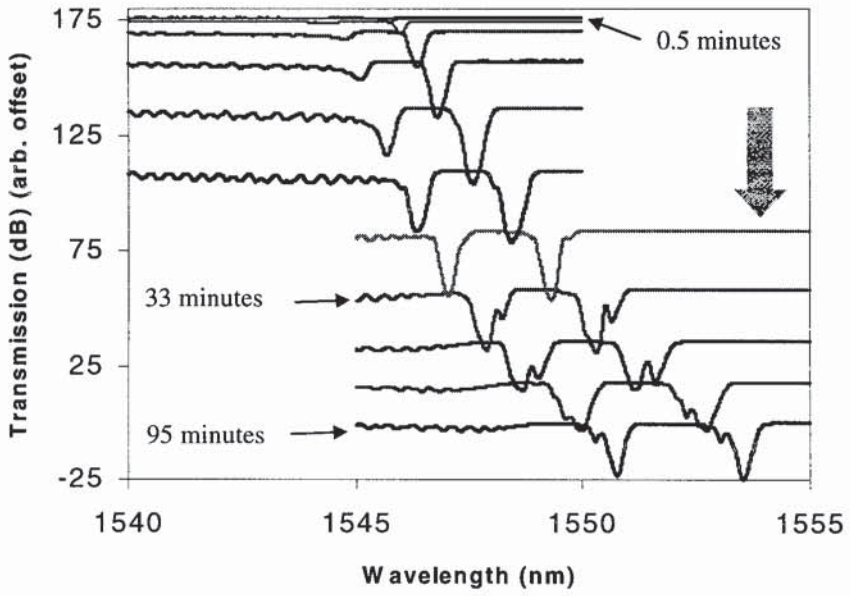

Figure 5.33 A selection of transmission spectra for one 8mm long grating fabricated using holographic method in hydrogenated standard fibre, showing an abnormal evolution of the transmission profiles with increasing UV exposure - narrow direction

5.7.3 Temperature coefficient

A changed temperature coefficient was observed experimentally for the two kinds of gratings. Type I gratings in hydrogenated B/Ge-doped fibre showed the temperature coefficient as 8.9pm/°C while the re-generated gratings were measured as 6.4pm/°C as shown in Figure 5.34.

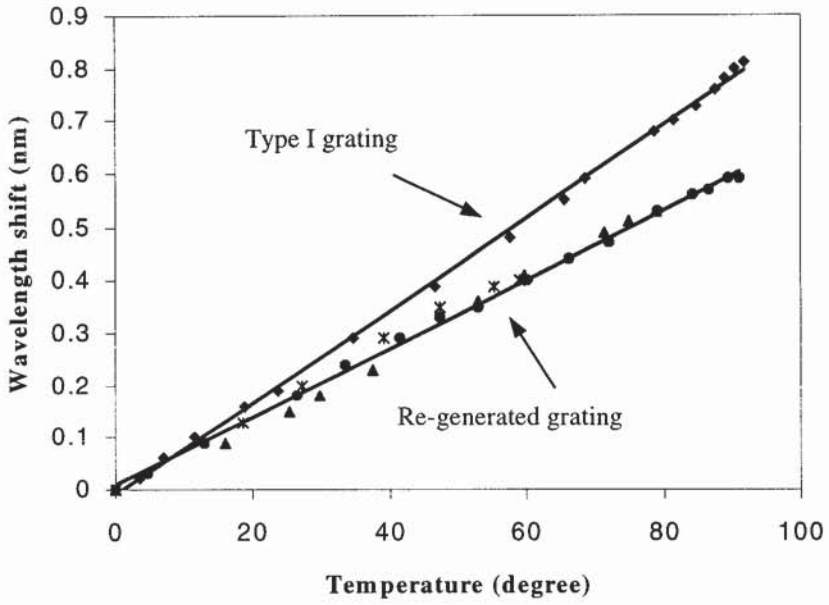

Figure 5.34 A graph showing the Bragg wavelength shift of the Type I and re-generated gratings fabricated in hydrogenated Be/Ge-doped fibre versus the temperatures: dots indicate the experimental results; solid line indicates the fitted of the experimental results

To summarise, gratings under the UV overexposure in B/Ge-doped fibres and standard fibres have been investigated experimentally in this section. The formation of Type IIa grating in non-hydrogenated fibre has been observed showing thermal stability. In hydrogenated B/Ge-doped fibre, followed by the erasure of the Type I grating, an abnormal spectral evolution of a re-generated grating with up to 18nm positive wavelength shift and 16dB-reflectivity has been obtained. This re-generated grating exhibits a reduced temperature coefficient.

5.8 Chapter Summary

This chapter detailed the modelling of numerous useful Bragg grating structures, including apodised, chirped, Moiré, sampled and phase-shifted Bragg gratings.

The modelling technique utilising matrix transforms discussed in Chapter 3 has been used. In grating apodisation, simulation results show gaussian profile apodisation *Gauss*(z,6) produces 62.8dB sidelobe suppression theoretically, but the small truncation affects the results. In order to overcome this limit, the gaussian function is forced to zero at the ends of the grating, an improved gaussian profile *ImGauss*(z,m) has been proposed. The simulation shows *ImGauss*(z,5.739) profile apodisation produces a 15.36dB improvement in the sidelobe suppression compared with the gaussian apodisation profile *Gauss*(z,6). Furthermore, in comparison with the well-known Blackman apodisation profile, the improved gaussian profile *ImGauss*(z,4.077) results in a 1.78dB improvement in sidelobe suppression and a smoother reflection profile. For apodisation profiles *ImGauss*(z,5) and *ImGauss*(z,6), the sidelobe suppression up to 66dB and 80dB, respectively, are obtained theoretically. For 30mm long 20dB-reflectivity gratings, more than 30dB sidelobe suppression have been obtained experimentally while it reaches 40dB suppression for 10dB-reflectivity gratings. The modelling has also demonstrated that a *sinc* profile apodisation results in a square shape reflection spectrum, which is a desirable filter to be used in WDM system.

For chirped Bragg gratings, simulation shows a strong background reflection in a uniform strength chirped Bragg grating. This can also be suppressed using an apodisation technique. The reflection profile of chirped Bragg gratings can be tailored by apodisation techniques and a higher-order gaussian profile offers a quasi-square reflection spectrum.

As a comb filter, chirped Moiré grating has been discussed. The theoretical spectrum and experimental results are in good agreement. The number of the transmission peaks depends on the central wavelength spacing of the two chirped gratings in modulus of the FSR of the grating Fabry-Perot cavity. This is equivalent to the nodes of the Moiré

period. Another kind of comb filters based on sampled fibre Bragg gratings have been discussed in this chapter. The wavelength spacing of the reflection peaks depends on the FSR of one sample length Fabry-Perot cavity. When a composite cosine sampling profile is applied to a uniform Bragg grating, a comb filter of multiple reflection peaks with equivalent reflectivities and wavelength spacing has been obtained theoretically. Due to the long-period sampling profile, the dual-characteristics of Bragg and long-period gratings have been observed in the sampled gratings.

The other useful transmission filter is a phase-shifted fibre Bragg grating. An analytical expression with clear physical picture described by complex Fabry-Perot cavity has been proposed. This expression extends to the cases of the two and three phase shifts with square transmitted profile. By pumping a highly Er^{+3}/Yb^{+3} doped fibre containing a phase-shifted grating, a distributed feed back fibre laser (DFB) with 1 kHz line-width single mode and single polarisation fibre laser has been achieved experimentally.

Additionally, the normal spectral evolution of Bragg gratings against the UV exposure has been examined experimentally and theoretically, where a visibility describing the quality of the interfering fringes has been introduced and the oscillations resulting from the distributed Fabry-Perot cavity has been investigated. For 8mm long gratings fabricated using holographic method and a 60mW UV beam overexposure B/Ge-doped non-hydrogenated fibres, the complete erasure of the Type I grating and followed by the formation of Type IIa gratings were observed. However, in the same experiment an abnormal spectral evolution of a re-generated grating was obtained in hydrogenated B/Ge-doped fibres. The red shift is up to 18nm shift and the reflectivity is around 16dB. The further investigation showed that these re-generated gratings have a reduced temperature coefficient compared with the Type I gratings.

CHAPTER 6

Long-Period Fibre Gratings

This chapter presents a theoretical and experimental investigation of long-period fibre gratings. The fabrication technique using the UV beam scanning across an amplitude mask was adopted experimentally. The calculated spectrum, the spectral evolution and the influence of the hydrogen out- and in-diffusion from the fibre core and cladding are discussed. As complex grating structures, phase-shifted and cascaded long-period fibre gratings are also studied.

6.1 Characteristics of Long-period Fibre Gratings

There have been numerous techniques reported for the fabrication of long period gratings [112, 154, 155, 156, 157]. The most widely used are the point-by-point writing and the UV beam scanning across the amplitude mask methods. These two fabrication techniques were adopted experimentally and the first was used in fabricating sampled Bragg gratings using a shutter blocking the UV beam as discussed in section 5.4. The long-period fibre gratings discussed within this chapter were fabricated using the technique of the amplitude mask. One significant difference from the Bragg grating fabrication as illustrated in Figure 4.9 is that a multiple-scan technique is used to control the UV exposure.

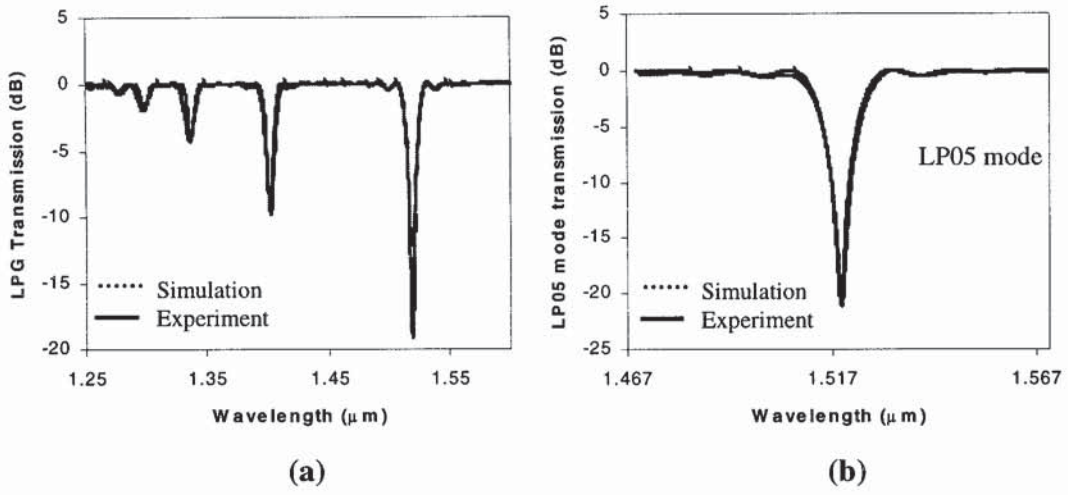

Figure 6.1 A typical transmission spectrum of a 40mm long 490μm periodicity long-period fibre grating: dot lines indicate calculated transmission; solid lines indicate experimental results; (a) full spectrum; (b) LP_{05}^{cl} mode transmission

For a 40mm long 490μm periodicity long-period grating, the full transmission spectrum is shown in Figure 6.1 (a). For the 5th-order cladding-mode LP_{05}^{cl}, the transmission is given by eqn. (3.114) as shown in Figure 6.1 (b). The calculation of the mode overlap factors C_{0p}^{cl}, mode indexes n_{01}^{co} and n_{0p}^{cl} (p=1, 2, ..) have been discussed in section 3.2, exhibiting $C_{01}^{cl} < C_{02}^{cl} < ... < C_{07}^{cl}$ and thus $\kappa_{01}^{cl}L < \kappa_{02}^{cl}L < ... < \kappa_{05}^{cl}L$. For $\kappa_{05}^{cl}L \leq \pi/2$, the resonance loss of cladding modes increases with the mode order as shown in Figure 6.1 (a). The calculated spectrum is in excellent agreement with the experimental results.

The coupling strength of long-period gratings is proportional to the number of scans when the scan velocity and the UV power remain unchanged. The spectral transmission is captured for different values of the UV exposure with further scanning. The resonance wavelengths shift to long wavelengths while the shape of transmission spectrum changes. The spectral evolution of a 40mm long-period fibre grating is shown in Figure 6.2 (a), (b), (c) and (d). At beginning, the resonance loss is in the order as illustrated by Figure 6.2 (a).

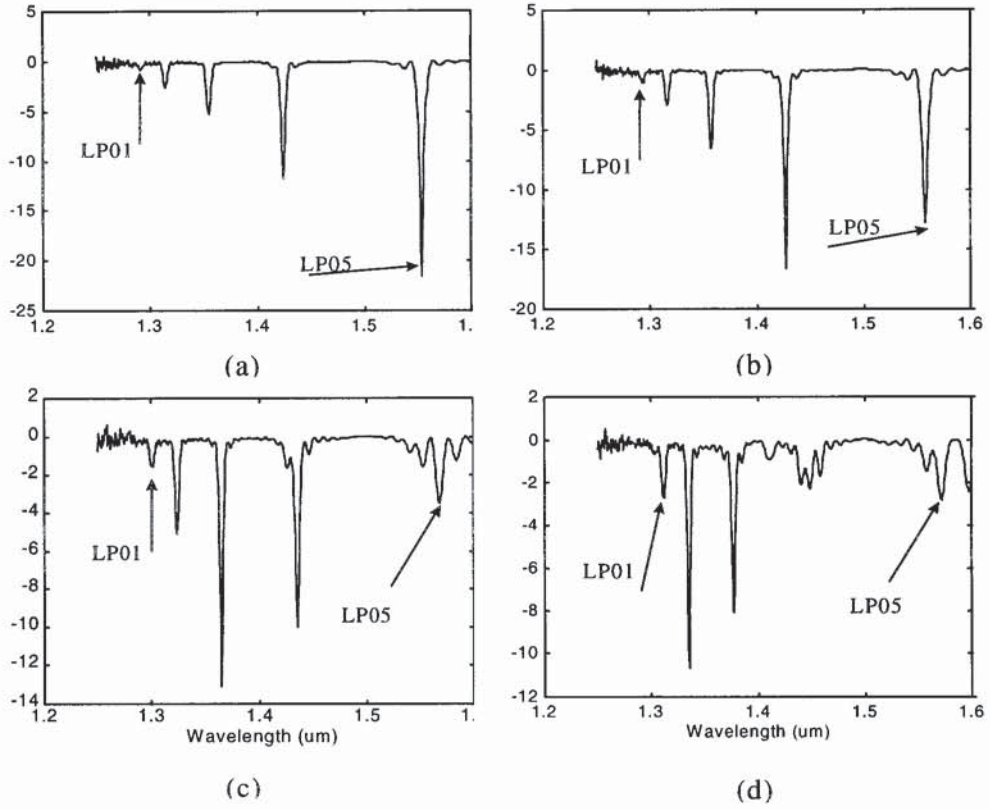

Figure 6.2 A selection of transmission spectra for one long-period grating, illustrating the change in transmission profile with increasing UV exposure: (a) $\kappa_{05}^{cl}L \le \pi/2$*; (b)* $\kappa_{05}^{cl}L > \pi/2$ *and* $\kappa_{04}^{cl}L < \pi/2$*; (c)* $\kappa_{04}^{cl}L > \pi/2$*; (d)* $\kappa_{02}^{cl}L \le \pi/2$, $\kappa_{03}^{cl}L > \pi/2$, *and* $\kappa_{05}^{cl}L \approx \pi$

With the increase in UV exposure, $\kappa_{05}^{cl}L$ increases, reaches $\pi/2$ and thus $T_{05}(\lambda_{05}) = 0$. This means that the core mode at resonance wavelength (λ_{05}) is wholly coupled to the fibre cladding, which results in the largest resonance loss. A further UV exposure, $\kappa_{05}^{cl}L$ coming to the regime of $\kappa_{05}^{cl}L > \pi/2$, LP_{05}^{cl} mode is coupled back to the fibre core from the cladding and thus this resonance loss is getting small while the resonance loss of LP_{04}^{cl} mode becomes the largest one as shown in Figure 6.2 (b). When $\kappa_{05}^{cl}L = \pi$, eqn. (3.115) yields $T_{05}(\lambda_{05}) = 1$ as shown in Figure 6.2 (d). This means that all power at the resonance (λ_{05}) is coupled back to the fibre core from cladding. However, for the wavelength off this resonance, there is still power coupling and the transmission

spectrum appears as two peaks. Further increasing UV exposure, the core mode is re-coupled to the cladding modes showing a periodic behavior.

Looking at LP_{05}^{cl} mode coupling as shown in Figure 6.2 (a) to (d), 50nm wavelength shift is obtained with the UV exposure and the total shift is up to 100nm. This shift is only 0.5nm in fibre Bragg gratings as discussed previously in section 5.5. In order to examine the resonance shifts with the coupling strength, the average photoinduced refractive index may be treated approximately as the increase of the mode index given by eqn. (3.117). The coupling strength ($\kappa_{0p}^{cl}L$) is thus derivable from eqn. (3.116) by measuring of the power transmission at the resonance. The resonance shift of LP_{0p}^{cl} mode is obtained by differentiating eqn. (3.104) as $\Delta\lambda_{0p} = \Delta\bar{n}_{01}^{co}\Lambda$ and given by

$$\Delta\lambda_{0p} \approx \frac{(\kappa_{0p}L)\lambda_{0p}\Lambda}{4C_{0p}^{cl}L} \tag{6.1}$$

where, $duty = 0.5$ has been used, $C_{05}^{cl} \approx 0.23$ is given in Table 3.2, $\kappa_{0p}^{cl}L$ is given by eqn. (3.116). Note that the approximation of $\Delta n_{01}^{co} \approx \Delta n_0$ and non-photosensitive cladding have been used. The comparison between the theoretical and experimental spectra for LP_{05}^{cl} mode shows excellent agreement both in the spectral profiles and the red shifts as shown in Figure 6.3 (a), (b) and (c).

Figure 6.3 (a)-(c) depicts LP_{05}^{cl} mode shifts of 98nm (from 1525.23nm to 1623.24nm) when the coupling strength varies from $\kappa_{05}^{cl}L$=0.12 (0.05dB) to $\kappa_{05}^{cl}L$=4.9. The shift of the LP_{05}^{cl} mode plotted against the coupling strength is shown in Figure 6.3 (d). The experimental results (dots) and the calculated results using eqn. (6.1) (solid line) are in good agreement, exhibiting a good liner relationship.

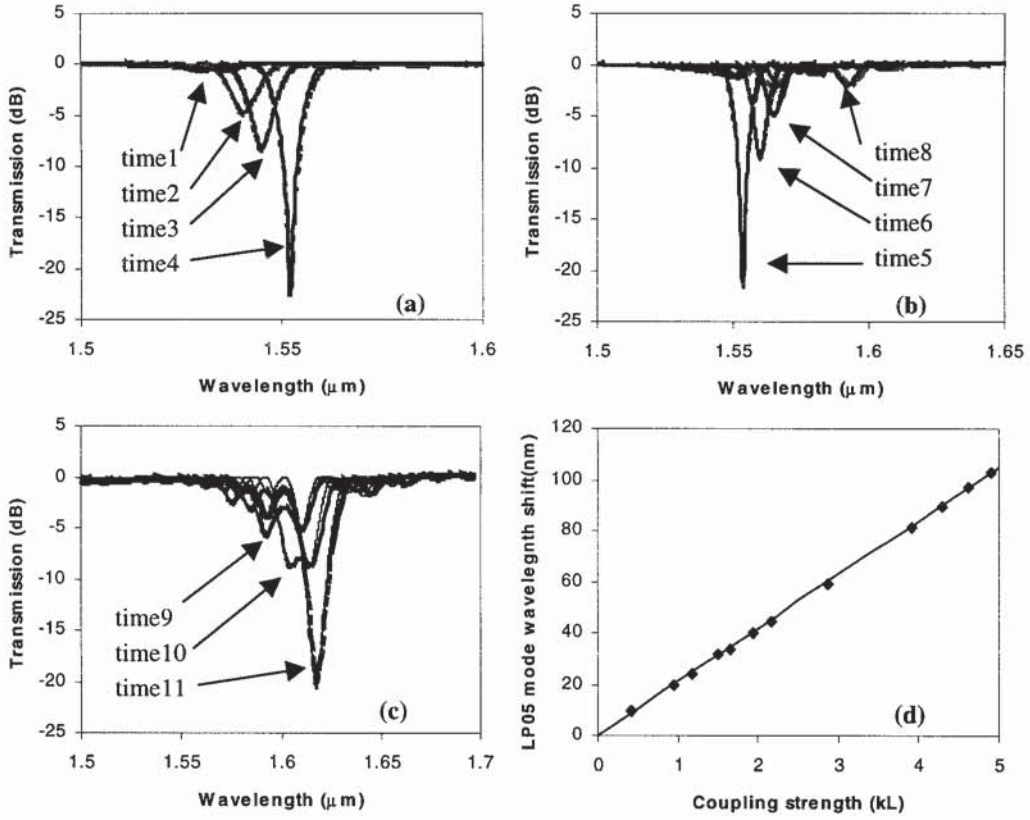

Figure 6.3 The Comparison between theoretical (——) and experimental (.....) transmission spectra for one 40mm long 490μm periodicity long-period grating with different values of: (a) $\kappa_{05}^{cl}L$=0.41, 0.96, 1.17, and 1.50; (b) $\kappa_{05}^{cl}L$=1.65, 1.93, 2.17, and 2.87; (c) $\kappa_{05}^{cl}L$=3.92, 4.30 and 4.62; (d) A comparison of experimental and calculated shifts of the LP_{05}^{cl} mode against the coupling strength: dots indicate the experimental results and solid line is the calculated using eqn. (6.1)

To summarise, the fabrication of the long-period fibre gratings, the characteristics of the calculated spectrum, the spectral evolution have been discussed in this section. The comparison between theoretical and experimental spectra shows excellent agreement. The shift of LP_{05}^{cl} -mode against the coupling strength exhibits a good linear characteristic and up to 100nm positive shift was observed experimentally.

6.2 Hydrogen out- and in-diffusion

This section discusses the investigation of hydrogen out- and in-diffusion from long-period fibre gratings. More than 150nm of wavelength shifts were observed experimentally when the hydrogen diffused out from the long-period gratings.

6.2.1 Introduction

Hydrogen-loading is an established technique to photosensitive fibres for fabricating fibre Bragg gratings and long-period gratings. The hydrogen-diffusion into the fibre cladding and core increases their refractive indexes and thus shifts the grating resonance. This effect is very small in Bragg grating and annealing for 12 hours at 70°C shifts the Bragg resonance about 0.5nm as mentioned in section 5.7.1. However, it is more than 150nm shifts in long-period fibre gratings.

6.2.2 Hydrogen out-diffusion

Long-period fibre gratings were fabricated in a B/Ge-doped non-hydrogenated photosensitive fibre. Then the gratings were put into a high pressure (150bar) hydrogen tube for hydrogen-loading for two days before taken out for a hydrogen out-diffusion monitoring. The transmission spectra before and after hydrogen-loading are shown in Figure 6.4 as LP_{0m}^{A} and LP_{0m}^{B}, respectively. It is clear that the resonance wavelengths of the long-period grating have a blue shift during the two days hydrogen-loading. A higher-order mode has a relatively larger blue shift. After removed out from the hydrogen tube, the transmission of long-period gratings was measured using an LED wide-band light source and an optical spectrum analyser (OSA). The monitoring was carried out every few minutes to start with, continuing every few hours, eventually every few days.

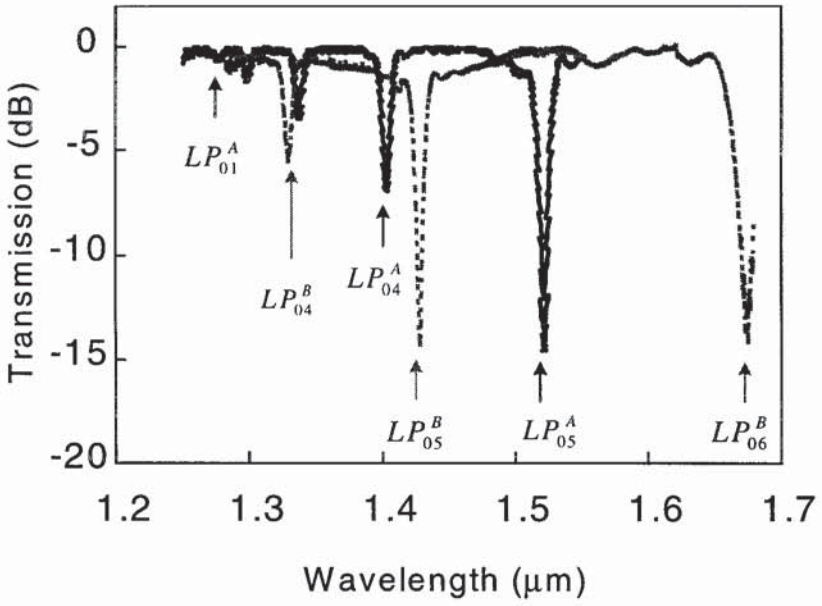

Figure 6.4 Experimental transmission spectrum of a long-period fibre grating before (LP_{0p}^{A}) and after (LP_{0p}^{B}) hydrogen-loading (p=1, 2, 3...)

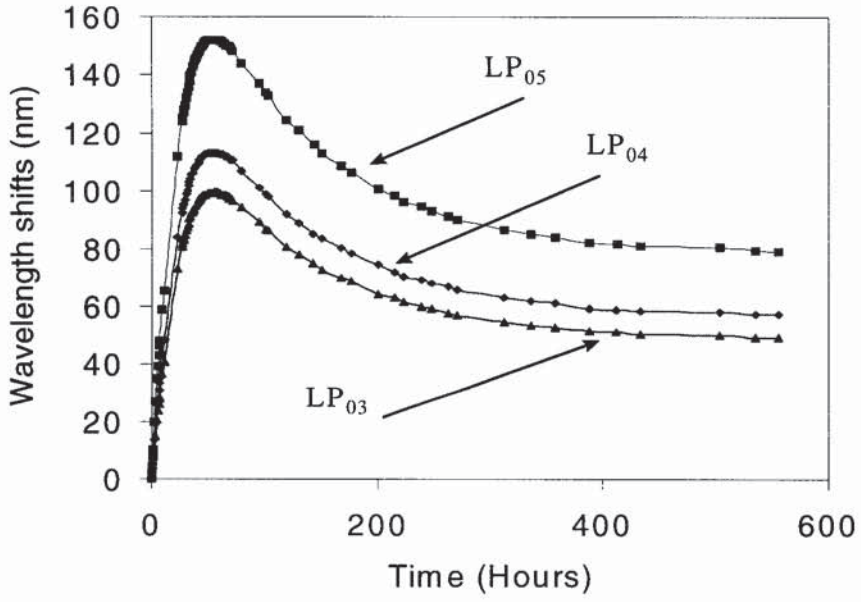

Figure 6.5 A graph showing shifts of cladding modes against the hydrogen out-diffusion time for a long-period grating fabricated in none-hydrogenated B/Ge-doped fibre and followed 2 days 150atm hydrogen-loading

Figure 6.5 shows a plot of the wavelength shifts against the diffusion time when the long-period grating was removed out from the high-pressure hydrogen tube. Two distinct trends are identifiable in the hydrogen out-diffusion process. The first trend, which is dominated by the hydrogen out-diffusion from the cladding, shows a rapid (~4nm/hour) and a massive red shift for all the modes of the long-period grating, typically 150nm for LP_{05}^{cl}. The second trend was a gradual blue shift towards their initial wavelengths after ~ 250 hours. In this trend, the hydrogen out-diffusion from the core played a major role. The residual hydrogen out-diffusion completely ceased after 550 hours. The three cladding modes have almost the same varying behaviors against the diffusion time.

When the gratings were hydrogenated at high pressure (150bar) for only two hours before being taken out for hydrogen out-diffusion monitoring, the LP_{05}^{cl} mode shift versus the time of hydrogen out-diffusion is shown in Figure 6.6. The varying behavior of the LP_{05}^{cl} mode is significantly different from the case as shown in Figure 6.5, resulting from hydrogen only diffusing out from cladding because hydrogen has only diffused into the cladding during the shorter hydrogen-loading time (2 hours).

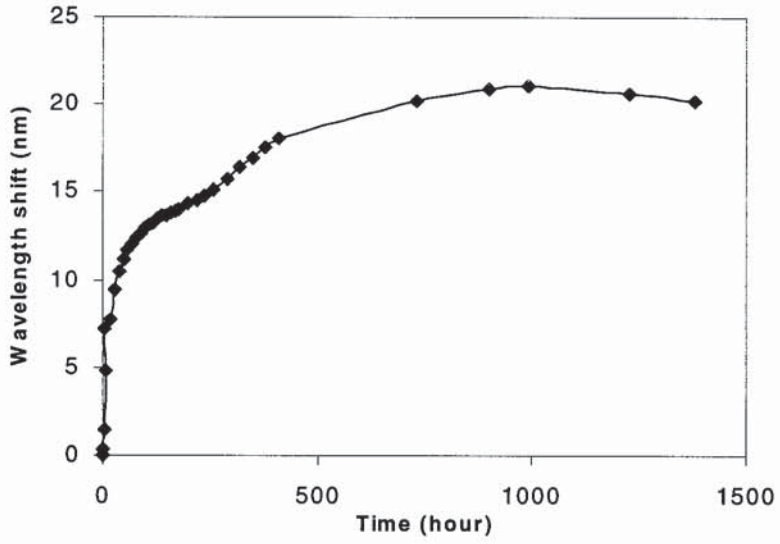

Figure 6.6 A graph showing LP_{05}^{cl} mode wavelength shifts of a long-period fibre grating fabricated in non-hydrogen B/Ge-doped fibre and followed by two hours 150atm hydrogen-loading against the time of the hydrogen out-diffusion

6.2.3 Hydrogen in-diffusion

To investigate the process of the hydrogen in-diffusion, the same long-period grating which was fabricated in the B/Ge fibre without hydrogen-loading was placed into a lower pressure (2~3 bar) hydrogen tube. Both sides of the long-period grating fibre were extended out of the hydrogen tube for measurement. In this case the, the blue shift is much smaller than that of the high-pressure case. In this experiment, a cascaded long-period grating structure was used to improve the spectral resolution. The transmission spectrum of the cascaded long-period grating is shown in Figure 6.7 (a). The wavelength shifts against the diffusion time is shown in Figure 6.7 (b). The maximum blue shift is recorded about 2nm.

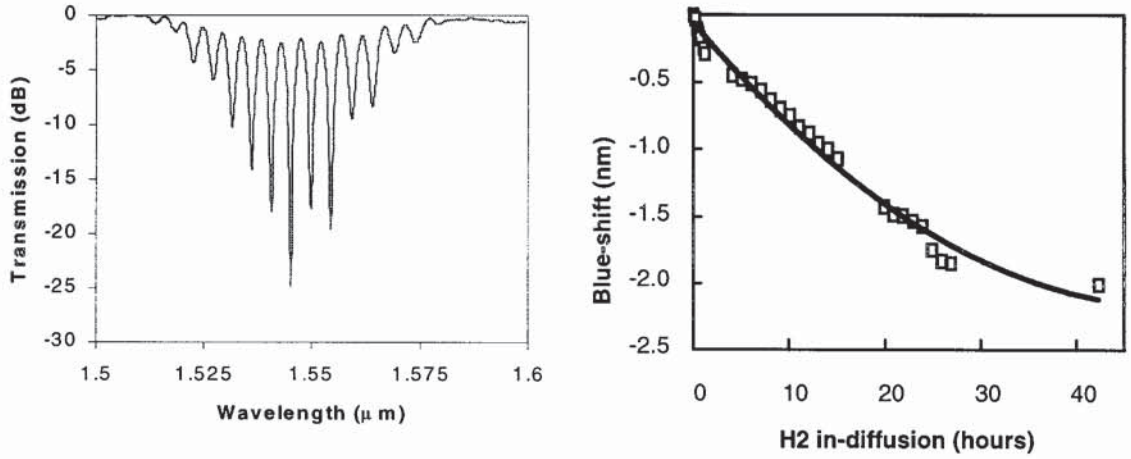

Figure 6.7 The measurement of low pressure hydrogen in-diffusion a fibre: (a) transmission spectrum of a cascaded long-period fibre grating; (b) LP_{05}^{cl} -mode blue shift versus the hydrogen in-diffusion time (3 bar hydrogen pressure)

To summarise, the process of the hydrogen out- and in-diffusion of the fibre has been investigated experimentally. Two distinct trends are identifiable in the hydrogen out-diffusion process. The first trend exhibits the hydrogen out-diffusion from the cladding is dominated. The resonance of long-period gratings shifts to longer wavelengths. Up to 150nm shifts were observed. The second trend was a gradual blue shift towards their initial wavelengths after ~ 250 hours. In this trend, the hydrogen out-diffusion from the fibre core played a major role.

6.3 Phase-shifted and Cascaded Long-Period Fibre Gratings

This section details the characteristics of phase-shifted and cascaded long-period gratings theoretically and experimentally. A wider and flattened or multipeak narrow transmission is achieved in the long-period grating stop-band.

6.3.1 Introduction

Photoinduced long-period fibre gratings have a broad stop-band (~20nm) and no guided mode reflection and have been demonstrated for communication applications such as gain spectrum flattening of Er-doped fibre amplifiers (EDFA) and for removing amplified spontaneous emission [100, 158]. The resonance wavelengths can be chosen in accordance with the application requirements, but the bandwidth can not be controlled effectively during grating fabrication. The loss peak of long-period gratings is typically too sharp to be used as a filter in EDFA gain flattening [101, 159]. It is necessary to find a way to design a precise long-period grating spectral shape to match the EDFA gain spectrum. For other applications such as long-period grating sensing, the grating spectrum is too wide to get a good resolution and signal/noise ratio though they are more sensitive to the strain, temperature, and ambient refractive index compared with Bragg gratings [102, 103].

6.3.2 Theory

The structure of phase-shifted and cascaded long-period gratings is treated simply as two sub-gratings (LPG_1 and LPG_2) separated by a phase shift (ϕ) and a length of fibre (d), as shown in Figure 6.8. For the structure with $d=0$ and $\phi \neq 0$, it is named as a phase-shifted long-period grating while for $d \neq 0$, a cascaded long-period grating. The matrix transforms for a long-period grating is given in eqn. (3.112) and eqn. (3.113) and the matrix for d length fibre and the phase shift are given in eqn. (3.99) and eqn. (3.100), respectively. Then, the eqn. (3.112) becomes

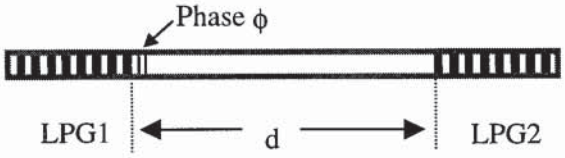

Figure 6.8 Schematic diagram showing the structure of phase-shifted and cascaded long-period fibre gratings

$$\begin{bmatrix} t \\ r \end{bmatrix} = \begin{bmatrix} t_2 & r_2 \\ r_2 & t_2^* \end{bmatrix} \begin{bmatrix} e^{j\delta_{0m}d} & 0 \\ 0 & e^{-j\delta_{0m}d} \end{bmatrix} \begin{bmatrix} e^{j\phi/2} & 0 \\ 0 & e^{-j\phi/2} \end{bmatrix} \begin{bmatrix} t_1 & r_1 \\ r_1 & t_1^* \end{bmatrix} \begin{bmatrix} 1 \\ 0 \end{bmatrix} \tag{6.2}$$

where the last matrix on the RHS of eqn. (6.2) indicates the boundary conditions as $A(0)=1$, $B_{0m}(0)=0$, t and r are the amplitude transmittance and the coupling ratio of LP_{0m}^{cl} cladding mode, while t_i and r_i (i=1, 2) describe the sub-grating LPG_i transmittance and cladding mode coupling ratio given by eqn. (3.110). δ_{0m} is the detuning given by eqn. (3.103). Simplifying eqn. (6.2) yields [160]

$$\begin{cases} t = e^{j[\delta_{0m}d+\phi/2]}t_1t_2 + e^{-j[\delta_{0m}d+\phi/2]}r_1r_2 \\ r = e^{j[\delta_{0m}d+\phi/2]}t_1r_2 + e^{-j[\delta_{0m}d+\phi/2]}r_1t_2^* \end{cases} \tag{6.3}$$

where energy is conserved as $|r|^2+|t|^2=1$. The power transmission (T) is gibe by

$$T = \left| e^{j\left[2\pi\left(n_{01}^{co}-n_{0m}^{cl}\right)d\left(\frac{1}{\lambda}-\frac{1}{\lambda_{0m}}\right)+\phi\right]}t_1t_2 + r_1r_2 \right|^2 \tag{6.4}$$

In the study of phase-shifted long-period gratings (d=0), LPG_1 and LPG_2 are treated as one grating with a length L_1+L_2. In this case, define the location of the phase shift as

$$q = \frac{z}{L_1+L_2} \tag{6.5}$$

where $L/2 \le z \le L/2$, $-0.5 \le q \le 0.5$, q indicates the location of the phase shift inside the long-period fibre grating, where q=0 indicates the phase shift located in the centre

while q=±0.5 indicates at one of the ends.

For cascaded long-period gratings, the phase delay is from the light propagating along the core and the cladding of the fibre along the length d separating the two sub-gratings. The phase delay is wavelength dependent and the transmission spectrum is modulated with multiple peaks. This device is similar to a Mach-Zehnder interferometer where the two gratings act as two couplers and the guided and cladding modes in the fibre between them acting as the two arms in the interferometer. The wavelength spacing ($\Delta\lambda$) between two neighbouring transmission peaks is obtained using eqn. (6.4) and given by

$$\left[\frac{2\pi\left(n_{01}^{co}-n_{0m}^{cl}\right)}{\lambda}-\frac{2\pi\left(n_{01}^{co}-n_{0m}^{cl}\right)}{\lambda+\Delta\lambda}\right]d=2\pi \tag{6.6}$$

Rearranging eqn. (6.6) yields

$$\Delta\lambda\approx\frac{\lambda^2}{\left(n_{01}^{co}-n_{0m}^{cl}\right)d} \tag{6.7}$$

The beat length, the distance for a 2π phase delay between the guide and cladding modes is given by

$$\Delta d=\frac{\lambda}{n_{01}^{co}-n_{0m}^{cl}} \tag{6.8}$$

For a fibre with NA=0.12 at wavelength λ=1.5μm, the beat length is around 0.3mm. Thus, if the fibre between two sub-gratings is strained by this beat length, the wavelength of the transmission peaks will shift by $\Delta\lambda$ thus offers the possibility of an enhanced spectral resolution if this device is used in sensing applications.

6.3.3 Phase-shifted long-period fibre gratings

For a 30mm long 475μm-period phase-shifted long-period grating (d=0) with varying phase shifts ϕ centrally placed (q=0), the calculated spectra are shown in Figure 6.9. As the phase shift increases the peak wavelength shifts to longer wavelengths, the bandwidth

remains fairly constant (11nm) and the maximum transmission loss in the main peak decreases while the loss in the single sidelobe increases. For π phase shift centrally located long-period gratings, the simulation shows that two peaks 20.7nm apart appearing symmetrically about a central wavelength are obtained and the grating becomes transmissive at the central wavelength as shown in Figure 6.9 [161].

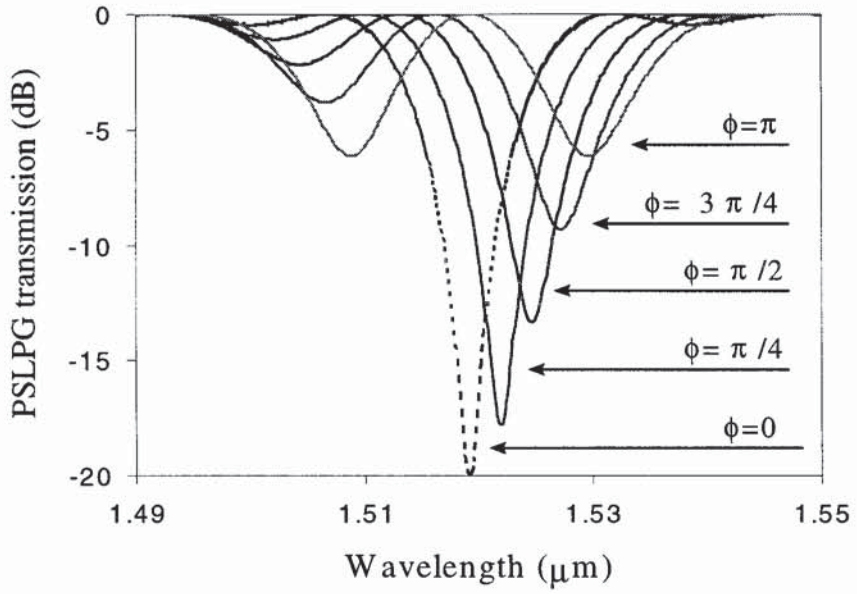

Figure 6.9 Calculated transmission spectra of a 30mm long-period fibre grating (LP_{05}^{cl} mode, $\kappa_{05}L=1.471$) with central located different values of phase shift: $\phi=0$, $\pi/4$, $\pi/2$, $3\pi/4$, π

Figure 6.10 (a) shows the calculated spectra for the introduction of a π phase shift off centre with varying values of q of ±0.30, ±0.32, and ±0.35. This leads to a broad spectrum with a sunken, flat or raised central region, which may be tailored for specific applications. With q=±0.32, the grating has a broad flattened region of 4.6±0.1dB loss over a spectral width of 7.9nm and a 3dB bandwidth of 23nm, twice the bandwidth of a conventional long-period grating.

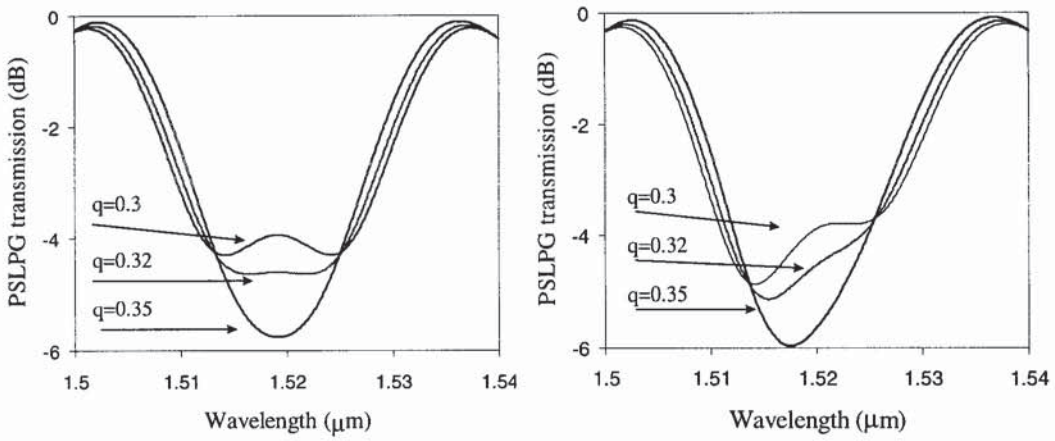

Figure 6.10 Calculated transmission spectra of a 30mm long-period fibre grating ($\kappa_{0m}L=1.471$) with the phase locations indicated by q and different values of phase shifts: (a) $\phi=180°$, (b) $\phi=190°$

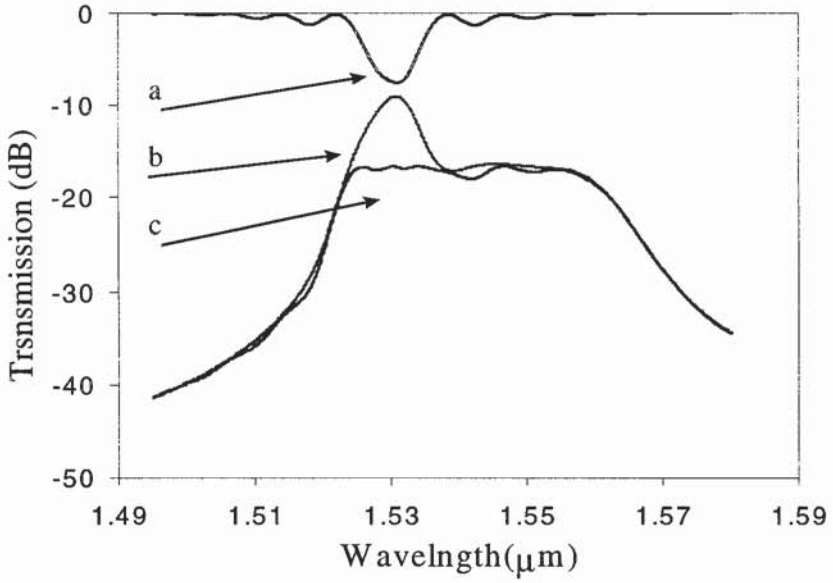

Figure 6.11 A graph showing the EDFA gain flattening using a phase-shifted long-period fibre grating: (a) indicates the transmission spectrum of a phase-shifted long-period grating; (b) indicates a EDFA gain spectrum pumped by 1.48μm LD; (c) indicates the flattened EDFA gain spectrum, ($\kappa_{0m}L=1.67$, $q=\pm0.33$, $w0=1530.3nm$)

If the phase shift is deviated slightly away from π, the calculation shows that the symmetry of the grating is broken and the spectrum deviates to longer wavelengths for

phase shifts less than π and to shorter wavelengths for phase shifts greater than π. In Figure 6.10 (b) it shows how the spectrum of the grating with a 190° phase shift varies with q. Thus, further tailoring of the long-period grating spectrum is possible. A potential application of such a device would be in erbium doped fibre amplifier (EDFA) gain flattening. To illustrate this we show, in Figure 6.11, the effect that such a device would have on a typical EDFA gain spectrum. Such an application requires careful adjustment of the grating wavelength and peak loss.

6.3.4 Cascaded long-period fibre gratings

Figure 6.12 and Figure 6.13 show the calculated and experimentally obtained spectra for cascaded long-period gratings with d=50mm and 190mm respectively. The slight differences are due to slight mismatches in terms of central wavelengths and coupling strengths in the gratings. For d=50mm (Figure 6.12) the wavelength spacing between neighbouring transmission peaks is 7.9nm. As the distance between two sub-gratings increases a transmission spectrum with narrower transmission peaks close together is obtained. Typical for d=190mm (Figure 6.13) there are 17 transmission peaks with more than 3dB extinction spaced by 2.5nm. The line-width of the transmission peaks depends on the separation of the two sub-gratings and the fibre *NA* so it is possible to control them effectively for different applications.

The overall spectral width of the cascaded long-period grating device is still limited by the two sub-grating bandwidths. An effective approach to increase this is to decrease the two sub gratings length while keeping a coupling strength of $\pi/4$. If the two cascaded long-period gratings are reduced to the length of 5mm and separated by 200mm, the simulation results show that more than forty transmission peaks in a 100nm wide spectral region are obtained.

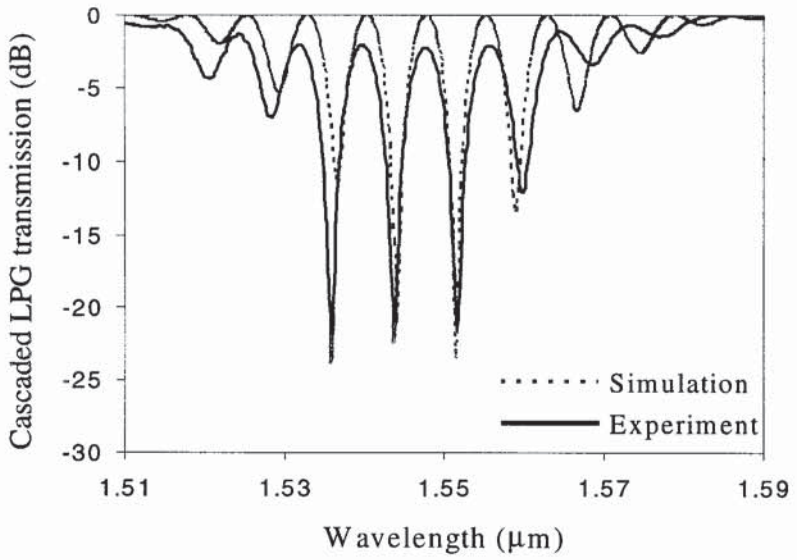

Figure 6.12 A comparison of theoretical and experimental transmission spectra of a cascaded long-period fibre grating, ($\kappa_{0m}L_i = \pi/4$, L_i=10mm, d=50mm)

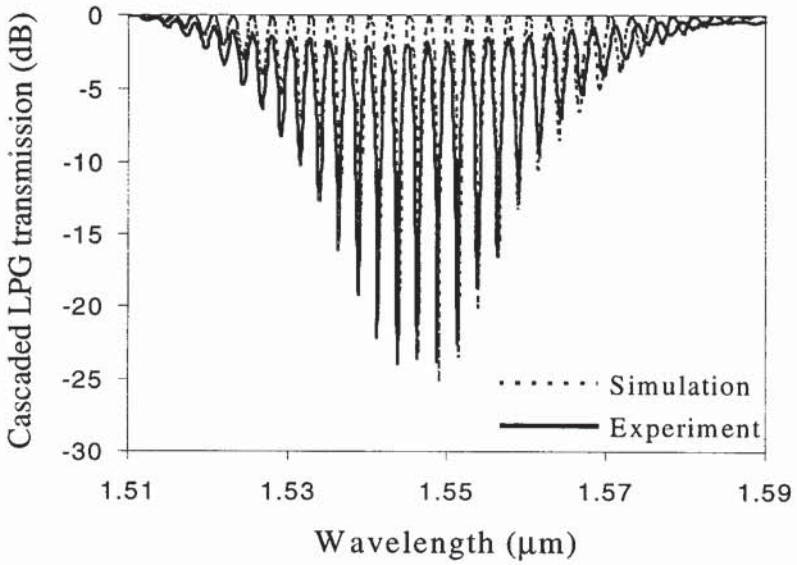

Figure 6.13 A comparison of theoretical and experimental transmission spectra of a cascaded long-period fibre grating, ($\kappa_{0m}L_i = \pi/4$, L_i=10mm, d=190mm)

To summarise, a simple analytical expression with clear physical meaning described by Mach-Zehnder interferometer for the transmission spectra of both phase-shifted and cascaded long period grating devices has been derived. By selecting different phase shifts and their locations, a tailored spectral response can be obtained suitable for many applications such as EDFA gain flattening. With cascaded long-period gratings, multiple peak transmission spectra have been obtained both in simulation and experiment. These have sharper spectral features than single long-period grating making them more suitable for use in sensing applications.

6.4 Chapter Summary

The theoretical and experimental investigation of long-period fibre gratings has been discussed in this chapter. The fabrication technique using the UV beam multiple scanning across an amplitude mask was adopted experimentally. With the increase in UV exposure, the resonance of long-period fibre gratings shifts to longer wavelength side. Up to 100nm shift has been observed and the resonance loss exhibits periodic changes. A comparison between calculated shifts and experimental results exhibits a good linear characteristic against the coupling strength. The calculated and experimental spectra are in excellent agreement. During the process of the hydrogen out- and in-diffusion from the fibre core and cladding, the resonance of long period gratings shift significantly, indicating two dominated processes of the hydrogen out-diffused from the fibre cladding and core, respectively. Up to 150nm shift was observed experimentally.

As complex structures, phase-shifted and cascaded long-period fibre gratings have been discussed. A simple analytical expression for the transmission spectra of both phase-shifted and cascaded long period grating devices has been presented. This allows for visualizing the physical picture as Mach-Zehnder interferometer. Calculated results show that by selecting different phase shifts and their locations, a tailored spectral response is obtained which maybe suitable for many applications like EDFA gain flattening. By cascading two 3dB long-period fibre gratings, multiple peak transmission spectra have been obtained both in simulation and experiment. These have sharper spectral features than normal long-period fibre grating, making them more suitable for use in sensing applications with enhanced spectral resolution.

CHAPTER 7

APPLICATIONS OF FIBRE GRATINGS

This chapter is the third part of this thesis, containing six relatively independent sections to present novel applications using fibre Bragg grating and long-period fibre grating structures. These applications are:

(1) Bragg grating edge filters based on tilted chirped gratings;

(2) Bragg grating intensity and wavelength division multiplexing sensing;

(3) Bragg grating based wide stop-band narrow transmission filters;

(4) Long-period fibre grating index sensing;

(5) Long-period fibre grating transverse pressure sensing;

(6) Long-period fibre grating bend sensing

The last section of this chapter is the summary.

7.1 Fibre Edge filters - Tilted Chirped Bragg Gratings

This section discusses a new technique for fabricating fibre edge filters with arbitrary spectral response based on tilted chirped fibre Bragg grating structures. The dependence of the spectral response on the tilting angle, chirp-rate, fibre type and the coupling strength are discussed. The near-linear wavelength response with tailorable slope efficiency is demonstrated over the filtering ranges from 2nm to 20nm. To demonstrate the application, the tilted chirped fibre grating edge filter was successfully used in fibre Bragg grating strain/temperature sensing for interrogating the Bragg wavelength shift by measuring the power intensity.

7.1.1 Introduction

Optical edge-filters have been used for interrogating fibre Bragg grating sensors based on the principle of converting the detection of a Bragg wavelength shift into optical intensity measurement [162, 163, 164, 165]. This interrogation technique has advantages of low-cost, fast response and ease of use. However, the majority of the edge-filters, which have been used so far are, either of the bulk configurations [162, 163] which offer suitable spectral performance, but suffer from fibre incompatibility, introducing high insertion loss, or of the wavelength-selective fibre devices, *e.g.* WDM fibre coupler [164, 166, 167], which do not provide high slope-efficiency and broad filtering-range. Recently, long-period gratings have been employed as edge-filters for interrogating fibre Bragg grating sensors [100, 168, 169]. Despite the low insertion loss and relatively high slope-efficiency they provide, long-period gratings are too sensitive to bending and environmental conditions. Furthermore, their spectral response cannot be tailored freely during fabrication. The suitability and availability of long-period gratings as edge-filters are, thus, limited for many applications.

Tilted uniform-period Bragg gratings have been used to flatten the gain-band of Er-doped fibre amplifiers by out-taping the light around 1530nm-region. This optical power out-tapping function results from the enhanced coupling between the guided light in the fibre core and the radiation mode field in a counter-propagating direction [170]. The radiation mode out-coupling, proportional to the tilting angle, generates a transmission loss peak at the short wavelength side of the Bragg resonance. The Bragg resonance also shifts to the long wavelength side as the fringes are tilted. The band-gap between the transmission loss peak and the Bragg resonance is determined by the NA of the fibre, typically a few nm for B/Ge co-doped and standard telecom fibres.

In the case of a tilted broadly chirped grating, the loss peak induced from radiation mode out-coupling is spectrally superimposed on the broad Bragg resonance, therefore, resulting in one broad transmission loss peak. The spectral response of this loss peak depends on the tilting angle, chirp rate and coupling strength. It is this dependence which

provides a basis for designing and fabricating fibre edge-filters.

7.1.2 Coupled-mode equation for tilted fibre Bragg gratings

The coupled-mode equation for radiation mode is given by [121, 170, 171, 172]

$$\frac{da^{+}(z)}{dz} = -\bar{\beta}\,\bar{\alpha}a^{+}(z) \tag{7.1}$$

where

$$\bar{\alpha}(z) = \kappa^{2}(z)\sum_{q}\frac{\beta\pi}{\rho}\left|\nu_{pq,01}\right|^{2} \tag{7.2}$$

$$\nu_{pq,01} = \frac{\bar{n}c\varepsilon_{0}}{2}\sqrt{\frac{1}{P_{\alpha q}P_{\alpha' q'}}}\int \vec{E}_{\alpha q}^{-*}(x,y)\times\exp\left(-2i\frac{2\pi}{\Lambda}x\sin\delta\right)\vec{E}_{\alpha' q'}^{+}(x,y)dxdy \tag{7.3}$$

where δ is the tilting angle of the grating index fringes. Clearly, when $\delta \neq 0$, the coupling of the radiation mode and cladding modes are significantly enhanced.

7.1.3 Fabrication of tilted fibre Bragg gratings

Tilted fibre Bragg gratings were fabricated holographically, as illustrated in Figure 4.1. In order to introduce a tilting angle into the grating fringes, the photosensitive fibre was mounted on a rotation stage for fibre-tilting operation and the fibre is slanted with angle (θ), as shown in Figure 7.1.

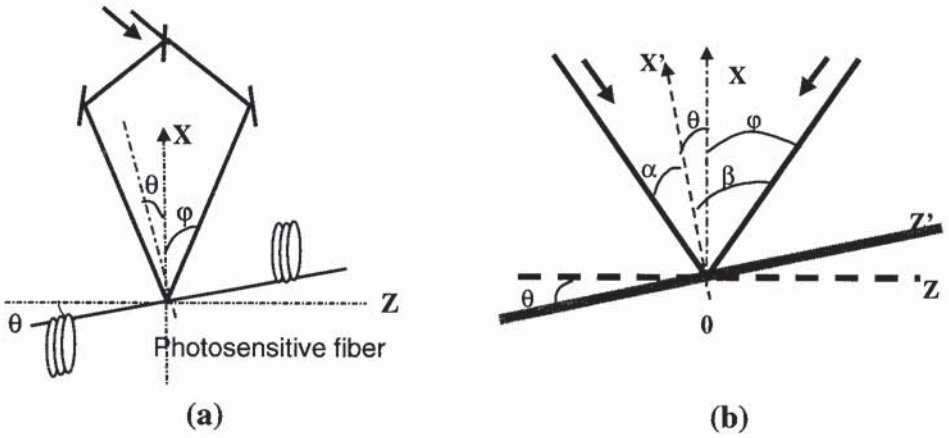

Figure 7.1 Schematic diagram of the optical set-up for fabricating titled fibre Bragg gratings using the two-beam holographic method

Due to the refraction of the UV beam at the interfaces of, air and the fibre cladding, the fibre cladding and fibre core, the tilting angle (δ) of the grating fringes is less than the slanting angle (θ). As illustrated in Figure 7.1, the meeting angle of the two UV beams is 2φ symmetrical to the **x**-axis. In the new X'-Z' coordinates system, the incident angles of the UV beams with respect to the new **x**'-axis are given by

$$\begin{cases} \alpha = \varphi - \theta \\ \beta = \varphi + \theta \end{cases} \tag{7.4}$$

where $\theta = \frac{1}{2}(\beta - \alpha)$ is the slanting angle of the fibre; $\theta = 0$ is the case of a non-slanted grating. The refraction of the UV light through air, the fibre cladding and core, yield

$$\begin{cases} \sin(\alpha) = n_{cl} \sin(\alpha^{cl}) = n_{co} \sin(\alpha^{co}) \\ \sin(\beta) = n_{cl} \sin(\beta^{cl}) = n_{co} \sin(\beta^{co}) \end{cases} \tag{7.5}$$

where n^{co} and n^{cl} are the refractive indexes of the *UV* beam in the fibre core and cladding, respectively. Using eqn. (7.5), the tilting angle of grating fringes is obtained as,

$$\delta = \frac{1}{2}\left\{ \arcsin\left[\frac{\sin(\varphi + \theta)}{n_{co}}\right] - \arcsin\left[\frac{\sin(\varphi - \theta)}{n_{co}}\right]\right\} \tag{7.6}$$

where $\delta = \frac{\beta^{co} - \alpha^{co}}{2}$ indicates the tilting angle of grating fringes. In experiment, $\theta << \varphi << 30^{\circ}$, with an approximation, eqn. (7.6) reduces to

$$\delta \approx \theta / n_{co} \tag{7.7}$$

Clearly, the tilting angle is less than the slanting angle, $\delta < \theta$. Using eqn. (4.6), the Bragg wavelength of a slanted grating is given by

$$\lambda = 2n_{eff} \frac{\lambda_{UV}}{\sin(\varphi - \theta) + \sin(\varphi + \theta)} \tag{7.8}$$

Rearranging eqn. (7.8), the shift of the Bragg wavelength relative to the non-slanted grating is given by

$$\lambda - \lambda_0 = \lambda_0 \left[\frac{1}{\cos(\theta)} - 1 \right] \tag{7.9}$$

where $\lambda_0 = \frac{n_{eff} \lambda_{UV}}{\sin(\varphi)}$ is the Bragg wavelength of the non-slanted grating. Obviously, with the increase of the slanting angle the grating wavelength shifts to long wavelengths.

7.1.4 Tilted uniform fibre Bragg gratings

The configuration of the tilted linear grating is shown in Figure 7.2 (a) and the experimental transmission spectrum is shown in Figure 7.2 (b). It can be seen clearly the enhanced cladding modes and the radiation mode located at the short wavelength side of the Bragg resonance. The coupling of the cladding modes disappears immediately when grating is immersed in index matching liquid, exhibiting a smooth profile as shown in Figure 7.2 (b).

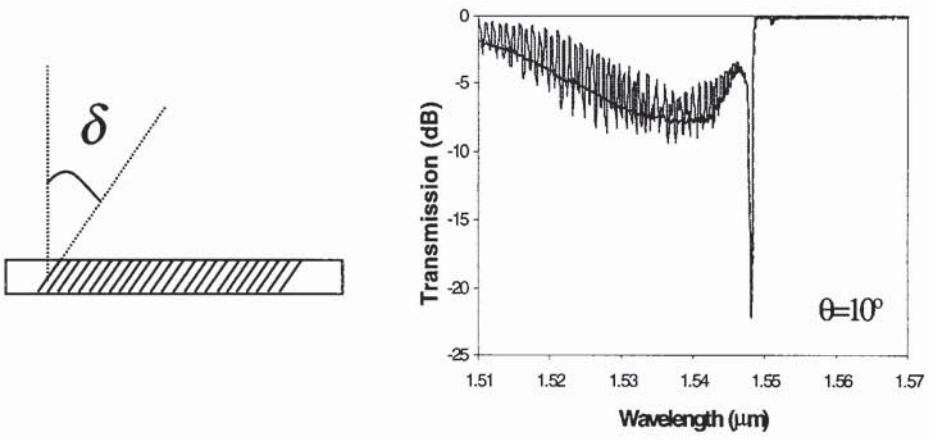

Figure 7.2 (a) Structure of tilted linear fibre Bragg gratings, (b) Transmission spectra of the tilted grating in air (with oscillations) and in the index matching liquid (smooth line), showing radiation mode loss and the removed cladding modes

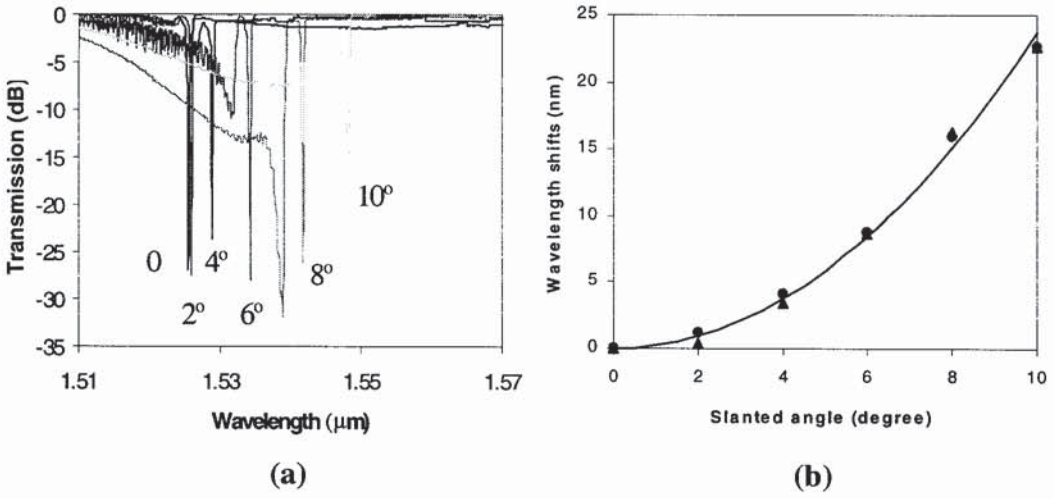

Figure 7.3 (a) Transmission spectra of the Bragg grating with different slanting angles: θ=0, 2°, 4°, 6°, 8°, 10°; (b) Solid line indicates the calculated shifts using eqn. (7.9), round and triangle points indicate the experimental measurements.

A series of tilted linear gratings for different values of slanting angle were fabricated and the transmission spectra were measured with the index matching liquid to remove the coupling of cladding modes. As shown in Figure 7.3 (a), the Bragg wavelength shifts to a longer wavelengths. Using eqn. (7.9), the calculated and the experimental wavelength

shifts are in good agreement as shown in Figure 7.3 (b).

7.1.5 Tilted chirped fibre Bragg gratings

Clearly, tilting grating fringes results in degrading the grating level because of the enhanced coupling of cladding modes and the radiation mode. However, when tilting a chirped grating, the coupling of the cladding modes is suppressed or removed automatically and the tailing of the radiation mode produces a grating slope edge filter.

The configuration of a tilted chirped grating structure and experimental spectrum are shown in Figure 7.4 (a) and (b). Note that, the spectrum is measured in air, exhibiting the absence of the cladding modes.

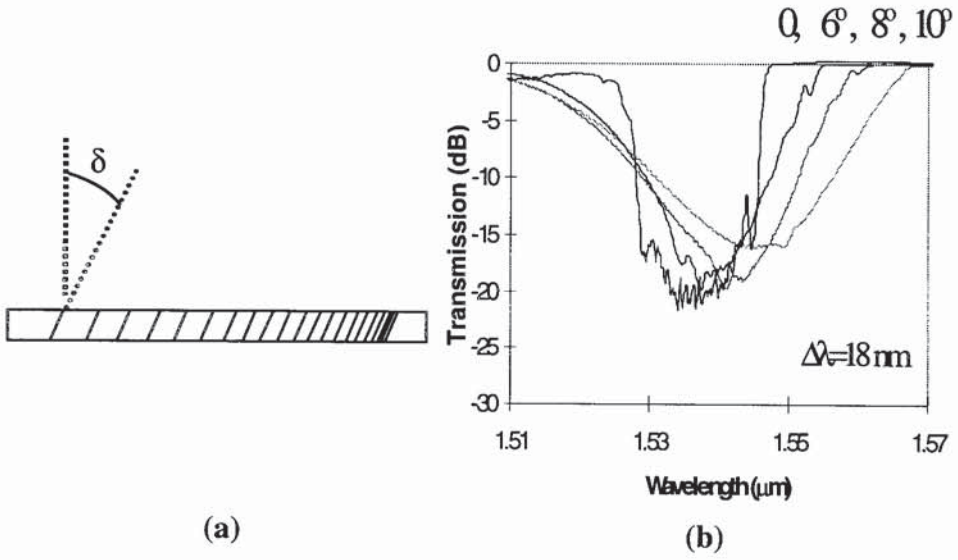

Figure 7.4 (a) Structure of a tilted chirped fibre Bragg grating; (b) Transmission spectra of 18nm bandwidth tilted chirped gratings with different slanting angles: 0, 6°, 8°, 10°

Figure 7.4 (b) shows the transmission profiles of four tilted chirped gratings with 18nm chirp-rate with slanting angles of 0°, 6°, 8° and 10°. The 0°-slanted chirped grating gives a near-square-like transmission response. When tilting a chirped grating, a remarkably broadened transmission loss peak with two edge slopes is formed, giving a typical edge-filter profile. As the slanting angle increases, the loss peak broadens while its central

wavelength shifts to long wavelengths. The slope-efficiency decreases as the grating coupling strength decreases. For a set of slanting angles, the transmission spectra of the chirped gratings with 13nm and 18nm bandwidths are shown in Figure 7.5 (a) and (b), respectively.

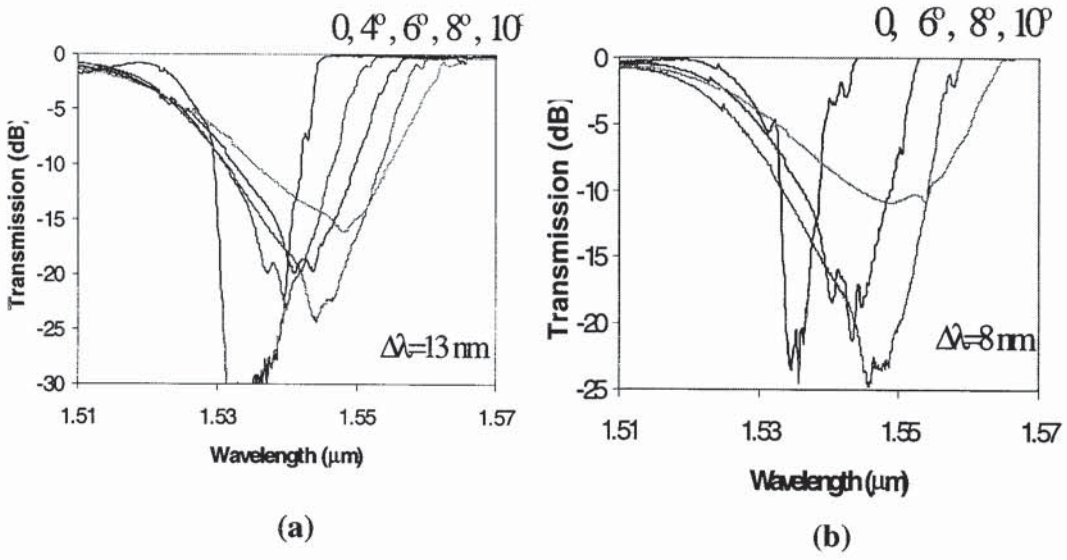

Figure 7.5 Transmission spectra of tilted chirped gratings with different slanting angles and chirps: (a) 13nm chirp but slanting angles: 0, 4°, 6°, 8°, 10°; (b) 8nm chirp but slanting angles: 0, 6°, 8°, 10°

Figure 7.6 shows the transmission profiles of three gratings with chirp rates of 8nm, 12nm and 16nm for an 8°-slanting angle. It shows that the bandwidths and the centres of the loss peaks are very similar for three different chirp rates indicating they are only slanting angle dependent, but the slope efficiency and the grating coupling strength decrease with the increase of the chirp rate. The grating with smaller chirp has the smaller dynamic spectrum region and deep slope while the grating with larger chirp has the larger dynamic spectrum region but shallow slope. For the same slanting angles and chirps, three grating spectra are illustrated in Figure 7.6 (b), illustrating good experimental repeatability in making such a device.

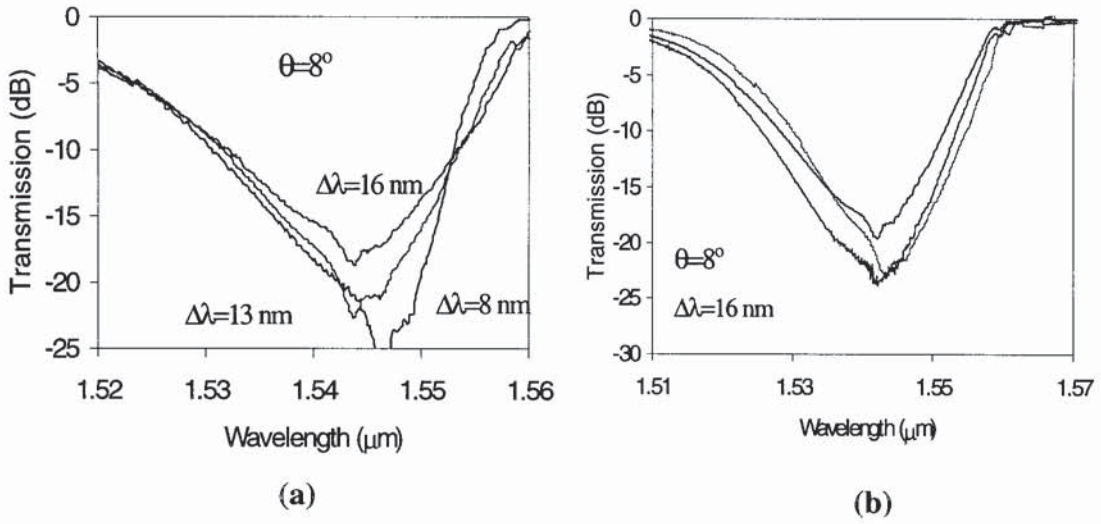

Figure 7.6 Transmission spectra of tilted chirped gratings, (a) 8° slanting angle but different chirps: 8nm, 13nm, and 16nm; (b) 8° slanting angle and 16nm chirp illustrating good experimental repeatability

The edge-filter-like spectral response of a tilted chirped grating formed by the superimposition of the radiation mode out-coupling loss and the broad Bragg resonance was experimentally confirmed by measuring the reflection from both short and long wavelength sides of the chirped grating. Figure 7.7 shows the measured two reflections and a transmission for a tilted grating with a 16nm chirp and an 8° slanting angle. The reflection shows the full bandwidth of ~16nm when it is measured from the short-wavelength side, whereas only ~2-3nm when measured from the long-wavelength side. The latter suggests that the radiation mode out-coupling actually occurs at 2-3nm shorter wavelength side from the longest Bragg resonance. Clearly, the broad transmission loss peak of the tilted chirped grating originates from the 'chirping' radiation mode out-coupling. The asymmetry of the loss peak is due to the fact that the slope edge at short wavelength side arises only from the radiation mode out-coupling, whereas the long wavelength side edge is the superimposition of this coupling loss and the Bragg resonance. This was further confirmed by a computer-performed superimposition of the transmission spectra of a succession set of 200 tilted uniform-period gratings as seen from Figure 7.2 (b). The resultant final response is a broad transmission loss peak and the ripples resulting from the cladding mode coupling are suppressed giving a smooth

response. This peak is remarkably similar to the measured transmission spectrum of the tilted chirped grating in Figure 7.5, Figure 7.6 and Figure 7.7.

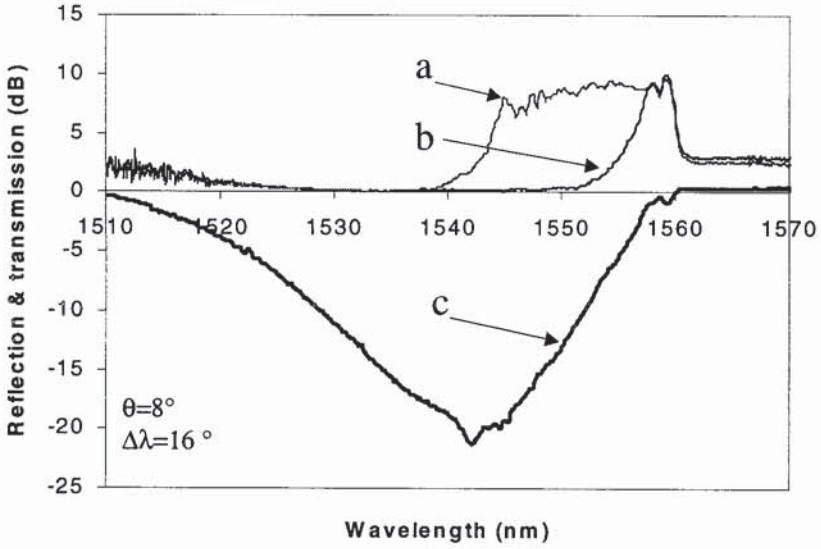

Figure 7.7 Typical spectra of a tilted chirped fibre Bragg grating: (a) and (b) indicate the spectra reflected from the short and long wavelength sides, respectively; (c) indicates the transmission spectrum

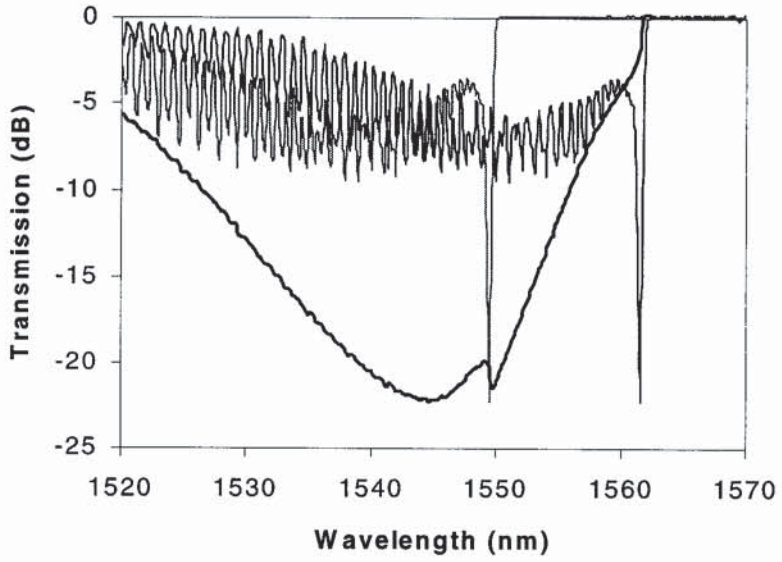

Figure 7.8 A graph showing the cancellation of cladding modes resulting from the average 200 linear gratings, which consist of the step chirped grating structure

In cladding depressed fibre, which is designed for decreasing the radiation mode and shifting the radiation mode to even short wavelength, the spectrum of the tilted linear grating with different slanting angle is shown in Figure 7.9 (a). The radiation mode is depressed even the slanting angle is 12°. This kind of fibre, therefore, is not suitable to make such an edge filter. The transmission spectrum of the tilted chirped grating in this kind of fibre is shown in Figure 7.9 (b). Clearly, the slope produced by radiation mode is out of the Bragg wavelength.

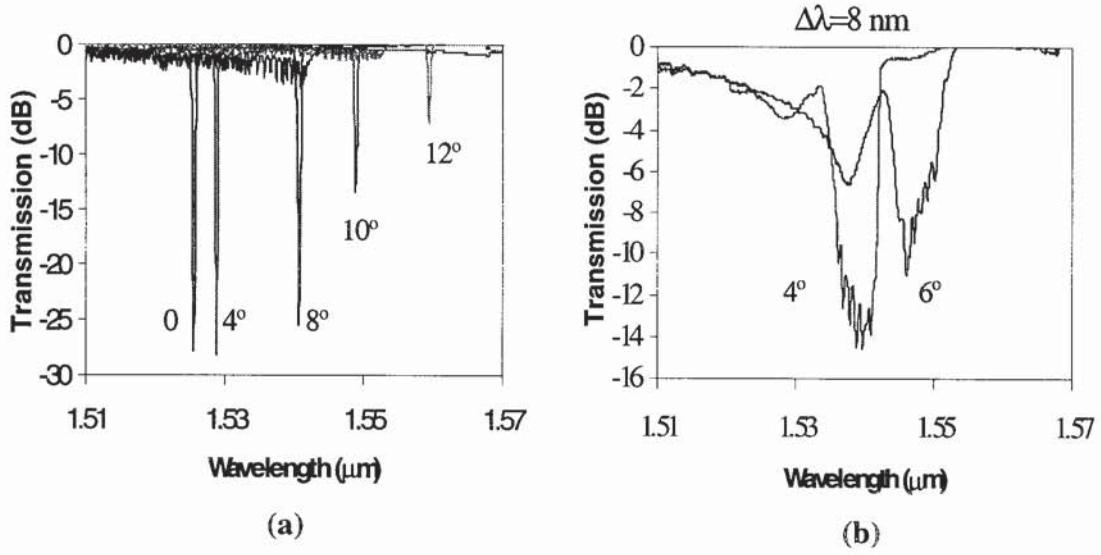

Figure 7.9 Transmission spectra of tilted fibre gratings fabricated in cladding depressed fibre, showing the suppressed radiation mode: (a) tilted linear grating with different slanting angles: 0°, 4°, 8°, 10°; (b) 8nm bandwidth tilted chirped gratings with different slanting angles: 4° and 6°

7.1.6 The application of the fibre edge filters

As an application, a tilted chirped fibre grating edge filter was used in a grating sensing systems to interrogate the Bragg wavelength shifts of the sensor head grating induced by the applied strain. As shown in Figure 7.10, the broad band light source is coupled into the sensor head grating for strain measurement through 3dB coupler C_1. The light reflected by the sensor head grating encoded the unknown strain by Bragg wavelength shifts is coupled to detector D_1 and D_2 through 3dB coupler C_1 and C_2 respectively. It is

clear that the wavelength shift of the reflected light is converted into an intensity signal measured by detector D_2. The measurement of detector D_1 is only for normalization to cancel out the fluctuation of the light source.

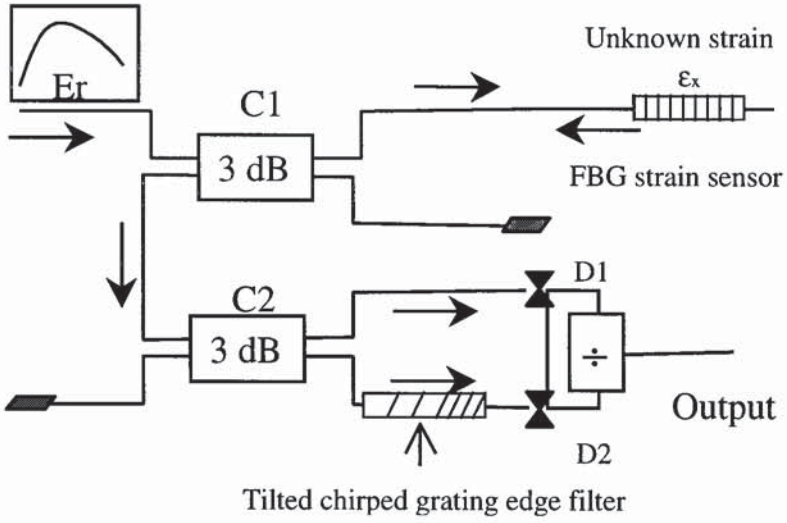

Figure 7.10 Experimental arrangement of fibre Bragg grating sensing systems using a tilted chirped fibre grating edge filter for interrogating the wavelength shifts

The spectrum after the tilted chirped grating edge filter is shown in Figure 7.11 (a). The normalized output of detector D_2 against the applied strain is shown in Figure 7.11 (a), exhibiting a good linearity.

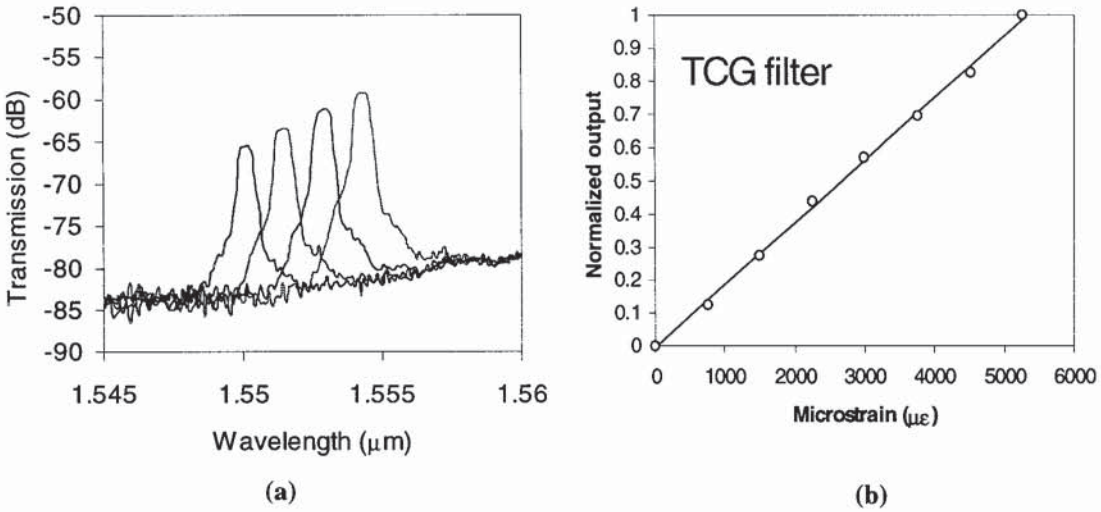

Figure 7.11 (a) The transmitted spectra of a tilted chirped grating edge filter; (b) the normalized output of intense measurement against the applied strain

To summarise, a new technique for fabricating fibre edge filters with arbitrary spectral response based on tilted chirped fibre Bragg gratings has been investigated. Experimental results show that a small chirp-rate and slanting angle result in a high slope-efficiency with a relatively small filtering range, and *vice versa*. The slope efficiency is also dependent on the maximum obtainable grating coupling strength, which is higher in B/Ge co-doped fibre than in standard telecom fibre. The central wavelength of the transmission loss band depends on the original Bragg wavelength and the slanting angle. Clearly, fibre edge-filters with arbitrary characteristics can be fabricated based on a tilted chirped grating utilising all these controllable parameters. Experimentally slope efficiency from 0.5dB/nm to 10dB/nm and filtering range from 2nm to 20nm has been demonstrated. An application in strain sensing using this kind of edge filters for interrogating the shift of the Bragg wavelength has been demonstrated experimentally.

7.2 Bandpass Filters

This section presents a high-rejection/low-loss bandpass filters theoretically and experimentally by cascading four chirped fibre Bragg gratings. The bandpass filters with 50nm stop-band and 1nm transmission located at wavelength 1555nm have been achieved experimentally.

7.2.1 Introduction

Fibre Bragg gratings are increasingly becoming important devices for applications in optical fibre telecommunications, signal processing and optical sensing. With advances in these areas, non-standard gratings, such as chirped, array and bandpass structures, now are especially in great demand. To date several methods have been demonstrated to fabricate bandpass filters [133, 134, 135, 173]. However, the bandpass structure with low-loss passband and high-rejection stop-band covering the entire ASE (amplified spontaneous emission) spectral range of EDFA (Er-doped fibre amplifier) has proved technically difficult. Although previously reported single-passband filters fabricated in hydrogenated B/Ge photosensitive fibre by chirped grating concatenation method achieved 30dB rejection for a 50nm stop-band, the loss in the passband was 5dB which is too high for applications [173]. Single bandpass filters by a post-UV exposure to introduce a π phase shift also showed 2dB loss in passband but the maximum rejection of the stop-band was only 9dB [135]. The low rejection of the stop-band and the high loss in the passband were mainly due to the limited photosensitivity of the fibre and the intrinsic cladding mode out-coupling loss. The spectral gaps between the Bragg resonance and the nearest cladding mode resonance are, typically, ~2nm for the standard telecom and B/Ge co-doped fibres and 6nm for high Ge doped fibre. Inevitably the cladding mode out-coupling occurs inside the stop-band of the broadly chirped gratings, consequently resulting in loss in the passband.

To tackle this problem, Dong *et al.* recently developed a cladding depressed photosensitive fibre [174]. In this fibre a depressed cladding is added between the

photosensitive core and the normal cladding. Such a depressed cladding effectively reduces the cladding mode field strength over the core region and therefore reduces the coupling strength between the guided mode to the cladding modes. We have carried out the fabrication of single bandpass filters in this fibre by chirped grating concatenation method. 50dB rejection has been achieved for 50nm wide stop-band and the loss in passband has been significantly reduced to ~1dB.

7.2.2 Calculated spectrum

The wide-stop-band single bandpass filters were specified and requested for WDM (wavelength-division-multiplexing) application by the European PHOTOS (PHOtosensitive Technology for Optical Systems) programme. The structure of the bandpass filters is shown in Figure 7.12. The initial specifications were defined as:

Passband: central at 1555nm; FWHM 1-3nm; loss < 2dB.
Stop-band: 50nm from 1520nm to 1570nm; rejection >30dB.
Device length: grating length <25mm; stripped fibre length <44mm.

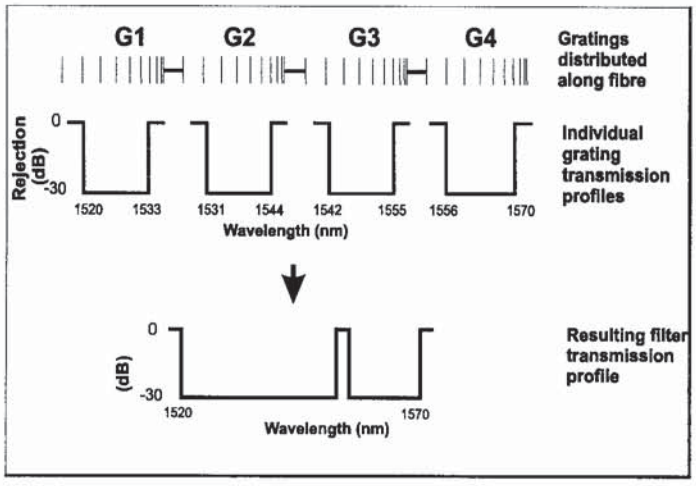

Figure 7.12 Schematic diagram showing the structure of bandpass filter by cascading four chirped fibre Bragg gratings

As detailed previously, the modelling of this kind of grating structure based on matrix transforms, expressing each chirped grating G_i (i=1, 2, 3, 4) and the gap between two neighbouring gratings by corresponding matrix, the matrix for the whole grating structure is obtained as

$$M = M^4 \cdot S_3 \cdot M^3 \cdot S_3 \cdot M^2 \cdot S_1 \cdot M^1 \tag{7.10}$$

where

$$M^i = M_N^i \cdot M_{N-1}^i \cdot M_{N-2}^i \cdots M_1^i \tag{7.11}$$

where, M^i (i=1, 2, 3, 4) indicates the matrix of chirped grating G_i, M_j^i (j=1, 2, .., N) is the matrix for each short length sub-grating given by eqn. (3.90), L_i and $\Delta\lambda_i$ are the length and chirp of grating G_i. S_i (i=1, 2, 3) is the matrix of the gaps between two neighbouring chirped gratings given by eqn. (3.99). Finally, the amplitude transmittance is given by eqn. (3.97) as $t = M11 - M12M21/M22$ and the calculated transmission spectrum is shown in Figure 7.13, where the condition of a linearly chirped profile has been used.

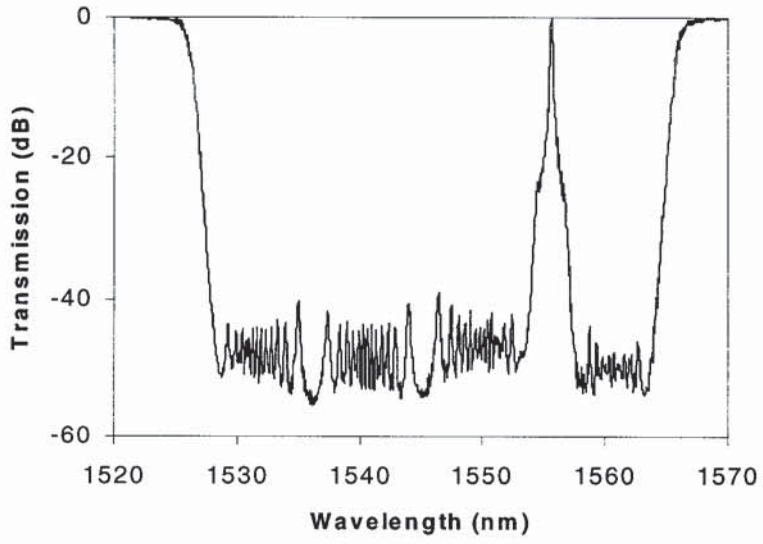

Figure 7.13 Calculated transmission spectrum of a bandpass filter by cascading 4 chirped Bragg gratings of 5mm long for κL=25, w_{01}=1531.65nm, $\Delta\lambda_1$=9.3nm, w_{02}=1540.65nm, $\Delta\lambda_2$=9.3nm, w_{03}=1549.9nm, $\Delta\lambda_3$=9.8nm, w_{04}=1560.75nm and $\Delta\lambda_4$=8.5nm

7.2.3 Experimental fabrication

Figure 7.12 has shown the design concept of grating cascading method. Four chirped gratings with a bandwidth of ~14nm were used. Three of them were centred at 1525nm, 1536nm and 1548nm respectively, ensuring the sufficient overlap in the spectra resulting in a stop-band of 34nm. The fourth chirped grating was centred at 1563nm in order to form a passband in the final structure. The overall spectrum from the concatenation gives a ~2nm passband at 1555nm with a 50nm stop-band covering from 1520nm to 1570nm [140].

The cladding depressed fibre used was hydrogenated prior to grating fabrication. The chirped gratings were fabricated holographically using the dissimilar wavefront method as shown in Figure 4.1. The stripped fibre was mounted on a translation stage. The length of each grating was ~5mm, with 1mm gap between each grating giving 24mm in length for the final structure. The growth of the gratings was monitored *in-situ* using a 980nm laser diode pumped EDFA and an optical spectrum analyser. The monitoring signal level was about 40-50dB, which was high enough to ensure examination of the full growth of the grating during the fabrication. Four chirped gratings were fabricated successively from the long wavelength to the short wavelength. The UV exposure for each grating was stopped when the rejection shown on the optical spectrum analyser reached 40-50dB. Figure 7.14 shows that the recorded spectrum for each exposure indicating clearly the sufficient spectral overlap between the three short wavelength chirped gratings and an accurate separation between them. The spectral gap between the first and the second grating is used to form a ~2nm passband at ~1554nm (slightly shorter than specified in order to accommodate the stretching effect in the packaging process). The fabrication process was repeatable as five spectrally identical filters were reproduced at the time. The rejection achieved for the stop-band was around 50dB. The loss in the passbands was about 1dB. This was confirmed by post fabrication re-measurement using the tunable laser at high resolution.

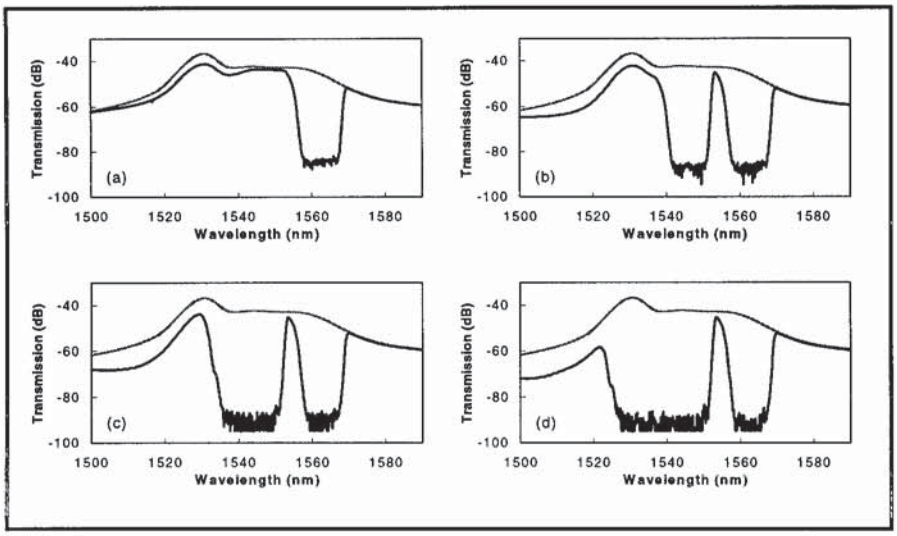

Figure 7.14 Transmission spectra for illustrating the forming process of the bandpass filters cascaded by (a) One CFBG, (b) two CFBGs, (c) three CFBGs, (d) four CFBGs.

For comparison, the bandpass filters were also produced in hydrogenated B/Ge co-doped, high Ge-doped and photosensitive cladding depressed fibres under identical conditions. The transmission spectrum of single bandpass filters produced is shown in Figure 7.15 (a), (b) and (d). The rejections achieved in the former two fibres were considerably lower (≈30dB) and the loss in the passband was much higher (3-5dB). Figure 7.15 (c) shows the transmission spectrum of a bandpass filter with a 50nm stop-band previously fabricated using the post-fabrication UV exposure method. As the entire structure of this filter was based on one broadly chirped grating, the rejection was only 9dB and the loss in the passband was about 2dB. Even with such a low rejection, it has shown an effect of suppression of ASE noise when used in a soliton transmission system to give Gordon-Haus jitter reduction [175]. The high-rejection and low-loss filters being reported here are expected to perform considerably better in WDM transmission testing system being developed by PHOTOS programme.

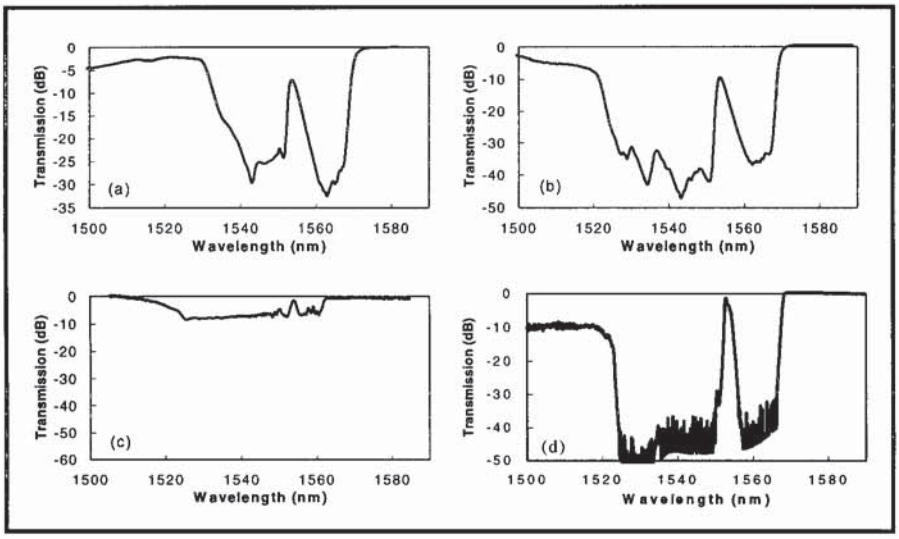

Figure 7.15 Transmission spectra of bandpass filters in different fibres, (a) B/Ge-doped fibre, (b) Hi-Ge-doped fibre, (c) Post-exposure method B/Ge-doped fibre, (d) Cladding depressed fibre

In summary, high-rejection/low-loss single bandpass filters have been successfully fabricated using specially designed and produced cladding depressed photosensitive fibre. For the first time, 50dB rejection has been achieved for 50nm wide stop-band covering the entire ASE range of EDFA. The suppression of the cladding mode out-coupling enables the formation of a low-loss passband within the broad stop-band.

7.3 Intensity and Wavelength Division Multiplexing Systems (IWDM)

This section details a new intensity and wavelength division multiplexing (IWDM) systems for addressing a fibre Bragg grating sensor array involving a novel concept of intensity and wavelength division multiplexing (IWDM). Experimental investigation shows IWDM can be used in fibre Bragg grating sensing to improve the capability in the same spectral region.

7.3.1 Introduction

Owing to their multiplexing capability, fibre Bragg gratings have attracted considerable interest as the most promising distributed sensing element for SMART structure applications [176]. Grating multiplexing techniques have been demonstrated including wavelength division multiplexing (WDM) [64, 177], time division multiplexing (TDM) [178], spatial division multiplexing (SDM) and their combinations [179, 180].

In comparison with the conventional WDM method, the proposed IWDM technique has an advantage of doubling the number of the fibre Bragg grating sensors to be multiplexed while keeping the same dynamic-range for each sensor. In order to utilise the intensity information, the sensor array addressed by the IWDM technique is formed from a set of spectrally distributed fibre Bragg gratings with low reflectivity (low-R) and high reflectivity (high-R) alternately placed along a fibre. It is this reflection-encoding that provides a mechanism for increasing the number of the sensors in the array, and consequently enhancing the multiplexing capacity of interrogation. In conjunction with the TDM and SDM, this technique will enable monitoring a very large number of fibre Bragg grating sensors.

7.3.2 The principle of IWDM

A schematic diagram of a fibre Bragg gratings multiplexing system using the proposed IWDM technique is shown in Figure 7.16. Fibre Bragg gratings in the sensor array are not just spectrally distributed but also reflection-encoded alternately with low-R and

high-R. This differs from the WDM where the reflectivity information is totally neglected. In WDM, the number of grating sensors (N) to be multiplexed is determined by the required operation wavelength domain ($\Delta\lambda$) of each grating sensor and the total useable bandwidth ($\Delta\lambda$) of the light source, i.e., $N \approx \Delta\lambda / \Delta\lambda_B$. Therefore, the adjacent gratings do not cross each other. In contrast, the reflectivity-encoding in IWDM allows the adjacent gratings to cross each other without losing their identity, so that an extra set of low-R gratings can be inserted alternately into the original high-R grating sensor array, resulting in the spectral spacing between the adjacent gratings being 1/2 of the original $\Delta\lambda$. Thus the total number of gratings can be multiplexed in the sensor array doubles, i.e., $2\times\Delta\lambda / \Delta\lambda_B$.

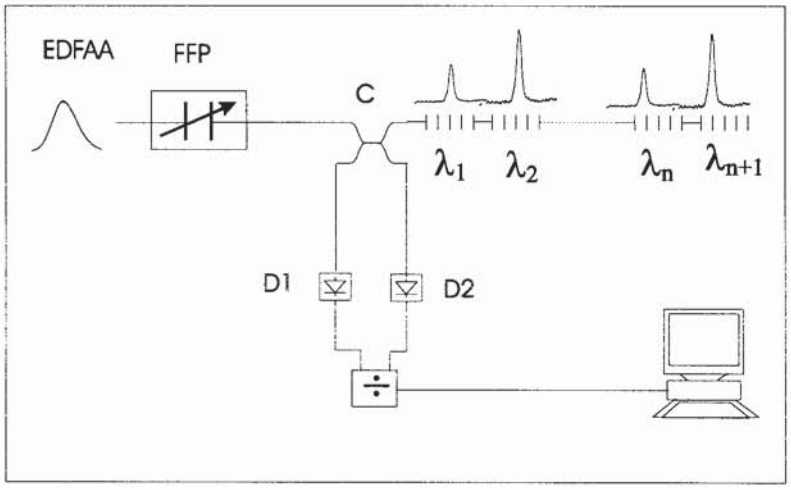

Figure 7.16 A schematic diagram showing the experimental arrangement of an IWDM system

However, as the grating has a certain bandwidth, the strain resolution in IDWM technique is inevitably limited when the low-R and high-R gratings cross to each other. The spectral crossing-behaviours and the achievable resolution using a 50% and a 95% reflectivity (50%-R and 95%-R) gratings with different bandwidths were investigated experimentally. In order to overcome the bandwidth-limited resolution, the dual-peak grating structure was then adopted in the interrogation. Both configurations are analysed in detail in the following sections.

7.3.3 Interrogation using 50%-R and 95%-R gratings

The first experiment carried out to evaluate the IWDM principle was to examine the spectral crossing behaviour of a 50%-R and a 95%-R gratings in an array with a 2nm spectral spacing and a typical grating bandwidth of ~0.4nm. The 95%-R grating was kept strain free while the 50%-R grating was strained in steps 80 με up to 4000 με, which is equivalent to ~4nm of the wavelength shift. The spectral evolution of both gratings was recorded using an EDFA light source and an optical spectrum analyser and is presented in Figure 7.17.

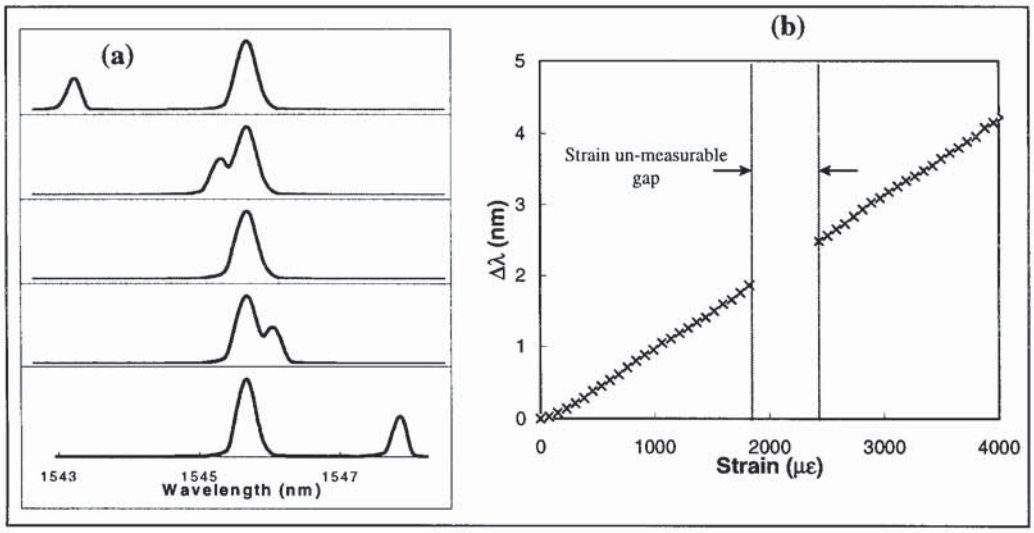

Figure 7.17 Schematic diagram of IWDM systems using low- and high- reflectivity gratings: (a) reflection profiles evolution with the applied strain; (b) wavelength shift against applied strain.

It clearly shows the 50%-R grating had crossed the 95%-R one in the strain process. The wavelength shift against the strain is plotted in Figure 7.17 (b). Both the apparent gap in the plot in Figure 7.17 (b) and the mono-peak position in Figure 7.17 (a) indicate that the strain could not be measured when the two gratings are spectrally overlap. In theory this gap can be minimised if the narrow spectral response gratings are used, but ultra narrow gratings will reflect less light to be measured, degrading the signal-to-noise ratio and resulting in inaccurate measurement. In order to reduce (or eliminate) this un-measurable strain range without using ultra-narrow gratings in the IWDM technique, we used the low-R grating with a dual-peak spectral response in the sensor array.

7.3.4 Interrogation using 50%-R dual-peaks and 95%-R gratings

The un-measurable strain range can be eliminated using the dual-peak low-R grating if the bandwidth of both peaks of the dual-peak grating is similar to that of the high-R grating. When the dual-peak grating is under strain, both peaks shift at the same rate so that the strain can still be measured from one peak when the other peak overlaps with the high-R grating. In the experiment, a 50%-R grating with a dual-peak profile replaced the original single-peak low-R grating and was then strained. The spectral response of both dual-peak low-R and high-R gratings was recorded and presented in Figure 7.18 (a). It shows that the strain-encoded wavelength shift can be measured from either peak of the dual-peak sensor and nevertheless resolved when both gratings overlap. The wavelength shifts of both peaks against the applied strain are plotted in Figure 7.18 (b) as cross-points and circular-points respectively. Although the gap, which corresponds to the region where strain cannot be accurately measured, still exists individually in each plot, however, it is much smaller if the strain measurement is taken from the alternative plot in the overlap region, suggesting the use of the dual-peak grating is effective. The remaining small gap is due to the relatively broad bandwidth of the high-R grating.

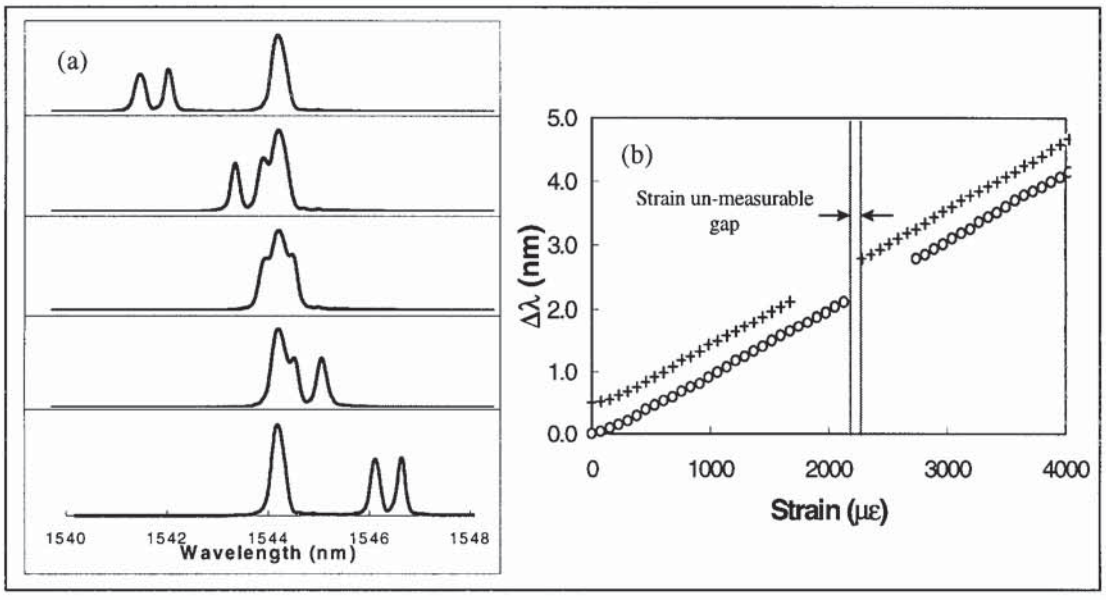

Figure 7.18 Schematic diagram of IWDM systems using dual-peak low-R grating and single-peak high-R wider line-width (0.35nm) grating: (a) reflection profile evolution; (b) wavelength shift of both peak against the applied strain

Further improvements were made by using a narrow high-R grating, as shown in Figure 7.19 (a); the experiment was repeated with this grating and the gap virtually disappeared indicating the resolution was not limited by using dual-peak grating in IWDM.

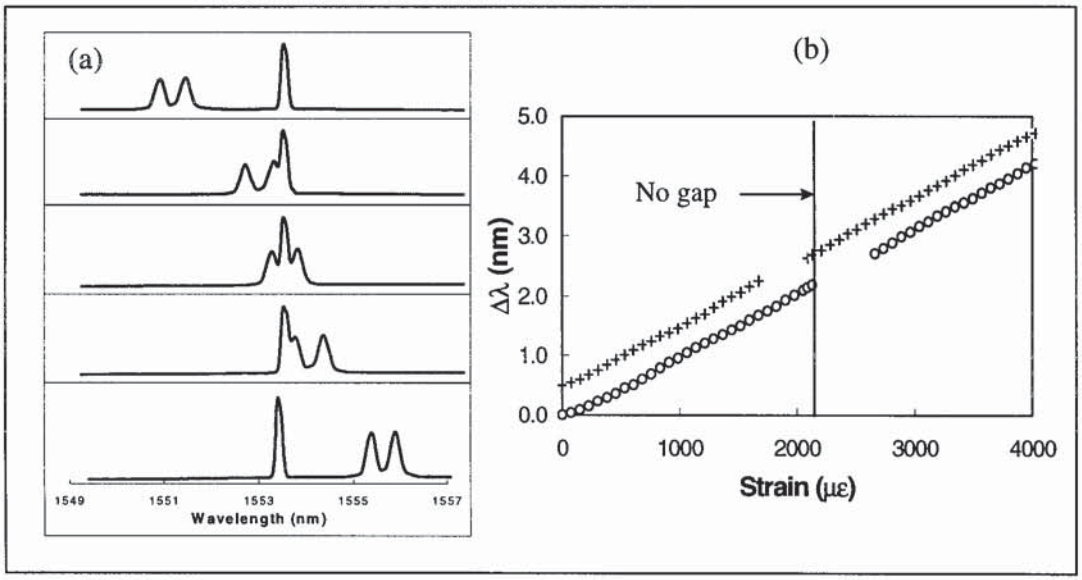

Figure 7.19 Schematic diagram of IWDM systems using dual-peak low-R grating and single-peak high-R narrower line-width (0.1nm) grating: (a) reflection profile evolution; (b) wavelength shift of both peaks against the applied strain

7.3.5 Realisation of a practical IWDM system

A practical system using the configuration of Figure 7.16 for implementing IWDM technique was demonstrated experimentally. The reflectivity-encoded and spectrally distributed grating arrays were fabricated using scanning phase mask technique.

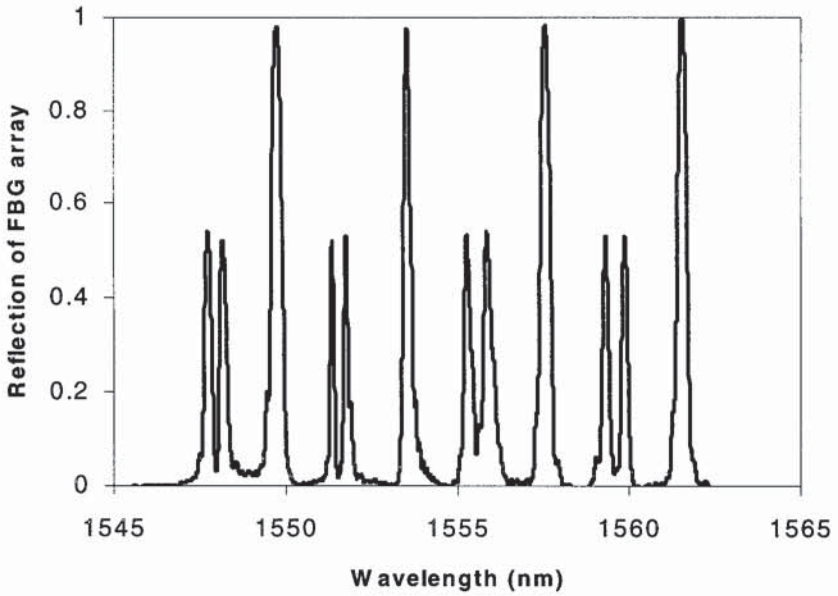

Figure 7.20 A graph showing the reflection spectrum of a grating array for IWDM systems

The interrogation system employed a tunable fibre Fabry-Perot filter with a FSR of 40nm. The reflection spectra were captured from the Fabry-Perot filter and thus the peak wavelengths are obtained by data processing of the peak-detection. The shifts of the wavelengths and the corresponding strains are then achieved. Since the fibre Fabry-Perot filter can work up to tens Hz, this system provides almost real time measurement. The LabVIEW control panel for this IWDM system is shown in Figure 7.21.

To summarise, a novel concept of multiplexing fibre Bragg grating sensors using the combination of reflection intensity and wavelength division multiplexing has been proposed and evaluated. In contrast to WDM, by using the intensity information, the IWDM permits the adjacent gratings crossing each other in the sensor array to multiplex more gratings in a single fibre. Furthermore, the strain resolution in the grating overlap region was remarkably improved by utilising the dual-peak reflection-encoded gratings into the sensor array. It is believed that in conjunction with TDM and SDM, this new technique will significantly enhance the multiplexing capacity of fibre grating strain sensing for SMART structure applications.

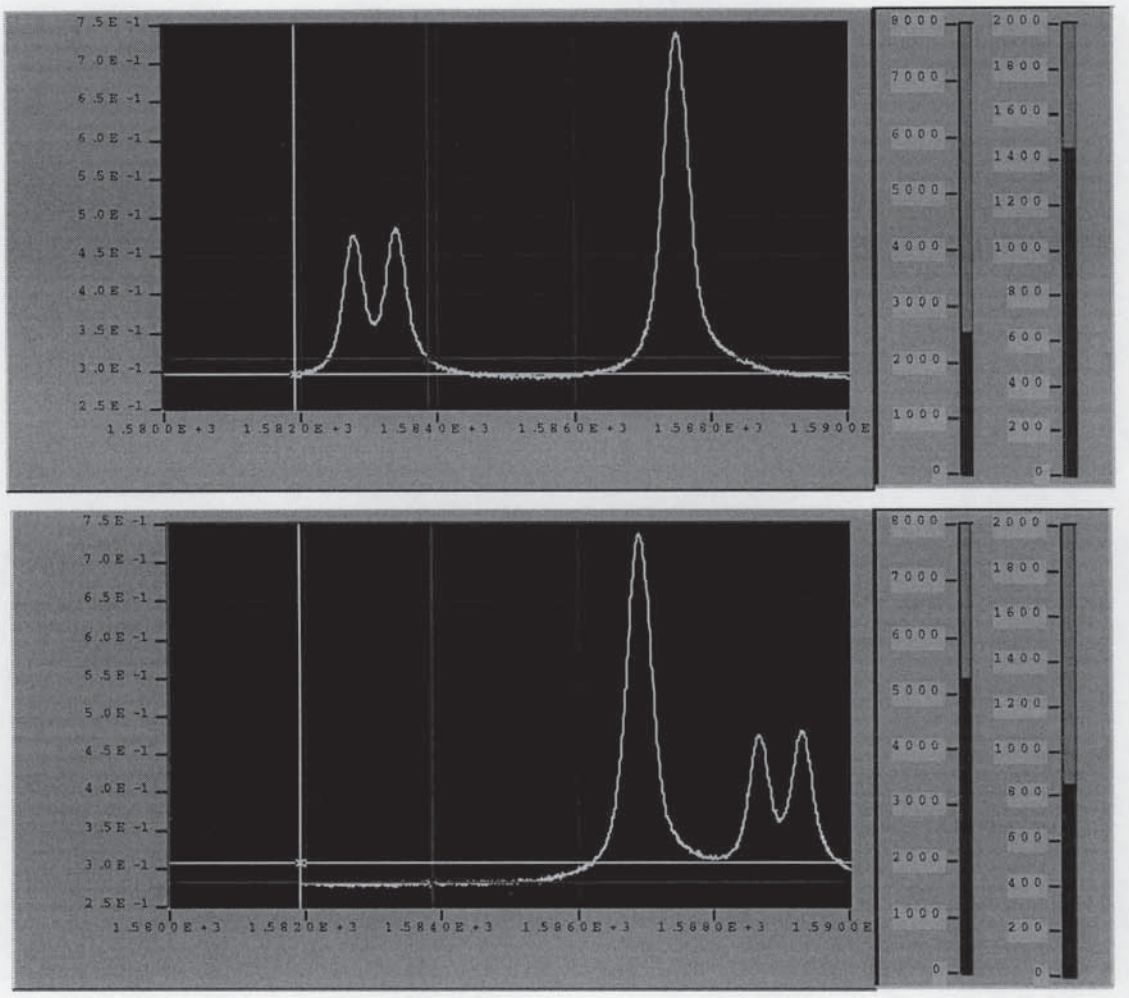

Figure 7.21 Schematic diagram of LabVIEW control panel for the real time measurement of IWDM systems

7.4 Refractive Index Sensing Using Long-period Fibre Gratings

This section details theoretically and experimentally the index sensing using long-period fibre gratings. With the increase of the ambient index, the resonance wavelengths of long-period fibre gratings shift to short wavelengths. When the ambient index is equal or larger than the cladding mode index, the maximum blue shift and the constant red shift were observed, respectively.

7.4.1 Introduction

Long-period fibre gratings are widely used as filters or sensors [100, 101]. The fundamental guided mode is coupled into forward propagating cladding modes through long-period index modulation [158]. The peak wavelengths of cladding modes are sensitive to the applied strain, ambient temperature, and index, which changes the coupling condition and would be encoded into the wavelengths of the resonance peaks. The wavelengths of cladding modes shift to short wavelengths by increasing the grating ambient refractive index [102, 107, 181]. With further increase in the ambient index to reach that of the cladding mode index, the shift of this cladding mode reaches its maximum and disappears since there is no boundary for the fibre cladding. When the ambient index is larger than the cladding mode index, this cladding mode reappears at the position of a longer wavelength compared with the case of air ambient. The maximum shift, the overall behaviors for different cladding modes and the positive shift are discussed theoretically and experimentally in this section.

7.4.2 Theory

For a weakly-guiding step-index fibre, a geometric-optics approximation may be used and the eigenvalue equation is given by eqn. (3.33), which is suitable for describing low-order cladding modes LP_{0m}^{cl} as [115]

$$\frac{2\pi}{\lambda_{0p}} D_{cl} \sqrt{{n_{cl}}^2 - \left(n_{0p}^{cl}\right)^2} - \left(p - \frac{3}{4}\right)2\pi = 2\cos^{-1} \sqrt{\frac{{n_{cl}}^2 - \left(n_{0p}^{cl}\right)^2}{{n_{cl}}^2 - {n_{amb}}^2}} \tag{7.12}$$

where D_{cl} is the diameter of the cladding. n_{0p}^{cl} is LP_{0p}^{cl}-mode index, n_{cl} and n_{amb} are the indexes of the fibre cladding and its ambient, respectively. The physical meanings of the LHS of eqn. (7.12) is the phase of the light transverse component in modulus of 2π for a light beam propagating along the fibre cladding. The RHS represents the phase delay due to the total internal reflection (TIR) at the interface between the cladding and the ambient.

For LP_{01}^{co} core mode, the internal reflection occurs at the interface between the fibre core and cladding and the eigenvalue equation is given by eqn. (3.34) as

$$\frac{2\pi}{\lambda_{01}} D_{co} \sqrt{{n_{co}}^2 - \left(n_{01}^{co}\right)^2} - \frac{\pi}{2} = 2\cos^{-1} \sqrt{\frac{{n_{co}}^2 - \left(n_{01}^{co}\right)^2}{{n_{co}}^2 - {n_{cl}}^2}} \tag{7.13}$$

where D_{co} is the diameter of the fibre core, n_{01}^{co} is LP_{01}^{co}-mode index, n_{co} is the fibre core index. Since the cladding modes distributed in the spectral region of several hundred nm, the material dispersion given by eqn. (3.40) requires to be considered.

The phase matching condition of a long-period fibre grating is given by eqn. (3.104) as $\lambda_{0p} = \left(n_{01}^{co} - n_{0p}^{cl}\right)\Lambda$, where Λ is the grating period in several hundred micrometers. The calculation of a cladding mode wavelength reduces to the calculation of the mode indexes n_{0p}^{cl} and n_{01}^{co} using eqn. (7.12) and eqn. (7.13). Simulation results show that the mode wavelengths shift to short wavelengths with the increase of the ambient index as shown in Figure 7.22. When the ambient index is equivalent to the mode index ($n_{amb} = n_{0p}^{cl}$), the right side of eqn. (7.12) becomes zero and the spectral shift of this mode reaches its maximum, but the boundary of cladding disappears in this case and thus the coupling of this mode disappears as well. The higher-order cladding mode disappears first with the increase the ambient index since a higher-order cladding mode has a smaller mode index.

When the ambient index is greater than cladding mode index ($n_3 > n_{0p}^{cl}$), the boundary of the fibre cladding is rebuilt and this cladding mode reappears. In this case there is no TIR at the boundary of the fibre cladding and the phase delay is a constant of π, which is well known. Replacing the RHS of eqn. (7.12) by π, the calculation shows that the mode wavelength is longer than the case of air ambient, exhibiting a constant red shift, shown in Figure 7.22. Since there is no TIR reflection, the poor reflectivity at the boundary of the cladding makes a weak coupling.

7.4.3 Experimental results

A 25mm long long-period fibre grating was made in a step-index single mode fibre by using an amplitude mask with period of 400μm. A series of Cargille refractive index oils were dropped on the long-period grating, while the transmission spectra were measured by an optical spectrum analyser. As illustrated as shown in Figure 7.22, the solid line is the calculated spectral displacements of LP_{04}^{cl} mode and circle points are experimental results. The overall discrepancy between the data set and the curve in Figure 7.22 results possibly from the dispersion of the refractive index of the oil since the indexes of the oils are specified at wavelength of 589.3nm.

Figure 7.22 (b) shows a set of transmission spectra taken at several values of surrounding indexes. When the long-period grating is surrounded by air, two cladding modes LP_{03}^{cl} and LP_{04}^{cl} were observed and the transmission spectrum was recorded as shown in Figure 7.22 (b) (a). For the ambient index near the LP_{04}^{cl} mode index, the spectral displacement of the LP_{04}^{cl} mode was measured experimentally to be -48nm as depicted in Figure 7.22 (b) (b). This shift closes to the calculated result -55nm. With a little more increment of the ambient index, this peak completely disappears while the LP_{03}^{cl} mode remains with a further negative shift as shown in the spectrum depicted in Figure 7.22 (b) (c), and then both peaks disappear as shown in Figure 7.22 (b) (d). When the ambient index is 1.64, both peaks reappear with positive spectral displacements. The positive shift of LP_{04}^{cl}

mode was measured to be +2nm, which is in agreement with the theoretical value of 1.95nm.

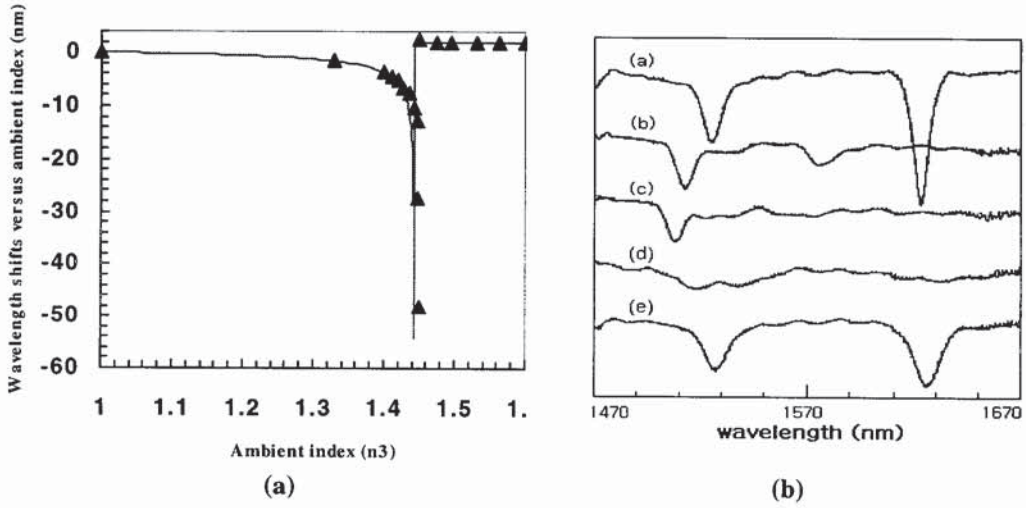

Figure 7.22 (a) A comparison of theoretical (solid line) and experimental shifts (triangle dots) of a long-period fibre grating resonance (LP_{04}^{cl} mode) against the ambient refractive index, (b) Transmission spectra of a long-period fibre grating with different values of ambient refractive index: (a) 1.0; (b) 1.456; (e) 1.64, the indexes of (c) and (d) are between 1.456 and 1.46

To summarise, a long-period fibre grating index sensing has been investigated theoretically and experimentally. With the increase of the ambient index, the resonance wavelengths of long-period fibre gratings shift to short wavelengths, typically ~ -48nm shift. When the ambient index is larger than the cladding mode index, a 2nm positive shift was obtained compared with the case of air ambient.

7.5 Transverse Pressure Sensing Using Long-period Fibre Gratings

This section presents a novel application of long-period gratings as fibre-optic load sensors based on the measurement of polarisation-mode splitting induced by the transverse pressure.

7.5.1 Introduction

Long-period gratings were fabricated in high-birefringence fibre (Hi-LPG) using the UV beam scanning across the amplitude mask technique. Experimental spectrum exhibits that there are two polarisation coupling separated by tens of nanometres with high extinction ratio and low loss for the same order cladding mode, showing considerable potential for use as fibre polarisers for optical signal processing [109, 110]. Hi-LPG is sensitive to transverse stress and can be used in sensing, compared with a short-period Bragg grating. High-birefringence fibre is made normally by introducing one direction transverse stress to the fibre core during the fibre fabrication. In sensing the transverse pressure on the fibre, the pressure will change the Hi-fibre inside pre-stress, depending on the direction of the applied pressure and inside pre-stress, resulting in a complicated relationship, which limit Hi-LPG applications.

This section reports a novel transverse pressure sensing using a long-period grating fabricated only in a non-birefringent fibre. The mode splitting observed in the long-period gratings hundreds of times higher than that in the previously reported fibre Bragg gratings has been achieved experimentally [182]. This demonstrates an extremely high transverse pressure sensitivity, which may lead to development of long-period gratings as low-cost, high-efficiency and truly practical fibre-optic load sensor devices for some applications.

7.5.2 Mode splitting in long-period and Bragg gratings

In single mode fibre, the core mode (LP_{01}^{co}) and cladding mode (LP_{0p}^{cl}) consists of two

orthogonal modes ($LP_{01}^{co,x}$, $LP_{01}^{co,y}$) and ($LP_{0p}^{cl,x}$, $LP_{0p}^{cl,y}$), respectively, with the same propagation constant $\beta_{01}^{co,x} = \beta_{01}^{co,y}$ and $\beta_{0p}^{cl,x} = \beta_{0p}^{cl,y}$, which are called two-fold degeneracy. When a transverse pressure or a pre-stress is applied on a fibre, the two-fold degenerate splits up. Using eqn. (3.104), the resonance condition of long-period gratings for the two orthogonal modes are given by

$$\begin{cases} \lambda_{0p}^{x} = \left(n_{01}^{co,x} - n_{0p}^{cl,x}\right)\Lambda \\ \lambda_{0p}^{y} = \left(n_{01}^{co,y} - n_{0p}^{cl,y}\right)\Lambda \end{cases} \tag{7.14}$$

where x and y indicate the two orthogonal polarisation states, named x-polarisation $LP_{0p}^{co,x}$ and y-polarisation $LP_{0p}^{co,y}$, respectively. $n_{01}^{co,x}$ and $n_{01}^{co,y}$ are the mode indexes of $LP_{01}^{co,x}$ and $LP_{01}^{co,y}$ modes, respectively while $n_{0p}^{cl,x}$ and $n_{0p}^{cl,y}$ are the mode indexes of $LP_{0p}^{co,x}$ and $LP_{0p}^{co,y}$ modes, respectively. The mode coupling occurs only between the same polarisation states, which requires a polarised light used to monitor the grating spectrum. For the transverse loading in **y**-axis, the index profile of the fibre cross-section is shown in Figure 7.23, resulting from a compress in **y**-axis direction and a strain in **x**-axis direction. Thus $LP_{0p}^{cl,x}$ mode shifts to short wavelengths while the $LP_{0p}^{cl,y}$ mode shifts to long wavelengths with increasing the weight loading.

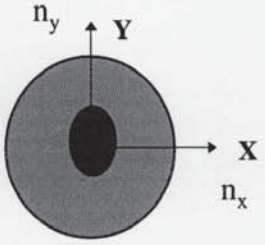

Figure 7.23 Schematic diagram showing the cross-section of the refractive index profile in a high-birefringence fibre

Using eqn. (7.14), the splitting between the two polarisation states is given by

$$\Delta\lambda_{0p} = \left[\left(n_{01}^{co,x} - n_{01}^{co,y}\right) - \left(n_{0p}^{cl,x} - n_{0p}^{cl,y}\right)\right]\Lambda \tag{7.15}$$

In the case of Bragg gratings, the resonance conditions of the two polarisation states are

given by

$$\begin{cases} \lambda_B{}^x = 2n_{01}^{co,x}\Lambda_B \\ \lambda_B{}^y = 2n_{01}^{co,y}\Lambda_B \end{cases} \tag{7.16}$$

and the mode splitting is thus

$$\Delta\lambda_B = 2\left(n_{01}^{co,x} - n_{01}^{co,y}\right)\Lambda_B \tag{7.17}$$

This splitting in Bragg gratings is normally less than 0.3nm, much smaller than the splitting in long-period gratings. In order to compare the mode splitting in the two types of gratings, using eqn. (7.15) and eqn. (7.17), the ratio of them is given by

$$\frac{\Delta\lambda_{0p}\big|_{LPG}}{\Delta\lambda_B\big|_{FBG}} = \frac{\left(n_{01}^{co,x} - n_{01}^{co,y}\right) - \left(n_{0p}^{cl,x} - n_{0p}^{cl,y}\right)}{2\left(n_{01}^{co,x} - n_{01}^{co,y}\right)} \frac{\Lambda_{LPG}}{\Lambda_B} \sim \frac{1}{2}\frac{\Lambda_{LPG}}{\Lambda_B} \sim 500 \tag{7.18}$$

where, the approximation $\left(n_{0p}^{cl,x} - n_{0p}^{cl,y}\right) << \left(n_{01}^{co,x} - n_{01}^{co,y}\right)$ has been used. Obviously, eqn. (7.18) shows that the mode splitting in long-period fibre gratings is hundreds of times higher than that in fibre Bragg gratings.

7.5.3 High-birefringence fibre gratings

The high-birefringence fibre was immersed in 150atm hydrogen tube for two weeks to enhance its photosensitivity. The Bragg gratings and long-period gratings were fabricated in the same high-birefringence fibre by using the holographic and the UV beam scanning across an amplitude mask methods, respectively. A fibre polarisation splitter and a fibre polarisation controller were placed between the broadband light source and the gratings to obtain the polarised light and to control its direction of the polarisation. The transmission spectra were characterized by launching polarised light into the gratings monitored by an optical spectrum analyser. The observed spectra are shown in Figure 7.24 (a), (b) and (c).

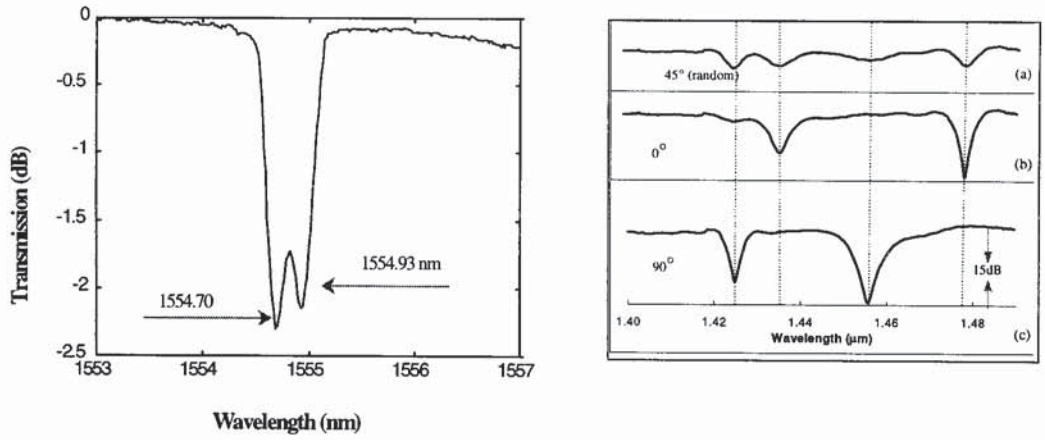

Figure 7.24 Transmissions spectra of gratings in high-birefringence fibre: (a) fibre Bragg grating showing 0.23nm modes splitting; (b) long-period fibre grating with 45°, 0°, and 90° polarisation light

Figure 7.24 (a) and (b) show a 0.23nm mode splitting in a Bragg grating and tens of nanometres in a long-period grating. When the light is randomly polarised (45°), two pairs of ≤3dB loss peaks appear, shown in Figure 7.24 (b). When the light was polarised at 0° (x-polarisation) or 90° (y-polarisation), two sets of stronger coupling modes with respect to the two polarisation were obtained. The polarisation extinction ratio and the birefringence induced splitting for the higher-order modes were about 15dB and 22nm respectively, and for the lower-order modes were only 10dB and 12nm, respectively. The polarisation extinction ratio could be further maximised by making stronger gratings. However, the birefringence-induced polarisation splitting achieved in Bragg gratings was only 0.23nm, which is only hundredth of what was achieved in long-period gratings, described by eqn. (7.18). In the last few years, there have been many attempts to solve the strain/temperature cross-sensitivity problem in grating sensors by utilising the differential response to the strain and temperature of the two polarisation modes of a Bragg grating in a hi-bi fibre, but the results have generally been poor [183]. In contrast, however, these results demonstrate that the large mode splitting exhibited by a long-period grating in a hi-bi fibre offers a potentially powerful solution to this problem.

7.5.4 Load sensing using Long-period fibre gratings

Long-period gratings were made in B/Ge-doped photosensitive fibre [184]. The experiment of the transverse loading was implemented by first laying a long-period grating fibre and a dummy fibre of the same type between two flat surfaces, and then, gradually increasing the weight on the fibres as shown in Figure 7.25 (a). The optical setup for measuring the transmission spectrum is shown in Figure 7.25 (c). A 30mm long-period grating was used and the maximum 8kg loading was applied to two 50mm long fibres.

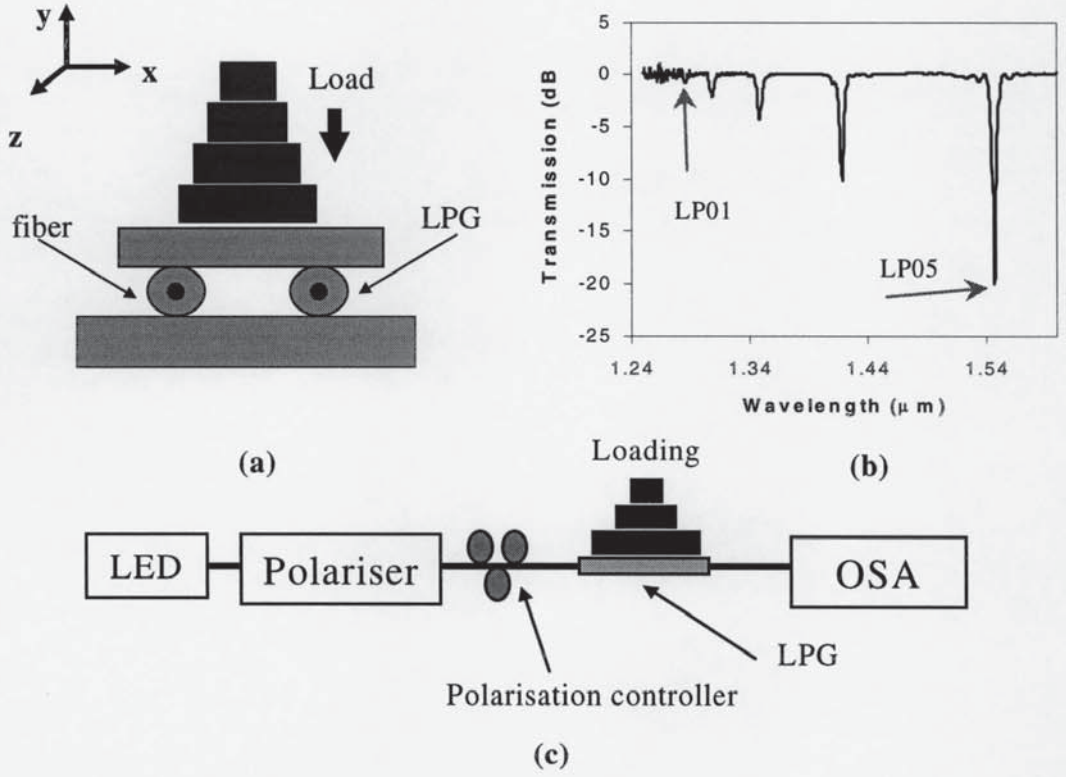

Figure 7.25 (a) Schematic diagram of a long-period fibre grating load sensing; (b) a typical transmission of a 30mm long 475μm periodicity long-period grating; (c) set-up for measurement

The transmission spectrum of the long-period grating without loading is shown in Figure 7.25 (b). When the weight load is 8kg, the full transmission spectrum of a long-period grating is shown in Figure 7.26. The maximum resonance could not be obtained simultaneously for all cladding modes resulting from the polarisation that depends on

wavelengths.

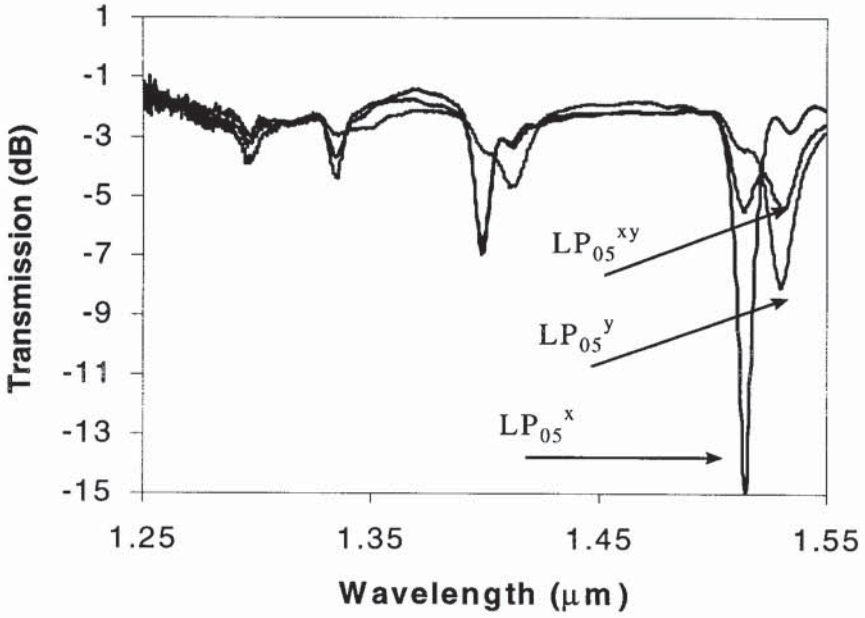

Figure 7.26 Transmission spectra of a long-period fibre grating under 0.8 kg/cm y-axis direction loading, LP_{05}^{x} and LP_{05}^{y} modes corresponding to the 0° and 90° polarisation states while LP_{05}^{xy} is the state of 45°

The transverse-pressure induced birefringence was immediately observed as soon as the long-period grating was subjected to loading. The devices exhibited an extremely high transverse pressure sensitivity. The spacing of the two polarisation states is as much as 20.5nm for LP_{05}^{cl}-mode when 0.08 kg/mm loading is applied as shown in Figure 7.27 (b). For 45° polarisation launched light, the transmission spectrum of the long-period grating with and without loading is shown in Figure 7.27 (a). Clearly, there are two modes with about 3dB sub-peaks loss when the light polarisation is 45°. The two orthogonal modes are switched by adjusting the polarised state. $LP_{05}^{cl,y}$-mode shifts to longer wavelengths while $LP_{05}^{cl,x}$-mode shifts to shorter wavelengths.

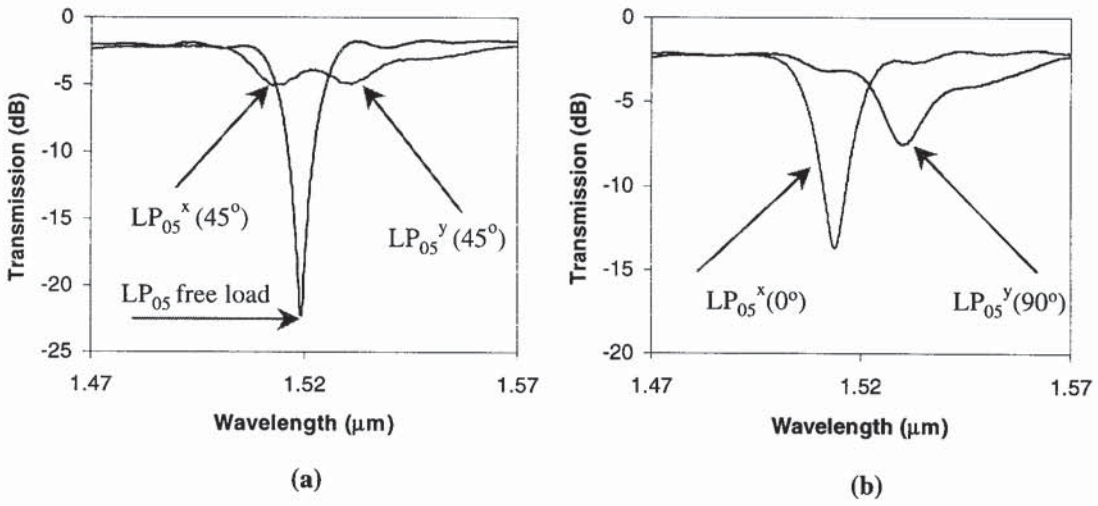

Figure 7.27 LP_{05}^{cl} mode transmission spectra of a long-period fibre grating under 0.8 kg/cm transverse pressure monitored by light with different polarisation states: (a) 45° polarisation; (b) 0° and 90° polarisation

A maximum polarisation extinction ratio of 11dB was achieved for $LP_{05}^{cl,x}$-mode, but only 5dB for $LP_{05}^{cl,y}$-mode as shown in Figure 7.27 (b). The low value for the y-polarisation was due to the out-coupling loss induced by the perturbations of the both loading plate surfaces.

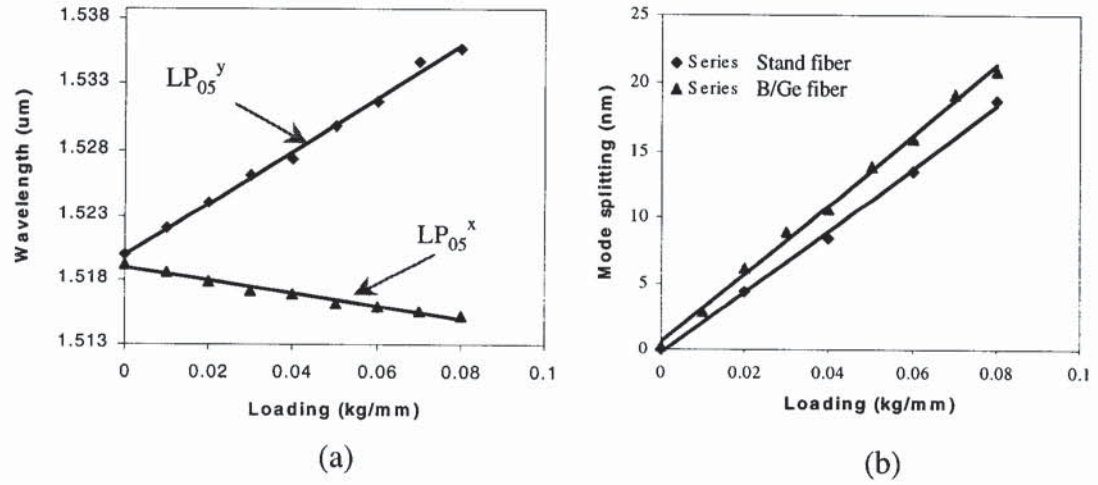

Figure 7.28 (a) Wavelength shifts of the two orthogonal polarisation modes, $LP_{05}^{cl,x}$ and $LP_{05}^{cl,y}$ against the load weight; (b) Mode splitting of the two orthogonal polarisation modes against the load weight

The wavelengths of the two orthogonal polarised modes against the loading weight is shown in Figure 7.28 (a) with one exhibiting red shift and the other blue shift. The separation of the two modes against the loading weight is illustrated in Figure 7.28 (b) showing a good linear response and high sensitivity. Specifically, 20.5nm mode splitting was obtained when 0.08kg/mm loading was applied, giving a transverse strain sensitivity of 250nm/(kg/mm). This value is several hundred times higher than the previously report using Bragg gratings [183, 185]. For comparison, the same loading experiment was performed using a Bragg grating and no mode splitting effect was observed even for the maximum loading of 8kg within 0.1nm optical spectrum analyser resolution.

To summarise, a novel application of long-period gratings as fibre-optic load sensors fabricated in non-birefringent fibre has been reported in this section. The transverse strain sensitivity exhibited by long-period gratings measured was several hundred times higher than that demonstrated by the previously reported Bragg gratings fabricated in both non- and high-birefringence fibres. It is anticipated that this very high transverse strain sensitivity will lead to development of practical fibre-optic load sensor devices.

7.6 Bend Sensing Using Long-period Fibre Gratings

This section discusses a new method of realising optical bend sensing based on the measurement of bending-curvature encoded resonance mode splitting of a long-period fibre grating. The bending induced mode splitting exhibits a near-linear response and the bend sensitivity achieved by this method is nearly three times higher than the previously reported using wavelength shift detection method.

7.6.1 Introduction

In single mode fibre, photoinduced long-period fibre gratings couple light from the fundamental LP_{01}^{co} core mode to LP_{0m}^{cl} cladding modes. The diameter of the fibre cladding is normally 125μm, which is much larger than the light wavelength propagating along the cladding. Thus any small bending will introduce a large phase shift into the cladding modes resulting in the resonance shifts. Several authors have demonstrated long-period grating bend sensors measuring curvature by detecting bending induced wavelength shifts [186, 187]. Recently, Rathje *et al.* have reported observation of resonance mode splitting of long-period gratings produced in the fibre of large core concentricity error [188]. The realisation of optical bend sensing based on the measurement of bending induced resonance mode splitting of long-period gratings produced in normal single mode B/Ge photosensitive fibre is presented in this section. The new approach utilising the property of resonance mode splitting has achieved a significantly higher bend sensitivity than the wavelength shift detection method [186]. The effect of the initial mode coupling strength on spectral response of the split modes under bending for realising practical bend sensors is also discussed.

7.6.2 Bending model

The fabrication of long-period gratings used in the bending experiment has been detailed in section 6.1. That is using the UV scanning across a 30mm-long 430μm-period amplitude mask fabricated in non-hydrogenated B/Ge co-doped photosensitive fibre. A

four-point bend system was designed for implementing a curvature measurement experiment. The geometric configuration of this system is shown in Figure 7.29 (a). A fibre containing a long-period grating in the centre was attached on a 0.5mm thick, 20mm wide and 200mm long metal plate. In order to eliminate the axial strain, only the two ends of a 10cm section of the fibre were fixed loosely on to the metal plate. As illustrated in Figure 7.29 (a), depressing the centre micrometer driver with a depth (h) the fibre was bent. The bend curvature ($1/R$) has a near linear relationship with the depressing depth (h).

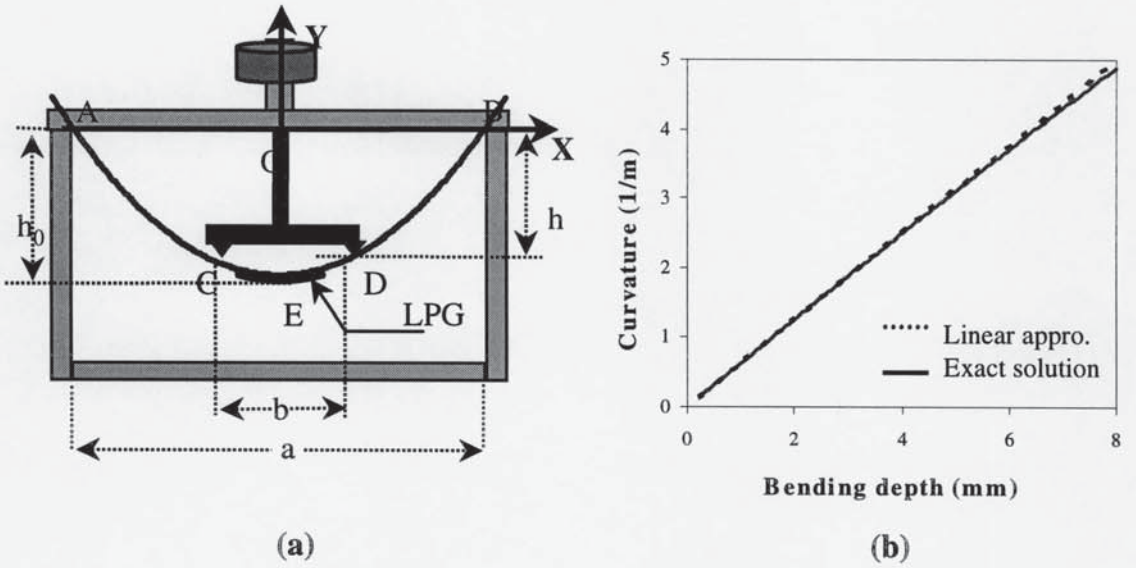

Figure 7.29 (a) Schematic diagram of the four-point bend system with a=120mm, b=20mm and bend depth h=0~8mm; (b) Plots of bend curvature against the bend depth calculated from equations eqn. (7.19) and eqn. (7.21).

According to the geometric configuration, the bend curvature of the fibre follows

$$\begin{cases} R^2 = \left(R - h_0\right)^2 + (a/2)^2 \\ (b/2)^2 + \left[-h - \left(R - h_0\right)\right]^2 = R^2 \end{cases} \tag{7.19}$$

where the R is the bend radius, h is the bend depth which can be accurately read from the micrometer driver, a and b are spacing of the two sets of forced points as shown in Figure 7.29 (a). Simplifying eqn. (7.19) yields

$$(a/2)^2 - 2R\left[R + h - \sqrt{R^2 - (b/2)^2}\right] + \left[R + h - \sqrt{R^2 - (b/2)^2}\right]^2 = 0 \tag{7.20}$$

For $R>>a$, b and h and also $a>>b$ and h, as an approximation, eqn. (7.20) reduces to

$$\frac{1}{R} = \frac{8h}{a^2 - b^2} \tag{7.21}$$

Clearly, eqn. (7.21) exhibits a linear relationship between the bend curvature and the bend depth. Figure 7.29 (b) plots the bend curvature ($1/R$) against the bend depth (h) according to the linear approximation defined in eqn. (7.21) and the exact solution of eqn. (7.19). The two curves nearly coincide in the curvature range between 0 and 5 m^{-1}.

7.6.3 Experimental results and discussion

Several long-period grating samples of various initial-coupling strengths were investigated under bending tests. Before the long-period gratings were subjected to bending, there were, as shown in Figure 7.30 (a), five single transmission loss peaks corresponding to five coupled cladding modes (LP_{01}^{cl} to LP_{05}^{cl}) appearing in the wavelength range between 1100nm and 1600nm. The mode splitting under bending was inevitable as bending fibre broke up the symmetry between the two normally degenerated spatial cladding modes thus introducing a refractive index difference between them [189]. However, this effect is not simply from the splitting of two orthogonal modes, as experimental results show the split modes are polarisation insensitive. In the experiment, the resonance splitting was not apparent until the applied curvature was 0.4 m^{-1}. With further bending, each individual single peak split into two visible peaks as illustrated in Figure 7.30 (a), and they moved away in opposite direction. Figure 7.30 (b) shows the mode splitting against the bend curvature for LP_{03}^{cl} and LP_{05}^{cl} modes. It is clear that the response of the mode splitting against the bend curvature is near-linearity with higher-order mode exhibiting higher bend sensitivity. Up to 70nm mode splitting was measured for LP_{05}^{cl} mode corresponding to a maximum bend curvature of 5 m^{-1}, giving a bend sensitivity of 14nm/m^{-1} which is nearly three times higher than the value demonstrated by

the wavelength detection method [186].

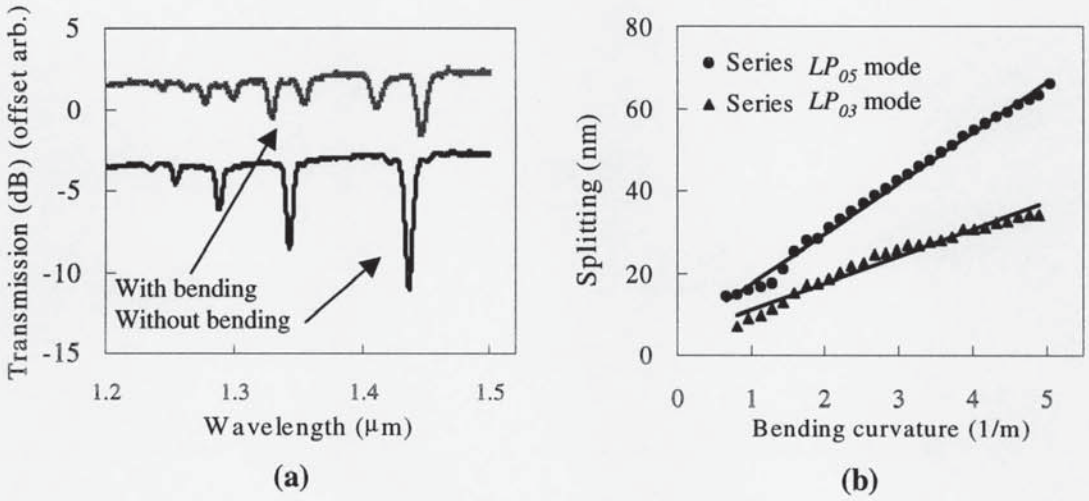

Figure 7.30 Transmission spectra of LP_{05}^{cl} mode (a) with and without resonance mode splitting; (b) Mode splitting against the bend curvature showing a near-linear response

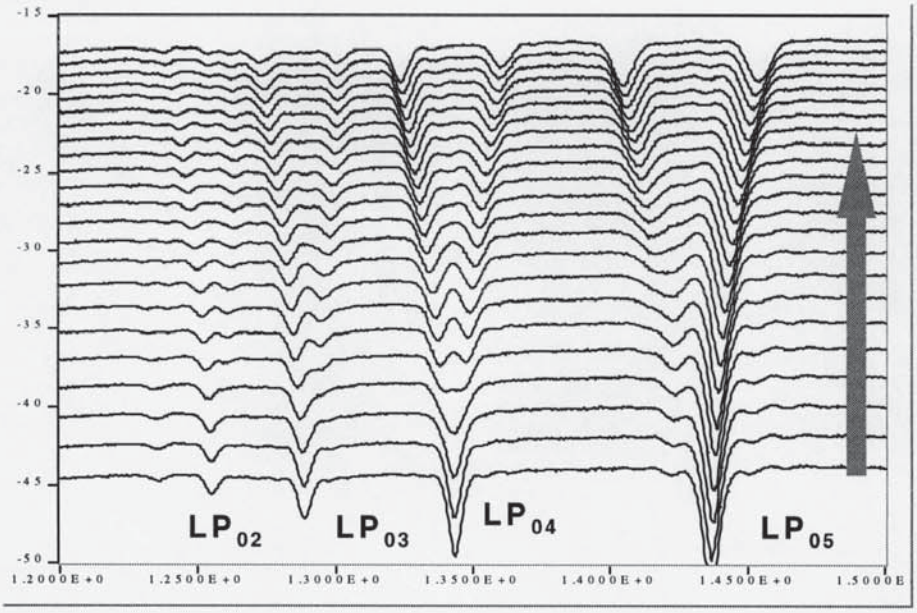

Figure 7.31: Transmission spectra of a long-period fibre grating against the bend curvature - the arrow direction

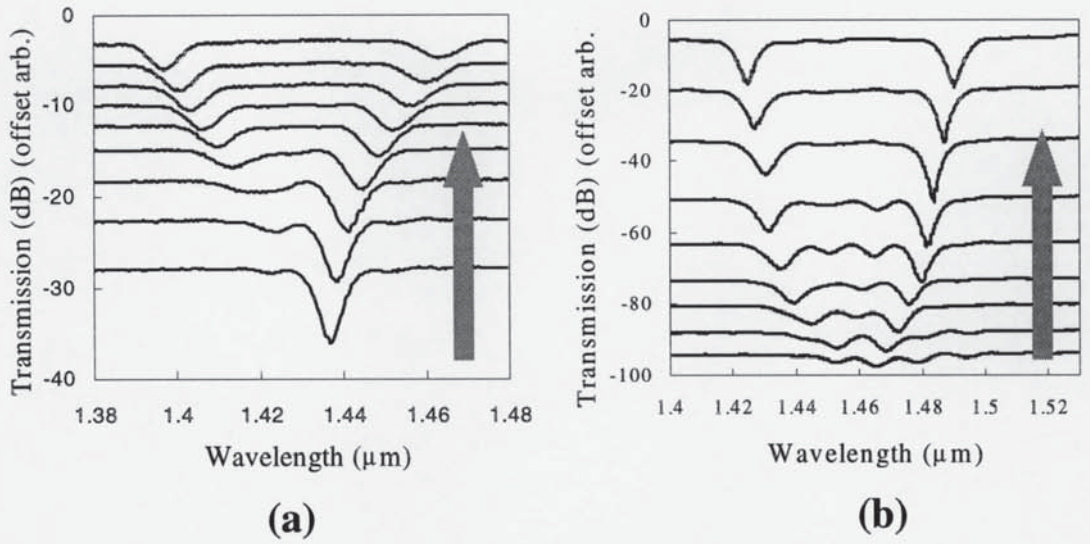

Figure 7.32 Transmission spectrum of LP_{05}^{cl} mode against the bend curvature with different initial coupling strengths: (a) $\kappa_{05}L < \pi/2$, (b) $\kappa_{05}L \approx \pi$.

The transmission loss of the split modes in the bending tests decreased or increased with the bend curvature depending on the initial mode coupling strengths of the grating. Figure 7.32 (a) and (b) illustrate the spectral evolution of LP_{05}^{cl} mode of two gratings showing opposite trends for the transmission loss. In the case of Grating A, which had a higher loss peak originally, its split peak at the long wavelength side gradually decreased whereas its other peak at the short wavelength side increased, both finally reaching a similar value of ~3dB. By contrast, both loss peaks of Grating B which, although its initial-coupling strength was higher than Grating A as it was overexposed to the UV, originally had a lower transmission loss, which grew higher with bending, eventually reaching a value of 10dB. In general, although the grating coupling strength increases with the UV exposure, the change in transmission loss does not follow this pattern. Figure 7.33 plots the transmission evolution of LP_{05}^{cl} mode with five values of coupling strengths, corresponding to different UV exposure time. The figure shows the transmission loss grows initially with the UV exposure reaching a maximum, and then decreases with further exposure. The dependence of transmission loss on the mode coupling strength can be understood from the coupled-mode theory, according to which the transmission of a long-period grating is expressed in eqn. (3.114) as

$$T_{0p} = 1 - \left| \frac{\kappa_{0p}^{cl}}{S_{0p}^{cl}} \sin\left(S_{0p}^{cl} L\right) \right|^2 \tag{7.22}$$

where $S_{0p}^{cl} = \sqrt{\left(\kappa_{0p}^{cl}\right)^2 + \left(\delta_{0p}^{cl}\right)^2}$ and $\delta_{0p}^{cl} = \pi(n_{01}^{co} - n_{0p}^{cl})(\frac{1}{\lambda} - \frac{1}{\lambda_{0p}})$, n_{01}^{co} and n_{0p}^{cl} are the effective indices of the core and the LP_{0p}^{cl} cladding modes respectively, and λ_{0p} is the resonance wavelength. At the phase match condition, $\delta_{0p}^{cl} = 0$, eqn. (7.22) yields $T_{0p} = 1 - \left|\sin\left(\kappa_{0p}^{cl} L\right)\right|^2$, where $\kappa_{0p}^{cl} L$ is the coupling strength. Clearly, when the coupling strength $\kappa_{0p}^{cl} L = \pi / 2$, the light is completely coupled to the cladding resulting in a maximum transmission loss whereas if $\kappa_{0p}^{cl} L = \pi$, all the light is coupled back to the core from the cladding indicating no transmission loss.

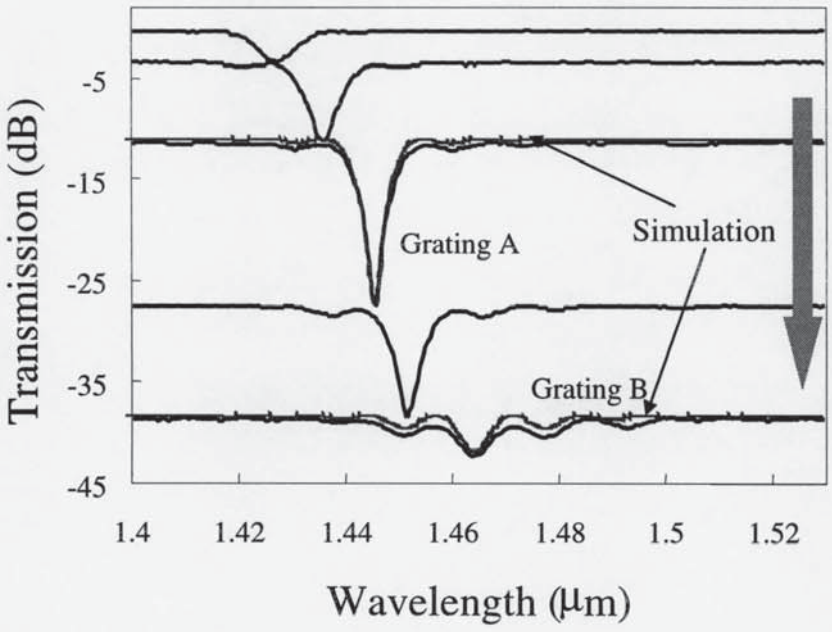

Figure 7.33 A graph illustrating the spectral evolution of the LP_{05}^{cl} mode against the UV exposure, showing the loss peak grows as $\kappa_{0m} L$ from 0 to π/2 indicated by grating A, then decreases from π/2 to π indicated by grating B (arrow pointing to the UV exposure)

The above analysis suggests that the original and the evolving transmission loss profiles

of gratings A and B can be well explained in terms of their coupling strengths. We have evaluated their initial coupling strength by modelling the measured spectra. Grating A exhibited a higher original transmission loss (~10dB) since its initial-coupling strength of 1.47 is close to $\pi/2$. When it was subjected to bending, the coupling strength decreased from $\sim\pi/2$ to 0 and the transmission loss was thus reduced. Grating B had a longer UV exposure but exhibited a lower transmission loss, which suggests that its initial-coupling strength is greater than $\pi/2$. This agrees with the calculated value of 2.44. Under bending, its coupling strength decayed from a value 2.44 to $\pi/2$, hence resulting in an increase in transmission loss.

Clearly, for practical sensing, sensors like Grating B that have a near-π initial-coupling strength are more preferred because they facilitate high precision measurement since their profiles are enhanced with bending. Such long-period grating sensors can be easily realised by properly controlling the UV exposure condition in fabrication. The mode splitting against the bend curvature is shown in Figure 7.34; two peaks with 65.6nm wavelength spacing and 12.4dB and 13.8dB peak strength were obtained.

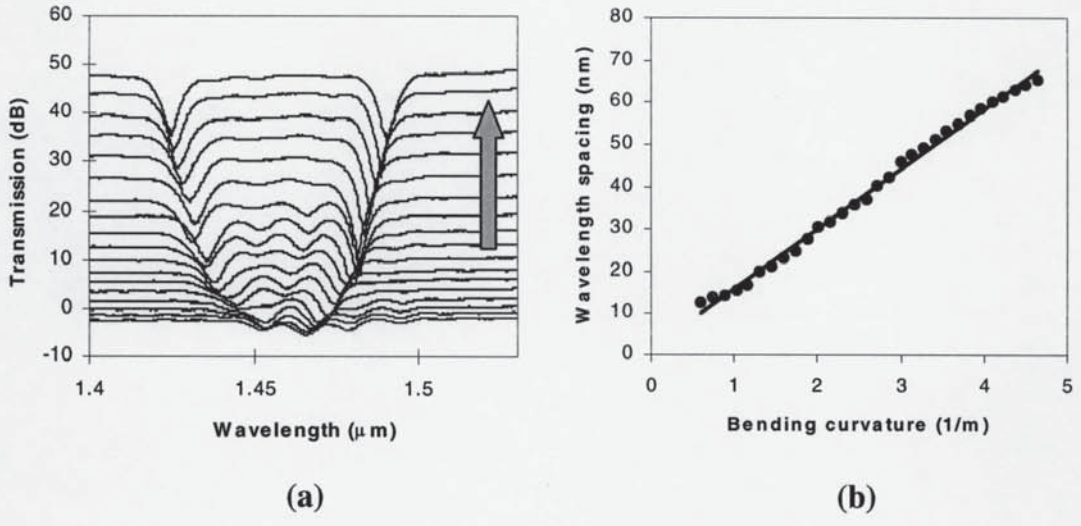

Figure 7.34 (a) Transmission spectra of LP_{05}^{cl} mode plotted against the bend curvature, (arrow pointing to the larger bend curvature); (b) mode splitting against the bend curvature: dash (...) is experimental data, the solid line is fitted with straight line

7.6.4 Dependence of fibre types

The mode splitting is sensitive to the fibre type. In two types of B/Ge doped fibre with slightly different B/Ge composition, which is almost not distinguished in making Bragg gratings and long-period gratings, the splitting has almost the same linear relationship against the bend curvature, but there is a constant shift as shown in Figure 7.35 (a).

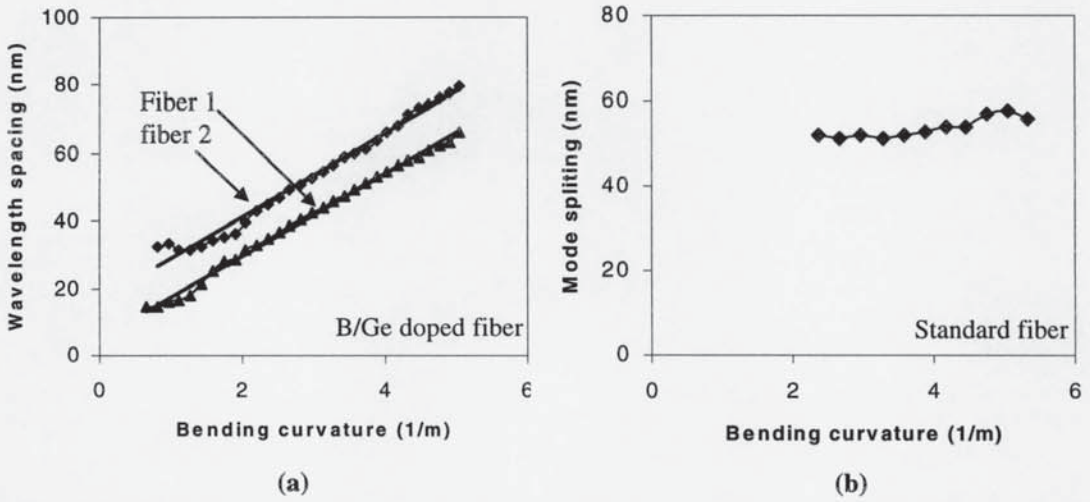

Figure 7.35 Mode splitting against the bend curvature in different types of fibres: (a) two types of B-Ge-doped fibres showing the similar response; (b) in standard communication fibre showing no bend response

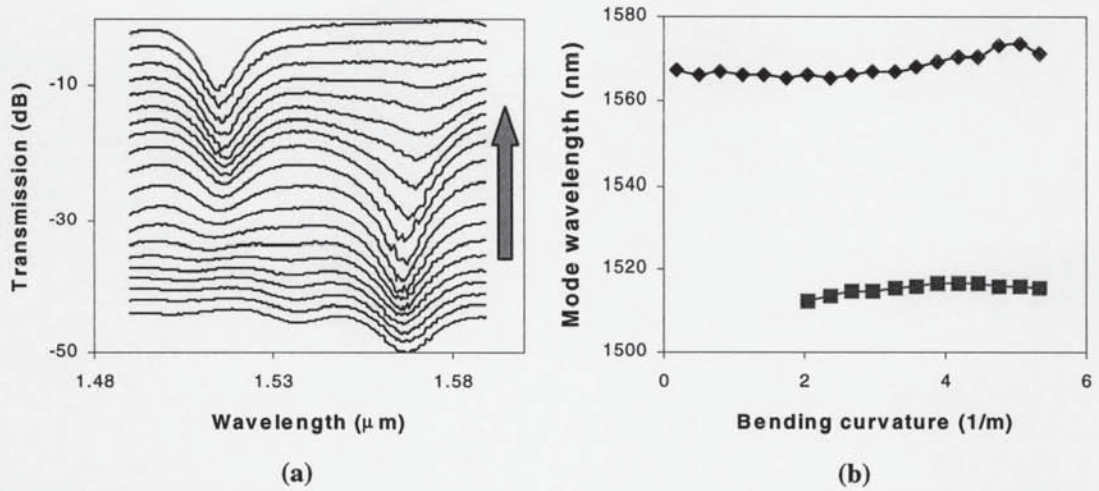

Figure 7.36 (a) Transmission spectra of a long-period fibre grating in standard fibre (arrow pointing to the larger bend curvature); (b) Mode splitting against the bend curvature showing no bend response

In standard communication fibre, experiment shows that there is no mode splitting under a smaller bend curvature and the mode splitting remains almost unchanged against the bend curvature as shown in Figure 7.35 (b) and Figure 7.36.

7.6.5 Dependence of bend directions

In order to inspect the dependence of a bend direction, long-period gratings were marked with a tape sticker to show the orientation and the gratings were rotated around its longitudinal axes at 90°. The transmission spectra were recorded for different bend curvature and the mode splitting versus the bend curvature is plotted as shown in Figure 7.37. The difference of the mode splitting between different bend directions is less than 5% and might result from the birefringence induced by UV exposing.

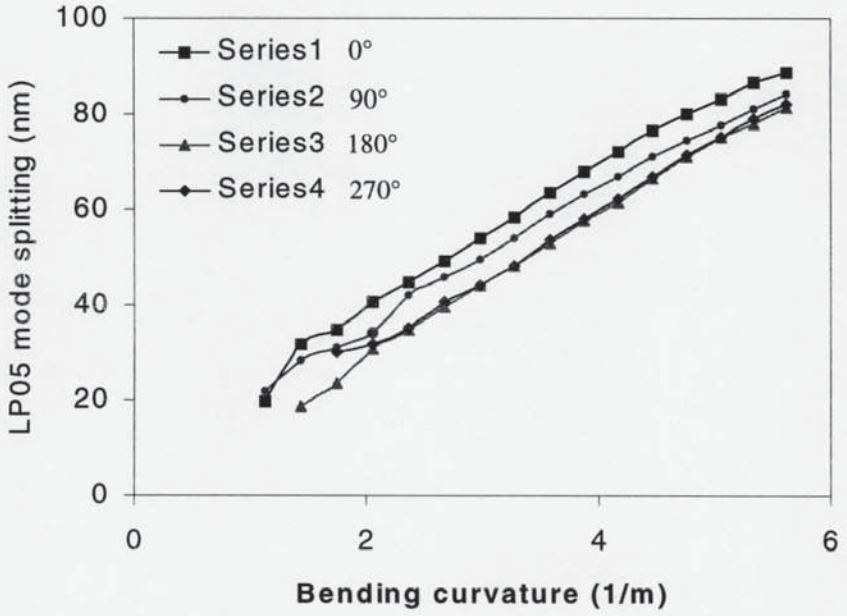

Figure 7.37 A graph showing the mode splitting against the bend curvature of a long-period fibre grating under four bend orientations: 0°, 90°, 180°, 270°

The cross-section of the B/Ge doped photosensitive fibre in which long-period gratings were fabricated is shown in Figure 7.38, exhibiting the concentricity error within 1μm. This results in the mode splitting direction independence.

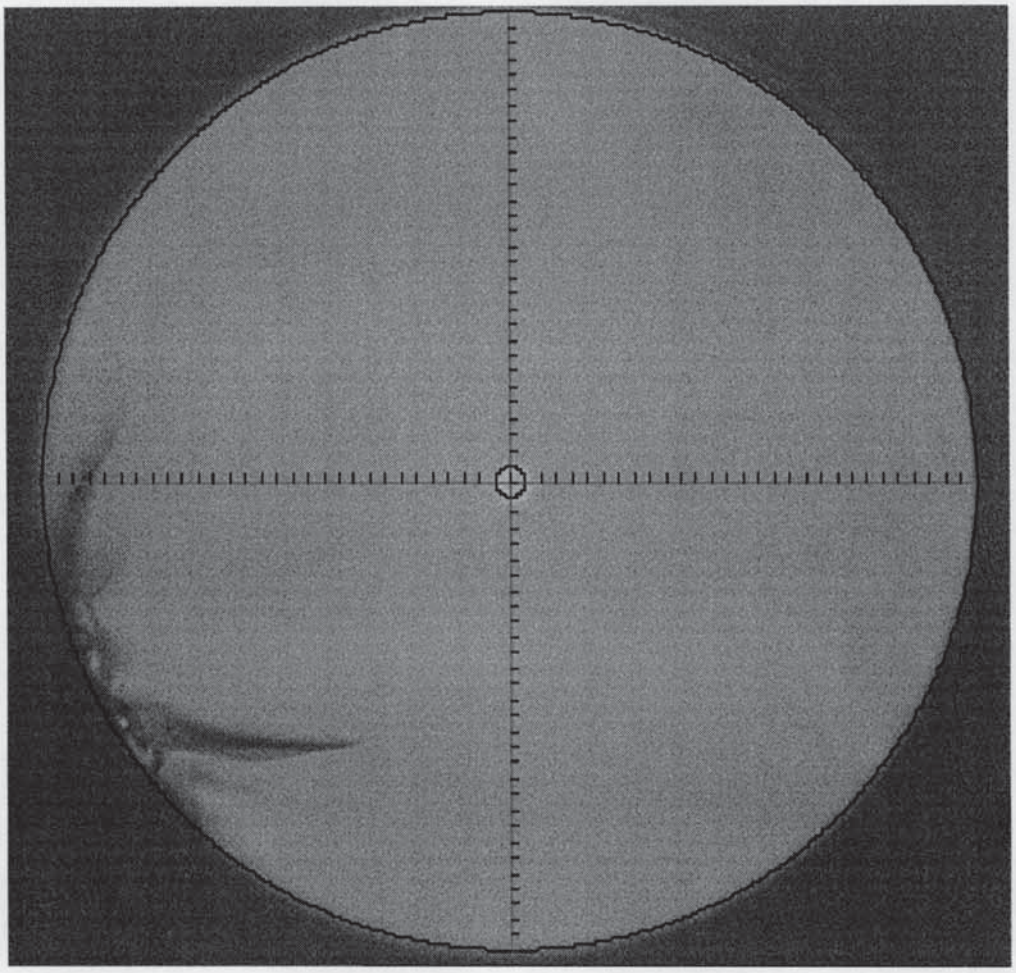

Figure 7.38 Schematic diagram showing the cross-section of B/Ge doped photosensitive fibre (2μm/division)

7.6.6 Model of the mode splitting

When an LPG is subjected to a gentle bend with an approximately uniform curvature K_{cur} as shown in Figure 7.39, the induced asymmetry splits the degeneracy of the cladding mode of the straight circular fibre. This effect results in two closely-separated cladding modes with their fields predominantly on the outer and inner sides of the fibre cladding relative to the centre of the bend, respectively [189]. Thus, with increasing bend curvature, the two splitting cladding modes propagate in a stained and compressed fibre cladding with a red and blue shifts, respectively. In order to calculate the splitting of the cladding modes, the bend radii of inner and outer cladding as shown in Figure 7.39 are

treated approximately as

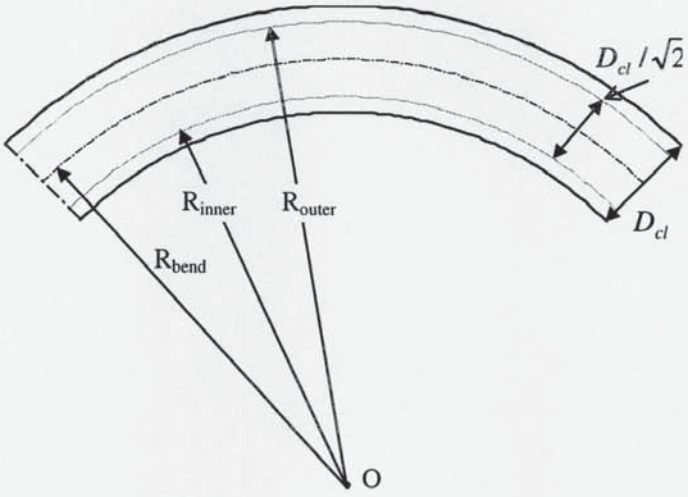

Figure 7.39 Schematic diagram of the bend fibre, showing a strain and compress to the outer and inner side cladding

$$R = R_{bend} \pm \frac{D_{cl}/2}{\sqrt{2}} \tag{7.23}$$

where D_{cl} is the diameter of the fibre cladding. $D_{cl}/\sqrt{2}$ is approximately the geometric diameter of the cladding mode field for a high order cladding mode, such as LP_{05}^{cl}. Then, the relative strain ε between the outer and inner cladding is given by

$$\varepsilon = \frac{D_{cl}}{\sqrt{2}} \cdot K_{bend} \tag{7.24}$$

Clearly, the relative stain ε results in the relative changes of the density and thus the refractive index. The relationship between the applied strain and the change of the refractive index is given by

$$\frac{\Delta n}{n} = -\rho_e \cdot \varepsilon \tag{7.25}$$

where, ρ_e is the photo-elastic constant (for a pure bulk silica glass, ρ_e=0.22), n is its refractive index. Using LPG resonance condition $\lambda_{0p} = \left(n_{01}^{co} - n_{0p}^{cl}\right)\Lambda$, the splitting of the

resonance is obtained as

$$\Delta\lambda \approx \Delta n_{0p}^{cl} \cdot \Lambda = \rho_e \cdot n_{0p}^{cl} \cdot \frac{D_{cl}}{\sqrt{2}} \cdot K_{bend} \cdot \Lambda \tag{7.26}$$

where the approximation that the cladding mode index n_{0p}^{cl} follows the eqn. (7.25) has been used while the core mode splitting is neglected as the diameter of the fibre core is much smaller than the cladding; Λ is the period of the LPGs. For a lower order cladding mode, the mode distribution is located closer to the fibre core compared with the higher order cladding mode, thus the average diameter of the mode filed is a slight smaller than $D_{cl}/\sqrt{2}$ and the mode splitting is less than the higher order mode. Exact analysis of the light propagation along a bend fibre taking account of the entire cross-section requires extensive numerical calculation and is beyond the scope of this thesis.

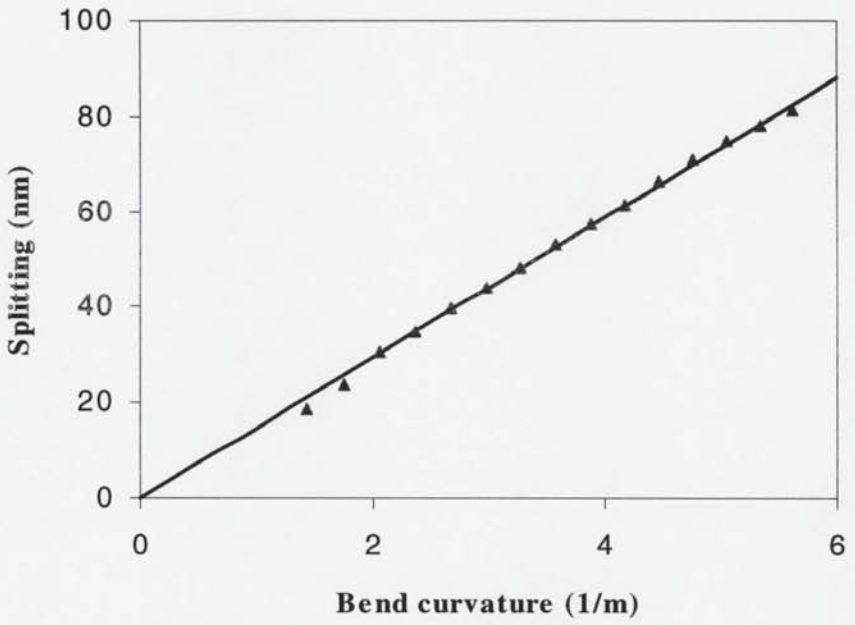

Figure 7.40 Mode splitting against the bend curvature, triangles: experimental results, straight line: plotted by eqn. (7.26) for ρ_e=0.23, n_{0p}^{cl}=1.444, D_{cl}=125μm and Λ=500μm

Consider that the photo-elastic constant of a fibre is a slight larger than that of the bulk glass, for ρ_e=0.23, n_{05}^{cl}=1.444, D_{cl}=125μm, Λ=500μm and K_{bend}=5.6/m, eqn. (7.26)

yields 82.2nm, which is excellent agreement with experimental results for LP_{05}^{cl} mode [190]. As shown in Figure 7.40, experimental results of the mode splitting against the bend curvature for LP_{05}^{cl} mode (triangles) are in good agreement with the values calculated by eqn. (7.26) (straight line). Over 80 nm mode splitting was measured under the bend curvature of 5.6 m^{-1}, giving a bend sensitivity of 14.5 nm/(m^{-1}), which is the largest mode splitting and the best sensitivity for obtained.

To summarise, a new optical bend sensing technique based on the measurement of bending induced resonance mode splitting of long-period gratings has been presented. The near-linear response and high sensitivity to bend curvature demonstrated by the mode splitting technique are more attractive for optical bend sensing. In addition, the study on effect of the initial mode coupling strength on transmission profile under bending suggests long-period gratings with near-π initial-coupling strength are more adequate for performing high precision measurement. A model of the split cladding modes that propagate in a strained and compressed cladding has been proposed to calculate the mode splitting showing a good agreement with the experimental results. Over 80 nm mode splitting was measured under the bend curvature of 5.6 m^{-1}, giving a bend sensitivity of 14.5 nm/(m^{-1}), which is the largest mode splitting and the best sensitivity for obtained

7.7 Chapter Summary

This chapter is the third part of this thesis, containing six relatively independent sections to present novel applications using fibre Bragg gratings and long-period fibre gratings, including Bragg grating edge filters, intensity and wavelength division multiplexing sensing systems, wide stop-band narrow transmission filters; long-period fibre grating index sensing, long-period fibre grating transverse pressure sensing and bend sensing.

In section 7.1, a new technique for fabricating grating edge filters with an arbitrary spectral response based on tilted chirped fibre Bragg gratings have been presented. Experimental results show that a small chirp-rate and slanting angle result in a high slope-efficiency with a relatively small filtering range, and *vice versa*. The slope efficiency is also dependent on the maximum obtainable grating coupling strength, which is higher in B/Ge co-doped fibre than in standard telecom fibre. Experimentally slope efficiencies from 0.5dB/nm to 10dB/nm and filtering range from 2nm to 20nm have been realised. An application in strain sensing using this kind of filters for interrogating the shift of the Bragg wavelength has been demonstrated experimentally.

The fabrication of high-rejection/low-loss single bandpass filters using specially designed and produced cladding depressed photosensitive fibre have been discussed experimentally and theoretically in section 7.2. For the first time, 50dB rejection has been achieved for 50nm wide stop-band covering the entire ASE range of EDFA. The suppression of the cladding mode out-coupling enables the formation of a low-loss passband within the broad stop-band.

A novel concept of multiplexing fibre Bragg grating sensors using the combination of reflection intensity and wavelength division multiplexing has been proposed and evaluated in section 7.3. In contrast to WDM, by using the intensity information, the IWDM permits the adjacent gratings crossing each other in the sensor array to multiplex more gratings in a single fibre. Furthermore, the strain resolution in the grating overlap region was remarkably improved by utilising the dual-peak reflection-encoded gratings

into the sensor array. In conjunction with TDM and SDM, this new technique will significantly enhance the multiplexing capacity of fibre Bragg grating strain sensing for SMART structure applications.

Refractive index sensing using long-period fibre gratings has been investigated theoretically and experimentally in section 7.4. The wavelengths of cladding modes shift to short wavelengths with the increase of the ambient index. The maximum spectral shifts for different cladding modes and the red shifts when the ambient index is larger than the cladding mode indexes were observed and explained with clear physical picture. For LP_{04}^{cl} -mode, the calculated positive and the maximum negative shifts are +1.95nm and -54nm, respectively, which are consistent with the experimental results.

A novel application of long-period fibre gratings as fibre-optic load sensors has been presented in section 7.5. The transverse strain sensitivity exhibited by the long-period gratings was several hundred times higher than that demonstrated by the previously reported fibre Bragg gratings fabricated in both conventional and hi-bi fibres. It anticipates that this very high transverse strain sensitivity will lead to development of practical devices for fibre-optic load sensing.

A new optical bend sensing technique based on the measurement of bending induced resonance mode splitting of long-period gratings has been presented in section 7.6. The near-linear response and high sensitivity to bend curvature demonstrated by the mode splitting technique are attractive for optical bend sensing. In addition, the study on effect of the initial mode coupling strength on transmission profile under bending suggests long-period gratings with near-π initial-coupling strength are adequate for performing high precision measurement. A model of the split cladding modes that propagate in a respective strained and compressed cladding has been proposed to calculate the mode splitting showing a good agreement with the experimental results. Over 80 nm mode splitting was measured under the bend curvature of 5.6 m^{-1}, giving a bend sensitivity of 14.5 nm/(m^{-1}), which is the largest mode splitting and the best sensitivity for obtained.

CHAPTER 8

CONCLUSIONS AND SUGGESTED FUTURE WORK

8.1 Conclusions

This thesis has detailed a systematic coupled-mode theory, modelling, fabrication and a number of novel applications of fibre Bragg gratings and long-period fibre gratings. The main results are summarized as: four types of new devices, fibre Bragg grating edge filters, intensity and wavelength division multiplexing systems, long-period fibre grating load sensors and bend sensors; simulation and fabrication programmes in LabVIEW for numerous grating structures including apodised, chirped, chirped Moiré, sampled, phase-shifted, cascaded, wavelength-shifted, and long length Bragg gratings, phase-shifted and cascaded long-period fibre gratings.

Starting from the Maxwell equations, the coupled-mode equations for both fibre Bragg gratings and long-period gratings have been derived. The mode overlap factors have been investigated analytically. Overlap factors for up to 60 cladding modes have been calculated, showing a slow varying profile with multiple minimums against the order of the cladding modes, which is in agreement with the experimental results. Simulation technique utilising matrix transforms method by solving the coupled-mode equations has been developed. This enables simulations of spectral response in terms of reflectivity, bandwidth, sidelobes and dispersion of gratings of different structures including uniform- and chirped, phase-shifted, apodised, Moiré and sampled fibre Bragg gratings, phase-shifted and cascaded long-period gratings. Although the majority of these structures were modelled numerically, analytical expressions with physical picture of complex Fabry-Perot cavity for phase-shifted Bragg gratings and Mach-Zehnder interferometer for phase-shifted and cascaded long-period gratings have been developed.

From the modelling of grating apodisation, an improved gaussian profile has been developed. Simulation results show that this improved gaussian profile apodisation produces a significant improvement in sidelobe suppression compared with the gaussian and the well-known Blackman apodisation profiles. The fabrication programmes in LabVIEW have been constructed and 20dB-reflectivity gratings with more than 30dB sidelobe suppression have been successfully fabricated experimentally. For chirped Moiré gratings, the characteristics of spectra, the relationship of Moiré period and the transmission peaks have been analysed theoretically and experimentally. For sampled fibre Bragg gratings, in order to obtain multiple peaks with the same reflectivity and constant wavelength spacing, a composite *cosine* sampling profile has been proposed. The dual-characteristics of Bragg and long-period gratings have been observed experimentally in sampled Bragg gratings. In addition, single mode and single polarisation DFB fibre lasers based on phase-shifted fibre gratings have been realised. Wide and flattened or multipeak transmission filters based on phase-shifted and cascaded long-period gratings have been investigated experimentally and theoretically. This kind of grating structures has been demonstrated in the application of EDFA gain flattening.

Some fundamental studies of grating growth and spectral evolution in relation to the UV-exposure and hydrogenation induced photosensitivities have been carried out. In particular, Type IIa gratings in non-hydrogenated B/Ge co-doped fibres and the formation of re-generated gratings in hydrogenated B/Ge fibres have been discussed experimentally. Up to 18nm red shift for the re-generated gratings with 16dB-reflectivity were first observed. Experimental results show these re-generated gratings have a reduced temperature coefficient (6.4pm/°C) compared with the Type I gratings (8.9pm/°C) in the same B/Ge co-doped fibres.

Development and standardisation of fibre grating fabrication techniques are the another major contribution of the research work presented in this thesis. Both the holographic and the phase mask techniques have been employed to fabricate Bragg and long-period

gratings of standard and novel structures. The operation principle of these two fabrication techniques has been discussed in detail. The analytical expressions for predicting the Bragg wavelength and chirp in the holographic fabrication technique have been proposed and the LabVIEW programmes have been constructed for high precision and efficiency grating fabrication. This study offers great convenience in guiding grating fabrication.

Significant improvements have been particularly made in the scanning phase mask method to enable arbitrary tailoring of the spectral response of grating devices. Two techniques – slow shifting and fast dithering phase-mask, were implemented by a computer controlled piezo. An inverse *cosine* relationship between the profiles of the grating coupling coefficient and the phase mask shift has been obtained in the slow shifting technique, while this relationship is an inverse *sinc* transform in the fast dithering technique. The shift regions of the phase mask in these two techniques are a quarter and a grating period, respectively. These techniques have been developed to fabricate complex grating structures including apodised, chirped Moiré, sampled, phase-shifted, wavelength-shifted, self-apodised and long-length fibre Bragg gratings. A number of LabVIEW programmes have been constructed to implement these grating structures and widely used in Photonics Research Group.

Optical sensing applications utilising fibre gratings form the third major part of the research work presented in this thesis. Several experiments of novel sensing and sensing-demodulating have been implemented. For the first time, an intensity and wavelength dual-coding interrogation technique has been demonstrated showing significantly enhanced capacity of grating sensor multiplexing. Grating edge fibers based on tilted chirped fibre Bragg gratings have been fabricated for the first time. These grating edge filters are stable to the ambient temperature and their slope, spectral range, loss depth, and the central wavelength are controlled effectively during grating fabrication. An application in strain sensing using this grating edge filters has been successfully demonstrated. For the refractive index sensing, the shifts of the cladding modes of long-period gratings against the ambient index have been investigated theoretically and

experimentally. By introducing a birefringence through a transverse pressure of weight loading, the long-period grating modes split into two orthogonal polarisation states. Mode splitting as much as 20.5nm has been presented for the first time and several hundred times sensitivity has been realised experimentally compared with the reported using fibre Bragg gratings. By bending long-period gratings, up to 85nm mode splitting has been achieved experimentally. This is a significant result obtained in the field of fibre sensors. In addition, high rejection (50dB) and wider stop-band (50nm) narrow transmission (1nm) filters based on cascaded four chirped gratings have been successfully fabricated experimentally. This kind of fibre transmission filters has been used in WDM systems.

8.2 Suggested Future Work

Although a systematic coupled-mode theory has been presented and numerous grating structures have been discussed in detail within this thesis, it has highlighted several areas that require further investigation.

The grating edge filters due to 'chirping' radiation mode presented in section 7.1 are very useful devices for interrogating the shift of the Bragg wavelength in grating sensing. Hence, this device highlights the requirement of the fibres with enhanced radiation mode coupling and theoretical modelling is also required for optimizing the fabrication parameters. The load sensing utilising the mode splitting of long-period fibre gratings presented in section 7.5 provides several hundred times sensitivity compared with the reported using Bragg gratings. For a practical application and commercial purpose, the theoretical analysis and modelling of the mode splitting due to the birefringence introduced by transverse weight loading is required. Section 7.6 reported a remarkable bend sensing using long-period fibre gratings. A fibre type dependent sensitivity, $14nm/m^{-1}$ splitting sensitivity for B/Ge-doped fibres and no bend-encoded for standard fibres has been observed. Thus this result highlights the design of the fibres for high- and low- bend sensitivity, respectively, for different applications.

For given profiles of the local Bragg wavelength and the coupling coefficient, the modelling of grating spectra has been discussed in Chapter 5. However, in order to obtain some specific reflection and dispersion profiles, such as dispersion-less grating filters with square reflection profile for WDM systems and chirped gratings for EDFA gain flattening, the profile of the coupling coefficient is required during the grating fabrication. This requirement highlights the techniques of modelling and fabrication of complex structure gratings.

Of the many applications envisaged for fibre Bragg gratings, their use as dispersion compensation elements has attracted particularly widespread interest, notably in high-bit-rate fibre transmission systems wherein cancellation of the ~17ps/nm/km dispersion of standard telecommunication fibres at 1550nm would enable its use in systems incorporating erbium-doped fibre amplifiers. However, the dispersion capacity of a normal chirped grating is limited by grating length. Furthermore, nonlinear dispersion becomes significant for very high-bit-rate long distance transmission systems. To this, very long length chirped gratings with arbitrary dispersion profile would be very attractive devices.

REFERENCES

1. I. Bennion, J. A. R. Williams, L. Zhang, K. Sugden, N. J. Doran, "UV-written in-fibre Bragg gratings", *Opt. Quan. Electron.*, Vol.**28**(2), pp.93-135, (1996).

2. K. O. Hill, Y. Fujii, D. C. Johnson, et al, "Photosensitivity in optical fiber waveguides: Application to reflection fiber fabrication", *Appl. Phys. Lett.*, Vol. 32(10), p647, (1978)

3. D. K. W. Lam and B. K. Garside, "Characterization of single-mode optical fiber filters", *Appl. Opt.* Vol. **20**(3), pp.440-445, (1981)

4. G. Meltz, W. W. Morey, W. H. Glenn, "Formation of Bragg gratings in optical fibers by a transverse holographic method ", *Opt. Lett.*, Vol.**14**(15), pp.823-825, (1989)

5. A. W. Snyder, "Coupled-mode theory for optical fiber", *J. Opt. Soc. Am.* Vol. **62**(11), pp.1267-1277, (1972)

6. A. Yariv, "Coupled-mode theory for guide wave optics", *IEEE J. Quantum Electron.*, Vol. **QE-9**(9), pp.919-933, (1973)

7. Peng, T. Tamir, and H. L. Bertoni, "Theory of periodic dielectric waveguides", *IEEE Trans. Microwave Tech.*, Vol. **MTT-23**, pp.123-133, (1975)

8. L. Jaggard and C. Elachi "Floquent and coupled waves analysis of higher-order Bragg coupling in a period medium", *J. Opt. Soc. Amer.*, Vol. **66**(7), pp.674-682, 1976

9. Yamamoto, T. Kamiya, and H. Y. Yanai, "Improved coupled mode analysis of corrugated waveguides and lasers", *IEEE J. Quantum Electron.*, QE-**14**, pp.245-258, (1978)

10. I. Stegeman, D. Sarid, and J. J. Burke, "Scattering of guided waves by surface periodic gratings for arbitrary angles of incidence: perturbation field theory and implications to normal-mode analysis", *J. Opt. Soc. Am.*, Vol. **71**, pp.1497-1057, (1981)

11. G. Hall, "Coupled-mode theory for corrugated optical waveguides", Opt. Lett., Vol. **15**(11), pp. 619-621, 1990.

12. E. Little and H. A. Haus, "A variational coupled-mode theory for periodic waveguides", *IEEE J. Quantum Electron.*, Vol. **31**, pp.2258-2264, (1995)

13. H. Kogelnik, "Filter response of nonuniform almost-periodic structure", *Bell Syst. Tech. J.*, Vol. *55*(1), pp.109-126, (1976)

14. B. G. Kim and E. Garmire, "Comparison between the matrix-method and the coupled-wave method in the analysis of Bragg reflector structures", *J. Opt. Soc. Am.* Vol. **9**(1), pp.132-136, (1992)

15. J. Hoge, W. Huang and Makion, "On the transfer-matrix method for distributed-feedback wave- guide devices", *J. Lightwave Technol.* Vol. **10**(12), pp.1860-1868, (1992)

16. K. D. Simmons, S. Larochelle, V. Mizrahi, G. I. Stegeman, D. L. Griscom "correlation of defect centers with a wavelength-dependent photosensitive response in germania-doped silica optical fibers", *Opt. Lett.*, Vol.**16**(3), pp.141-143, (1991)

17. R. M. Atkins, "Measurement of the ultraviolet-absorption spectrum of optical fibers", *Opt. Lett.*, Vol.**17**(7), pp.469-471, (1992)

18. J. Nishii, H. Yamanaka, H. Hosono, H. Kawazoe, "Preparation of Bragg Gratings In Sputter-Deposited Geo2-Sio2 Glasses By Excimer-Laser Irradiation", *Opt. Lett.*, Vol.**21**(17), pp.1360-1362, (1996)

19. T. E. Tsai, E. J. Friebele, M. Rajaram, S. Mukhapadhyay, "Structural origin of the 5.16-ev optical-absorption band in silica and Ge-doped silica", *App. Phys. Lett.*, Vol.**64**(12), pp.1481-1483, (1994)

20. R. M. Atkins, V. Mizrahi, T. Erdogan, "248nm induced vacuum UV spectral changes in optical-fiber preform cores - support for a color center model of photosensitivity", ***Electron. Lett.***, Vol.**29**(4), pp.385-387, (1993)

21. R. M. Atkins, V. Mizrahi, "Observations of changes in uv absorption-bands of singlemode germanosilicate core optical fibers on writing and thermally erasing refractive-index gratings", *Electron. Lett.*, Vol.**28**(18), pp.1743-1744, (1992)

22. D. L. Williams, S. T. Davey, R. Kashyap, J. R. Armitage, B. J. Ainslie, "Direct observation of uv induced bleaching of 240-nm absorption- band in photosensitive germanosilicate glass-fibers", *Electron. Lett.*, Vol.**28**(4), pp.369-371, (1992)

23. D. P. Hand, P. S. Russell, "Photoinduced refractive-index changes in germanosilicate fibers", *Opt. Lett.*, Vol.**15**(2), pp.102-104, (1990)

24. R. Kashyap, J. R. Armitage, R. Wyatt, S. T. Davey, D. L. Williams, "All-fiber narrow-band reflection gratings at 1500 nm", *Electron. lett.*, Vol.**26**(11), pp.730-732, (1990)

25. B. Malo, K. A. Vineberg, F. Bilodeau, J. Albert, D. C. Johnson, K. O. Hill, "Ultraviolet-light photosensitivity in ge-doped silica fibers - wavelength dependence of the light-induced index change", *Opt. Lett.*, Vol.**15**(17), pp.953-955, (1990)

26. T. E. Tsai, C. G. Askins, F. J. Friebele, "Photoinduced grating and intensity dependence of defect generation in ge-doped silica optical fiber", *Appl. Phys Lett.*, Vol.**61**(4), pp.390-392, (1992)

27. T. E. Tsai, E. J. Friebele, D. L. Griscom, "Thermal-stability of photoinduced gratings and paramagnetic centers in ge-doped and Ge/P-doped silica optical fibers", *Opt. Lett.*, Vol.**18**(12), pp.935-937, (1993)

28. W. X. Xie, P. Niay, P. Bernage, M. Douay, J. F. Bayon, T. Georges, M. Monerie, B. Poumellec, "Experimental-evidence of 2 types of photorefractive effects occurring during photoinscriptions of Bragg gratings within germanosilicate fibers", *Opt. Commun.*, Vol.**104**(1-3), pp.185-195, (1993)

29. P. Cordier, J. C. Doukhan, E. Fertein, P. Bernage, P. Niay, J. F. Bayon, T. Georges, "TEM characterization of structural-changes in glass associated to Bragg grating inscription in a germanosilicate optical-fiber preform", *Opt. Commun.*, Vol.**111**(3-4), pp.269-275, (1994)

30. P. Niay, P. Bernage, S. Legoubin, M. Douay, W. X. Xie, J. F. Bayon, T. Georges, M. Monerie, B. Poumellec, "Behavior of spectral transmissions of Bragg gratings written in

germania-doped fibers - writing and erasing experiments using pulsed or cw uv exposure", *Opt. Commun.*, Vol.**113**(1-3), pp.176-192, (1994)

31. J. P. Bernardin, N. M. Lawandy, "Dynamics of the formation of Bragg gratings in germanosilicate optical fibers", *Opt. Commun.*, , Vol.79(3-4), pp194-199, (1990)

32. K. S. Chiang, M. G. Sceats, D. Wong, "Ultraviolet photolytic-induced changes in optical fibers - the thermal-expansion coefficient", *Opt. Lett.*, , Vol.**18**(12), pp.965-967, (1993)

33. M. D. Gallagher, U. L. Osterberg, "Ultraviolet-absorption measurements in single-mode optical-glass fibers", *Appl. Phys. Lett.*, Vol.**60**(15), pp.1791-1793, (1992)

34. D. L. Williams, S. T. Davey, R. Kashyap, J. R. Armitage, B. J. Ainslie, "Ultraviolet-absorption studies on photosensitive germanosilicate preforms and fibers", *Appl. Phys. Lett.*, , Vol.**59**(7), pp.762-764, (1991)

35. B. Malo, J. Albert, D. C. Johnson, F. Bilodeau, K. O. Hill, "Elimination of photoinduced absorption in ge-doped silica fibers by annealing of ultraviolet color-centers", *Electron. Lett.*, Vol.28, No.17, pp.1598-1599, (1992)

36. D. L. Williams, B. J. Ainslie, J. R. Armitage, R. Kashyap, R. Campbell, "Enhanced uv photosensitivity in boron codoped germanosilicate fibers", *Electron. Lett.*, , Vol.**29**(1), pp.45-47, (1993)

37. P. J. Lemaire, R. M. Atkins, V. Mizrahi, W. A. Reed, "High-pressure H_2 loading as a technique for achieving ultrahigh UV photosensitivity and thermal sensitivity in geo2 doped optical fibers", *Electron. Lett.*, Vol.**29**(13), pp.1191-1193, (1993)

38. R. M. Atkins, P. J. Lemaire, T. Erdogan, V. Mizrahi, "Mechanisms of enhanced UV photosensitivity via hydrogen loading in germanosilicate glasses", *Electron. Lett.*, Vol.**29**(14), pp.1234-1235, (1993)

39. H. G. Limberger, P. Y. Fonjallaz, R. P. Salathe, F. Cochet, "Compaction- and photoelastic-induced index changes in fiber Bragg gratings", *Appl. Phys. Lett.*, Vol.**68**(22), pp.3069-3071, (1996)

40. P. Y. Fonjallaz, H. G. Limberger, R. P. Salathe, F. Cochet, B. Leuenberger, "Tension increase correlated to refractive-index change in fibers containing UV-written Bragg gratings", *Opt. Lett.*, Vol.**20**(11), pp.1346-1348, (1995)

41. P. J. Lemaire, A. M. Vengsarkar, W. A. Reed, V. Mizrahi, and K. S. kranz, Conference on Optical Fibre Communication (OFC"94), San Jose, California, 1994, Technical Digest, p.47

42. V. Mizrahi, P. J. Lemaire, T. Erdogan, W. A. Reed, D. J. Digiovanni, R. M. Atkins, "Ultraviolet-laser fabrication of ultrastrong optical-fiber gratings and of germania-doped channel wave-guides", *Appl. Phys. Lett.*, Vol.**63**(13), pp.1727-1729, (1993)

43. J. L. Archambault, L. Reekie, P. S. J. Russell, "100% reflectivity bragg reflectors produced in optical fibres by single excimer laser pulses", *Electron. Lett.*, Vol.**29**(5), pp.453-455, (1993)

44. I. Bennion, D. C. G. Reid, C. J. Rowe, W. J. Stewart, "High-reflectivity monomode-fibre grating filters", *Electron. Lett.*, Vol.**22**(6), pp.341-343, (1986)

45. S. J. Mihailov, M. C. Gower, "Periodic cladding surface structures induced when recording fiber Bragg reflectors with a single pulse from a KrF excimer laser", *Appl. Phys. Lett.*, Vol.**65**(21), pp.2639-2641, (1994)

46. J. Canning, M. Aslund, "Correlation of ultraviolet-induced stress changes and negative index growth in type IIa germanosilicate waveguide gratings", *Opt. Lett.*, Vol.**24**(7), pp.463-465, (1999)

47. J. Canning, D. Moss, M. Aslund, M. Bazylenko, "Negative index gratings in germanosilicate planar waveguides", *Electron. Lett.* , Vol.**34**(4), pp.366-367, (1998)

48. L. Dong, W. F. Liu, L. Reekie, "Negative-index gratings formed by a 193-nm excimer laser", *Opt. Lett.*, Vol.**21**(24), pp.2032-2034, (1997)

49. W. X. Xie, P. Niay, P. Bernage, M. Douay, T. Taunay, J. F. Bayon, E. Delevaque, M. Monerie "Photoinscription of Bragg gratings within preform plates of high NA germanosilicate fibers: Searching for an experimental evidence of type II A photosensitivity in preform plates", *Opt. Commun.*, Vol.124(3-4), pp.295-300, (1996)

50. J. D. Prohaska, E. Snitzer, S. Rishton, V. Boegli, "Magnification off mask fabricated fiber Bragg Gratings", *Electron. Lett.*, Vol.**29**(18), pp.1614-1615, (1993)

51. R. J. Campbell, R. Kashyap, "Spectral Profile And Multiplexing of Bragg gratings in Photosensitive Fiber", *Opt. Lett.*, Vol.**16**(12), pp.898-900, (1991)

52. Q. Zhang, D. A. Brown, L. Reinhart, T. F. Morse, J. Q. Wang, G. Xiao, "Tuning Bragg wavelength by writing gratings on prestrained fibers", IEEE Photonics Technology Letters, Vol.**6**(7), pp.839-841, (1994)

53. J. Martin, F. Ouellette, "Novel writing technique of long and highly reflective in-fiber gratings", *Electron. Lett.*, Vol.**30**(10), pp.811-812, (1994)

54. H. N. Rourke, S. R. Baker, K. C. Byron, R. S. Baulcomb, S. M. Ojha, S. Clements, "Fabrication and characterization of long, narrow-band fiber gratings by phase mask scanning", *Electron. Lett.*, Vol.**30**(16), pp.1341-1342, (1994)

55. M. Durkin, M. Ibsen, M. J. Cole, R. I. Laming "1m long continuously-written fibre Bragg gratings for combined second- and third-order dispersion compensation", *Electron. Lett.*, Vol.**33**(22), pp.1891-1893, (1997)

56. K. C. Byron, K. Sugden, T. Bricheno, I. Bennion, "Fabrication of chirped Bragg gratings in photosensitive fiber", *Electron. Lett.*, Vol.**29**(18), pp.1659-1660, (1993)

57. K. Sugden, I. Bennion, A. Molony, N. J. Copner, "Chirped gratings produced in photosensitive optical fibers by fiber deformation during exposure", *Electron. Lett.*, Vol.**30**(5), pp.440-442, (1994)

58. K. C. Byron, H. N. Rourke, "Fabrication of chirped fiber gratings by novel stretch and write technique", *Electron. Lett.*, Vol.**31**(1), pp.60-61, (1995)

59. R. C. Tiberio, D. W. Carr, M. J. Rooks, S. J. Mihailov, F. Bilodeau, J. Albert, D. Stryckman, D. C. Johnson, K. O. Hill, A. W. McClelland, B. J. Hughes, "Fabrication of electron beam generated, chirped, phase mask (1070.11-1070.66 nm) for fiber Bragg grating dispersion

compensator", *J. Vacuum Science & Technol. B.*, Vol.**16**(6), pp.3237-3240, (1998)

60. M. C. Farries, K. Sugden, D. C. J. Reid, I. Bennion, A. Molony, M. J. Goodwin, "Very broad reflection bandwidth (44nm) chirped fiber gratings and narrow bandpass-filters produced by the use of an amplitude mask", *Electron. Lett.*, Vol.**30**(11), pp.891-892, (1994)

61. W. W. Morey, G. Meltz, W. H. Glenn, "Fiber optic bragg grating sensors", *Fiber Optic And Laser Sensors VII*, Ch.69, pp.98-107, (1990)

62. J. R. Dunphy, G. Meltz, F. P. Lamm, W. W. Morey, "Multifunction, distributed optical fiber sensor for composite cure and response monitoring", *Fiber Optic Smart Structures And Skins III*, Ch.37, pp.116-118, (1990)

63. W. W. Morey, J. R. Dunphy, G. Meltz, "Multiplexing fiber Bragg grating sensors", *Distributed And Multiplexed Fiber Optic Sensors*, Ch.23, pp.216-224, (1992)

64. M. A. Davis, D. G. Bellemore, M. A. Putnam, A. D. Kersey, "Interrogation of 60 fibre Bragg grating sensors with microstrain resolution capability", *Electron. Lett.*, Vol.**32**(15), pp.1393-1394, (1996)

65. A. D. Kersey and T. A. Berkoff, "Dual wavelength fiber interferometer with wavelength selection via fiber Bragg grating elements", *Electron. Lett.*, Vol. 28(13), pp1215-1216, (1992)

66. K. P. Koo and A. D. Kersey, "Fiber laser sensor with ultrahigh strain resolution using interferometric interrogation", *Electron. Lett.* Vol. **31**(14), pp1180-1182, (1995)

67. S. Legoubin, E. Fertein, M. Douay, P. Bernage, P. Niay, F. Bayon, T. Georges, "Formation of moire grating in core of germanosilicate fiber by transverse holographic double exposure method", *Electron. Lett.*, Vol.**27**(21), pp.1945-1946, (1991)

68. L. Zhang, K. Sugden, I. Bennion, A. Molony, "Wide-stopband chirped fiber moire grating transmission filters", *Electron. Lett.*, Vol.**31**(6), pp.477-479, (1995)

69. F. Bilodeau, K. O. Hill, B. Malo, D. C. Johnson, J. Albert, "High-return-loss narrowband all-fiber bandpass Bragg transmission filter", *IEEE Photon. Technol. Lett.*, Vol.**6**(1), pp.80-82, (1994)

70. D. C. Johnson, K. O. Hill, F. Bilodeau, S. Faucher, "New design concept for a narrowband wavelength-selective optical tap and combiner", *Electron. Lett.*, Vol.**23**(13), pp.668-669, (1987)

71. G. E. Town, K. Sugden, J. A. R. Williams, I. Bennion, S. B. Poole, "Wide-band Fabry-Perot-like filters in optical fiber", *IEEE Photon. Technol. Lett.*, Vol.**7**(1), pp.78-80, (1995)

72. B. J. Eggleton, P. A. Krug, L. Poladian, F. Ouellette, "Long periodic superstructure Bragg gratings in optical fibers", *Electron. Lett.*, Vol.**30**(19), pp.1620-1622, (1994)

73. M. Ibsen, B. J. Eggleton, M. G. Sceats, F. Ouellette, "Broadly tunable DBR fiber laser using sampled fiber Bragg gratings", *Electron. Lett.*, Vol.**31**(1), pp.37-38, (1995)

74. R. P. Davey, R. P. E. Fleming, K. Smith, R. Kashyap, J. R. Armitage, "Mode-locked erbium fiber laser with wavelength selection by means of fiber Bragg grating reflector", *Electron. Lett.*, Vol.**27**(22), pp.2087-2088, (1991)

75. G. A. Ball, W. W. Morey, "Continuously tunable single-mode erbium fiber laser", *Opt. Lett.*, Vol.**17**(6), pp.420-422, (1992)

76. M. E. Fermann, K. Sugden, I. Bennion, "High-power soliton fiber laser-based on pulse-width control with chirped fiber Bragg gratings", *Opt. Lett.*, Vol.**20**(2), pp.172-174, (1995)

77. G. A. Ball, W. W. Morey, "Compression-tuned single-frequency Bragg grating fiber laser", *Opt. Lett.*, Vol.**19**(23), pp.1979-1981, (1994)

78. G. A. Ball, W. W. Morey, "Efficient integrated Nd^{3+} fiber laser", *IEEE Photon. Technol. Lett.*, Vol.**3**(12), pp.1077-1078, (1991)

79. D. Pureur, M. Douay, P. Bernage, P. Niay, J. F. Bayon, "Single-polarization fiber lasers using Bragg gratings in hi-bi fibers", *J. Lightwave Technol.*, Vol.**13**(3), pp.350-355, (1995)

80. M. Douay, T. Feng, P. Bernage, P. Niay, E. Delevaque, T. Georges, "Birefringence effect of optical fiber laser with intracore fiber Bragg grating", *IEEE Photon. Technol. Lett.*, Vol.**4**(8), pp.844-846, (1992)

81. J. Y. Allain, J. F. Bayon, M. Monerie, P. Bernage, P. Niay, "Ytterbium-doped silica fiber laser with intracore Bragg gratings operating at 1.02 mu-m", *Electron. Lett.*, Vol.**29**(3), pp.309-310, (1993)

82. J. T. Kringlebotn, J. L. Archambault, L. Reekie, J. E. Townsend, G. G. Vienne, D. N. Payne, "Highly-efficient, low-noise grating-feedback $Er^{3+}Yb^{3+}$ codoped fiber laser", *Electron. Lett.*, Vol.**30**(12), pp.972-973, (1994)

83. D. U. Noske, M. J. Guy, K. Rottwitt, R. Kashyap, J. R. Taylor, "Dual-wavelength operation of a passively mode-locked "figure-of-eight" ytterbium-erbium fibre soliton laser", *Opt. Commun.*, Vol.**108**(4-6), pp.297-301, (1994)

84. J. T. Kringlebotn, J. L. Archambault, L. Reekie, D. N. Payne, "Er^{3+}:Yb-codoped fiber distributed-feedback laser", *Opt. Lett.*, Vol.**19**(24), pp.2101-2103, (1994)

85. S. Boj, E. Delevaque, J. Y. Allain, J. F. Bayon, P. Niay, P. Bernage, "High-efficiency diode-pumped thulium-doped silica fiber lasers with intracore Bragg gratings in the 1.9-2.1-μm-band", *Electron. Lett.*, Vol.**30**(13), pp.1019-1020, (1994)

86. J. L. Zyskind, J. W. Sulhoff, P. D. Magill, K. C. Reichmann, V. Mizrahi, D. J. Digiovanni, "Transmission at 2.5 Gbit/s over 654 km using an erbium-doped fibre grating laser source", *Electron. Lett.*, Vol.**29**(12), pp.1105-1106, (1993)

87. F. Delorme, G. Alibert, C. Ougier, S. Slempkes, H. Nakajima, "Sampled-grating DBR lasers with 101 wavelengths over 44 nm and optimized power variation for WDM applications", *Electron. Lett.*, Vol.**34**(3), pp.279-281, (1998)

88. P. N. Kean, J. W. D. Gray, I. Bennion, N. J. Doran, "Dispersion-modified actively modelocked erbium fiber laser using a chirped fiber grating", *Electron. Lett.*, Vol.**30**(25), pp.2133-2135, (1994)

89. M. E. Fermann, K. Sugden, I. Bennion, "Generation of 10nJ picosecond pulses from a modelocked fibre laser", *Electron. Lett.*, Vol.**31**(3), pp.194-195, (1995)

90. S. V. Chernikov, J. R. Taylor, R. Kashyap, "Coupled-cavity erbium fiber lasers incorporating fiber grating reflectors", *Opt. Lett.*, Vol.**18**(23), pp.2023-2025, (1993)

91. F. Ouellette, "Dispersion cancellation using linearly chirped Bragg grating filters in optical waveguides", *Opt. Lett.*, Vol. **12**(10), pp.847-849, (1987)

92 S. Thibault, J. Lauzon, J. F. Cliche, J. Martin, M. A. Duguay, M. Tetu, "Numerical-analysis of the optimal length and profile of a linearly chirped fiber bragg grating for dispersion compensation", *Opt. Lett.*, Vol.**20**(6), pp.647-649, (1995)

93. C. J. Brooks, G. L. Vossler, K. A. Winick "Integrated-optic dispersion compensator that uses chirped gratings", *Opt. Lett.*, Vol.**20**(4), pp.368-370, (1995)

94. J. A. R. Williams, I. Bennion, K. Sugden, N. J. Doran, "Fiber dispersion compensation using a chirped in-fiber Bragg grating", *Electron. Lett.*, Vol.**30**(12), pp.985-987, (1994)

95. R. Kashyap, S. V. Chernikov, P. F. Mckee, J. R. Taylor, "30ps chromatic dispersion compensation of 400fs pulses at 100 gbits/s in optical fibers using an all-fiber photoinduced chirped reflection grating", *Electron. Lett.*, Vol.**30**(13), pp.1078-1080, (1994)

96. D. Garthe, R. E. Epworth, W. S. Lee, A. Hadjifotiou, C. P. Chew, T. Bricheno, A. Fielding, H. N. Rourke, S. R. Baker, K. C. Byron, R. S. Baulcomb, S. M. Ohja, S. Clements, "Adjustable dispersion equaliser for 10 and 20 Gbit/s over distances up to 160 km", *Electron. Lett.*, Vol.**30**(25), pp.2159-2160, (1994)

97. K. O. Hill, S. Theriault, B. Malo, F. Bilodeau, T. Kitagawa, D. C. Johnson, J. Albert, K. Takiguchi, T. Kataoka, K. Hagimoto, "Chirped in-fiber Bragg grating dispersion compensators - linearization of dispersion characteristic and demonstration of dispersion compensation in 100-km, 10-gbit/s optical-fiber link", *Electron. Lett.*, Vol.**30**(21), pp.1755-1756, (1994)

98. U. Eriksson, P. Blixt, J. A. Tellefsen, "Design of fiber gratings for total dispersion compensation", *Opt. Lett.*, Vol.**19**(14), pp.1028-1030, (1994)

99. J. A. R. Williams, I. Bennion, N. J. Doran, "The design of in-fiber Bragg grating systems for cubic and quadratic dispersion compensation", *Opt. Commun.*, Vol.**116**(1-3), pp.62-66, (1995)

100. A. M. Vengsarkar, P. J. Lemaire, J. B. Judkins, V. Bhatia, T. Erdogan J. E. and Spie, "Long-period fibre gratings as band-rejection filters", *J. Lightwave Technol.*, Vol. **14**(1), pp.58-65, (1996)

101. A. M. Vengsarkar, J. R. Pedrazzani, J. B. Judkins, P. J. Lemaire, N. S. Bergano, C. R. Davidson, "Long-period fiber-grating-based gain equalizers", *Opt. Lett.*, Vol. **21**(5), pp.336-338, (1996)

102. V. Bhatia, A. M. Vengsarkar, "Optical fiber long-period grating sensors", *Opt. Lett.*, Vol. **21**(9), pp.692-694, (1996)

103. H. J. Patrick, G. M. Williams, A. D. Kersey, J. R. Pedrazzani, A. M. Vengsarkar, "Hybrid fiber Bragg grating/long period fiber grating sensor for strain/temperature discrimination", *IEEE Photon. Technol. Lett.*, Vol. **8**(9), pp.1223-1225, (1996)

104. R. W. Fallon, L. Zhang, L. A. Everall, J. A. R. Williams, I. Bennion, "All-fibre optical sensing system: Bragg grating sensor interrogated by a long-period grating", *Meas. Sci. technol.*, Vol. **9**(12), pp.1969-1973, (1998)

105. J. Meissner, W. Nowak, V. Slowik and T. Klink, "Strain monitoring at a prestressed concrete bridge", *Proc. Of 12th International Conf. on Optical Fibre Sensors*, pp.408, (1997)

106. H. J. Patrick, A. D. Kersey, F. Bucholtz, "Analysis of the response of long period fiber gratings to external index of refraction", *J. Lightwave Technol*, Vol. **16**(9), pp.1606-1612, (1998)

107. B. H. Lee, Y. Liu, S. B. Lee, S. S. Choi, J. N. Jang, "Displacements of the resonant peaks of a long-period fiber grating induced by a change of ambient refractive index", *Opt. Lett.*, Vol. **22**(23), pp.1769-1771, (1997)

108. Z. Zhang and J. S. Sirkis, "Temperature-compensated long period grating chemical sensor", *Proc. Of 12th International Conf. on Optical Fibre Sensors*, pp.294, (1997)

109. B. Ortega, L. Dong, W. F. Liu, J. P. deSandro, L. Reekie, S. I. Tsypina, V. N. Bagratashvili, R. I. Laming, "High-performance optical fiber polarizers based on long-period gratings in birefringent optical fibres", *IEEE Photon. Technol. Lett.*, Vol. **9**(10), pp.1370-1372, (1997)

110. A. S. Kurkov, M. Douay, O. Duhem, B. Leleu, J. F. Henninot, J. F. Bayon, L. Rivoallan, "Long-period fibre grating as a wavelength selective polarisation element", *Electron. Lett.*, Vol. **33**(7), pp.616-617, (1997)

111. L. A. Everall, R. W. Fallon, J. A. R. Williams, L. Zhang and I. Bennion, "Flexible fabrication of long period in-fibre gratings", *Proc. of Conference on Lasers and Electro-Optics (CLEO'98),* pp.513 , (1998)

112. B. Malo, K. O. Hill, F. Bilodeau, D. C. Johnson, J. Albert, "Point-By-Point Fabrication Of Micro-Bragg Gratings In Photosensitive Fiber Using Single Excimer Pulse Refractive-Index Modification Techniques", *Electron. Lett.*, Vol. **29**(18), pp.1668-1669, (1993)

113. D. D. Davis, T. K. Gaylord, E. N. Glytsis, S. C. Mettler, "CO2 laser-induced long-period fibre gratings: spectral characteristics, cladding modes and polarisation independence", *Electron. Lett.,* Vol. **34**(14), pp.1416-1417, (1998)

114. N. Godbout, X. Daxhelet, A. Maurier and S. Lacroix, "Long-period fibre grating by electrical discharge", *Proc. Of 24th European Conference on Optical Communication*, pp.397, (1998)

115. M. J. Adams, An Introduction to Optical Waveguide, pp.223-233.

116. G. P. Agrawal, Fiber-Optics Communication System, pp.22-44

117. D. Marcuse, "Coupled-mode theory of round optical fibers", *Bell Syst. Tech. J.*, Vol. **52**(6), pp.817-842, (1973)

118. D. G. Hall, "Vector-beam solutions of Maxwell's wave equation", *Opt. Lett.*, Vol.**21**(1), pp.9-11, (1996)

119. L. Poladian, "Graphical and WKB analysis of nonuniform Bragg gratings", *Physical Review*

E, Vol. **48**(6), pp.4758-4767, 1993.

120. C. Martijn de Sterke and N. G. R. Broderick, "Coupled-mode equations for periodic superstructure Bragg gratings", *Optics Letters*, Vol. **20**(20), pp.2039-2041, (1995)

121. V. Mizrahi and J. E. Sipe, "Optical properties of photosensitive fiber phase gratings", *J. Lightwave Technology*, Vol. **11**(10), pp.1513-1517, (1993)

122. J. L. Cruz, L. Dong, S. Barcelos, L. Reekie, "Fiber Bragg gratings with various chirp profiles made in etched tapers", *Appl. Opt.*, Vol.**35**(34), pp.6781-6787, (1996)

123. H. G. Winful, "Pulse compression in optical fiber filters", *Appl. Phys. Lett.* Vol. **46**(6), pp.527-529, (1985)

124. D. S. Peter, W. Hodel, and H. P. Weber, "Compression of pulses spectrally broadened by self-phase modulation using a fiber-grating: a theoretical study of the compression efficiency", *Opt. Commun.*, Vol. **112**(1-2), pp.59-66, (1994)

125. R. Kashyap, P. F. Mckee, R. J. Campbell, D. L. Williams, "Novel Method Of Producing All-Fiber Photoinduced Chirped Gratings", Electron. Lett., Vol.**30**(12), pp.996-998, (1994)

126. W. H. Loh, R. I. Laming, A. D. Ellis, D. Atkinson, "10 Gb/s transmission over 700 km of standard single-mode fiber with 10-cm chirped fiber grating compensator and duobinary transmitter", IEEE Photon. Technol. Lett., Vol.8(9), pp.1258- 1260, (1996)

127. K. O. Hill, F. Bilodeau, B. Malo, T. Kitagawa, S. Theriault, D. C. Johnson, J. Albert, K. Takiguchi, "Chirped in-fiber bragg gratings for compensation of optical- fiber dispersion", *Opt. Lett.*, Vol.19(17), pp.1314-1316, (1994)

128. B. Malo, S. Theriault, D. C. Johnson, F. Bilodeau, J. Albert, K. O. Hill, "Apodised in-fiber bragg grating reflectors photoimprinted using a phase mask", *Electron. Lett.*, Vol.**31**(3), Pp.223-225, (1995)

129. J. Albert, K. O. Hill, B. Malo, S. Theriault, F. Bilodeau, D. C. Johnson, L. E. Erickson, "Apodization of the spectral response of fiber bragg gratings using a phase mask with variable diffraction efficiency", *Electron. Lett.*, , Vol.**31**(3), pp.222-223, (1995)

130. W. H. Loh, M. J. Cole, M. N. Zervas, S. Barcelos, R. I. Laming "Complex grating structures with uniform phase masks based on the moving fiber-scanning beam technique", *Opt. Lett.*, Vol.**20**(20), pp.2051-2053, (1995)

131. W. H. Loh, R. I. Laming, X. Gu, M. N. Zervas, M. J. Cole, T. Widdowson, A. D. Ellis "10 cm chirped fibre Bragg grating for dispersion compensation at 10 Gbit/s over 400km of non-dispersion shifted fibre", Electron. Lett., Vol.31(25), pp.2203-2204, (1995)

132. M. J. Cole, W. H. Loh, R. I. Laming, M. N. Zervas, S. Barcelos, "Moving fiber/phase mask-scanning beam technique for enhanced flexibility in producing fibre gratings with uniform phase mask", *Electron. Lett.*, Vol.**31**(17), pp.1488-1490, (1995)

133. R. Kashyap, P. F. Mckee and D. Armes, "UV written reflection grating structures in photosensitive optical fibers using phase-shifted phase mask", *Electron. Lett.* Vol. **30**(23), pp.1977-1978, (1994)

134. J. Canning and M. G. Sceats, "π phase shifted periodic distributed structures in optical fibers by UV post-processing", *Electron. Lett.*, Vol. **30**(16), pp.1344-1345, (1994)

135. L. Zhang, K. Sugden, J. A. R. Williams, and I. Bennion, "Postfabication exposure of a gap-type bandpass filters in broadly chirped fiber gratings", *Opt. Lett.* Vol. **20**(18), pp.1927-1929, (1995)

136. M. Okai, I.F. Lealman, L.J. Rivers, C. Dix and M.J. Robertson, "In-line Fabory-Perot optical waveguide filter with quasi-chirped gratings", *Electron. Lett.* **32**(2), pp.108-109, (1996)

137. M. Janos, J. Canning and M.G. Sceats, "Transient transmission nothces induced in Er^{3+} doped optical fiber Bragg gratings", *Electon. Lett.* Vol. **32**(3), pp.245-246, (1996)

138. J. Albert, K. O. Hill, D. C. Johnson, F. Bilodeau, and M. J. Rooks, "Moire phase masks for automatic pure apodisation of fiber Bragg gratings", *Electron. Lett.*, Vol. **32**(24), pp.2260-2261, (1996)

139. D. Pastor, J. Capmany, D. Ortega, V. Tatay, and J. Marti, "Design of apodized linearly chirped fiber gratings for dispersion compensation", *J. Lightwave Technol.*, Vol. **14**(11), pp.2581-2588, (1996)

140. L. Zhang, Y. Liu, I. Bennion, K. Sugden, L. Dong, "Fabrication of high-rejection-low-loss single-passband filters in cladding depressed fiber by the chirped-grating concatenation method", *Opt. Lett.,* Vol.**23**(21), pp.1665-1667, (1998)

141. R. Feced, M. N. Zervas, M. A. Muriel, "An efficient inverse scattering algorithm for the design of nonuniform fiber Bragg gratings", *IEEE journal of quantum electronics*, Vol.**35**(8), pp.1105-1115, (1999)

142. J. M. Jouanno, J. Hubner, J. E. Pedersen, R. Kromann, T. Feuchter, M. Kristensen, "Strong Bragg gratings for WDM devices in non-sensitized low-loss Ge-doped waveguides", *Electron. Lett.,* Vol.**32**(23), pp.2151-2152, (1996)

143. L. R. Chen, D. J. F. Cooper, P. W. E. Smith, "Transmission filters with multiple flattened passbands based on chirped Moire gratings", *IEEE Photon. Technol. Lett.,* Vol.**10**(9), pp.1283-1285, (1998)

144. A. D. Kersey, M. A. Davis, H. J. Patrick, M. LeBlanc, K. P. Koo, C. G. Askins, M. A. Putnam, E. J. Friebele, "Fiber grating sensors", *J. of Lightwave Technol.,* Vol.**15**(8), pp.1442-1463, (1997)

145. D. C. J. Reid, C. M. Ragdale, I. Bennion, D. J. Robbins, J. Buus, W. T. Stewart, "Phase-shifted Moiré grating fibre resonators", Electron. Lett., Vol.**26**(1), pp.10-12, (1990)

146. R. C. Alferness, C. H. Joyner, M. D. Divino, M. J. R. Martyak, L. L. Buhl, "Narrowband grating resonator filters in InGaAsP/InP waveguides", *Applied Phys. Lett.*, Vol.**49**(3), pp.125-127, (1986)

147. G. P. Agrawal, S. Radic, "Phase-shifted fiber Bragg gratings and their application for wavelength demultiplexing", *IEEE photon. Technol. Lett.*, Vol.**6**(8), pp.995-997, (1994)

148. R. Zengerle, O. Leminger, "Phase-shifted Bragg-grating filters with improved transmission characteristics", *J Lightwave Technol.*, Vol.**13**(12), pp.2354-2358, (1995)

149. M. J. Guy, J. R. Taylor and R. Kashyap, "Single-frequency erbium fiber ring laser with intracavity phase-shifted fiber Bragg grating narrowband filter", *Electron. Lett.* Vol. **31**(22), pp.1924-1925, (1995)

150. W. P. Huang, Q. Guo, C. Wu, "A polarization-independent distributed Bragg reflector based on phase-shifted grating structures", *J Lightwave Technol.*, Vol.**14**(3), pp.469-473, (1996)

151. G. P. Agrawal and S. Radic, "Phase shifted fiber Bragg gratings and their application for wavelength de-multiplexing", *IEEE Photonics Technol. Lett.* Vol. **6**(8), pp.995-977, (1994)

152. I. Riant, F. Haller, "Study of the photosensitivity at 193 nm and comparison with photosensitivity at 240 nm influence of fiber tension : Type IIa aging : Fiber gratings, photosensitivity, and poling", *J Lightwave Technol.*, Vol.**15**(8), pp.1464-1469, (1997)

153. M. Douay, W. X. Xie, T. Taunay P. Bernage, P. Niay, P. Cordier, B. Poumellec, L. Dong, J. F. Bayon, H. Poignant, E. Delevaque, "Densification involved in the UV-based photosensitivity of silica glasses and optical fibers : Fiber gratings, photosensitivity, and poling", *J Lightwave Technol.*, Vol.**15**(8), pp.1329-1342, (1997)

154. H. J. Patrick, C. G. Askins, R. W. McElhanon, E. J. Friebele, "Amplitude mask patterned on an excimer laser mirror for high intensity writing of long period fibre gratings", *Electron. Lett.*, Vol.33(13), pp.1167-1168, (1997)

155. S. Yamasaki, M. Akiyama, K. Nishide, A. Wada, R. Yamauchi, "Characteristics of long-period fiber grating utilizing periodic stress relaxation", *IEICE Transactions on Electronics*, Vol. E83-C(3), pp.440-443, (2000)

156. E. M. Dianov, V. I. Karpov, M. V. Grekov, K. M. Golant, S. A. Vasiliev, O. I. Medvedkov, R. R. Khrapko, "Thermo-induced long-period fibre gratings", *IEE conference publication*, No.448, pp.53-56, (1997)

157. D. D. Davis, T. K. Gaylord, E. N. Glytsis, S. G. Kosinski, S. C. Mettler, A. M. Vengsarkar, "Long-period fibre grating fabrication with focused CO_2 laser pulses", *Electron. Lett.*, Vol.34(3), pp.302-303, (1998)

158. S. A. Vasiliev, E. M. Dianov, D. Varelas, H. G. Limberger, R. P. Salathe, "Postfabrication resonance peak positioning of long-period cladding-mode-coupled gratings", *Opt. Lett.*, Vol. **21**(22), pp.1830-1832, (1996)

159. P. F. Wysocki, J. Judkins, R. Espindola, M. Andrejco, A. Vengsarkar, K. Walker, "Erbium-doped fiber amplifier flattened beyond 40 nm using long-period grating", *OFC'97 Technical Digest*, pp. PD2-1, (1997)

160. Y. Liu, S. B. Lee, and S. S. Choi, "Design of long-period fiber grating spectrum with a phase-shift", *Korean Optical Communications*, pp.129-130. (1997)

161. Bakhti, P. Sansonetti, "Realization of low back-reflection, wideband fiber bandpass filters using phase-shift long-period gratings", *OFC'97 Technical Digest*, pp.349-350, (1997).

162. S. M. Melle, K. Liu and R. M. Measures, "A passive wavelength demodulation system for guided-wave Bragg grating sensors", *IEEE Photon. Technol. Lett.*, Vol. **4**(5), pp.516-518, (1992)

163. R. M. Measures, A. T. Alavie, R. Maaskant, M. Ohn, S. Karr and S. Huang, "Bragg grating structural sensing system for Bridge monitoring", *Proc. SPIE,* Vol. **2294,** pp.53-60, (1994)

164. M. A. Davis and A. D. Kersey, "All-fibre Bragg grating strain-sensor demonstration technique using a wavelength division coupler", *Electron. Lett.*, Vol. **30**(1), pp.75-77, (1994)

165. R. Kashyap, P. F. Mckee, D. J. Armes, M. Shabeer, D. Cotter, "Measurement of ultra-steep edge, high rejection fiber bragg grating filters", *Electron. Lett.*, Vol.**31**(15), pp.1282-1283, (1995)

166. Q. Zhang, D. A. Brown, H. Kung, J. E. Townsend, M. Chen, L. J. Reinhart and T. F. Morse, "Use of highly overcoupled couplers to detect shifts in Bragg wavelength", *Electron. Lett.*, Vol. **31**(6), pp.480-482, (1995)

167. A. B. L. Riberio, L. A. Ferreira, M. Tsvetkov and J. L. Santos, "All-fibre interrogation technique for fibre Bragg sensors using a biconical fibre filter", *Electron. Lett.*, Vol. **32**(4), pp.382-383, (1996)

168. R. Fallon, L. Zhang and I. Bennion, "Long-period grating interrogating FBG strain sensor achieving a combination of large dynamic range and high resolution", *EURO/CLEO Proc.* CWP3, (1998)

169. J. Meissner and W. Nowak, "Strain Monitoring at a Pre-stressed Concrete Bridge", *12th Interna. Conf. On Optical Fiber Sensors Proc.* OThC1, (1997)

170. T. Erdogan and J. E. Sipe, "Radiation-mode coupling loss in tilted fiber phase gratings", *Opt. Lett.,* Vol. **20**(18), pp.1838-1840, (1995)

171. Lee M K, Little G R, "Study of radiation modes for 45-deg tilted fiber phase gratings", *Optical Engineering*, Vol. **37**(10), pp.2687-2698, (1998)

172. T. Erdogan, "Cladding-mode resonances in short- and long-period fiber grating filters", J. Opt. Soc. Am. Vol.**14**(8), pp.1760-1773, (1997)

173. K. Sugden, L. Zhang, J. R. A. Williams, R. W. Fallon, L. A. Everall, K. E. Chisholm, I. Bennion, "Fabrication and characterization of bandpass filters based on concatenated chirped fiber gratings ", *J. Lightwave Tech.*, Vol. **15**(8), pp.1424-1432, (1997)

174. L. Dong, L. Reekie, J. L. Cruz, J. E. Caplen, J. P. deSandro, D. N. Payne, "Optical fibers with depressed claddings for suppression of coupling into cladding modes in fiber Bragg gratings", *IEEE Photonics Letters*, Vol. **9**(1), pp.64-66, (1997)

175. P. Harper, F. M. Knox, P. N. Kean, L. Zhang, N. J. Doran, I. Bennion, CLEO Europe, Hamburg, Germany, September 1996, CThF3.

176. P. D. Foote, "fiber Bragg grating strain sensors for aerospace smart structures", *Glasgow, SPIE.* Vol. 2361, pp.290-293, (1994)

177. A. D. Kersey, T. A. Berkoff, W. W. Morey, "Multiplexed fiber Bragg grating strain-sensor system with a fiber Fabry-Perot wavelength filter", *Opt. Lett.*, Vol. **18**(16), pp.1370-1372, (1993)

178. R. S. Weis, A. D. Kersey, T. A. Berkoff, "A 4-element fiber grating sensor array with phase-

sensitive detection", *IEEE Photon. Technol. Lett.*, Vol. **6**(12), pp.1469-1472, (1994)

179. M. A. Davis, D. G. ellemore and A. D. Kersey, "structural strain mapping using a wavelength time-division addressed fiber Bragg grating array", *Proc. 2nd Euro. Conf. On Smart Structures and Materials, (Glasgow, UK'1994), SPIE.* Vol. 2361, pp.342-345, (1994)

180. Y. J. Rao, "In-fibre Bragg grating sensors", *Meas. Sci. Technol.*, Vol. **8**(4), pp.355-375, (1997).

181. J. Patrick, A. D. Kersey, F. Bucholtz, K. J. Ewing, J. B. Judkins, A. M. Vengsarkar, *Conference on Laser and Electro-Optics (CLEO'97)*, pp.420-422, (1997)

182. Bjerkan, K. Johannessen and X. Guo, "Measurement of Bragg grating birefringence due to transverse compressive force", *Proc. Of 12th International Conf. on Optical Fibre Sensors*, p., 1997

183. M. Sudo, M. Nakai, K. Himeno, S. Suzaki, A. Wada, R.Yamauchi, "Simultaneous measurement of temperature and strain using PANDA fibre grating", *Proc. Of 12th International Conf. on Optical Fibre Sensors*, p.170, (1997)

184 Y. Liu, L. Zhang, and I. Bennion, "Fibre-optic load sensors with high transverse strain sensitivity based on long-period gratings in B/Ge co-doped fibre", *Electron. Lett.*, Vol. **35**(8), pp.661-663 (1999)

185. E. Udd, D. Nelson and C. Lawrence, "Multiple axis strain sensing using fibre gratings written onto birefringent single mode optical fibre", *Proc. Of 12th International Conf. on Optical Fibre Sensors*, p.48, (1997)

186. H. J. Patrick, C. C. Chang, S. T. Vohra, "Long-period fiber gratings for structure bend sensing", *Electron. Lett.*, Vol. **34**(18), pp.1773-1775, (1998)

187. H. J. Patrick and S. T. Vohra, "Directional shape sensing using sensitivity of long period fiber gratings", *OFS-13*, Korea, pp.561-564, (1999)

188. J. Rathje, M. Kristensen and J. Hubner, "Effects of core concentricity error on bend direction asymmetry for long-period fibre gratings", *BGPW'99*, Florida, pp.283-285, (1999)

189. V. V. Steblina, J. D. Love, R. H. Stolen, J. S. Wang, "Cladding mode degeneracy in bent W-fibres beyond cutoff", *Opt. Comm.*, Vol. **156**(4-6), pp.271-274, (1998)

190 Y. Liu, L. Zhang, J. A. R. Williams and I. Bennion, "Optical bend sensor based on measurement of resonance mode splitting of long-period fibre grating", *Photonics Technology Letters,* Vol. **12**(5), pp.531-533, 2000

APPENDIX

A.1 Publications

[1] **Y. Liu**, L. Zhang, J. A. R. Williams and I. Bennion, "Optical bend sensor based on measurement of resonance mode splitting of long-period fibre grating", *Photonics Technology Letters,* Vol. **12**(5), pp. 531-533, 2000

[2] S. Li, K. S. Chiang, W. A. Gambling, **Y. Liu**, L. Zhang, and I. Bennion, "Novel tunable all-optical incoherent negative-tap fiber-optic transversal filter based on DFB laser diode and fibre Bragg gratings", *Photonics Technolnology Letters,* Vol. **12**(9), 1207-1209, (2000)

[3] S. Li, K. S. Chiang, W. A. Gambling, **Y. Liu**, L. Zhang, and I. Bennion, "Self-seeding of Fabry-Perot laser diode for generating wavelength-tunable chirp-compensated single-mode pulses with high-sidemode suppression ratio", *Photonics Technology Letters*, Vol 12,(11), pp.1441-1443, (2000)

[4] **Y. Liu**, L. Zhang, and I. Bennion, "Fabricating fibre edge filters with arbitrary spectral response based on tilted chirped grating structures", *Meas. Sci. Tech.* Vol.**10**(L1-L3), (1999)

[5] L. Zhang, **Y. Liu**, L. Everall, J. A. R. Williams, and I. Bennion, "Design and realisation of long-period grating devices in conventional and hi-bi fibres and their novel applications as fibre-optic load sensors", *IEEE Journal Of Selected Topics In Quantum Electronics (IEEE JSTQE),* Vol.**5**(5), pp.1373-1378, (1999)

[6] L. Zhang, **Y. Liu**, J. A. R. Williams, I. Bennion, "Enhanced FBG strain sensing multiplexing capacity using combination of intensity and wavelength dual-coding technique", *IEEE PHOTONICS TECHNOLOGY LETTERS*, Vol.**11**(12), pp.1638-1640, (1999)

[7] **Y. Liu**, J. A. R. Williams, L. Zhang, and I. Bennion, "Phase shifted and cascaded long-period fiber gratings", *Optical Communications*, Vol.**164**, pp. 27-31, (1999)

[8] **Y. Liu**, L. Zhang, and I. Bennion, "Fibre-optic load sensors with high transverse strain sensitivity based on long-period gratings in B/Ge co-doped fibre", *Electronics Letters* Vol.**35**(8), pp.661-663, (Apr 1999)

[9] L. Zhang, **Y. Liu**, I. Bennion, K. Sugden, and L. Dong, "Fabrication of high-rejection/low-loss single passband filters in cladding depressed fibre by chirped grating

concatenation method", *Optical Letters,* Vol.**23**(21), pp.1665-1667, (Nov 1998)

[10] S. Li, K. T. Chan, **Y. Liu**, L. Zhang, and I. Bennion, "Multiwavelength picosecond pulses generated from a self-seeded Fabry-Perot laser diode with a fibre external cavity using fibre Bragg gratings", *IEEE Photonics Technology Letters,* Vol.**10** (12), pp.1712-1714, (Dec 1998)

[11] **Y. Liu**, L. Zhang, J. A. R. Williams, I. Bennion, "Long-period fibre grating bend sensor based on measurable of resonance mode splitting", *Conference on Lasers and Electro-Optics (CLEO'2000),* (May, 2000, San Francisco, California, USA)

[12] **Y. Liu**, L. Zhang and I. Bennion, "Bending curvature sensing based on measurement of resonance mode splitting of long-period fibre grating", *14th International Conference on Optical Fibwe Sensors (OFS'2000),* (Oct. 2000, Italy)

[13] **Y. Liu**, L. Zhang and I. Bennion, "Long-period fibre grating load sensors with high transverse strain sensitivity", *14th International Conference on Optical Fibwe Sensors, (OFS'2000),* (Oct. 2000, Italy)

[14] B. A. L. Gwandu, L. Zhang, K. Chisholm, **Y. Liu** and I. Bennion, "Compact FBG grating array structure for high spatial resolution distributed strain sensing", *14th International Conference on Optical Fibwe Sensors (OFS'2000),* Technical Digest, (Oct. 2000, Italy)

[15] **Y. Liu**, L. Zhang and I. Bennion "Novel optical sensing applications of long-period fibre gratings", *Institute of Physics Meeting on In-Fibre Bragg Gratings and Special Fibres,* London (Sept., 2000)

[16] H. J. Booth, M. R. H. Knowles, R. A. Benfield, A. J. Andrews, A. J. Kearsley, R. T. Thomas, L. Zhang, **Y. Liu**, "Advances in UV-copper vapour lasers and results on the production of fibre Bragg gratings", *Institute of Physics Meeting on In-Fibre Bragg Gratings and Special Fibres,* London (Sept., 2000)

[17] B. A. L. Gwandu, L. Zhang, K. Chisholm, **Y. Liu** and I. Bennion "High-spatial-resolution distributed sensing using compact FBG grating array structures", *Institute of Physics Meeting on In-Fibre Bragg Gratings and Special Fibres,* London (Sept., 2000)

[18] D. J. L. Birkin, E. U. Rafailov, W. Sibbett, L. Zhang, **Y. Liu**, and I. Bennion, "Compression of 980 nm diode laser pulses using an aperiodic Bragg-grating fibre", *Conference on Lasers and Electro-Optics (CLEO'1999), Technical Digest,* San Francisco, California (May, 1999)

[19] L. Zhang, **Y. Liu**, I. Bennion, D. Coutts, C. E. Webb, "Fabrication of short and long period gratings using 255 nm light from a frequency-doubled copper vapour laser", *Institute of Physics Meeting on In-Fibre Bragg Gratings and Special Fibres,* London (May, 1999)

[20] L. Zhang, **Y. Liu**, I. Bennion, D. Coutts, C. E. Webb, "Fabrication of short and long period gratings using 255 nm light from a frequency-doubled copper vapour laser", *Institute of Physics Meeting on In-Fibre Bragg Gratings and Special Fibres*, London (May 1999)

[21] X. Wang, K. T. Chan, **Y. Liu**, L. Zhang, and I. Bennion, "Novel temporal/spectral coding technique based on fibre Bragg gratings for fibre-optic CDMA application", *Conference on Optical Fibre Communications (OFC'99)*, Techn Digest, San Diego, California, WM50 (Feb 1999)

[22] L. Zhang, K. Sugden, **Y. Liu**, I. Bennion, and L. Dong, "High-rejection/low-loss single passband filters with 50nm stopband in depressed cladding fibre by chirped grating concatenation method", *Proceedings of the 24th European Conference on Optical Communications (ECOC'98)*, Madrid, Spain, pp. 191-192 (Sep 1998)

[23] **Y. Liu**, L. Zhang, and I. Bennion, "Design and fabrication of edge filters based on tilted chirped gratings and their application in strain and temperature optical sensing", *Institute of Physics Meeting on In-Fibre Bragg Gratings and Special Fibres*, London (May 1998)

[24] L. Zhang, **Y. Liu**, J. A. R. Williams, and I. Bennion, "Enhanced multiplexing capacity of FBGs strain sensing using combination of intensity and wavelength division multiplexing", *14th International Conference on Optical Fibre Sensors (OFS'99)*, Technical Digest, Kyongju, Korea (Apr 1999)

[25] **Y. Liu**, L. Zhang, and I. Bennion, "Arbitrary spectral response fibre edge filters based on tilted chirped grating structures", *Conference on Lasers and Electro-Optics (CLEO'99)*, Technical Digest, (1999)

[26] **Y. Liu**, L. Zhang, W. Zhang, J. A. R. Williams, and I. Bennion, "Investigation of H2 in- and out-diffusion in long-period grating devices", *Conference on Lasers and Electro-Optics (CLEO'99)*, Technical Digest, (1999)

A.2 List of Programmes

1. Simulation program for holographic fabrication technique (in Matlab)

- Plot the real size optical setup
- Setting grating wavelength
- Setting grating chirp
- Setting the wavelength shift by shifting one cylindrical lens,

2. Simulation programme for phase mask fabrication technique (in Matlab)

- Plot the real size optical setup
- Plot the writing efficiency against the UV beam width
- Confirm a cylindrical lens cab be used to resize the UV beam-width

3. Simulation programme for holographic fabrication technique (in LabVIEW)

- Setting grating wavelength by changing the interfere-arm length
- Setting gratings chirp
- Timer the shutter by computer.

4. Programmes for data capture and data processing (in LabVIEW)

- Capture the data from different Optical Spectrum Analysers (OSAs)
- Multiple sections capture to increase the spectral resolution
- Auto capture for the study of spectral evolution
- Transfer data as ***.txt** and ***.xls** file in three forms:
  - (a) One trace respect to one file
  - (b) Multiple traces to one file with format of [x1; y1, y2, y3..]
  - (c) Multiple traces to one file with format of [x1, y1; x2, y2; x3, y3;…]
- Normalization one trace or multiple traces
- Re-scale and zoom the traces
- Peak detection, Linewidth measurement
- Fitting, filtering and averaging a waveform,

5. IWDM system -real time strain measurement (in LabVIEW),

- IWDM system for real time strain measurement using scanning Fabry-Perot
- Auto show the measurement for demonstration

6. Programmes for modelling of FBGs and LPGs (in LabVIEW)

- Uniform fibre Bragg gratings
- One or multiple π phase-shifted fibre Bragg gratings
- Chirped fiber Bragg gratings with apodisation
- Band-pass filters by cascading a series of chirped Bragg gratings
- Chirped Moire Bragg gratings, moire fringes

- Apodisated Bragg gratings with more than ten kinds of apodisation profiles
- Sampled Bragg grating with rectangular and composite cosine profiles
- Fabry-Perot oscillations and spectral evolution of fibre Bragg gratings
- Uniform long-period fibre gratings
- Spectral evolution of long-period fibre gratings
- Phase shifted and cascaded long-period fibre gratings
- Refractive index sensing using Long-period fibre gratings

7. Motion stage (MM2000) fabrication system (in LabVIEW)

- Simple grating fabrication
- Apodised grating fabrication I
  Dithering phase mask with a triangle wave using a PZT stage and DAQ I/O card
- Apodised gratings fabrication II
  Slow shifting phase mask using a PZT stage and DAQ I/O card
- Phase shifted grating fabrication
  Multiple π phase-shifted fibre Bragg gratings using PZT stage and DAQ I/O card
- The fabrication of square reflection profile gratings
- Sampled grating fabrication
  * Rectangular profile sampled fiber Bragg gratings using a shutter to block the UV beam on and off
  * Composite cosine profile for multiple peaks reflection with the same reflectivity
- Chirped Moiré grating fabrication
- Chirping scan of the translation stage
- Programmes for fibre alignment
  Programme control
  Hand control with an extra logic box

8. Motion stage (MM4005) fabrication system (in LabVIEW)

- Simple grating fabrication
- Apodised grating fabrication
  Gaussian apodisation profile
  Improved gaussian apodisation profile
  Blackman apodisation profile,
  ...
- The fabrication of square reflection profile gratings
- Sampled grating fabrication
- Chirped Moiré grating fabrication
- Long-length grating fabrication

A.3 Expression of three phase-shifted Bragg gratings

Three phase shifts within a fibre Bragg grating separate the grating length into four sub-gratings G_i described by r_i and t_i, respectively. The transform matrix for the entire grating structure is then given by

$$M = M_4 \cdot P_3 \cdot M_3 \cdot P_2 \cdot M_2 \cdot P_1 \cdot M_1 \tag{A.1}$$

where, i=1, 2, 3, 4 indicates the four sub-gratings and three phase shifts, M_i and P_i are the matrixes of the sub-grating G_i and phase ϕ_i expressed in eqn. (3.96) and eqn. (3.100). Substituting the corresponding matrix into eqn. (A.1) yields

$$M = \begin{bmatrix} \frac{1}{t_4^*} & \frac{r_4}{t_4} \\ -\frac{r_4}{t_4} & \frac{1}{t_4} \end{bmatrix} \begin{bmatrix} e^{j\phi_3/2} & 0 \\ 0 & e^{-j\phi_3/2} \end{bmatrix} \begin{bmatrix} \frac{1}{t_3^*} & \frac{r_3}{t_3} \\ -\frac{r_3}{t_3} & \frac{1}{t_3} \end{bmatrix} \begin{bmatrix} e^{j\phi_2/2} & 0 \\ 0 & e^{-j\phi_2/2} \end{bmatrix} \begin{bmatrix} \frac{1}{t_2^*} & \frac{r_2}{t_2} \\ -\frac{r_2}{t_2} & \frac{1}{t_2} \end{bmatrix} \begin{bmatrix} e^{j\phi_1/2} & 0 \\ 0 & e^{-j\phi_1/2} \end{bmatrix} \begin{bmatrix} \frac{1}{t_1^*} & \frac{r_1}{t_1} \\ -\frac{r_1}{t_1} & \frac{1}{t_1} \end{bmatrix} \tag{A.2}$$

where the relationship $(r_i / t_i)^* = -r_i / t_i$ for uniform gratings has been used. Multiplying every two matrixes of eqn. (A.2) yield

$$M = \begin{bmatrix} \frac{1}{t_4^*} & \frac{r_4}{t_4} \\ -\frac{r_4}{t_4} & \frac{1}{t_4} \end{bmatrix} \begin{bmatrix} \frac{e^{j\phi_3/2}}{t_3^*} & \frac{r_3}{t_3} e^{j\phi_3/2} \\ -\frac{r_3}{t_3} e^{-j\phi_3/2} & \frac{e^{-j\phi_3/2}}{t_3} \end{bmatrix} \begin{bmatrix} \frac{e^{j\phi_2/2}}{t_2^*} & \frac{r_2}{t_2} e^{j\phi_2/2} \\ -\frac{r_2}{t_2} e^{-j\phi_2/2} & \frac{1}{t_2} e^{-j\phi_2/2} \end{bmatrix} \begin{bmatrix} \frac{e^{j\phi_1/2}}{t_1^*} & \frac{r_1}{t_1} e^{j\phi_1/2} \\ -\frac{r_1}{t_1} e^{-j\phi_1/2} & \frac{e^{-j\phi_1/2}}{t_1} \end{bmatrix} \tag{A.3}$$

Again, multiplying every two matrixes of eqn. (A.3) yields

$$M = \begin{bmatrix} \dfrac{e^{j\phi_3/2}}{t_3^{*}t_4^{*}} - \dfrac{r_3}{t_3}\dfrac{r_4}{t_4}e^{-j\phi_3/2} & \dfrac{r_3}{t_3 t_4^{*}}e^{j\phi_3/2} + \dfrac{r_4}{t_3 t_4}e^{-j\phi_3/2} \\ -\dfrac{r_4}{t_3^{*}t_4}e^{j\phi_3/2} - \dfrac{r_3}{t_3 t_4}e^{-j\phi_3/2} & -\dfrac{r_4}{t_4}\dfrac{r_3}{t_3}e^{j\phi_3/2} + \dfrac{1}{t_3 t_4}e^{-j\phi_3/2} \end{bmatrix} \tag{A.4}$$
$$\times \begin{bmatrix} \dfrac{e^{j(\phi_2+\phi_1)/2}}{t_1^{*}t_2^{*}} - \dfrac{r_1}{t_1}\dfrac{r_2}{t_2}e^{-j\phi_1/2}e^{j\phi_2/2} & \dfrac{r_1}{t_1 t_2^{*}}e^{j(\phi_2+\phi_1)/2} + \dfrac{r_2}{t_2}\dfrac{e^{-j\phi_1/2}}{t_1}e^{j\phi_2/2} \\ -\dfrac{r_2}{t_1^{*}t_2}e^{-j\phi_2/2}e^{j\phi_1/2} - \dfrac{r_1}{t_1 t_2}e^{-j(\phi_2+\phi_1)/2} & -\dfrac{r_1}{t_1}\dfrac{r_2}{t_2}e^{-j\phi_2/2}e^{j\phi_1/2} + \dfrac{1}{t_1 t_2}e^{-j(\phi_2+\phi_1)/2} \end{bmatrix}$$

Then, the element *M22* of the matrix is obtained as

$$M22 = \left(-\frac{r_4}{t_3^{*}t_4}e^{j\phi_3/2} - \frac{r_3}{t_3 t_4}e^{-j\phi_3/2}\right)\left(\frac{r_1}{t_1 t_2^{*}}e^{j(\phi_2+\phi_1)/2} + \frac{r_2}{t_2}\frac{e^{-j\phi_1/2}}{t_1}e^{j\phi_2/2}\right) \tag{A.5}$$
$$+\left(-\frac{r_4}{t_4}\frac{r_3}{t_3}e^{j\phi_3/2} + \frac{1}{t_3 t_4}e^{-j\phi_3/2}\right)\left(-\frac{r_1}{t_1}\frac{r_2}{t_2}e^{-j\phi_2/2}e^{j\phi_1/2} + \frac{1}{t_1 t_2}e^{-j(\phi_2+\phi_1)/2}\right)$$

Simplifying eqn. (A.5) yields

$$M22 = -\frac{r_1 r_4}{t_1 t_2^{*} t_3^{*} t_4}e^{j(\phi_3+\phi_2+\phi_1)/2} - \frac{r_2 r_3}{t_1 t_2 t_3 t_4}e^{-j\phi_3/2}e^{-j\phi_1/2}e^{j\phi_2/2} \tag{A.6}$$
$$-\frac{r_1 r_3}{t_1 t_2^{*} t_3 t_4}e^{-j\phi_3/2}e^{j(\phi_2+\phi_1)/2} - \frac{r_2 r_4}{t_1 t_2 t_3^{*} t_4}e^{j\phi_3/2}e^{-j\phi_1/2}e^{j\phi_2/2} +$$
$$\frac{r_4}{t_4}\frac{r_3}{t_3}\frac{r_1}{t_1}\frac{r_2}{t_2}e^{j\phi_3/2}e^{-j\phi_2/2}e^{j\phi_1/2} + \frac{1}{t_1 t_2}\frac{1}{t_3 t_4}e^{-j(\phi_2+\phi_1)/2}e^{-j\phi_3/2}$$
$$-\frac{r_1 r_2}{t_1 t_2 t_3 t_4}e^{-j\phi_2/2}e^{j\phi_1/2}e^{-j\phi_3/2} - \frac{r_3 r_4}{t_1 t_2 t_3 t_4}e^{-j(\phi_2+\phi_1)/2}e^{j\phi_3/2}$$

Simplifying eqn. (A.6) yields

$$M22 = \frac{1}{t_1 t_2 t_3 t_4}\begin{bmatrix} -\dfrac{r_1 r_4}{t_2^{*}/t_2 \cdot t_3^{*}/t_3}e^{j(\phi_3+\phi_2+\phi_1)/2} - r_2 r_3 e^{-j\phi_3/2}e^{-j\phi_1/2}e^{j\phi_2/2} \\ -\dfrac{r_1 r_3}{t_2^{*}/t_2}e^{-j\phi_3/2}e^{j(\phi_2+\phi_1)/2} - \dfrac{r_2 r_4}{t_3^{*}/t_3}e^{j\phi_3/2}e^{-j\phi_1/2}e^{j\phi_2/2} + \\ r_1 r_2 r_3 r_4 e^{j\phi_3/2}e^{-j\phi_2/2}e^{j\phi_1/2} + e^{-j(\phi_2+\phi_1)/2}e^{-j\phi_3/2} \\ -r_1 r_2 e^{-j\phi_2/2}e^{j\phi_1/2}e^{-j\phi_3/2} - r_3 r_4 e^{-j(\phi_2+\phi_1)/2}e^{j\phi_3/2} \end{bmatrix} \tag{A.7}$$

Simplifying eqn. (A.8) yields

$$M22 = \frac{e^{-j(\phi_3+\phi_2+\phi_1)/2}}{t_1 t_2 t_3 t_4}\begin{bmatrix} -\dfrac{r_1 r_4}{t_2^{*}/t_2 \cdot t_3^{*}/t_3} e^{j(\phi_3+\phi_2+\phi_1)} - r_2 r_3 e^{j\phi_2} - \dfrac{r_1 r_3}{t_2^{*}/t_2} e^{j(\phi_2+\phi_1)} \\ -\dfrac{r_2 r_4}{t_3^{*}/t_3} e^{j(\phi_3+\phi_2)} + r_1 r_2 r_3 r_4 e^{j(\phi_3+\phi_2)} + 1 - r_1 r_2 e^{j\phi_1} - r_3 r_4 e^{j\phi_3} \end{bmatrix} \quad \text{(A.8)}$$

The amplitude transmittance is thus given by

$$t = \frac{1}{\mathrm{M22}} = \frac{e^{j(\phi_3+\phi_2+\phi_1)/2} t_1 t_2 t_3 t_4}{\left\{\begin{array}{l} 1 - r_1 r_2 e^{j\phi_1} - r_2 r_3 e^{j\phi_2} - r_3 r_4 e^{j\phi_3} - r_1 r_3 e^{j[\phi_2+\phi_1+2\arg(t_2)]} \\ - r_1 r_4 e^{j[\phi_3+\phi_2+\phi_1+2\arg(t_2)+2\arg(t_3)]} - r_2 r_4 e^{j[\phi_3+\phi_2+2\arg(t_3)]} + r_1 r_2 r_3 r_4 e^{j(\phi_3+\phi_2)} \end{array}\right\}} \quad \text{(A.9)}$$

where, the relationship $t_i/(t_i)^{*} = 2\arg(t_i)$ has been used to describe the sub-grating transmission phase.

It can be seen clearly that eqn. (A.9) reduces to the case of two phase-shifts for $r_4 = 0$, $t_4 = 1$, or $\phi_3 = 0$ as

$$t = \frac{e^{j(\phi_2+\phi_1)/2} t_1 t_2 t_3}{1 - r_1 r_2 e^{j\phi_1} - r_2 r_3 e^{j\phi_2} - r_1 r_3 e^{j[\phi_2+\phi_1+2\arg(t_2)]}} \quad \text{(A.10)}$$

Furthermore, for $r_3 = 0$, $t_3 = 1$, or $\phi_2 = 0$, eqn. (A.10) reduces to the case of one phase-shift as

$$t = \frac{e^{j(\phi_1)/2} t_1 t_2}{1 - r_1 r_2 e^{j\phi_1}} \quad \text{(A.11)}$$

and eqn. (A.11) reduces to normal uniform gratings for $r_2 = 0$, $t_2 = 1$ or $\phi_1 = 0$.